Elucidating the role of *Hmx1* during mouse development

THÈSE N^{O} 6630 (2015)

PRÉSENTÉE LE 29 OCTOBRE 2015

À LA FACULTÉ DES SCIENCES DE LA VIE
INSTITUT DES NEUROSCIENCES
PROGRAMME DOCTORAL EN NEUROSCIENCES

ÉCOLE POLYTECHNIQUE FÉDÉRALE DE LAUSANNE

POUR L'OBTENTION DU GRADE DE DOCTEUR ÈS SCIENCES

PAR

Linda BAPST

acceptée sur proposition du jury:

Prof. J. Gräff, président du jury
Prof. D. F. Schorderet, directeur de thèse
Prof. H. Dollfus, rapporteuse
Prof. F. Munier, rapporteur
Prof. R. Schneggenburger, rapporteur

ÉCOLE POLYTECHNIQUE
FÉDÉRALE DE LAUSANNE
Suisse
2015

Acknowledgment

First of all, I want to thank my thesis director, Daniel Schorderet, for accepting me in his lab, for his advice, for his support during my entire thesis and especially for his open-minded attitude regarding my unusual career path. Thank you to the president of the jury of my thesis, Prof. Johannes Gräff, and to the experts, Prof. Hélène Dollfuss, Prof. Ralph Schneggenburger and Prof. Francis Munier.

Thanks to my colleagues at the Institute for Research in Ophthalmology for the happy memories I will bring home. Thanks to the biologists and other PhD students for their advice and ideas which help me during these years at the lab. Thanks to the technicians for their receptiveness, their help and technical tips they provided me. Thank to the secretariat for their help concerning all administrative complications, to the informatics team and to the animal carers. And I want particularly to thank my colleagues Fabienne Marcelli and Arnaud Boulling for their collaboration in my thesis project.

An indescribable thank to my husband for his unconditional support during all the ups and down of my thesis. Thank you to my family, father, brothers, sister-in-law and grandmother who always supported and encouraged me. Thank you to my mother, not with us anymore, who gave me my unwavering determination.

Finally, thank you to Sue, Mélanie, Andy and Mark for revising my manuscript.

Lausanne, March 23rd 2015.

Abstract

This thesis focuses on the study of H6 homeobox 1 (*HMX1*) gene, a homeobox-containing transcription factor involved in sensory organ and eye development and responsible for the oculo-auricular syndrome of Schorderet-Munier-Franceschetti. The purpose of my PhD thesis is to better understand the mechanism and role of this transcription factor. My thesis is divided into three parts. The first part proposes a predictive promoter model approach to identify new *HMX1* target gene. The second part concerns an animal model of *Hmx1* mutation, the dumbo mouse model, and brings a new insight into lethal craniofacial defects. The third part concerns the characterization of the visual capacity of the dumbo mice and a description of a new pattern of vision-linked defects.

In the first part of this PhD thesis we propose a predictive promoter model approach based on transcriptomic analysis of post-natal day 15 mouse retina from dumbo and wild type mouse. This method revealed that *Sgcg*, *Tshz2* and *Slc6a9* were *Hmx1* targets in the mouse retina. *Ptpro*, *Sema3f*, and *Epha6* belong to the retinal axon guidance pathway and play an important role in retinotopic mapping. Significant enrichment of HMX1 binding site confirmed this pathway and we validated the transcriptional activity of *Hmx1* on *Ptpro*, *Sema3f* and *Sgcg* by Luciferase assay.

In the second part of this PhD thesis we investigate the dumbo mouse model, carrying a stop codon in *Hmx1*, and representing the first animal model for the oculo-auricular syndrome of Schorderet-Munier-Franceschetti. The homozygous $Hmx1^{dmbo}$ is a semi-lethal mutation and stillborns present severe craniofacial defects, including cleft palate, chest defect and bone hypoplasia of maxilla, zygomatic process, mandible and frontal.

In the third part of this PhD thesis we provide a complete description of the vision in dumbo mouse. Despite a normal retinal phenotype, the vision of this mouse is completely impaired. We demonstrate that this was caused by abnormal retinotopic mapping and optic nerve hypoplasia. In dumbo mice the retinal ganglion cells axon projections failed to target the visual output, namely the dorsal lateral geniculate nucleus and the superior colliculus, and present abnormal patterning.

Keywords : *HMX1*, dumbo, oculo-auricular syndrome, *EphA6*, *Sema3f*, *Ptpro*, *Sgcg*, craniofacial, cleft palate, retinotopic mapping, microphthalmia, cataract, optic nerve hypoplasia, vision

Résumé

Cette thèse se concentre sur l'étude du gène H6 homeobox 1 (*HMX1*), un facteur de transcription à homéo-domaine impliqué dans le développement des organes sensoriels et de l'œil et responsable du syndrome oculo-auriculaire de Schorderet-Munier-Franceschetti. Le but de mon étude est d'améliorer notre compréhension du mécanisme et du rôle de ce facteur de transcription. Ma thèse est divisée en trois parties. La première partie propose un modèle d'approche de prévision de promoteur pour identifier des nouveaux gènes cibles de *HMX1*. La deuxième partie concerne le modèle animal de la mutation de *Hmx1*, le modèle de souris dumbo, et apporte un nouvel aperçu sur des défauts craniofaciaux létaux. La troisième partie concerne la caractérisation des compétences visuelles de la souris modèle dumbo et la description d'un nouveau panel de déficits visuels.

Dans la première partie nous proposons un modèle d'approche de prévision de promoteur basé sur l'analyse du transcriptome de la rétine de souris sauvage et dumbo à 15 jours postnatal. Cette méthode a révélé que *Sgcg*, *Tshz2* and *Slc6a9*, sont des cibles de *Hmx1* dans la rétine de souris. *Ptpro*, *Sema3f*, et *Epha6* appartiennent à la voie de guidage des axones de la rétine et jouent un rôle important dans la configuration rétinotopique. Un enrichissement significatif des sites de lien de HMX1 a confirmé cette voie et nous avons validé l'activité transcriptionelle de *Hmx1* sur *Ptpro*, *Sema3f* et *Sgcg* par essai luciférase.

Dans la deuxième partie du projet nous examinons le modèle de souris dumbo, qui porte un codon stop dans *Hmx1*, et représente le premier modèle animal du syndrome oculo-auriculaire de Schorderet-Munier-Franceschetti. La mutation homozygote $Hmx1^{dmbo}$ est semi létale et les mort-nés présentent de sévère anomalie craniofaciale, incluant des fentes palatines, des malformations du torse and des hypoplasies de la maxilla, le processus zygomatique, la mandibule et l'os frontal.

Dans la troisième partie de la thèse nous fournissons une description complète de la vision de la souris dumbo. Malgré un phénotype rétinien normal, la vision de la souris est complètement détériorée. Nous démontrons que cela est causé par une configuration rétinotopique anormale et une hypoplasie du nerf optique. Chez la souris dumbo les projections axonales des cellules ganglionnaires rétiniennes ne réussissent pas à cibler le bon destinataire visuel, pour les nommer le noyau du corps genouillé latéral et le colliculus supérieur, et présentent une configuration anormale.

Mot-clé : *HMX1*, dumbo, syndrome oculo-auriculaire, *EphA6*, *Sema3f*, *Ptpro*, *Sgcg*, craniofaciale, fente palatine, configuration rétinotopique, microphtalmie, cataracte, hypoplasie du nerf optique, vision.

Table of contents

List of figures and tables

List of symbols and abbreviations

A

A: amacrine cells

ABCA4: ATP-binding cassette, sub-family A (ABC1), member 4

Aca: anterior part of anterior commissure

aef: anterior ethmoid foramen

Agilent: PfuUltra High-Fidelity DNA Polymerase

Agp: angular process

AMD: age related macular degeneration

ANTP: antennapedia

Ta: annealing temperatures

ANOVA: analysis of variance

APE 1: apurinic/apyrimidic endonuclease 1

ARVO: Association for Research in Vision and Ophthalmology

Arg: arginine

Asn: asparagine

as: alisphenoid

av: anteroventral thalamic nucleus

at-Ral: all-*trans*-retinal

B

B: bipolar cell

BA: branchial arche

bHLH: basic helix-loop-helix

Bmp: bone morphogenetic protein

Bnc2: Basonuclin 2

bo: basisoccipital

bs: basisphenoid

Bss: binding sites

C

C: cone

Ca^{2+}: calcium diprotic

CB: cell bodies

cc: corpus callosum

cDNA: coding deoxyribonucleic acid

cGMP: cyclic guanosine mono phosphate

cdp: condylar process

cl pl: cleft palate

CNC: cranial neural crest

CRM: cis-regulatory module

CNTF: ciliary neurotrophic factor

crp: coronoid process

crx: cone rod homeobox

ctx: cortex

D

D: dorsal

DAPI: diamidino-2-phénylindole

dg: dentate gyrus

DiI: dioctadecyltetramethylindocarbocyanine,

DiO: dioctadecyloxacarbocyanine perchlorate,

dlg: dorsal lateral geniculate nucleus

dLGN: dorsal lateral geniculate nucleus

Dlx: distal less homeobox

dmbo: dumbo

DMEM/F12: Dulbecco/Vogt modified Eagle's minimal essential medium F12

dnt: dentary

drg dorsal root ganglia

d3v: dorsal 3rd ventricle

E

ec: external capsule

Edn1: endothelin 1

Ebf1: early B-cell factor 1

ENU mutagenesis: N-ethyl-N-nitrosourea mutagenesis

eo: exooccipital

EphAs: ephrin type A receptor

EphBs: ephrin type B receptor

ER: endoplasmic reticulum

ERG: electroretinograms

E#: embryonic day #

F

F: fovea

FDR: false discovery rate

fi: fimbria of the hippocampus

FSAG: faciostatoacoustic ganglion complex

ft: frontal

Fgf: fibroblast growth factor

G

g: gonal

GABA: gamma-Aminobutyric acid

γ-SG immunostaining: gamma sarcoglycan immunostaining

GC: ganglion cell

GCL: ganglion celly layer

GD: gestational day

GDP: guanosine diphosphate

GTP: guanosine triphosphate

Gfap: Glial fibrillary acidic protein

Gln: glutamine

GO: Gene Ontology

H

H: horizontal cell

hip: hippocampus

HMX: Homeobox

HMX1 : H6 homebox 1

HMX1-Bss: HMX1 binding sites

HT: heterozygous

hyp: hypothalamus

hy: hyoid

I

I: iris

IS: inner segment

i: incus

IGL: intergeniculate leaflet

INL: inner nuclear layer

INBL: inner neuroblastic layer

I/OS: Inner-/outer segment border

ip: interparietal

ipRGC: intrisincally photosensitive retinal ganglion cell

IPL: inner plexiform layer

IRBP: interphotoreceptor retinoid binding protein

J

jg: jugal

K

N;KEGG: Kyoto Encyclopedia of Genes and Genomes

KOH: potassium hydroxyde

kV: kilo Volt

L

L: lens

la: lachrymal

LCA: Leber congenital amaurosis

ld: laterodorsal thalamic nucleus

LGN: lateral geniculate nucleus

Leu: leucine

li: lower incisor

LM: limiting membrane

lo: lamina obturans

LP: lens placode

LS-PPM: low specific PPM

LRAT: lecithin retinol acyltransferase

lv: lateral ventricle

Lhx gene: LIM homeobox gene

M

M: macula

M: Müller glia

m: malleus

ma: manubrium

MARCKS: Myristoylated alanine-rich C-kinase substrate

md: mandible

MIM: mendelian inheritance in man

µg: microgramme

min: minutes

mGluR6: metabotropic glutamate receptor

mpe: misplaced ear

mn: mandibular process

mnTG: mandibular lobe of the trigeminal ganglion

MRI: magnetic resonance imaging

mRNA: messenger ribonucleic acid

mV: mili volt

mx: maxilla

mx: maxillary process

mxTG: maxillary lobe of the trigeminal ganglion

µA: micro Amper

ms: mili second

N: nasal

Na^+: sodium mono protic

na: nasal

NADPH : nicotinamide adenine dinucleotide phosphate-oxidase

nc: nasal capsule

Neuro-2a or N2a aka: Mouse neuroblastoma cells

NFL: nerve fiber layer

ng: nanogrammes

NPCs : neural progenitor cell

Nkl: neural like homeobox

Nrp: neuropilin 2 receptor

Nrl: Neural retina-specific leucine zipper protein

N2A: neuro 2 A cells

O

OAS-SMF: oculo-auricular syndrome of Schorderet-Munier-Franceschetti

ob: otic bulla

oc: optic chiasm

OCT: Optical coherence tomography

OD: optic disc

OFL: optic fiber layer

OLM: Outer limiting membrane

on: optic nerve

ON: optic nerve

ONH: optic nerve hypoplasia

ONL: Outer nuclear layer

ONBL: outer neuroblastic layer

op: optic nerve layer of superior colliculus

op: optic vesicle

OPL: outer plexiform layers

Opn1sw: opsin 1 short wave

opt: optic tract

os: orbitosphenoid

OS: outer segment

OS: optic stalk

ot: nucleus of the optic tract

ov: otic vesicle

P

pa: parietal

PBS: phosphate-buffered saline

PCR: polymerase chain reaction

Pde6b: phosphodiesterase 6b

PEDF: pigment epithelium derived growth factor

PFA: paraformaldehyde

Phe: phenlalanine

P#: postnatal day #

pl: palate

pmx: premaxilla

POS: photoreceptor outer segment

PPM: predictive promoter model

Proteintech: anti-SGCG primary antibody

ps: presphenoid

pt: pterygoid

Ptpro: protein tyrosine phosphatase, receptor type, O

Q

qPCR: Quantitative Reverse Transcription PCR

R

R: rod

RAR: retinoic acid receptor

Rd1: retinal degeneration mutation of Pde6b

RDH: retinal dehydrogenase

RET: retina

RefSeq: reference/sequence

RGC: Retinal ganglion cells

Rho: rhodopsin

RNA: ribonucleic acid

ROX: FastStart Universal SYBR Green Master

RP: retinite pigmentosa

RPE/CC: Retinal pigment epithelium/Choriocapillary complex

RT-PCR: reverse transcriptase polymerase chain reaction

S

s: stape

SC: superior colliculus

sc-#: Santa Cruz Biotechnology #

SD-OCT: spectral domain optical coherence tomography

SE: surface ectoderm

Sema3f: semaphorin 3f

SEPT4: septin 4

Sgcg: sarcoglycan gamma

SH3KBP1: SH3 domain-containing kinase-binding protein 1

Shh: Sonic hedgehog

Slc6a9: solute carrier family 6 (neurotransmitter transporter, glycine), member 9

so: supraoccipital

SOHo: sensory organ homeobox protein

sq: squamosal

st: stenebra

T

t*: tooth missing

T: temporal

TdT: terminal deoxynucleotidyltransferase

TFBSs: transcription factor binding sites

TH: thyroid hormone

Thy: Thymine

TLC: transient layer of Chievitz

Trp: triptophane

Tshz2: Tshirt zinc finger family member 2

TSS: transcription start site

TVL: tunica vascular lentis

ty: tympanic ring

Tyr: tyrosine

U

UDG: uracil DNA glycosylase

UHRF1: Ubiquitin-like, containing PHD and RING finger domains, 1

5'UTR: 5' untranslated region

V

V: ventral

VEGF: vascualar epithelium growth factor

VLS-PPM: very low specific PPM

vhc: ventral hippocampal commissure

vo: vomer

3v: 3rd ventricle

W

WT: wild-type

X

xi: xiphisternum

xi c: xiphoid cartilage

Y

Z

zpmx: zygomatic process of the maxilla

zps: zygoamtic process of the squamosal

1. Introduction

My thesis is based on the study of the H6 family homeobox 1 (*HMX1*), a transcription factor involved in the oculo-auricular syndrome of Schorderet-Munier-Francescetti (OAS-SMF) and mutated in the dumbo mouse model. I will start with a general introduction on eye anatomy, development, function, concerning both human and mouse, and then focus on the mouse retinotopic mapping and craniofacial development. After these sections, I will present the *HMX1* gene in details, and in between also briefly introduce the others genes involved in this *HMX1* studies: *EphA6*, an ephrin receptor, *Sema3f*, a signalling molecule, and *Ptpro*, a regulator of ephrin expression.

1.1. The anatomy of the eye

The vertebrate eye is a globe formed by three basic layers. Taken successively, the outer protective corneo-scleral envelope and the middle vascular layer also called the uveal tract, providing crucial vegetative support to the innermost layer, the neural retina.

1.1.1. The corneo-scleral layer

The corneo-scleral layer is a solid envelope protecting and supporting the inner ocular tissues. All extraocular muscles enabling eye movement are attached to it. This fibrous layer is composed of three distinct elements. The cornea, at the anterior part of the eye, is a transparent stratified epithelial layer which permits the transmission of visible light. The second element of the fibrous layer is the sclera, composing the major part of this later. The sclera acts as a protection and partially elastic envelope maintaining the eye shape upon intraocular pressure variation. Outside of this layer and surrounding the cornea, a loose tissue, the conjunctiva, covers the ocular surface of the globe. The conjunctiva is highly vascularised and is part of the lymphoid system. The third element is the junction region of the corneo-scleral layer, the limbus, where the conjunctival surface vessels terminate, leaving the cornea an avascular structure. The limbus is multifunctional, providing nourishment, wound healing and immunosurveillance of the ocular surface and cornea. Finally it contains the pathways of aqueous humour outflow, thus playing a role in the regulation of the intraocular pressure (figure 1.1).

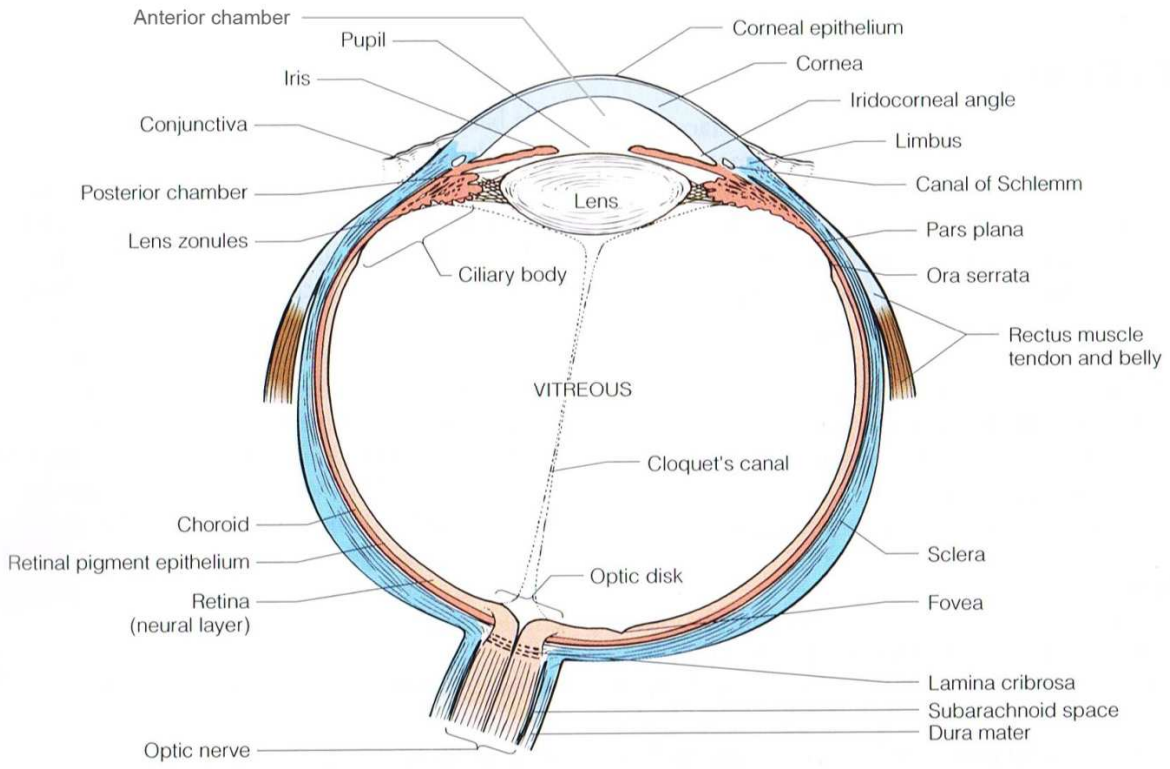

Figure 1.1: Detailed schematic diagram of the human eye (Forrester, Dick, McMenamin; Lee, 2002).

1.1.2. The vascular layer

The vascular layer or uvea is a pigmented layer composed by the iris, ciliary body and choroid. They are contiguous one to another with two opening, anteriorly the pupil and posteriorly the optic nerve canal. At the anterior side, the iris is a contractile and heavily pigmented disk surrounding the pupil opening. The iris regulates the size of the pupil and thus the amount of light entering the eye. It also separates the anterior chamber, situated behind the cornea, and the posterior chamber, which lies on front of the lens. The ciliary body is a wide ring extending from the sclera anteriorly to the ora serrata posteriorly, the transition site to neural retina. The ciliary body ensures various functions, including the accommodation of the lens via the ciliary muscle. It also produces the aqueous humour, lens zonules (suspensory ligaments holding the lens), vitreal collagen, and vitreal hyaluronic acid. The choroid is the posterior section of the middle vascular envelope of the eye. It is a thin, vascular and highly pigmented connective tissue, whose major function is to nourish the outer layer of the retina (figure 1.1). It also prevents unwanted light to reflect back by absorption by choroidal pigment.

1.1.3. The neural retina

The third layer is the neural retina. The task of the retina is to convert the light information from the environment into neural signals that are transmitted to the brain. It can be divided into two parts, the inner neurosensory layer and the outer retinal pigment epithelium (RPE). In humans, the retina possesses several distinct regions. The optic disc is a blind spot where all axons from the ganglion cell converge to form the optic nerve head: there are no retinal cell layers here. Also emerging from the optic disc, the blood vessels spread across the whole retina except over the fovea. The fovea is a thin region responsible for the sharp visual acuity due to a high density of cone photoreceptors. It is comprised in a larger region called the macula located in the centre of the retina. The macula possesses a majority of cone and several layers of ganglion cells, whereas the peripheral retina is mostly rod-dominated and contains one layer of ganglion cells.

In detail, the retina is composed of seven layers of various cell types and the RPE on the external side. Composing those layers, one can find six neuronal and three glial cell's types. The photoreceptor layer is, as its name implies, composed of the outer segments (OS) of the rod and cone photoreceptors. Their nuclei are located beneath the outer limiting membrane and compose the outer nuclear layer (ONL). The synapse between the photoreceptors, the bipolar and the horizontal cells form the outer plexiform layer (OPL). The inner nuclear layer (INL) is composed of the nuclei of the horizontal and bipolar cells, plus the amacrine and glial Müller cell nuclei. Notice that there is a spatial distribution of the nuclei, with bipolar homogeneously present over the INL, horizontal cells at the boundary of OPL, and the amacrine at the boundary with the inner plexiform layer (IPL). The IPL is thus composed of synapses connecting the INL and the ganglion cell layer (GCL). The innermost layer is the optic fiber layer (OFL), where the ganglion cells and their axons target the optic disc (figure 1.2).

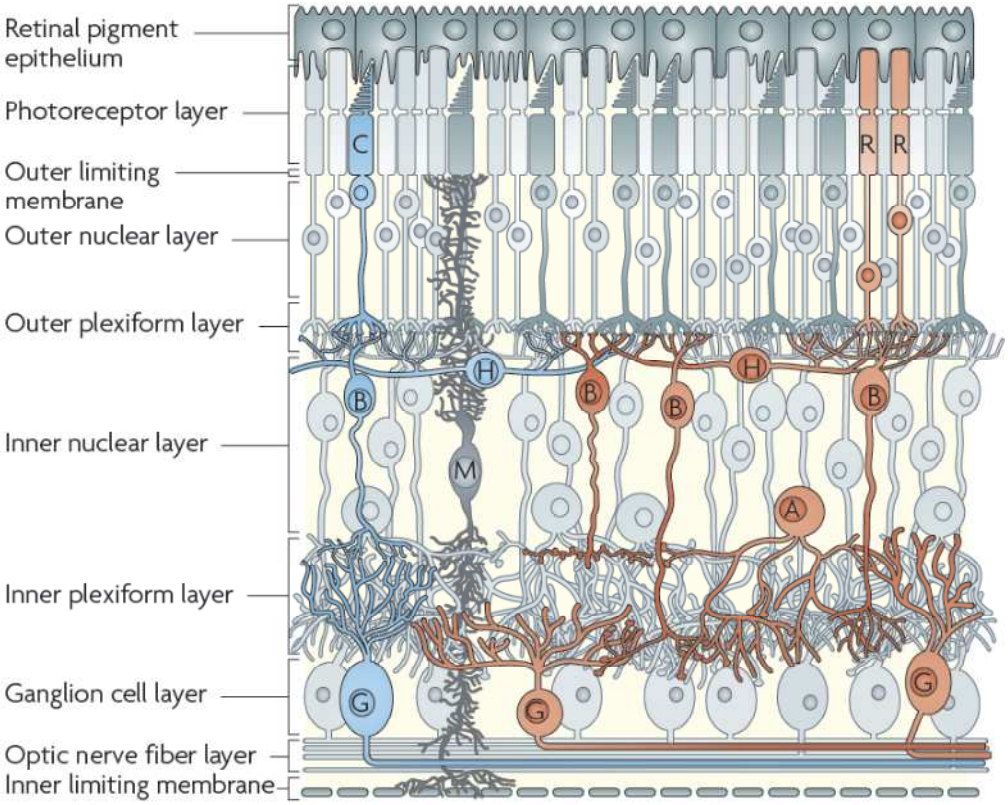

Figure 1.2: functional circuitry of the retina. R: rod, C: cone, B: bipolar cells, H: horizontal cells, M: Müller glia, A: amacrine cells, G: ganglion cells. (Swaroop et al., 2010).

1.1.3.1 Photoreceptors

The photoreceptors are present in two forms, the rods and cones, named after their outer segment's shape. These are the cell type responsible for the light absorption and transformation into a nerve impulse. Humans have about 6.5 million cones and 115 million rods heterogeneously spread over the retina. They are three types of cones in human: blue, green and red, also termed short, medium and long-wavelength. The cones react in bright light and allow colour vision, with fine and spatial resolution. The rods allow vision in the dark or dim light. They do not detect colours but sense contrast, brightness and motion. They contain the photopigment rhodopsin, which is sensitive to blue-green light. As mentioned above, in the fovea there is a majority of red and green cone, whereas in the peripheral retina there are more blue cones and rods.

Photoreceptors are composed of synapses, a cell body with nucleus, an inner segment, and an outer segment in contact with RPE. The inner segment contains the metabolic organelles, such as the endoplasmic reticulum (ER), Golgi apparatus and mitochondria. The outer segment is a stack of disks containing either the opsins or rhodopsin, and chromophores, and it is the place where phototransduction occurs. Unlike cones, rod discs are made of individual stacks surrounded by a plasma membrane unconnected to the ciliary plasma membrane and are

constantly phagocytised by the RPE once used. Cone outer segments (OS) are phagocytised in a less extent due to lower shedding rates (Kevany et al., 2010).

1.1.3.2 Bipolar cells

Bipolar cells transfer the electric signal from photoreceptors to ganglion and amacrine cells. They exist in various subtypes, depending on their synaptic partners and functions. In the foveal area, the ratio is equivalent with cones and ganglion cells, whereas in the peripheral retina they can receive input from up to 100 rods.

1.1.3.3 Retinal ganglion cells

Retinal ganglion cells (RGC) collect all signals from bipolar and amacrine cells. Their axons converge on the optic disc to form the optic nerve and transmit the visual information to the visual output of the brain, the lateral geniculate nucleus (LGN) and the superior colliculus. Upon exiting through the lamina cribrosa, the RGC axons become myelinated with oligodendrocytes.

A subfamily of RGCs, the intrinsically photosensitive retinal ganglion cells (ipRGC) are responsible for the phototrainment of the circadian system and the pupillary light reflex through non-visual photosensitivity of the melanopsin photopigment.

1.1.3.4 Amacrine cells

Amacrine cells modulate the signals conveyed by bipolar cells to ganglion cells. They display a wide range of morphological diversity, and are composed of 25 different types at least. They also vary in neurotransmitter types; some are GABAergic, other dopaminergic or can release acetylcholine.

1.1.3.5 Horizontal cells

Horizontal cells are three distinct morphological varieties in the retina, based on the type of contact to the cones and to a lesser extent to the rods. They have an integrative role in retinal processing and give a negative feedback signal to the photoreceptors through inhibitory neurotransmitters, which allows the visual system to adjust to light contrast and intensity.

1.1.3.6 Müller cells

Müller cells are the principal supporting glial cells of the retina. They extend through the entire retina from the inner surface up to the photoreceptors. They maintain the homeostasis of the retinal space, nourish the retina, degrade excitotoxic glutamate, and secrete neurotrophic factors and antioxydants.

1.1.3.7 Astrocytes

Asctrocytes are secondary glia in the retina, and predominantly located in the GCL and IPL. Their role is to isolate the receptive surface of neurones in the retina thus preventing unwanted signals or secondary effects in neighbouring neurones.

1.1.3.8 Microglia

Microglias from the retina play an analogue role as in the brain. They become activated upon injury and assure wandering phagocytosis. Their process spread through the whole retina with exception of the photoreceptor location.

1.1.3.9 Retinal pigment epithelium

The RPE is a continuous monolayer of cuboidal epithelial cells extending from the margins of the ora serrata to the optic nerve head. The apical membrane is covered by microvilli and faces the photoreceptor outer segment (POS); the basolateral membrane faces Bruch's membrane, which separates the RPE from the choriocapillaris, thus forming part of the blood-retina barrier. This layer ensures many crucial functions of the normal visual process such as metabolites transport, absorption of light by its pigment, phagocytosis of POS, regeneration of all-*trans*-retinal for the visual cycle, stabilize ion composition of the subretinal space, and secretion of growth factors.

1.1.4. Internal components of the eye

Three others structures compose the internal part of the eye: the lens, the vitreous and aqueous humours. The lens is an important component of the optical system of the eye as, like the cornea, it alters the refractive index of light entering the eye to focus on the retina. This capsule is a biconvex transparent highly organized system of specialized cells that has the ability to change shape under the influence of the ciliary muscle. The vitreous humour lies in the largest cavity of the eye; it is a transparent viscous gel mainly constituted by collagen fibres types II and IX, and hyaluronic acid. Finally, the aqueous humour fills both the anterior and posterior chambers; it is continuously produced by the ciliary process of the ciliary body. Its two major roles are to provide metabolites to the avascular lens and cornea, and to remove toxic metabolites produced by the cornea and iris.

1.2. The mouse eye

Mice are an animal model widely use in scientific research due to the ability to create transgenic animals and the relative ease of breeding. But the degree to which the findings can be extrapolated to humans is often a question of critical importance.

1.2.1. Anatomy

The anatomy of the mouse eye is comparable to the human one. All three surrounding layers and internal components are found (figure 1.3).

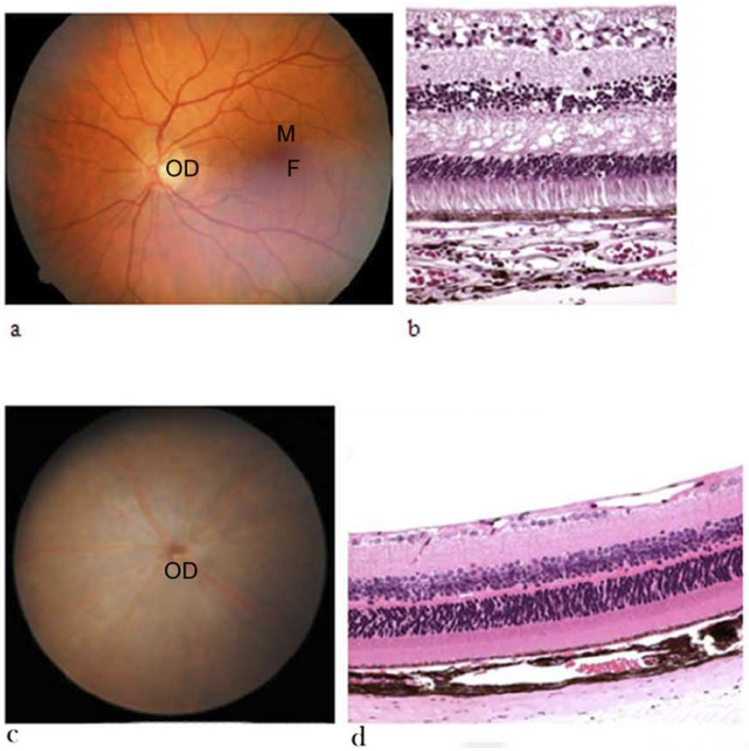

Figure 1.3 : A comparison of the mouse (c) and human (a) fundus, (b) histological picture of human maculae and mouse retina (d).F: fovea, OD: optic disc, M: macula. (Adapted from Ramkumar et al., 2010, only normal human and mouse panel are shown).

It is a small organ, about 3.4 mm size, with a much bigger lens than in humans constituting, with the cornea, about 60% of the total length of the eye (figure 1.4). As a nocturnal animal, the vision is not the most important sense and therefore there are some differences in the light processing.

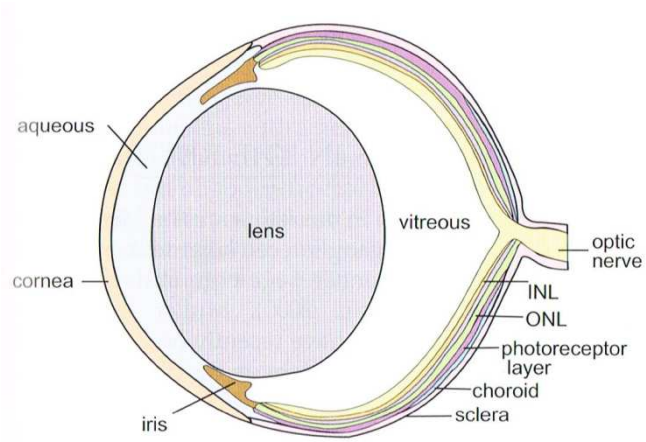

Figure 1.4: A diagram of the mouse eye. (Watson, Paxinos, Puelles, 2012).

1.2.2. Differences between mice and humans

The photoreceptor layer of the mouse is mostly composed of rods rather than cones; the ratio is about 30 to 1. Therefore the mouse has neither the macula nor the fovea. Moreover, mice possess only two types of cones: blue and green ones (figure 1.5). They have a dichromic vision instead of the human trichromic.

More precisely, in the mouse cones are scattered throughout the retina, with M-cones (green) predominating in the dorsal retina and S-cones (blue) predominating in the ventral retina in response to a gradient of thyroid hormone (TH). As mentioned previously, this differs from the human retina and its spatial arrangement of rods and cone (figure 1.5).

Mouse

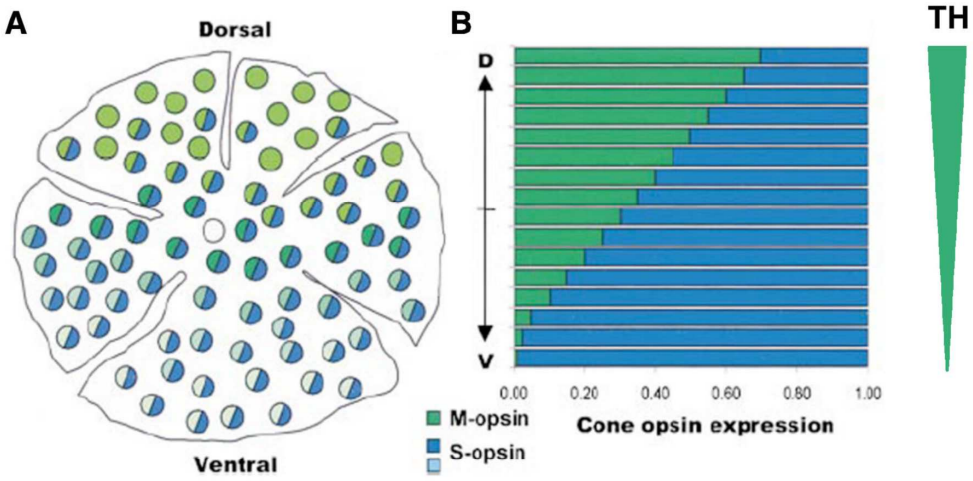

Human

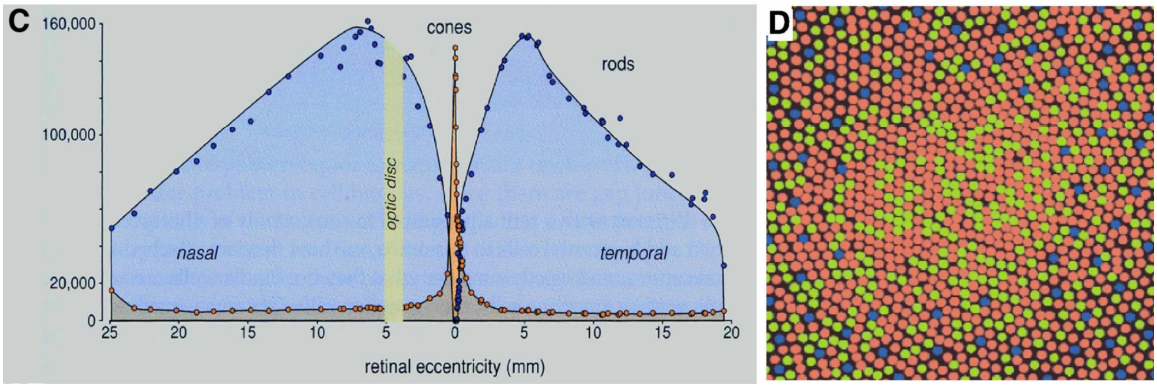

Figure1.5: Distribution of cones and opsin expression in mouse (A,B) and human retina(C) and fovea (D). (Hennig et al., 2008).

Finally in terms of development, even if the scale is much more reduced in a mouse, which is a clear advantage for research, we can find a certain homology with human. But it is important to mention that the end of rod differentiation in mice happens at the eye opening day, around P12, which is not the day of birth (figure 1.6).

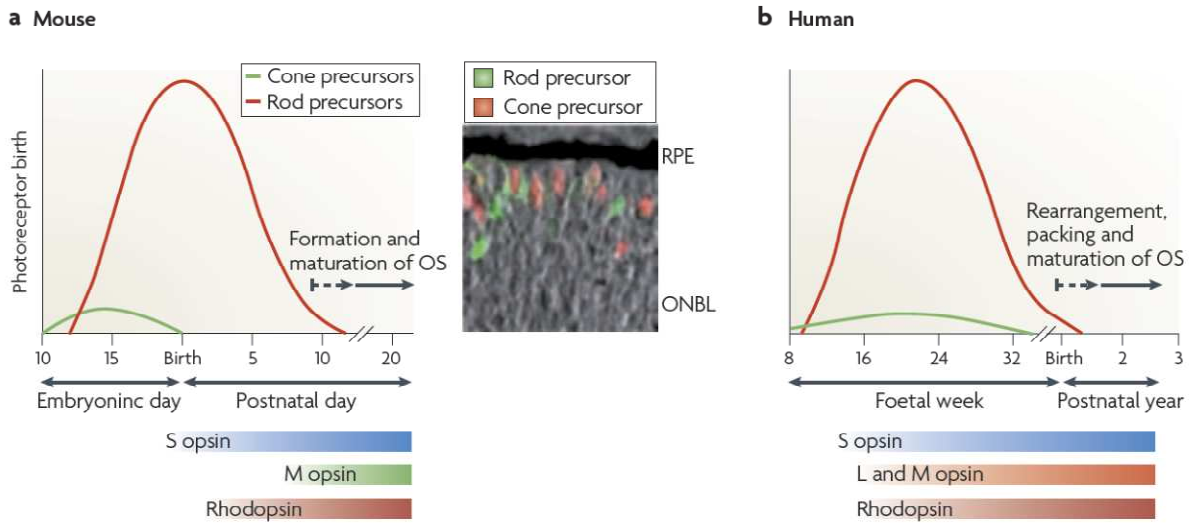

Figure 1.6: Photoreceptors maturation in mice and humans. (Swaroop et al., 2010).

1.3. Vision

The process of vision can be classified into three steps: the refraction of light, the neural processing by the retina and the integration towards the central visual pathway.

1.3.1. Refraction

In order to focus correctly onto the retina, the light is deviated by the cornea and the lens. The refraction of the cornea is constant but the lens has the ability to stretch and therefore modulate the focus of the light on the retina.

1.3.2. Neural processing by the retina

Neural processing is the most complex process of visual information treatment. It starts with the photon absorption by photoreceptors. Rods have high sensitivity and to allow very low level of light detection they can form clusters that synapse to single ganglion cells, leading to the poor and blurry night vision. In contrast cones have very high intensity thresholds, can decipher colours and each is related to a single ganglion cell in the fovea, allowing extremely resolved vision.

Thanks to combinations of stimulations of their three types of opsins (short, medium and long), humans detect light wavelength from 400 to 700 nm, ranging from purple to red.

Depending on the type of information two type of ganglion cells are observed: low and slow for the parvocellular system managing spatial resolution and colour vision at the fovea; large and fast for magnocellular system managing luminance and motion detection within the rest of the retina.

The visual cycle is divided into the phototransduction occurring in the photoreceptor and the retinoid cycle taking place in the RPE. The conversion of light into neural signal occurs in the photoreceptor through the switching of a photosensitive molecule called the 11-*cis* retinal, a vitamin A derivative. It is bound to opsin and upon photon absorption isomerizes into all-*trans*-retinal (at-Ral) and detaches from the opsin. The transport of at-Ral from the intradiscal face to the cytosolic face is performed by the ABCA4 transporter in a combined enzymatic reaction with NADPH-dependent all-trans-retinol dehydrogenase (RDH). Then the chaperone interphotoreceptor retinoid binding protein (IRBP) carries the molecule to the RPE where it is reconverted into 11-*cis* retinal by three enzymes; lecithin:retinol acyltransferase (LRAT), isomerhydrolase retinal pigment epithelium-specific protein 65kDa (RPE65) and another RDH (figure 1.7). Once restored it is transported back by another IRBP to recombine with opsin in the photoreceptor.

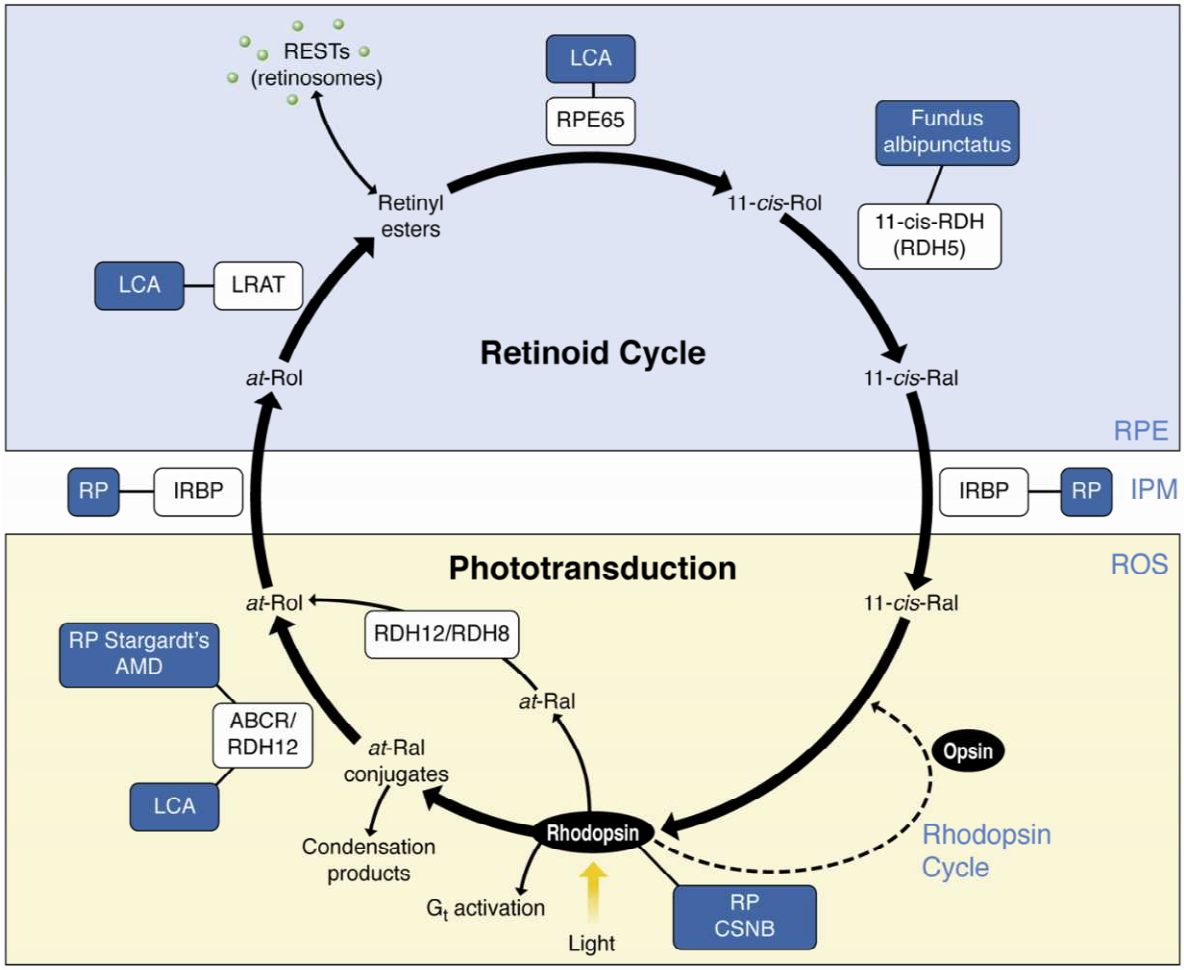

Figure 1.7: The visual cycle and associated disease (in blue). (Kiser et al., 2012).

More precisely, concerning the light transduction within the photoreceptor, the release of the photopigment triggers a cascade of reactions leading to the hyperpolarisation of either the cone or rod. In the dark, cyclic guanosine monophosphate (cGMP) binds to sodium (Na^+) channels in the outer segment organelle of the photoreceptor, and maintains them open creating a depolarized state. Thus, Na^+ continuously enters, resulting in a membrane potential of roughly -40mV. As in other nerve cells, this current maintain voltage-sensitive calcium (Ca^{2+}) channels open in synaptic termination, allowing photoreceptors to liberate neurotransmitters into synapses with bipolar cells. Upon absorption of light, the change of conformation of the opsin will activate transducin, a G-protein coupled receptor subunit, which will in turn exchange the bound GDP for GTP. In this state transducin activates of the phosphodiesterase (PDE), which hydrolyzes the cGMP and leads to the closure of the cGMP-gated Na^+ channels. As potassium channels of the photoreceptor remain open, a potential of about -65mV is produced and inhibits neurotransmitter liberation. This process persists until inactivation of PDE and transducin (Arshavsky et al, 2013).

Sensitivity and saturation are controlled by side reaction, essentially a back loop of guanylate cyclase and Na^+ channels affinity to cGMP controlled by calcium concentration. An arrestin protein also prevents activated opsin to function and the return to initial state occurs when the retinal achieve the retinoid cycle. Note that the range of sensitivity and the rate of reaction between photopigment, opsin and rhodopsin, is responsible for the pannel of light and colour detection.

The basis of light transduction into visual information starts at the level of the photoreceptor and bipolar cells, with light-linked graded release of glutamate neurotransmitters. An even more tuned mechanisms offered by ganglion cells, allows the refinement of vision. They manage visual input of the circular portion of the retina; those receptive fields can be divided into central and peripheral portion. Ganglion cells are classified in two type; ON-centered and OFF-centered ganglion cells, depending to their type of reaction to light. ON-centered ganglion cells fire action potentials when light hits the centre of the receptive field and are inhibited when it occurs at the periphery. OFF-centered ganglion cells act in opposite. As each part of the retina is covered by both types of ganglion cells, the brain obtains the necessary information to depict increase and decrease of luminance.

The decrease of glutamate release by the photoreceptor in response to light will differently stimulate ON and OFF-centered bipolar cells. ON-centered bipolar cells have metabotropic glutamate receptors (mGluR6) coupled to a G-protein. In response to glutamate, cGMP-depending sodium channels close, hyperpolarizing the cell. In contrast OFF-centered bipolar cells react through AMPA and kainate receptors and depolarize in response to glutamate. (figure 1.8).

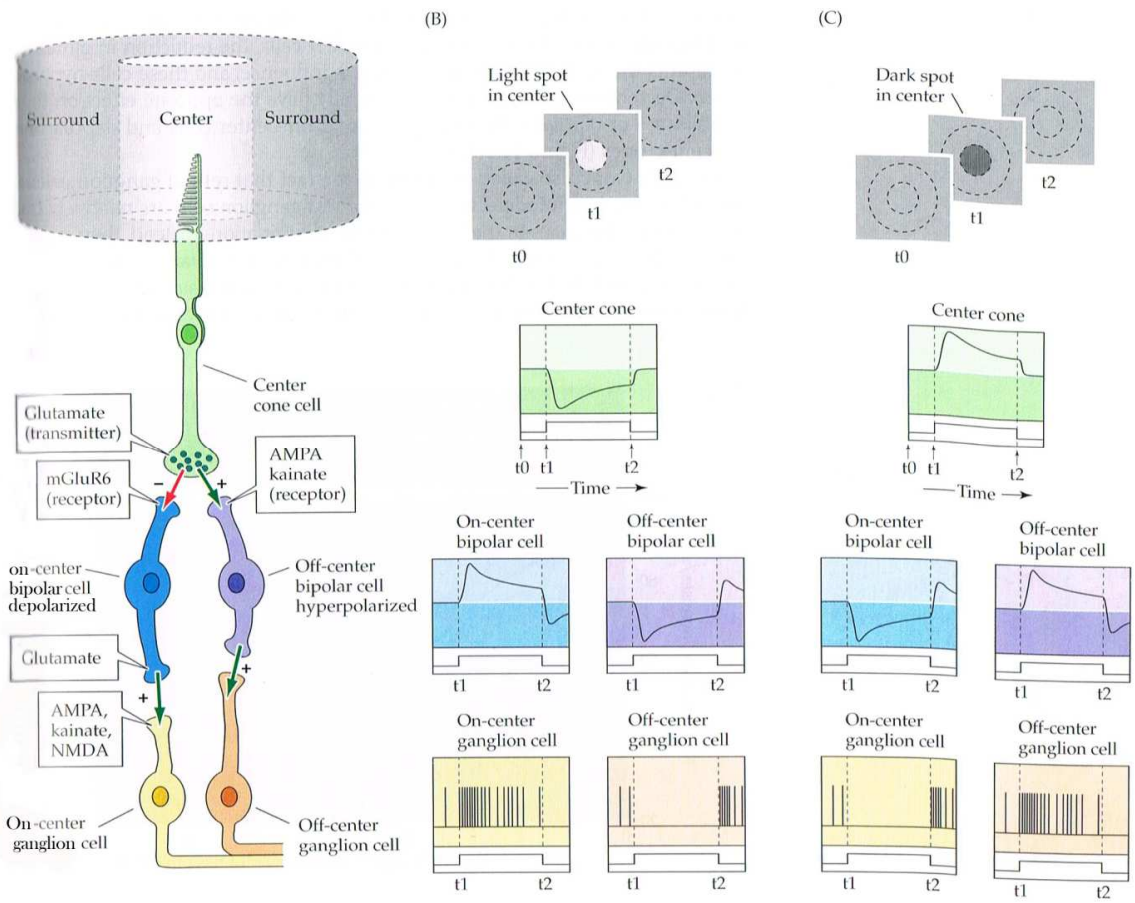

Figure 1.8: Circuitry responsible for generating receptive field centre responses of RGC. (Purves et al., 2008).

Finally an adaptive mechanism takes place to regulate action potential firing when both center and peripheral receptive field are stimulated. This occurs via horizontal cells that depolarize with glutamate release from the photoreceptor. With a decrease of glutamate horizontal cells could hyperpolarize the photoreceptor termination with GABA, an inhibitory neurotransmitter. This mechanism allows a reduction of response to light global illumination and a sensitive reaction to contrast conditions.

To conclude, when the signal leaves the retina, the regulative process of the neural retina has already enhanced the light signal.

1.4. The visual pathway

1.4.1. Human

The visual pathway starts in the retina, where light goes through all the retinal layers to be transduced into a neural signal by photoreceptors. Then axons from ganglion cells form the optic nerve at the optic disc and separate at the optic chiasm between the ipsilateral (nasal input) and contralateral (temporal input) projection. This process allows our sophisticated binocular vision which is composed of 50/50 contribution from both retinas in humans. The optic tracts then separate into a lateral root targeting the lateral geniculate nucleus (LGN) and the medial root targeting the pretectal area and the superior colliculus (SC) (figure 1.9).

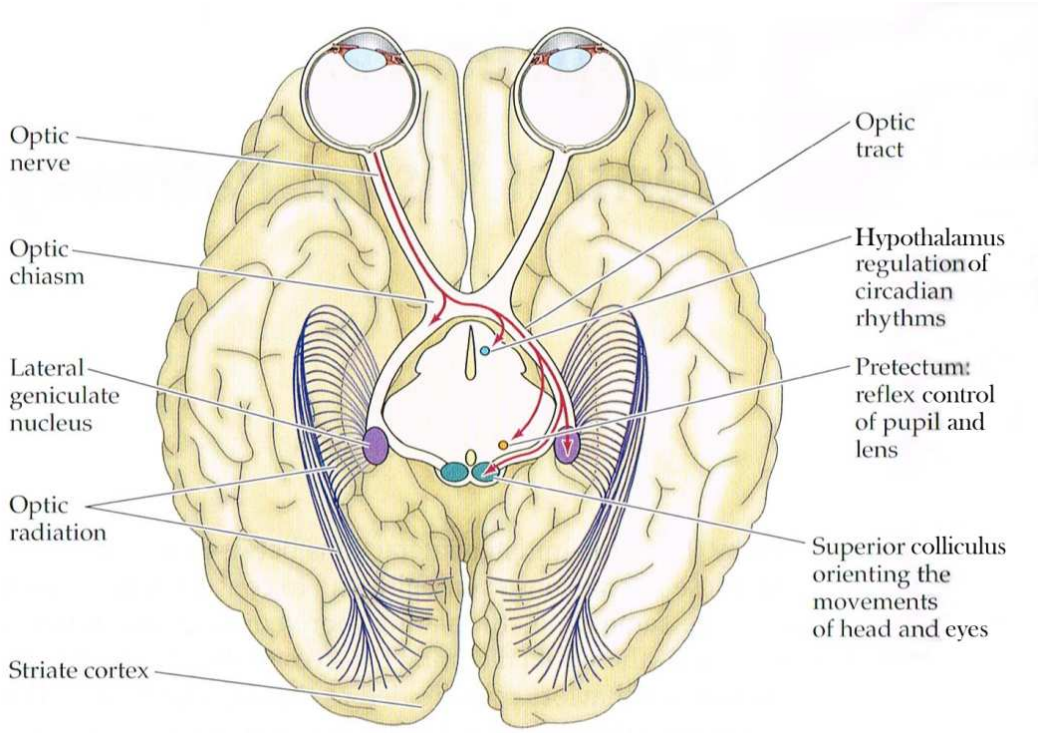

Figure 1.9: Central projection of retinal ganglion cells. (Purves et al., 2008).

The LGN is responsible for conscious visual sensation and the SC is involved in the visual grasp reflex, the automatic scanning with coordination of head and eye, and visual associations, finally pretectal regions serve the pupillary light reflex.

The response from neurons to central and peripheral, luminance intensity and separation of ipsilateral and contraletal inputs is conserved in the LGN. In mammals, there are seven layers in the SC and retinal output projects into the three most superficial ones. Whereas the retinotopic mapping is well preserved within the primary visual output, a spatiotemporal tuning occurs in the primary visual cortex. Cortical neurons combine information from both eyes, enabling our

binocular vision. The visual signal is transmitted to the striate cortex via optic radiation to produce dynamic images.

1.4.2. Mouse

Mice also have binocular vision, but unlike in human, only 3% of their RGCs project ipsilaterally, specifically the one located in the ventrotemporal retina. Whereas the size and location of these structures vary in mice, RGC outputs remain in the dorsal lateral geniculate nucleus (dLGN) that conveys information to the visual cortex for the image-forming pathway and in the superior colliculus (SC), involved in non-image forming visual pathway, such as the control of the head and eye-movement. In both outputs, ipsilateral and contralateral terminals are segregated.

The development of the eye-specific maps starts when RGCs extend their axon out of the retina to reach the optic chiasm between E12 and P0 and reach the dLGN at E16 and SC from E18. Even if ipsilateral axons arrive early at the optic chiasm (E12–E17) they innervate and spread within the dLGN only from P0, the segregation with contralateral axons occurs after P4 and is completed at P15. A similar process occurs for eye-specific map creation in the SC (figure 1.10).

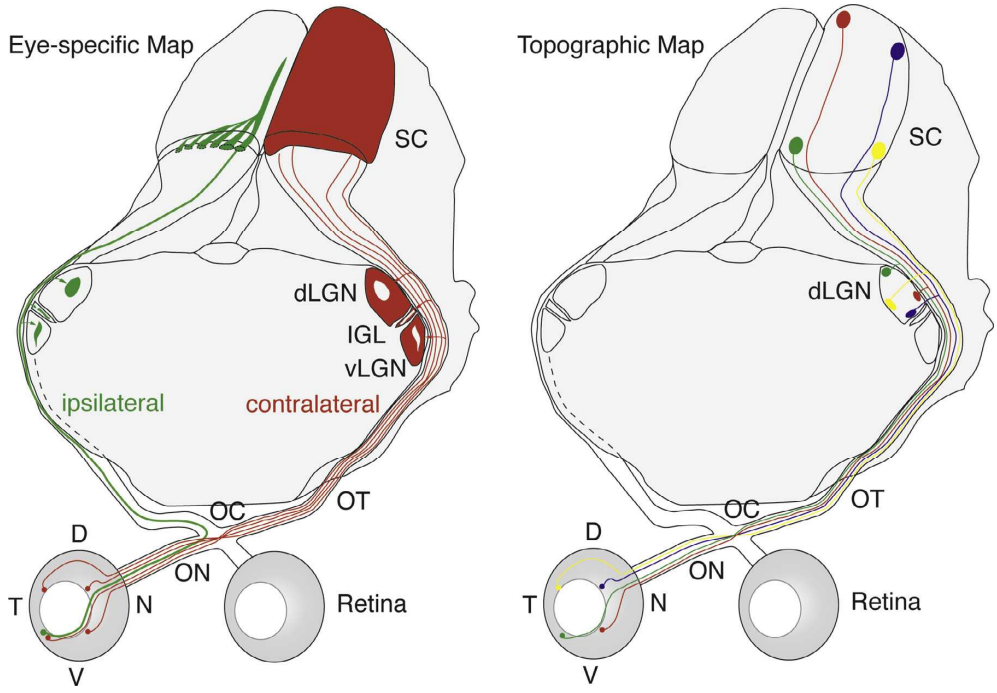

Figure 1.10: Retinotopic map in the mouse visual system. ON: optic chiasm; OT: optic tract; vLGN: ventral lateral geniculate nucleus; dLGN: dorsal lateral geniculate nucleus; IGL: intergeniculate leaflet; SC: superior colliculus; D: dorsal; N: nasal; V: ventral; T: temporal. (Assali et al., 2014).

Although vision is not a crucial sense in mice, as they are nocturnal and not predators, the connectivity map of visual cortex is well developed and striates far beyond from primary visual area (Ackman et al., 2014).

1.5. The development of the eye and the retina

1.5.1. The eye

In mammalian, three embryonic tissues contribute to the formation of the eye: the neural ectoderm, the surface ectoderm, and the periocular mesenchyme (Heavner et al., 2012) (figure 1.11). The neuroectoderm differentiates into the retina, iris, and optic nerve; the surface ectoderm gives rise to the lens and the corneal epithelium; the mesoderm differentiates into the extraocular muscles and the fibrous and vascular coats of the eye. A fourth source, the neural crest cells, becomes the corneal stroma sclera and corneal endothelium (Harada et al., 2007).

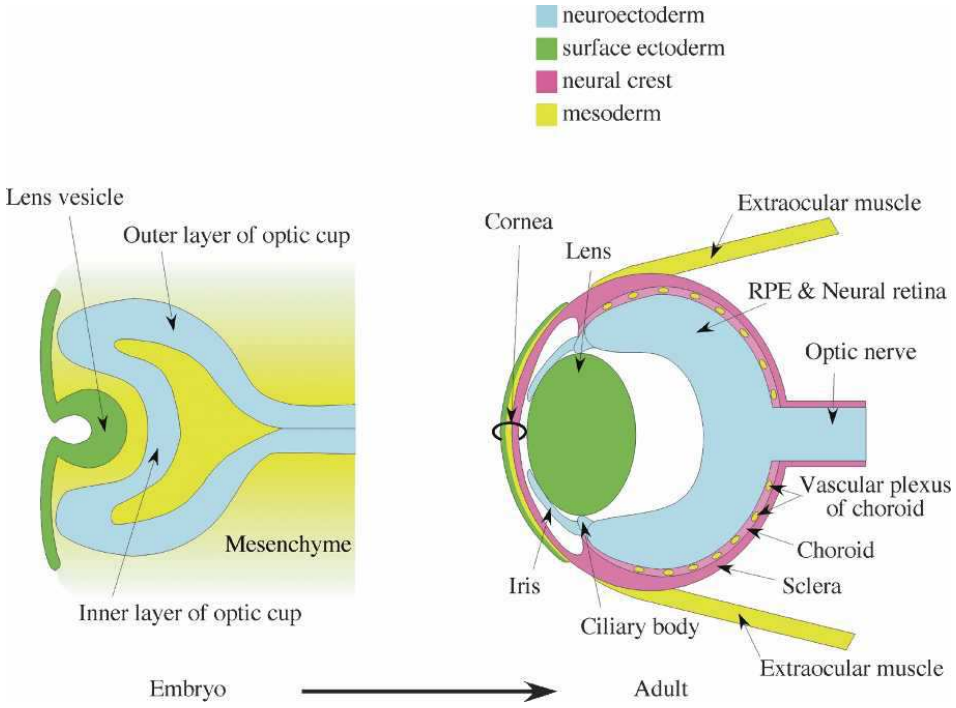

Figure 1.11: Embryonic lineages contributing to the eye. (Harada et al., 2007).

Both in humans and mice, eye development begins with the separation of the eye field into two optic primordia and the formation of bilateral evaginations of the ventral forebrain which will form the optic vesicles. They then induce the surface ectoderm to form the lens primordia and the lens placode. After contact of the optic vesicles with the lens placode, both tissues invaginate to form a two-layered optic cup and lens vesicle. As development proceeds, the optic stalk is formed proximally and the distal part of the optic cup surrounds the forming lens. During the process, the outer layer of the optic cup forms the retinal pigmented epithelium (RPE) and the inner layer forms the neural retina that consists of multipotent progenitor cells. Mice and

humans exhibit similar developmental step of the eye with species adapted timetable (Furimsky et al., 2006) (figure 1.12).

The development of the eye is controlled by transcription factors whose strict expression patterns and regulation within defined populations of cells are required for appropriate patterning. Major transcription factors include; Pax6, Rax, Six3, and Lhx2 constituting a regulatory network required for eye development (Heavner et al., 2012).

In eye development, Pax6 is the master gene, as it is involved throughout species from flies to humans. In mice, Pax6 and Pax2 are involved in optic cup and optic stalk formation. The Vax family of homeodomain transcription factors is also required for appropriate development of the ventral optic vesicle and optic stalk.

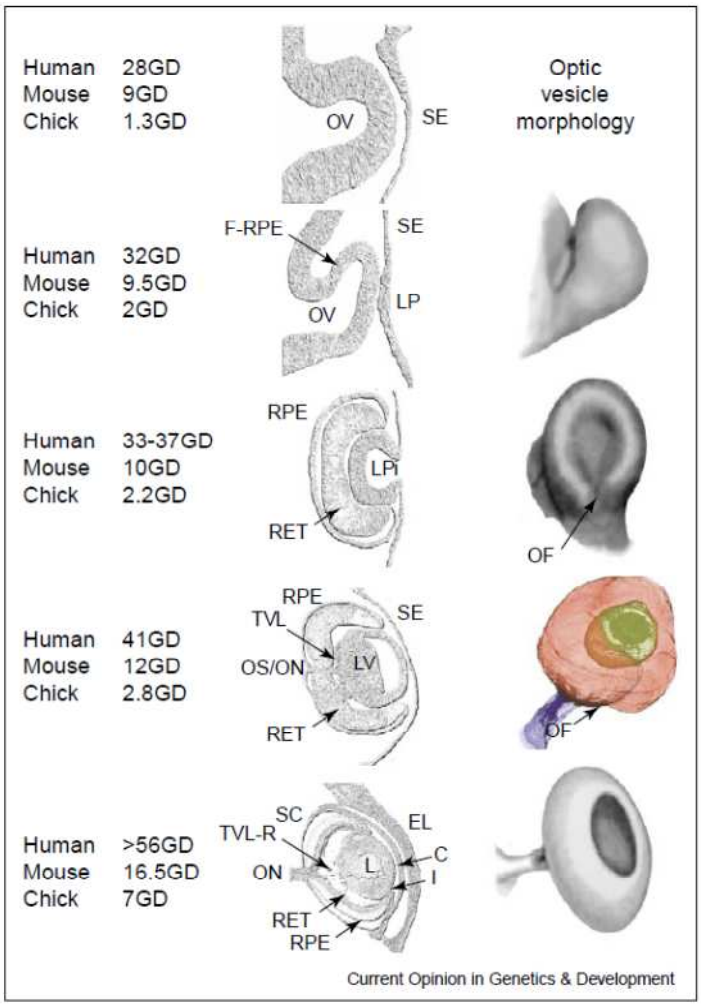

Figure 1.12: Major time point of eye development.GD: gestational days, OV: optic vesicle, SE: surface ectoderm, LP: lens placode, RPE: retinal pigment epithelium, OS: optic stalk, I: iris, L: lens, ON: optic nerve, RET: retina, TVL: tunica vascular lentis (vasculature). (FitzPatrick et al., 2005).

Vax1 is expressed in the optic stalk and ventral optic cup. Vax2 is found in the ventral optic cup and is required for closure of the optic fissure, determination of eye polarity, and maintenance of appropriate axon connections to the brain. The secreted morphogen Sonic hedgehog (Shh)

plays also a role in ocular development. In mice, it initiates the ocular morphogenesis at E8.0 when secreted by the prechordal plate and ventral forebrain. Later, Shh expression by RGC at E12 signals retinal precursor cells to control cell proliferation, differentiation, and organization. The downstream effectors of the Shh pathway are the Gli transcription factors, primarily Gli2 and Gli3 in mice (Furimsky et al., 2006).

As mentioned above, many genes are involved in the development and maturation of the eye structures. Mutations of those are associated with various defects in humans that have also been observed and studied in mice (table 1.1).

Gene	MIM	Locus	Mode	MAC phenotype	B/U	Syndromic	Animal model[a]
Transcription factors							
SOX2	184429	3q26.33	AD	A, M, CM, C	B/U	Y/N	M, ZF(MO)
OTX2	600037	14q22.3	AD	A, M, CM, C	B/U	Y/N	M, ZF(MO)
FOXE3	601094	1p32	AR	M, CM	B	N	M, ZF(MO)
VSX2	142993	14q24.3	AR	A, M, CM	B	N/Y	M, ZF(MO)
RAX	601881	18q21.32	AR	A, M	B	N/Y	M, ZF, XP, MK
			AD	A, M, C	U	N/Y	
PAX6	607108	11p13	AD	M, C	B/U	N	M, ZF, R
			AR[b]	A, M	B	Y	
PITX3	602669	10q25	AR/AR[b]	M	B	Y/N	M, ZF(MO), SH
SALL2[c]	602219	14q11.2	AR	C	B/U	N	M
SIX6[c]	606326	14q23.1	AD/AR	M	B	N	M, ZF(MO)
ATOH7	609875	10q21.3	AR	M	B	N	M, ZF
TGFß/BMP signaling molecules							
BMP4	112262	14q22.2	AD	A, M	B/U	Y	M
BMP7	112267	20q13.31	AD	A, C	B/U	Y/N	M
GDF6	601147	8q22.1	AD	A,M,CM, C	B/U	Y/N	M, XP(MO), ZF
GDF3	606522	12p13.31	AD	M, CM, C	B/U	Y/N	ZF(MO)
Retinoic acid pathway							
ALDH1A3	600463	15q26.3	AR	A, M, CM, C	B	N/Y	M, ZF(MO)
STRA6	610745	15q24.1	AR	A, CM	B	Y/N	M
RARB	180220	3p24.2	AD	A, M	B/U	Y	M
Genes with other or unknown function							
SHH	600725	7q36	AD	M, CM, C	B/U	N/Y	ZF, CH
ABCB6	605452	2q35	AD	C, CM	NS	N	ZF(MO)
MAB21L2	604357	4q31.3	AD	A, CM, C	B	Y/N	M, ZF
			AR	C, CM	B	N	
C12orf57	615140	12p13.31	AR	CM, C	B	Y	–
TENM3[c] *(ODZ3)*	610083	4q35.1	AR	CM	B	N	M, Z(MO)
PXDN	605158	2p25.3	AR	M	B	N	M
YAP1	606608	11q22.1-q22.2	AD	C	B	Y/N	–
HMGB3[c]	300193	Xq28	XR	CM	B	Y	XP(MO)
CRIM1[c]	606189	2p22.3-p22.2	AD	CM	B	N	M

AD, autosomal dominant; AR, autosomal recessive; XR, X-linked recessive; U, unilateral; B, bilateral; NS, not specified; A, anophthalmia; M, microphthalmia; CM, colobomatous microphthalmia; C, coloboma; Y, syndromic cases only; N, no syndromic cases reported; Y/N, Usually syndromic but isolated cases also reported; N/Y, Usually non-syndromic, but extra-ocular features occasionally reported.

[a]Animal models displaying ocular anomalies (MAC for most, please see text) are listed: M, Mouse; ZF, Zebrafish; (MO), Morpholino only; XP, Xenopus; MK, Medaka; SH, Sheep; R, Rat; CH, Chicken.

[b]Autosomal-recessive inheritance of MAC due to compound heterozygous or homozygous mutations inherited from heterozygous parents affected with a less severe ocular phenotype.

[c]Only one affected family has been reported.

Gene	Human*	Mouse*	Tissue of expression	Mutation	Human phenotype	Mouse phenotype
PITX2	4q25	3 (58)	Periocular and anterior eye mesenchyme, umbilicus, heart, gut, dental epithelia, limb bud and pituitary	LOF or missense, HI or D	Rieger syndrome: eye, tooth and umbilical anomalies, occasionally heart and iridogoniodysgenesis, Peters anomaly	Null KO homozygote: early embryo lethality Heterozygote: Rieger syndrome-like, incomplete penetrance, partial LOF
FOXC1	6p25	13 (20)	Nearly ubiquitous, but also periocular and pre-endothelial mesenchyme, sclera, cornea, adult trabecular meshwork and conjunctival epithelium	Missense, deletion (Hsa), D, HI, DU	Heterozygote: anterior segment and iris anomaly, glaucoma	KO heterozygote: anterior segment anomaly, glaucoma and ocular drainage defects Homozygote: congenital hydrocephalus, cardiac and skeletal anomalies, lethal
EYA1	8q13	1 (10)	Nasal placode, kidney, ear, branchial arches and eye	BOR, LOF and missense (Hsa) HI, D Eye: missense (Hsa) D, KO (Mmu), mild HI, severe R	Few cases: Peters anomaly, cataract, nystagmus Most cases: BOR	Heterozygote: BOR-like kidney, hearing anomalies Homozygote: lethal, multiple anomalies
MAF	16q23	8 (61)	Lens, lens placode, lens vesicle and cerebellum	Distant translocation (1 Mb upstream of *MAF*), missense D (Hsa and Mmu)	Cataract, microphthalmia, coloboma, anterior segment dysgenesis	(*Of1* mutant) Heterozygote: cataract Homozygote: microphthalmia, cataract and other anomalies, for example, kidney
CHX10	14q24	12 (38)	Neural retina, brain and spinal cord	Missense (R), same amino acid altered in two families but different nucleotide changes	Microphthalmia and cataract	Alleleocular retardation: reduced total eye size
MITF	3q14.1 –p12.3	6 (40)	RPE, optic vesicle, neural crest cells, brain and heart	LOF	Waardenburg syndrome	Microphthalmia, various recessive and dominant alleles
PAX2	10q22	19 (43)	Optic cup, nerve and stalk, retina, brain, ear and kidney	LOF, D	Renal coloboma syndrome: kidney and eye anomalies	Renal coloboma syndrome: kidney and eye anomalies
MSX2	5q34	13 (32)	Optic vesicle, cornea, branchial arches, limb, tooth and brain	Missense, nonsense, deletion, D, HI	Cranial malformations including myopia or hyperopia	Overexpression: apoptosis in the optic vesicle
OTX1	2p13	11 (12)	Optic vesicle, nerve and stalk, neural retina, RPE and brain	ND	ND	KO: defects in the visual sense organ
VSX1	20p11	2 (83)	Retina	Missense, D	Keratoconus, corneal dystrophy	ND

*Chromosome (centimorgans). BOR, branchio-oto-renal syndrome; *CHX10*, *C. elegans* ceh-10 homeodomain-containing homologue; D, dominant; DU, duplication (dosage sensitivity); *dyl*, dysgenic lens mutant; *EYA1*, eyes absent 1 homologue; *FOX*, forkhead box; HI, haploinsufficiency; Hsa, *Homo sapiens*; KO, targeted knock-out; LOF, loss of function; *MAF*, musculoaponeurotic fibrosarcoma oncogene; *MITF*, microphthalmia-associated transcription factor; Mmu, *Mus musculus*; *MSX*, msh-like homeobox; ND, not determined; *Of1*, opaque flecks in lens; *OTX1*, orthodenticle homologue 1; *PAX*, paired box gene; *PITX*, paired-like homeodomain transcription factor; R, recessive; RPE, retinal pigment epithelium; *RX*, retina and anterior neural fold homeobox; *SOX2*, SRY-box-containing gene 2; *VSX1*, visual system homeobox 1 homologue.

Table 1.1: Major genes implicated in developmental eye defect. Note that it does not include crystallins gene involved in lens development. (First pannel: Reis et al., 2015 and second pannel: modified from Graw, 2003).

1.5.2. The retina

The neural retina arises from the inner layer of the forming optic cup. The cells of this developing retina generate a range of glia, ganglion neurons, interneurons and light-sensitive photoreceptor neurons. In humans, retinal differentiation begins around day 47 of gestation, and cones and rods are distinguishable at week 15 of gestation. Development continues until the eighth month and the fovea becomes fully functional only after birth (Graw, 2003) (figure 1.13).

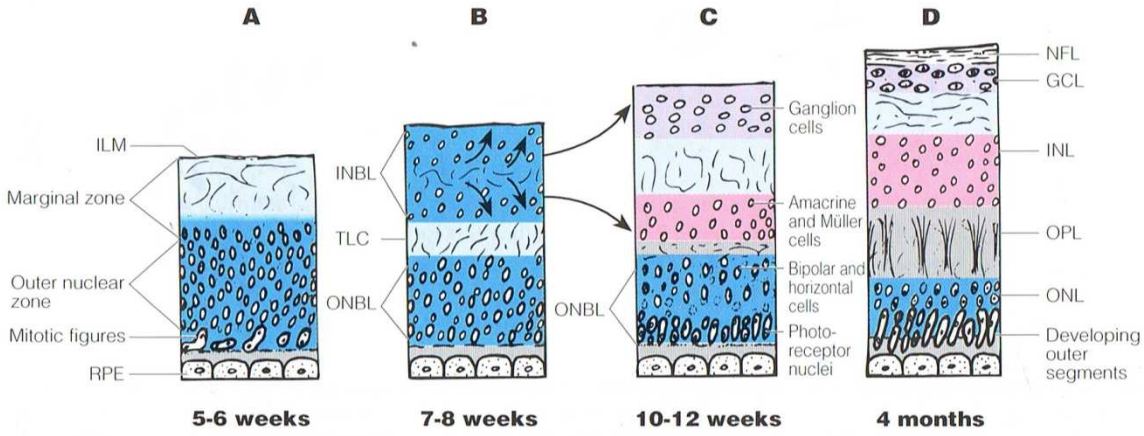

Figure 1.13: Development of human retina. LM: limiting membrane, RPE: retinal pigment epithelium, INBL: inner neuroblastic layer, TLC: transient layer of Chievitz, ONBL: outer neuroblastic layer, NFL: nerve fiber layer, GCL: ganglion cell layer, INL: inner nuclear layer, OPL: outer plexiform layer, ONL: outer nuclear layer. (Forrester, Dick, McMenamin; Lee, 2002).

Throughout neurogenesis retinal progenitor cells undergo symmetric and asymmetric cell divisions, giving rise to postmitotic neurons as well as progenitor cells. Postmitotic neurons are translocated to their final layer, either towards the outer neuroblastic layer (photoreceptors and horizontal cells) or towards the inner neuroblastic layer (ganglion and amacrine cells). These two layers are separated by the transient layer of Chievitz which is acellular. A first wave of early neuronal differentiation in the retina is characterized by the production of early-born retinal neurons: ganglion cells, horizontal interneurons, cone photoreceptors, and amacrine interneurons. A second differentiation potential of retinal neural progenitor cells leads to the production of late-born rod photoreceptors, bipolar interneurons, and Müller glia. In vertebrate, retinal neural progenitor cells (NPCs) remain multipotent and during the consecutive developmental stages, or for each cell division, their progenies can assume several different cell fates. In mice, similar processes occur (figure 1.14).

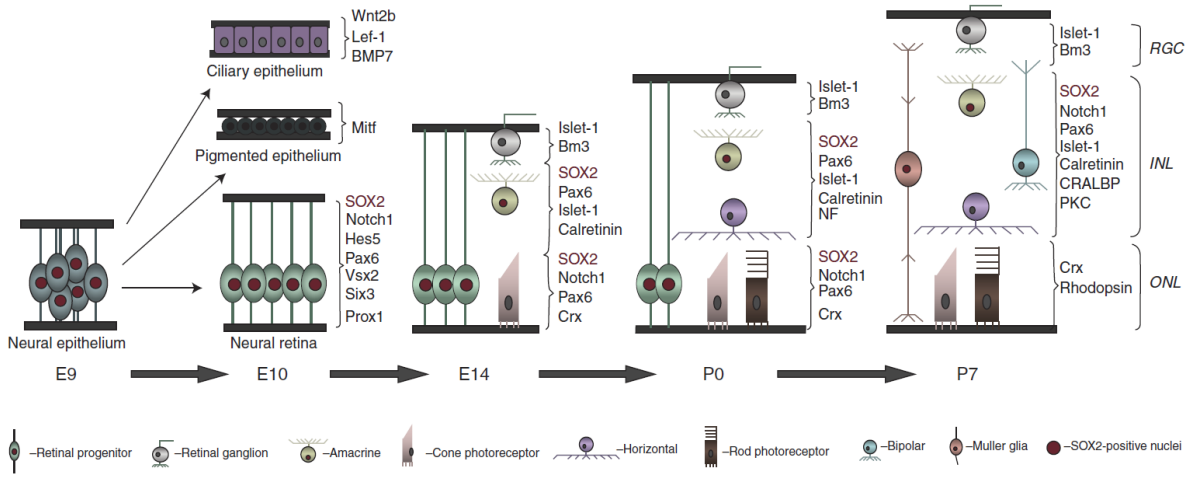

Figure 1.14: Temporal progression of retinogenesis in the mouse. (Heavner et al., 2012).

1.5.3. Optic nerve

The optic stalk expands across the brain establishes the connection with the eye at 47-48 days of gestation in human or E11.5 in the mouse. The axons from the RGC meet at the optic nerve head, travel down to the optic stalk and form the optic nerve at E15.5 in the mouse. This concludes the connections between the eye and the visual centres of the brain. Later in gestation the axons of the optic nerve become myelinated (Graw et al., 2003).

1.5.4. Retinal cell differentiation

There are four important steps in the process of generating the mature retina from retinal progenitor cells. Retinal progenitor cells must expand through cell division, exit the cell cycle, commit to a particular cell fate, and then execute the differentiation program for the committed cell type. During cell expansion, Hes1 inhibits neuronal differentiation and maintains progenitor cells. Proliferation of retinal progenitors may also be partly controlled by extrinsic cues such as ciliary neurotrophic factor (CNTF), bone morphogenetic protein (BMP), and fibroblast growth factor (FGF) molecules. Retinal development is controlled primarily by transcription factors of the basic helix–loop–helix (bHLH) and homeobox families. Generally homeodomain factors regulate layer specificity while bHLH activators determine cell (figure 1.15) (Harada et al., 2007). Concerning photoreceptor, homeobox genes, OTX2 and CRX, are key regulators of both rod and cone photoreceptor lineages. As mentioned previously whereas human possesses three types of cone, mice have only two. TRb2, RORb and RXRg have essential functions in cone differentiation. The NRL transcription factor, which is expressed preferentially in rods and pineal gland, is a critical regulator of rod photoreceptor cell fate (Cheng et al., 2011).

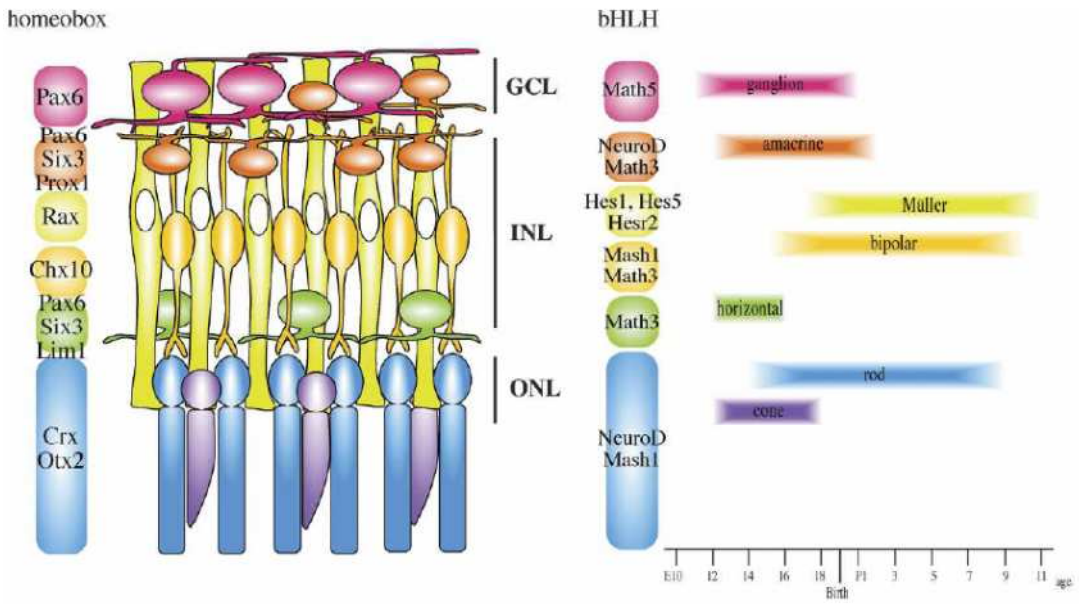

Figure 1.15: Homeobox and bHLH genes determining retinal cell fates. (Harada et al., 2007).

1.6. The retinotopic mapping genesis in mouse

1.6.1. Spatiotemporal mapping of retinal projection

Spatiotemporal patterns of neural activity, or 'retinal waves', govern the development of the earliest connections made between excitable cells in the developing eye. During waves, RGC fire bursts of action potentials that propagate across the retina. They play a crucial role in the development and refinement of synaptic connections between different parts of the visual system. Many factors and gene are implicated in the highly developed architecture of the retina and retinal ganglion cell projections (Ackman et al., 2014). The fact that the retinotopic map is achieved prior to the onset of visual experience implies elements such as cell adhesion and axon guidance molecules establish the basis of visual circuit connections prior to subsequent modification upon visual experience (Huberman et al., 2008).

1.6.2. Retinal polarity

In addition to the layering order achieved in the retina, genetic also influences retinal progenitor cells positional identity (figure 1.16). Although a direct comparison between humans and others species is difficult, several transcription factors and guidance molecules that establish nasal-

temporal (N-T) and dorsal-ventral (D-V) retinal polarity, are shared within some species. The N-T axis is set early in retinal development with expression of the two winged-helix transcription factors, BF1 and BF2. Then, two homeobox containing genes, SOHo1 and GH6, are expressed in high nasal and low temporal pattern. Both SOHo1 and GH6 can repress the expression of EphA3 at later stages. Thereafter, ephrin receptor, EphA5 and EphA6 are expressed in high temporal and low nasal gradient. D-V polarity develops soon after N-T polarity is established. BMP4 expression in the dorsal retina and Shh and Ventroptin in the ventral retina inhibit one another. BMP4 activates Tbx5 and represses Vax2 transcription factor. Tbx5 activates ephrin-B1 and ephrin-B2 and suppresses Vax2 and receptors EphB2 and EphB3. Vax2 promotes the transcription of EphB2 and EphB3 and represses ephrin-Bs, BMP4, and Tbx5. In contrast, ectopic expression of Shh results in dorsal inhibition of BMP4 and enhancement of Vax2 (figure 1.16) (Harada et al., 2007).

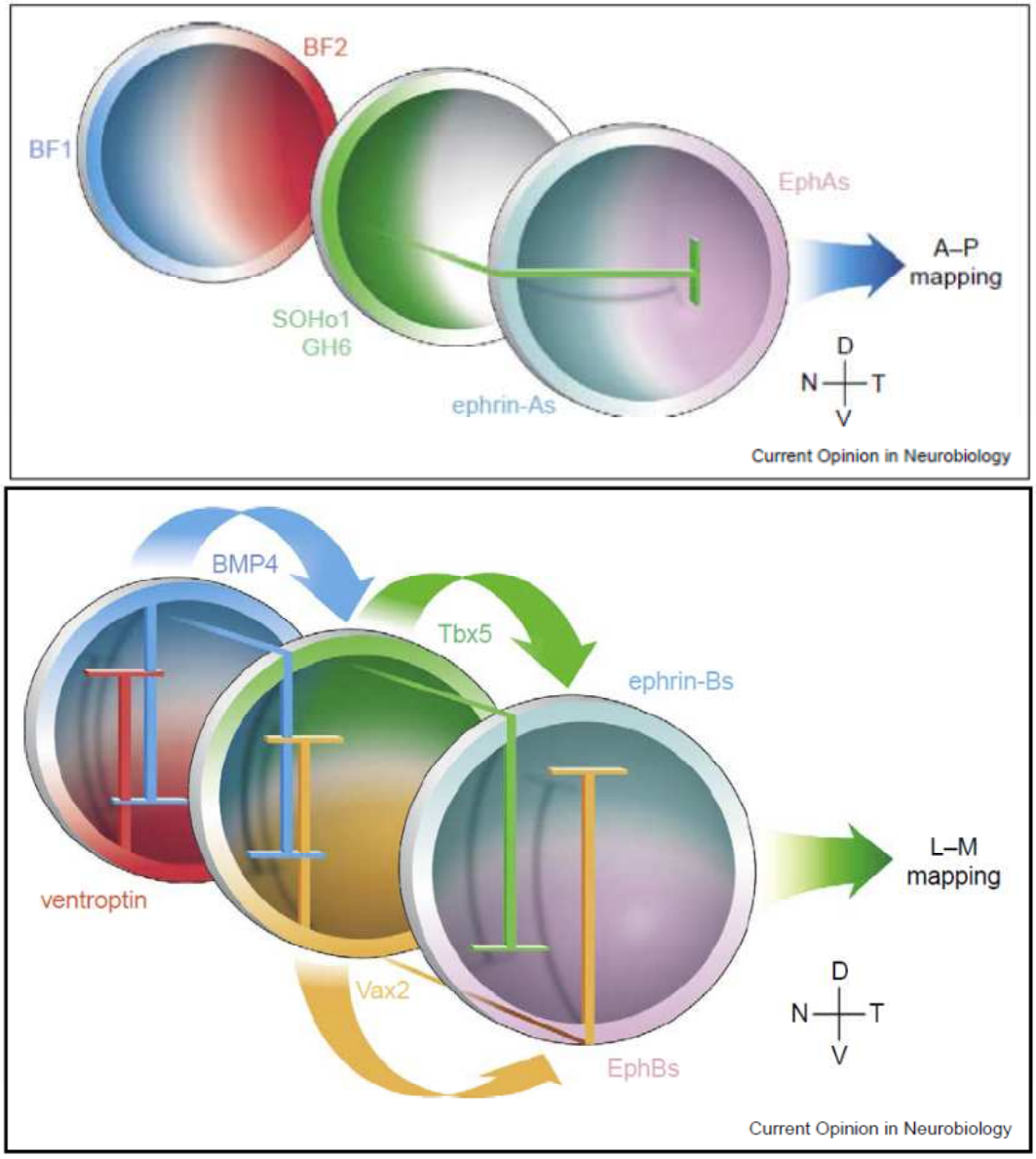

Figure 1.16: Regulation of axial patterning of the retina. (McLaughin et al., 2003).

1.6.3. Retinal ganglion cells axon guidance

Once retinal polarity is established, RGCs extend axons to the optic nerve head and form the optic nerve head. RGCs extend their axon out of the retina to reach the optic chiasm between E12 and P0 and reach de dLGN at E16 and the SC at E18 in mice. Complete segregation of synapse of output according to eye specific domain is achieved at P15. Retinotopic mapping is preserve in the LGN and in the SC. The process and maturation of the topographic maps include different steps. First, RGC projections distribute in the entire target, then upon Eph/ephrins encoded gradient, the proper localization of the termination zone through repulsive interactions. After that, the axonal arborisation develops within the correct location. Finally, a last refinement occurs after eye opening (Assali et al., 2014).

RGCs axon growth in the eye is initially controlled by the inhibitory effect of chondroitin sulphate proteoglycan, targeting extension towards the central optic disc. Crossing decision at the optic chiasm relies on topographic mapping of the retina and also on regulation event occurring in the optic stalk. Axon guidance molecules, such as netrin-1, L1 and laminin-1 are also involved in axon exit at the optic disc. Netrin-1 exerts attractant influence on RGC axons after the eye exit. At the ventral diencephalon Sema5A and Slit1/2 exert repulsive action, establishing a corridor for RGC axon expressing Robo2 and semaphorin receptors (Harada et al., 2007) (figure 1.17). Semaphorins are the largest family of inhibitory axon guidance molecules. Sema6D has been shown to play a role in contralateral projection (Kuwajiama et al., 2012) and other semaphorins (class 3 to 6) are found in nerve and retina between E13 and E15 (Oster et al., 2002).

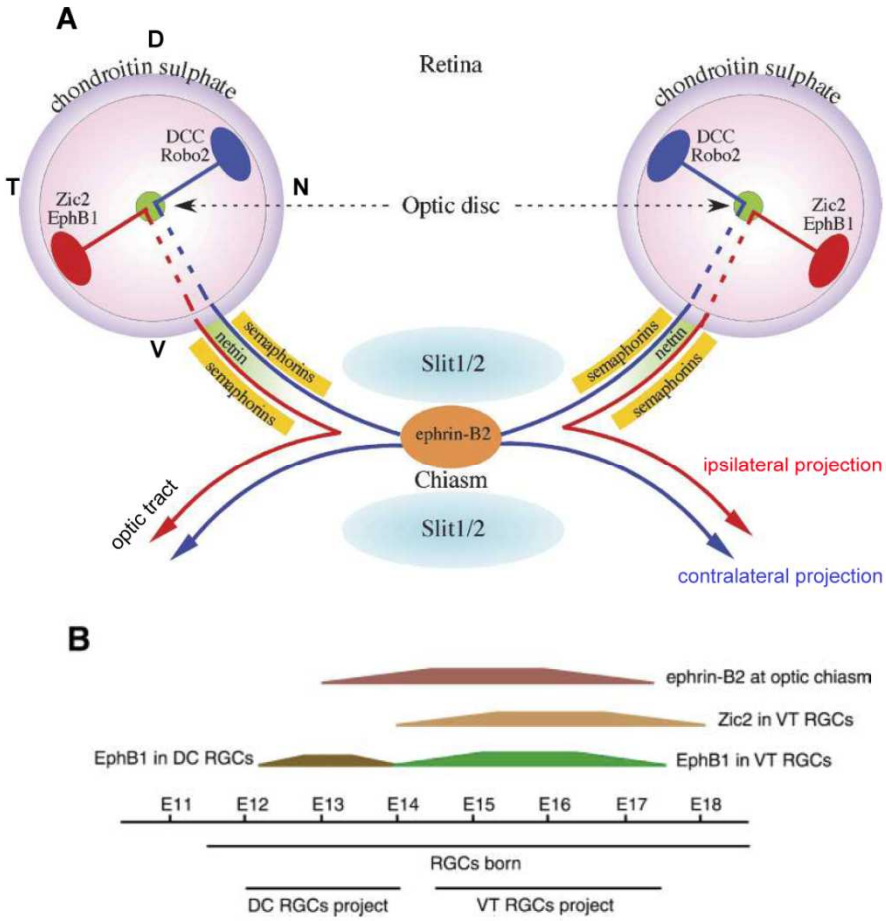

Figure 1.17: RGC axon guidance (modified from Harada et al., 2007, and Rasband et al., 2003).

Uncrossing decision at the optic chiasm is controlled by ephrin-B2, expressed by glial cells, and EphB1 expressed by ventrotemporal RGCs. Additionally, Zic2 regulates EphB1 expression in RGCs (Harada et al., 2007).

Shh, secreted from RGCs, upregulates *Vax1* which maintains *Pax2* in the optic stalk. *Pax2* is essential for glial cells specification at the optic stalk. Gliogenesis of the optic nerve is performed by oligodendrocytes which migrate toward the optic nerve upon attractive effect of netrin-1 guidance molecule. Type-1 and type-2 astrocytes also populate the optic nerve, the first glia being the largest population (Harada et al., 2007).

1.6.4. Topographic mapping of dLGN and SC

Retinogenicular and retinocollicular mapping follow the retinal topography. Upon crossing the midline, RGC axons project to SC and dLGN. The mapping in visual target occurs orthogonally to the axes of the retina, N-T axis maps the posterior-anterior (P-A) axis and D-V the lateral-medial (L-M). Master regulators of those patterns are the repellent ephrin and their recpetors. Generally Ephrin-As act at the P-A level and Ephrin-Bs at the L-M. In the dLGN ephrin-A2 and

ephrin-A5 are expressed in ventral-lateral-anterior-high and dorsal-medial-posterior-low gradients, whereas ephrin-A3 is expressed in small amounts. In the SC, ephrin-A2 and ephrin-A5 follow a P-A gradient. EphA7 shows the strongest P-A gradient of the SC. It is important to mention that L-M gradient of ephrin-B1 attract EphBs expressing axons in contrast to the ephrin-B2 at the optic chiasm (figure 1.18) (Harada et al., 2007).

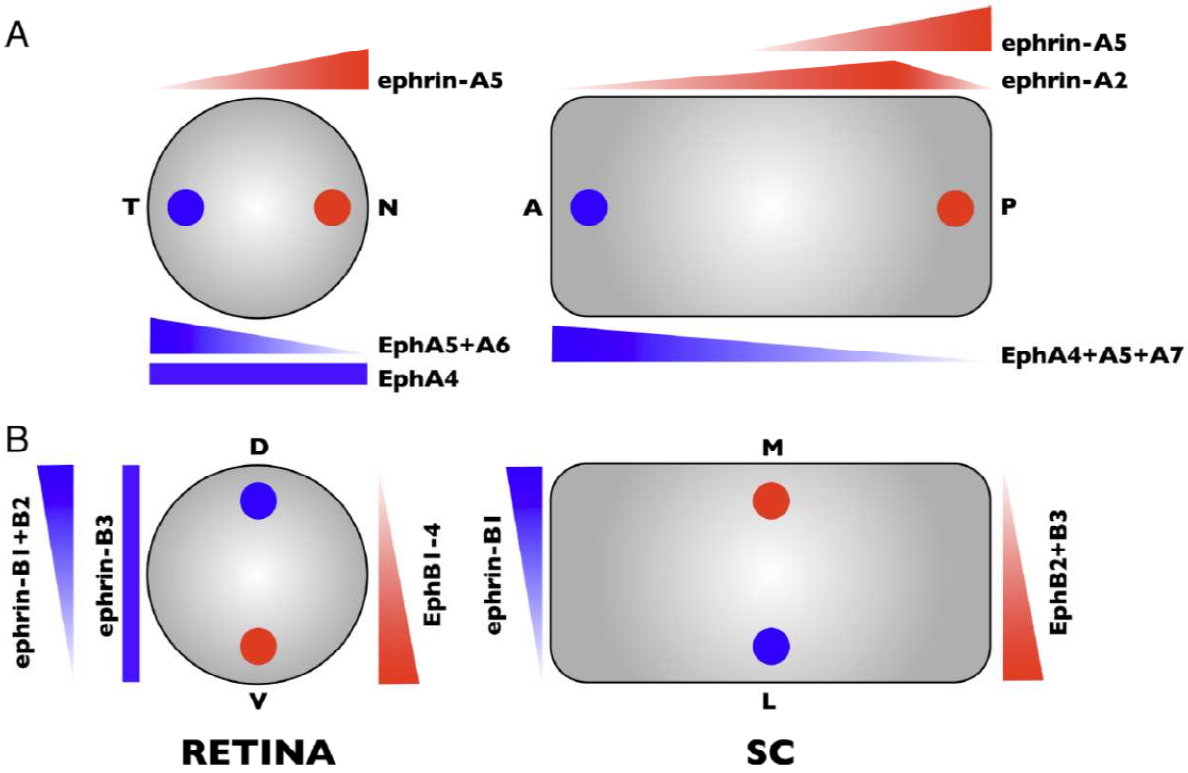

Figure 1.18: Expression patterns of Ephs and ephrins in the retinocollicular system. (Triplett et al., 2012).

It is also important to mention that as both Ephs and ephrins are cell surface molecules they can signal in the forward and reverse directions, and complete mechanism of the ephrin signalling is complex (Triplett et al., 2012).

Table 1.2 and 1.3 depict all the guidance cues and regulatory gene involved in RGC axon pathfinding.

Molecule	Expression	Role in retina	Role at chiasm	Role in optic tract/visual targets
CSPGs (Direct effect or modulation of other cues?)	High peripheral–low central wave in retina; bordering chiasm and optic tract.	Timing and polarity of RGC outgrowth (r; Brittis et al., 1992).	Path followed by RGC axons (m; Chung et al., 2000).	Inhibit outgrowth restricting axons to optic tract (c; Ichijo and Kawabata, 2001).
EphBs (reverse signalling)	High V–low D gradient in retina; Low M–high L gradient in tectum/SC.	Targeting of dorsal RGC axons to optic disc (m; Birgbauer et al., 2000).		Mapping along M–L axis of tectum (x; Mann et al., 2002).
EphrinAs	High N–low T gradient in retina; low A–high P gradient in tectum/SC; low M–high L gradient in LGN.			Mapping along A–P axis of tectum/SC and L–M axis of LGN. Organisation of eye specific layers (e.g. Frisen et al., 1998; Feldheim et al., 1998).
EphrinBs	High D–low V gradient in retina; chiasmatic midline; High M–low L gradient in tectum/SC.		Establishment of binocular visual pathways (x; Nakagawa et al., 2000; m; Williams et al., 2003).	Mapping along M–L axis of SC (m; Hindges et al., 2002).
netrin-1	Optic disc	Exit into the optic nerve (m; Deiner et al., 1997; x; Höpker et al., 1999).		
NrCAM	Contralaterally projecting RGC axons; chiasmatic midline.	Promotes growth towards and out of the optic disc (c; Zelina et al., 2005).	Promotes midline crossing of late-generated RGC axons (m; Williams et al., 2006).	
Sema3D	Midline of ventral diencephalon; Low M–high L gradient in tectum.		Promotes midline crossing and growth into contralateral optic tract (z; Sakai and Halloran, 2006).	Mapping along M–L axis of tectum (z; Liu et al., 2004).
Shh	High central–low peripheral wave in retina; midline of CNS except chiasm.	Promotes growth towards optic disc (c; Kolpak et al., 2005).	Inhibits growth; absence from midline required for crossing (c; Trousse et al., 2001; m; Torres et al., 1996; z; Macdonald et al., 1997).	
Slits	Lens; inner region of the retina; bordering chiasm and tract	Polarity of RGC axon outgrowth (m). Restrict axons to OFL via inhibitory (m; Thompson et al., 2006a) or attractive (c; Jin et al., 2003) signalling.	Inhibit outgrowth controlling position of chiasm and path followed by RGC axons (m; Plump et al., 2002).	Inhibit outgrowth restricting axons to optic tract (m; Thompson et al., 2006b).
Wnt3	Low M–high L gradient in tectum			Mapping along M–L axis of tectum (c; Schmitt et al., 2006).

A, anterior; D, dorsal; L, lateral; M, medial; N, nasal; P, posterior; T, temporal; V, ventral; c, chick; m, mouse; r, rat; x, Xenopus; z, zebrafish.

Table 1.2: Role of specific guidance cues in directing RGC axon pathfinding. (Erskine et al., 2007).

Thalamocortical projections of the dLGN are essential for the relay and processing of visual information. The reciprocal connections are regulated during the activity-independent mechanism by guidance cues such as *Ebf1*, a bHLH transcription factor, and *Dlx1* and *Dlx2* homeodomain transcription factors. EphA/ephrin-A and neurotrophins are also shown to be involved (Harada et al., 2007).

Gene	Expression	Function
Bm3b	Majority of RGCs	Controls intrinsic transcriptional network required for guidance in retina, optic chiasm and tract and mapping in SC (m; Erkman et al., 2000).
En-1/2	Low A–high P gradient in the tectum/SC	Control mapping in the tectum by regulating ephrinA expression (c; Friedman and O'Leary, 1996; Itasaki and Nakamura, 1996).
FoxD1	VT quadrant of retina, developing chiasmatic region.	Patterning of retina and ventral diencephalon required for normal chiasm formation (m; Herrera et al., 2004) and A–P mapping in tectum (c; Yuasa et al., 1996).
FoxG1	Nasal RGCs; ventral diencephalon anterior to chiasm.	Patterning of retina and ventral diencephalon underlying establishment of binocular visual pathways (m, Pratt et al., 2004) and A–P mapping in tectum (c; Takahashi et al., 2003; Yuasa et al., 1996).
GH6	High N–low T gradient in retina	Controls mapping in tectum by regulating negatively EphA3 expression (c; Schulte and Cepko, 2000)
Irx4	Subset of cells in RGC layer of retina.	Controls RGC axon fasciculation and guidance within the retina by regulating negatively Slit1 expression (c; Jin et al., 2003).
Islet2	Contralaterally projecting RGCs	Specification of contralaterally projecting RGCs by repressing Zic2 expression (m; Pak et al., 2004).
Lhx2	Retina; ventral diencephalon including pre-optic area	Controls expression of guidance cues in preoptic area of diencephalon required for chiasm formation (z; Seth et al., 2006).
Pax2	Proximal region of retina; glial cells of optic stalk; midline of ventral diencephalon.	Represses Shh from the chiasmatic midline enabling formation of the crossed chiasmatic projection (m; Torres et al., 1996; z; Macdonald et al., 1997).
SOHo	High N–low T gradient in retina	Controls mapping in tectum by regulating negatively EphA3 expression (c; Schulte and Cepko, 2000)
Tbx5	Dorsal retina	Controls mapping in the tectum by regulating EphB/ephrinB expression (c; Koshiba-Takeuchi et al., 2000).
Vax1	Glial cells of optic nerve; CNS midline.	Controls expression of attractive guidance cues required for growth of RGC axons into the brain (m; Bertuzzi et al., 1999).
Vax2	Ventral retina	Patterning of retina underlying establishment of binocular visual pathways and mapping in tectum/SC (m; Mui et al., 2002; Barbieri et al., 2002; c; Schulte et al., 1999).
Zic2	Ipsilaterally projecting RGCs	Specification of ipsilaterally projecting RGCs (f, m, x; Herrera et al., 2003).
Zic3	Receding high peripheral — low central gradient in the retina	Controls expression of inhibitory guidance cue(s) required for intraretinal RGC axon pathfinding (c; Zhang et al., 2004).

A, anterior; D, dorsal; N, nasal; P, posterior; T, temporal; V, ventral; c, chick; f, ferret; m, mouse; x, Xenopus; z, zebrafish.

Table 1.3: Regulatory genes controlling RGC axon pathfinding. (Erskine et al., 2007).

1.7. Mouse development

1.7.1. Embryogenesis and branchial arch system

Neurulation is a fundamental process of embryogenesis, it consist in the formation of the neural tube after progressive infolding of the neural plate. Within the tube regionalization, patterns of regulatory genes are expressed and will lead embryonic development. Prosomeric modelisation of the mouse embryo characterizes region based on genetic and morphologic evidences.

The major transitional tissue of embryogenesis is certainly the neural crest. Neural crest cells arise along the margins of the neural folds at the boundary between the surface and the neural ectoderm. During neurulation, these cells migrate throughout the body where they, later in development, will differentiate into a particularly wide range of cell type. It is not long ago that specific lineage markers allowed scientists to analyze precise origin of precursor cells that contributes to particular structure development. Neural crest cell lineage marker, *Wnt1-Cre/R26R*, and mesoderm lineage cell marker, *Mesp1-Cre/R26R* have allowed great advance in developmental analysis (McBratney-Owen et al., 2008). Cranial neural crest cells (CNC) migration

is controlled by a wide range of molecular mechanism, and major signalling pathways manage their patterning within the branchial arches.

Branchial aches (BA), or pharyngeal arches, are structures found within vertebrate mostly involved in the development of the face and the neck. BA1 can be subdivided into a maxillar and mandibular component. BAs expand during embryonic development by proliferation of neural crest cells from the neural plate: forebrain, midbrain and hindbrain (Minoux et al., 2010). This migration of CNC cells occurs between the rostral cranial axis and the posterior-anterior cranial axis and is concomitant with the activation of several homeodomain transcription factors, including Hox, Dlx, Otx and Emx genes (Noden et al., 2005; Matsuo et al.,1995).

Endothelin-1 (Edn1) is one of the primary signals that establish the identities of neural crest cells within the mandibular portion of the BA1. Signaling through its cognate receptor, the endothelin-A receptor, is critical for patterning the ventral/distal portion of the arch (lower jaw) and also participates with Hox genes in patterning more posterior arches. Edn1/Ednra signalling modulates Dlx and ephA2 expression (figure 1.19) (Clouthier et al., 2010).

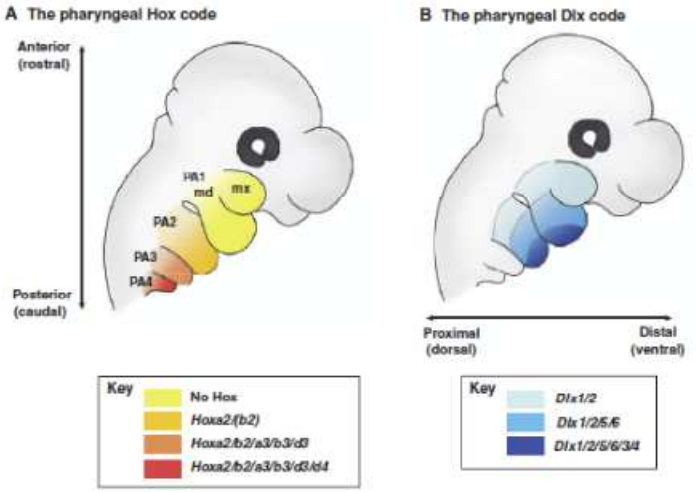

Figure 1.19: Intrinsic transcriptional programs underlying cranial neural crest cells positional identity in E10.5 mouse embryo. (Minoux et al., 2010).

Others molecular mechanisms are involved in establishing and maintaining the migration of segmentally restricted CNC streams into the BAs, such as Erbb4 (v-erb-a erythroblastic leukemia viral oncogene homologue 4), neuropilin/semaphorin 3 (Nrp/Sema3) and ephrinB2/EphA4 (Eph receptor A4)/EphB1 (figure 1.20) (Minoux et al., 2010).

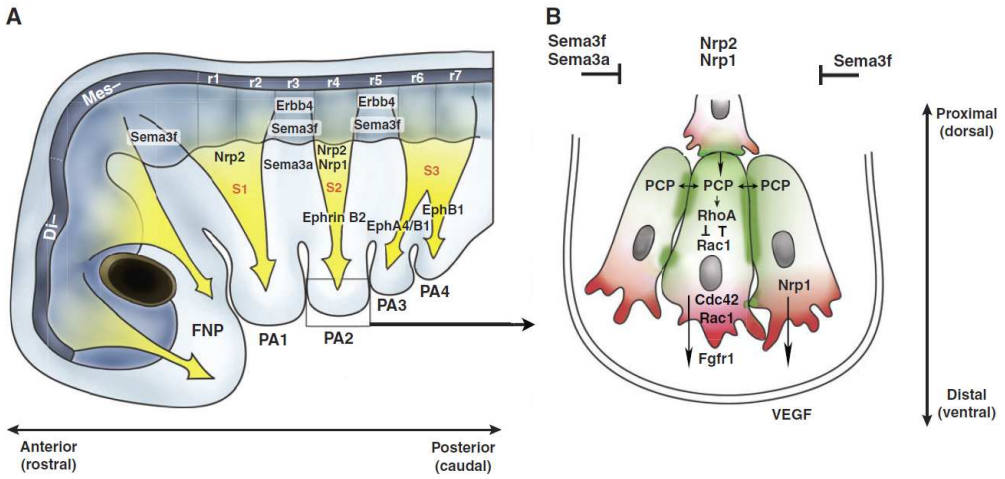

Figure 1.20: Segmental and directional migration of cranial neural crest cells at E10.5. (Minoux et al., 2010).

1.7.2. Visual area of the brain

In embryo, visual areas are located on bilateral evagination forming optic cup and later connection between RGC and neurons of the SC occur at E15, their maturation is achieved by P6.

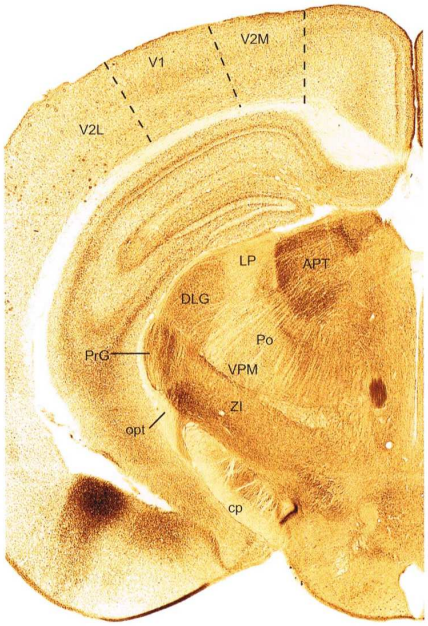

Figure 1.21: A photograph of a coronal section of mouse brain through the middle of the dorsal lateral geniculate nucleus (stained with acetylcholinesterase). APT: anterior pretectal nucleus, DLG: dorsal lateral geniculate nucleus, cp: cerebral peduncle. LP: lateral posterior nucleus of the thalamus, opt: optic tract, Po: posterior complex of the thalamus, PrG: , VPM: ventral posteromedial nucleus, V1: primary visual cortex, V2L and V2M: visual association cortex, ZI:zona incerta (Watson, Paxinos, Puelles, 2012).

Refinement of the visual area occurs postnatal in parallel with nervous system maturation (Wilks et al., 2013). In adult mice, visual related areas are easily recognized along the retinotopic path (Figure 1.21 and 1.22).

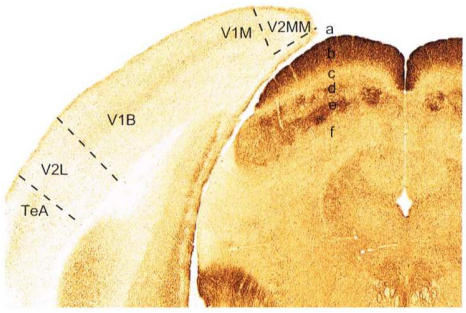

Figure 1.22: A photograph of a coronal section of mouse brain through the middle of the superior colliculus (stained with acetylcholinesterase). V1M and V1B: primary visual cortex, V2MM and V2L: visual association areas, TeA: temporal association cortex. The layers of the superior colliculus are labelled a to f. (Watson, Paxinos, Puelles, 2012).

1.7.3. Craniofacial and skeletal development

The head structure, from the hyoid to the tip of the parietal, emerges from the extension of branchial arches (BA) 1 to 4. The exact origin of craniofacial element has been well established during last decade, whether concerning their BAs origins or their cell lineage origin (figure 1.23 and table 1.4).

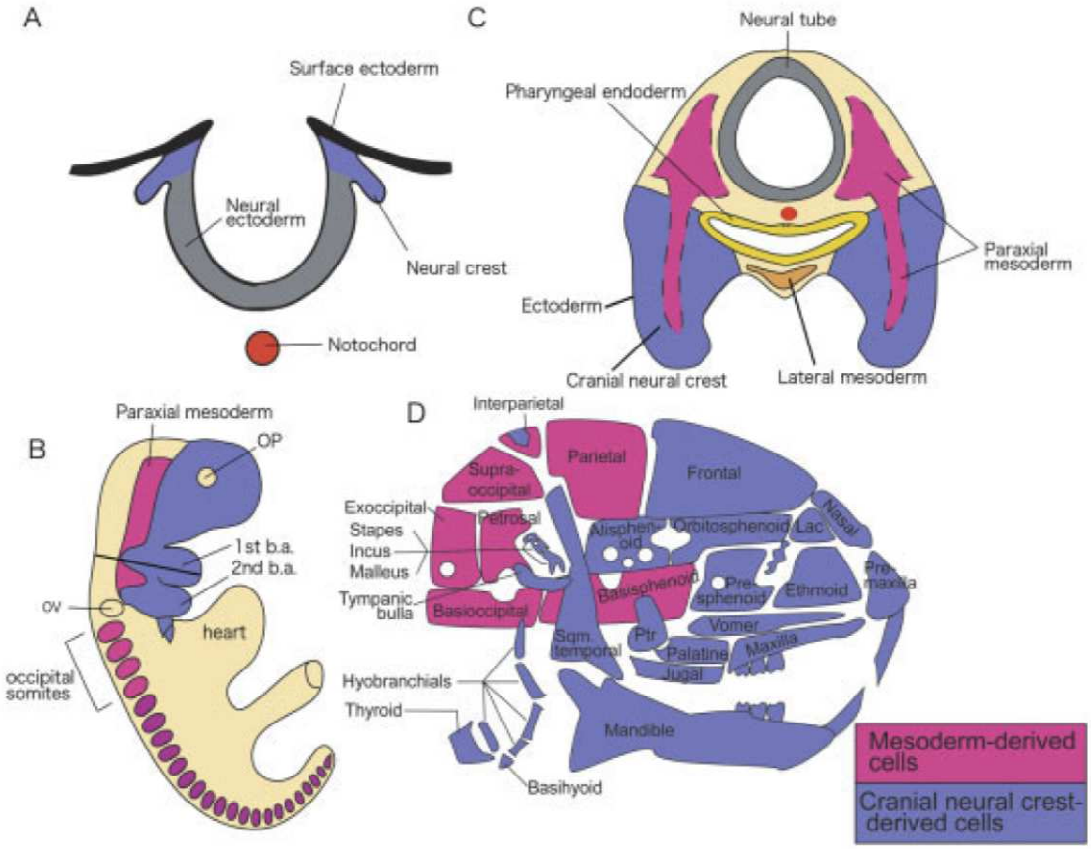

Figure 1.23: Contribution of cells lineage during craniofacial development. (Chai et al., 2006).

Table 1: Derivatives of the BAs

Location	Cleft	Arch	Nerve	Pouch
First	External ear canal	Mandible, muscles of mastication, 5th cranial nerve, malleus, and incus	Trigeminal nerve (V2 and V3)	Eustachian tube, tympanic cavity, mastoid air cells
Second	Cervical sinus of His	Muscles of facial expression, body and lesser horns of hyoid, 7th and 8th cranial nerves, stapes	Facial nerve (VII)	Palatine tonsil
Third	Cervical sinus of His	Superior constrictor muscles, internal carotid artery, 9th cranial nerve, greater horn, and body of hyoid	Glossopharyngeal nerve (IX)	Inferior parathyroid, thymus, pyriform fossa
Fourth	Cervical sinus of His	Thyroid and cuneiform cartilages, 10th cranial nerve, aortic arch and right subclavian artery, part of laryngeal muscles	Vagus nerve (X), superior laryngeal nerve	Superior parathyroid, apex of pyriform sinus
Fifth and sixth	None	Portions of the laryngeal muscles and skeleton, inferior pharyngeal constrictor muscles, 11th cranial nerve	Vagus nerve (X), recurrent laryngeal nerve	Parafollicular "C" cells of thyroid gland

Table 1.4: Branchial arch derivatives. (Johnson et al., 2011).

The chondrocranium develops between E11 and E16 in the mouse, beginning with development of the caudal (occipital) chondrocranium, followed by chondrogenesis rostrally to form the nasal capsule, and finally fusion of these two parts via the midline central stem and the lateral struts of the vault cartilages. Neural crest cells contribute to all of the cartilages that form the ethmoid, presphenoid, and basisphenoid bones with the exception of the hypochiasmatic cartilages. The basioccipital bone and non-squamous parts of the temporal bones are mesoderm derived (McBratney 2008) (figure 1.24 and 1.25).

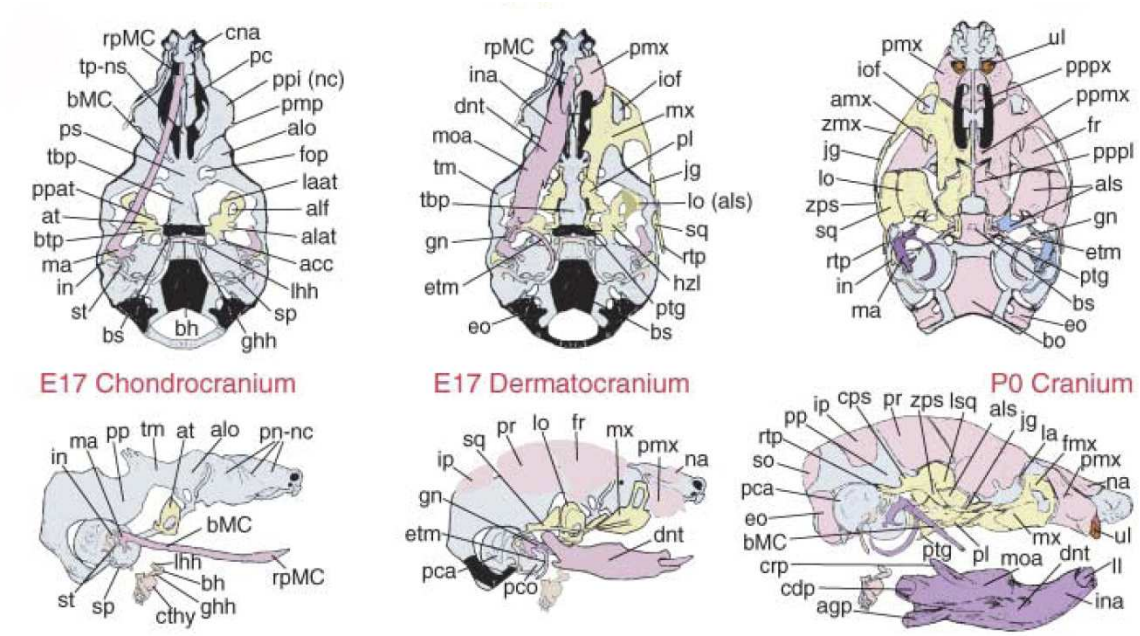

Figure 1.24: Schematic representation of murine skulls. Elements in yellow are maxillary arch derivatives, lavender for mandibular and salmon for caudal. Acc, alicochlear commisure; agp, angular process; alat, anterolateral process of ala temporalis; alf, alisphenoid foramen; alo, ala orbitalis; als, alisphenoid; amx, alveolus of maxilla; at, ala temporalis; bh, body of hyoid; bMC, body of Meckel's cartilage; bo, basioccipital; bs, basisphenoid; btp, basitrabecular process; cdp, condylar process; cna, cupola nasi anterior of nasal capsule; cpr, crista parotica; cps, caudal process of squamosal; cthy, thyroid cartilage; dnt, dentary; eo, exoccipital; etm, ectotympanic process; fmx, frontal process of maxilla; fop, orbitonasal fissure; fr, frontal; ghh, greater horn of the hyoid; gn, gonial; hzl, horizontal lamina; in, incus; ina, incissive alveolus of dentary; iof, infraorbital foramen of maxilla; ip, interparietal; jg, jugal; la, lacrimal; laat, lamina ascendens ala temporalis; lhh, lesser horn of hyoid; LI, lower incisor; lo, lamina obturans; lsq, squamosal lamina; ma, malleus; moa, molar alveolus of dentary; na, nasal; pc, paraseptal cartilage; pca, pars canalicularis; pco, pars cochlearis; pl, palatine; pmp, posterior maxillary process; pmx, premaxilla; pnnc, paries nasi – nasal capsule; pp, parietal plate; ppat, pterygoid process of ala temporalis; ppi (nc), prominentia pars intermedia (nasal capsule); ppmx, palatal process of maxilla; pppl, palatal process of palatine; pppx, palatal process of premaxilla; pr, parietal; ps, presphenoid; ptg, pterygoid; rpMC, rostral process of Meckel's cartilage; rtp, retrotympanic process; so, supraoccipital; sp, styloid process; sq, squamosal; st, stapes; tbp, trabecular basal plate; tm, taenia marginalis; tp-ns, trabecular basal plate – nasal septum; UI, upper incisor; zmx, zygomatic process of maxilla; zps, zygomatic process of squamosal. (Depew et al., 2005).

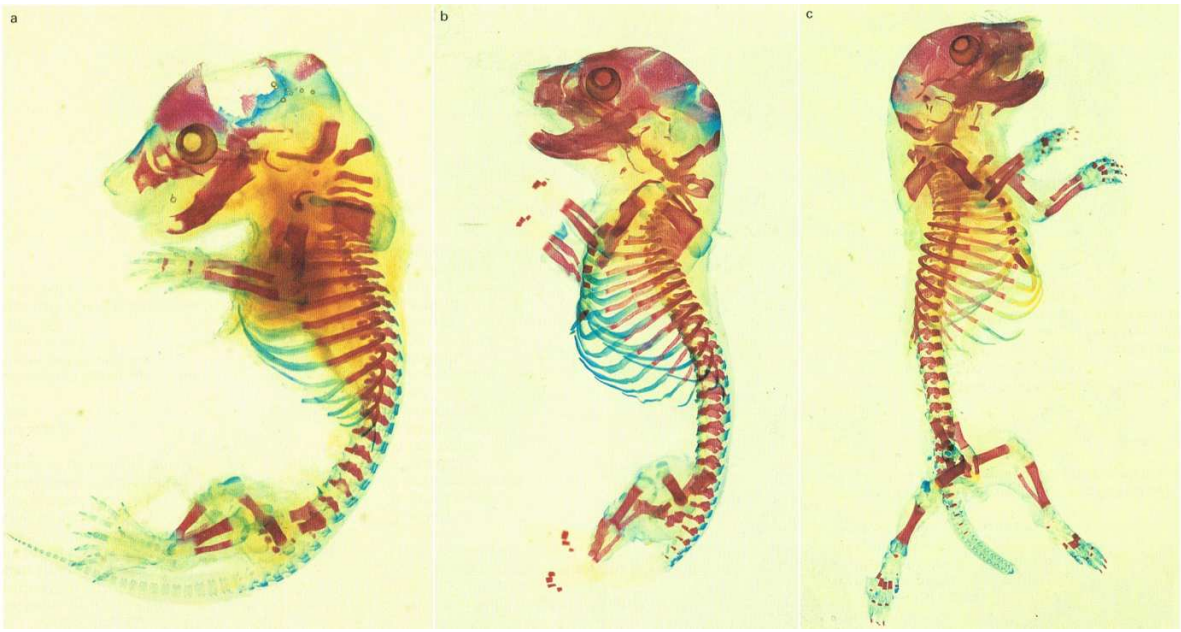

Figure 1.25: Ossification and cartilaginous skeleton of mouse embryon (alcian and alizarin staining). (a) E16.5, (b) E17.5, (c) E18.5. (Kaufmann, 1998).

1.8. HMX1

1.8.1. *Hmx* family and function

The phylogenetically conserved homeobox of *Hmx* family is a helix-loop-helix-turn-helix type, and there are two conserved regions, SD1 and SD2, immediately adjacent the 3' side of the homeobox (Yoshiura et al., 1998). *Hmx* family belongs to the NKL subclass of the ANTP class of homeoboxes, and were firstly named *NKX5* family. These genes are known to play role in developing sensory organs (Wang et al., 2000).

Concerning *Hmx* family members, both *Hmx2* and *Hmx3* are required for cell fate determination and subsequent morphogenesis of the developing inner ear. Loss of both *Hmx2* and *Hmx3* results in the absence of the entire vestibular system. *Hmx* family play an important role with other control genes of the inner ear development (Fgfs, Shh, Wnts, RARs, Hmx1, Hmx2, Hmx3, and Dlx5, etc.) but are differentially active in temporal and spatial domains (Wang et al., 2005) (table 1.5). Consistent with its expression during inner ear development, *Hmx1* plays an essential role for the survival of neurons in the facio-acoustic ganglia and also the geniculate ganglion (Wang et al., 2005; Quina et al., 2012). Moreover *Hmx1* is required for the control of noradrenergic and cholinergic sympathetic neurons diversification via *Tlx3* and *Ret* and cell fate control (Furlan et al., 2013). Studies have also proposed that *HMX1* may act as a critical transcriptional switch between neuronal versus glia-melanocyte fate in the ventral neural crest pathway (Adameyko et al., 2009).

Animal	Gene	Craniofacial region	Nervous system	Other
Mouse	*Hmx1*	2nd branchial arch Dorsolateral mesenchyme Retina, lens	NV ganglion NX ganglion Sympathetic nerve ganglion Dorsal root ganglion	
Mouse	*Hmx3*[b] (*Nkx5.1*) (day 8.5)	Branchial arch (between 2nd and 3rd) Otic vesicle Optic cup Lateral mesenchyme	Thalamus Preoptic area Mammillary area Pons Medula Dorsal root ganglia Peripheral nerve ganglia	
Mouse	*Hmx2*[b] (*Nkx5.2*) (day 14.5)	Inner ear	Same as *Hmx3*, except thalamus	

Table 1.5: Expression pattern of Hmx gene family in mouse (adapted from Yoshiura et al., 1998).

1.8.2. Characteristics

In contrast to other transcription factors, HMX1 prefers a CAAG(TG) binding site rather than the usual TAAT. In vitro experiments have shown that NKX2.5 binds to the same site as HMX1 and

attenuates the repression effect of HMX1. In turn HMX1 is able to antagonize NKX2.5 activation (Amendt et al., 1999). Despite extensive study, the promoter region of the murine *Hmx1* still remains to be resolved. As there is no usual TATA box or CAAT-like motif, only potential promoter region was proposed between -416 and -166, but this remains to be fully understood (Nichini & Schorderet, 2008).

1.8.3. *HMX1* gene : Comparison of human and mouse genes

The human H6 homeobox 1, mapped the chromosome 4p16.1 (Stadler et al., 1992) and is composed of 1047 base pairs coding a 348 amino acid protein. *HMX1* gene bears across species the conserved homeobox-specific amino acids: Arg-5, Gln-12, Leu-16, Tyr-25, Leu-40, Trp-48, Phe-49, Asn-51 and Arg-53. The murine *Hmx1* maps to chromosome 5 (Wang et al., 1997) and is composed of 999 base pairs coding for 332 amino acids (Yoshiura et al., 1998). There is an 85% homology at the amino acid level between the human and mice sequence, but no significant homology in the 5' and 3'UTR (figure 1.26). Both human and murine genes are formed of two exons and one intron, with the homeobox located in exon2.

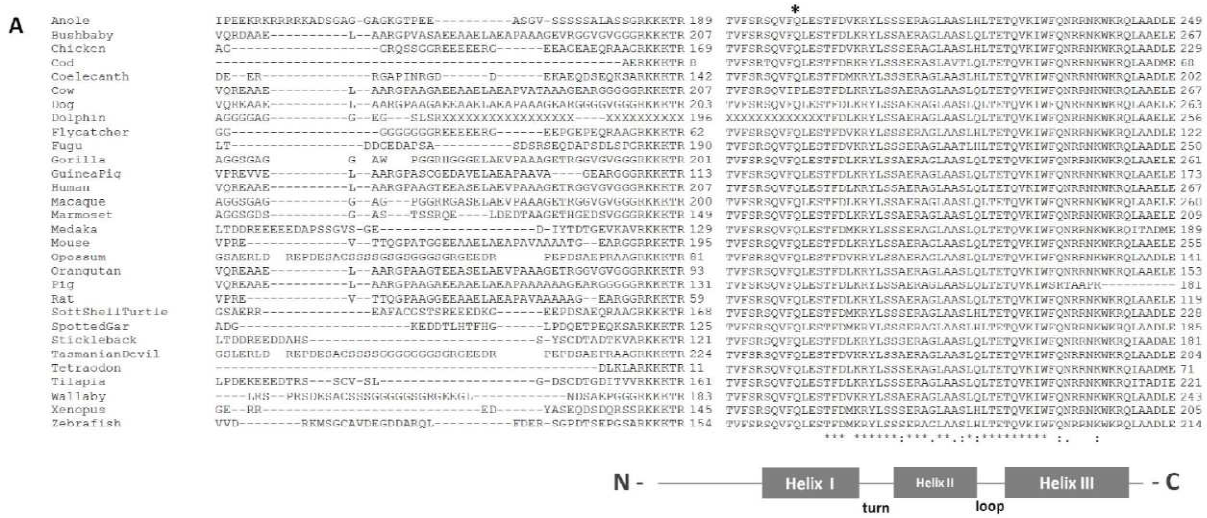

Figure 1.26: Multispecies alignment of HMX1 amino acid sequence. (Gillespie et al., 2015)

1.8.4. Expression pattern in humans and mice

In humans, HMX1 is expressed in the retina in 5 week-old human embryos, in the developing auricular mesenchymal cells and in the perichondrium of the intrinsic cartilages of the pinna in 20 week-old fetuses (Schorderet et al., 2008).

In mice, Hmx1 expression starts at E9.5 in the trigeminal ganglion and is maintained up to E16. Expression in the eye, BA2 and dorsal root ganglions (DRG) starts by E10.5. In addition, there is also expression in the mesenchyme proximally along the caudal margin of BA1, part of the

mandibular component, and in the faciostatoacoustic ganglion complex near the otic vesicle (figure 1.27). At E11.5 the pattern in the eye refines to the lens and the neural epithelium which persist at E13.5, this is followed by a decrease in DRG. At E12.5 Hmx1 is also found in the dorsal-lateral area of the head mesenchyme. Finally, expression in the sympathetic ganglion, otic vesicle, and vagal nerve ganglion is observed at E14, as well as in DRG, and by E16 sympathetic trunk ganglia present Hmx1 expression (Yoshiura et al., 1998; Wang et al., 2000; Munroe et al., 2009; Quina et al., 2012; Schorderet et al., 2008)

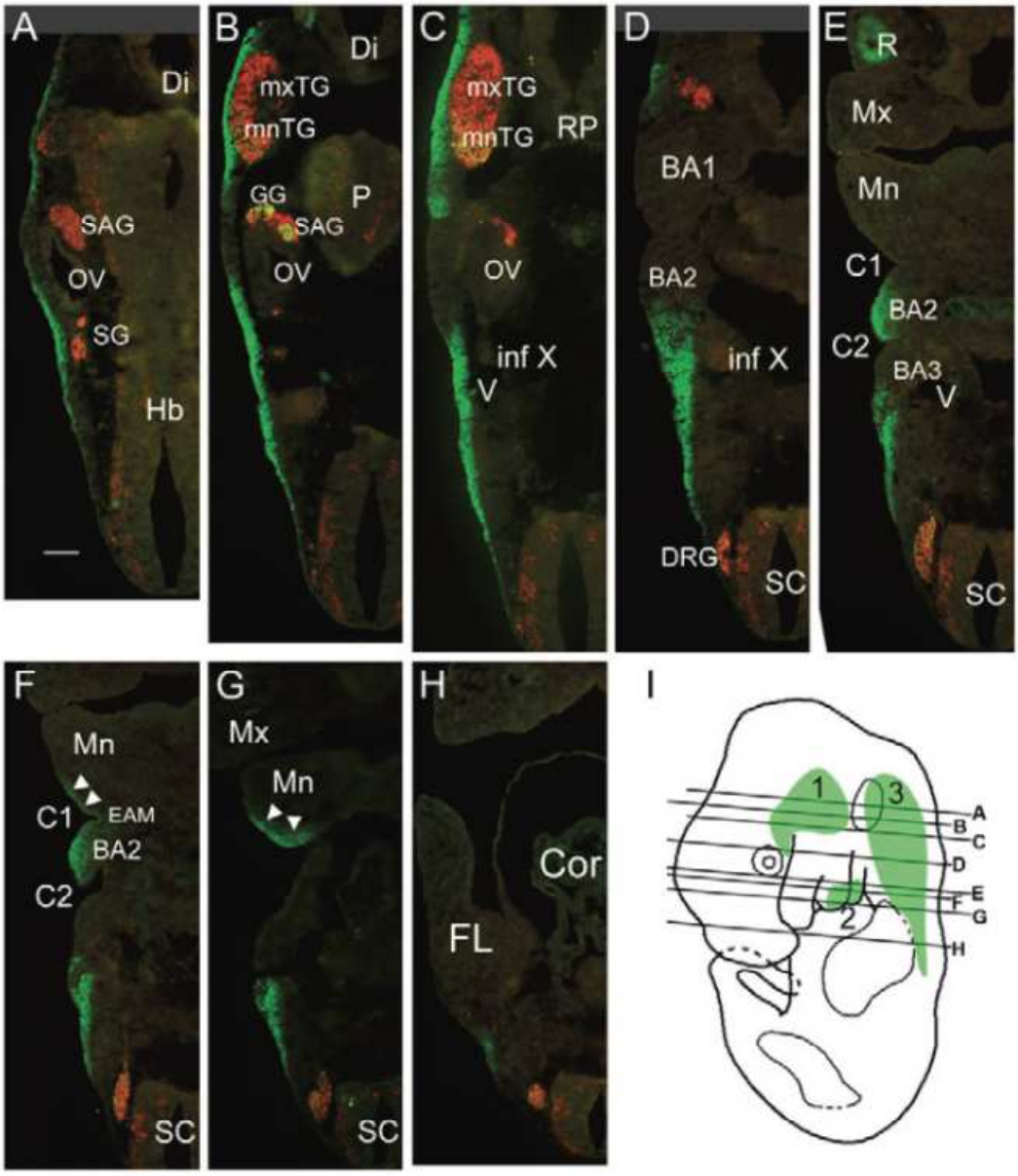

Figure 1.27: Hmx1 expression in developing mouse craniofacial mesenchyme. (Quina et al., 2012b).

1.9. Oculo-auricular syndrome of Schorderet-Munier-Franceschetti

The ocular-auricular syndrome of Schorderet-Munier-Franceschetti was first described in 1945 in a three-year old girl and her six-year old brother presenting a bilateral microphthalmia and malformation of the external ear. These defects' association were rare enough to let the authors speculate of a common origin of these malformations.

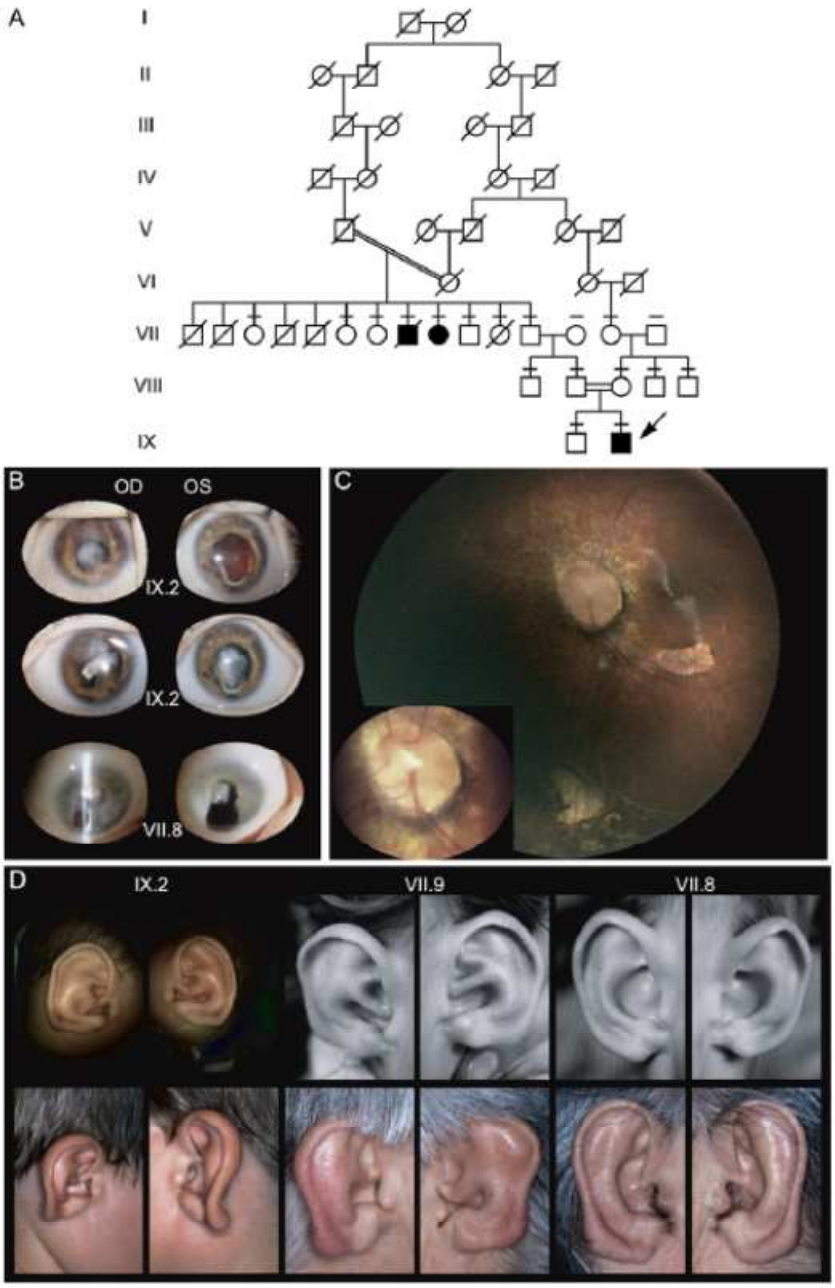

Figure 1.28: Family tree and eye and ear phenotype of the three members affected. (Schorderet et al., 2008).

In 2008, a new member of this family was examined (figure 1.28) and the mutation involved in this disorder discovered (Schorderet et al., 2008). The mutation consists in a homozygous 26 base pair deletion in exon 1 of *HMX1*, present in the three patient of this first family (figure 1.29). The mutation created a frameshift and a termination codon, preventing translation of the homeobox (black box figure 1.29).

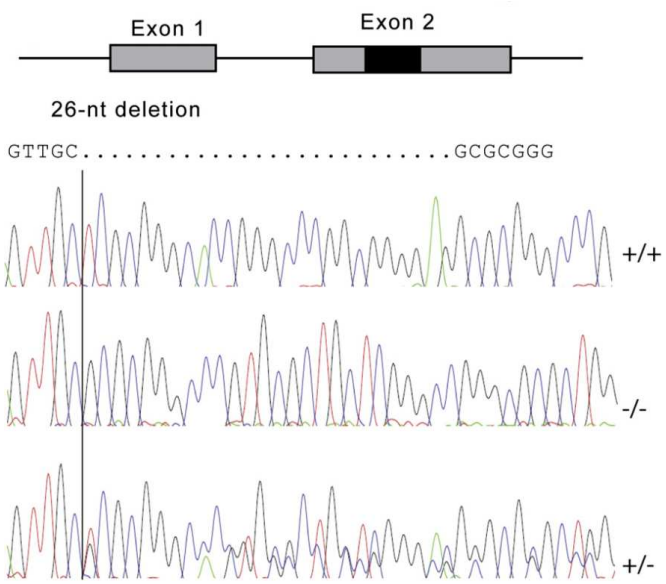

Figure 1.29: DNA sequence of HMX1 in control (+/+), and deletion found in heterozygous parent (+/-), and homozygous proband (-/-). (Schorderet et al., 2008).

In 2015, a second family was described with two children affected. The major features again were microphthalmia and particular ear lobe malformation (Gillespie et al., 2015) (figure 1.30). Screening of *HMX1* allowed authors to detect a second homozygous mutation in the gene, a missense mutation within the homeodomain that altered its function.

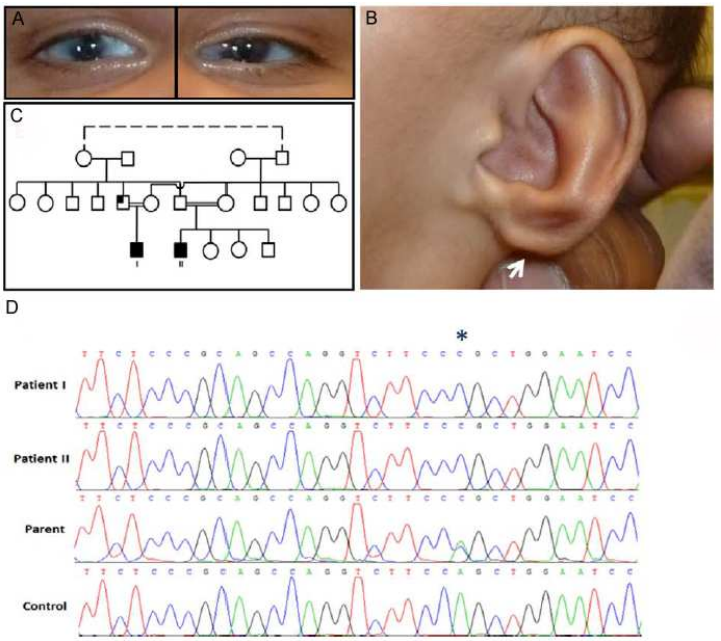

Figure 1.30: (C) Family tree, (A) eye and (B) ear phenotype of a member affected in the second family, (D) chromatogram of the homozygous HMX1 mutation. (Gillespie et al., 2015).

Even if the types of mutations within HMX1 are not the same, they both lead to OAS-SMF. Patients from both family share common clinical features: microcornea, microphthalmia, cataract, anterior-segment dysgenesis, optic nerve dysplasia, coloboma, rod-cone dystrophy, and aberration of the retinal pigment epithelium and an unusual cleft or aplastic ear lobule.

Detailed descriptions of each patient from both families are classified in table 1.6.

TABLE. Phenotypic Details of Patient I and Patient II and the Original OAS Family Reported by Schorderet et al.[2]

	Patient I	Patient II	Proband*	Individual 1 (VII.8)*	Individual 2 (VII.9)*
Eye					
Anterior segment					
Cornea	Posterior embryotoxon (L) Localized sclerocornea (R) Microcornea (7 mm [R]; 8 mm [L])	Posterior embryotoxin (L) Gross sclerocornea (opaque and vascularized in [R]) Microcornea (6 mm [R]; 6.75 mm [L])	Microcornea	Sclerocornea	Microcornea
Lens	Bilateral dense CC	Dense central & nuclear bilateral CC	Rapidly progressive bilateral CC	Cataract (onset not clear)	Cataract (onset not clear) Microphakia
Iris	Inferior iris coloboma	Inferior iris coloboma Anterior synechiae (L)	Posterior synechiae Incomplete iris coloboma	Inferior iris coloboma	Iris coloboma
Posterior segment					
Retina	Bilateral uveoretinal coloboma Small dysplastic optic discs	Small, tilted, dysplastic optic discs	Bilateral optic nerve dysplasia Macular hypoplasia Peripheral infero-nasal chorioretinal coloboma Circumferential abnormalities of the RPE Mottled RPE appearance (aged 4 y) Equatorial chorioretinal atrophic lacunae Thinning of the retinal vessels	Inferior chorioretinal coloboma (R) Inferior chorioretinal atrophy lacunae (L) Pigment deposits within the RPE	Retinal detachment
ERG	N/A	Significantly attenuated light & dark ERGs (age 14 y)	Moderately severe, generalized retinal dystrophy, apparent loss of rod photoreceptor function, mild cone abnormality (aged 6 y). Rod-cone dystrophy (aged 7 y) Almost undetectable rod specific ERG, severe cone ERG abnormalities (aged 12 y)	N/R	N/R
Other					
Globe	Colobomatous microphthalmia Short axial length (13.9 mm [R]; 14.9 mm [L])	Gross microphthalmia Slightly short axial length (17 mm [L]; 16.9 mm [R]) Enophthalmos	Colobomatous microphthalmia (R) Esotropia (R) (aged 4 y)	Microphthalmia Increased IOP	Microphthalmia
Other	Congenital nystagmus Divergent strabismus (R) Naso-lacrimal duct obstruction	x-NEW-CELL-x	Congenital nystagmus	Nystagmus	(L) eye enucleated due to painful complications of partially calcified phthisis bulbi
Visual symptoms	Poor peripheral vision Poor dark adaptation (age 2.5 y)	Good light response, poor dark adaptation (age 5 mo)	Poor visual acuity from infancy, marked visual field constriction (aged 9 y)	Vision limited to light perception (aged 6 y). Normal eye tension and some vision maintained through inferior iris coloboma until aged 65 y when cataracts progressed	N/R

TABLE. Continued

	Patient I	Patient II	Proband*	Individual 1 (VII.8)*	Individual 2 (VII.9)*
Ear					
Phenotype	Low-set Lobule aplasia Narrow external acoustic meatus	Low-set Lobule aplasia Narrow external acoustic meatus 'Crumpled' appearance	Lobule aplasia Narrow intertragic incisures Abnormal bridging between the crus of helix and antihelix Narrow external acoustic meatus Small eardrum with normal appearance	Strikingly abnormal appearance of the pinna Lobule aplasia	Strikingly abnormal appearance of the pinna Lobule aplasia
Hearing	Normal	Normal	Normal	N/R	N/R
Other	Excessive sweating	Excessive sweating High palate Extra dentition Small atrial septal defect Micrognathia Mild plagiocephaly	N/R	3 maxillary dental rows	Spina bifida occulta Moderate dyscrania with flattening of the cranial base Short mandibular rami

R, right eye; L, left eye; N/A, not available; N/R, not reported.
* Indicates affected individuals described in the original OAS family.

Table 1.6: Description of the phenotypic traits of patient within both families. (Gillespie et al., 2015).

1.10. Animal model for *Hmx1*

1.10.1. Dumbo mouse model

For the study of Hmx1 in my thesis, I worked on the dumbo mouse model. The dumbo mouse originates from a random ENU mutagenesis of proximal mouse chromosome 5 (Wilson et al., 2005). The Hmx1 dmbo allele involves a nonsense mutation that lies in the amino-terminal side of the homeodomain, resulting in an undetectable truncated mutant protein. The Hmx1 dmbo allele is thus considered a functionally null mutation (Munroe et al., 2009) (figure 1.31).

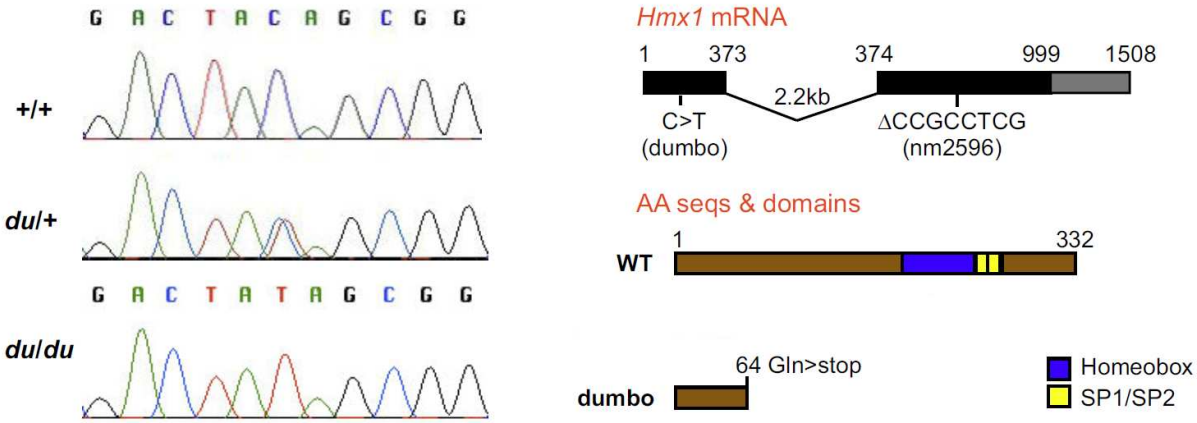

Figure 1.31: Details of the dmbo mutation. (Adapted from Munroe et al., 2009).

Dumbo mice exhibited enlarged ear pinnae with apparent ventrolateral shift (figure 1.32). Skull malformations were mild, with only hyperplasia of the gonial bone and irregularities along the caudal border of the squamous temporal bone. Beside these mild malformations, no vestibular or hearing defects were observed. Moderate degrees of microphthalmia were reported, 9% reduction of the eye size at birth, with low grade of keratoconjunctivitis sicca. No retinal degeneration was detected, whether in young or adult mice (Munroe et al., 2009). Homozygous dumbo mice were reported to be lighter than their heterozygous littermates between P3 and P9. Partial perilethality of the *dmbo* mutation is controversial between the two studies performed on this model (Munroe et al., 2009; Quina et al., 2012a).

Concerning the development of sensory nervous system, no abnormalities were observed in the trigeminal system and dorsal root ganglion. But marked defect were observed at the level of the geniculate ganglion during embryogenesis; its size was decreased and projecting fibers were disrupted leading to complete atrophy of the ganglion (Quina et al., 2012a).

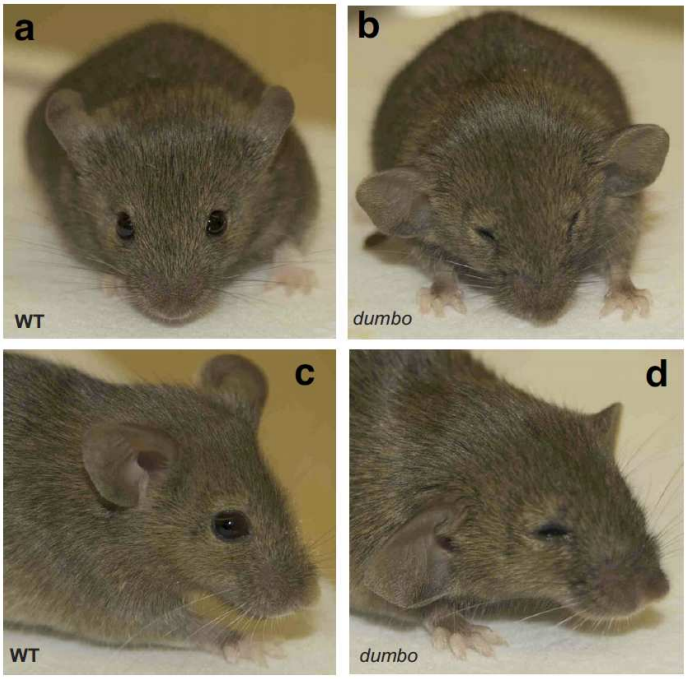

Figure 1.32: Heterozygote and homozygote dumbo mice. (Munroe et al., 2009).

1.10.2. Other models

Mouse misplaced ears (mpe) mutant arose spontaneously (Munroe et al., 2009) and generally displays the same phenotype as the dumbo mouse model. The mutation consists of a deletion of eight nucleotides appending 171 unrelated amino acids to the HMX1 protein after the 226th amino acids.

Transgenic model of zebrafish does not exist; a morpholino-based knockdown was done and shown delayed development of the eye and microphthalmia (Schorderet et al., 2009; Boisset et al., 2012).

Dumbo rat presents a different type of mutation, as it consists of a deletion of a conserved regulatory element of *Hmx1* gene, required for expression in the cranial-crest derived craniofacial mesenchyme. This leads to a phenotype resembling the dumbo mouse, with microphthalmia and ear displacement. (Kuramoto et al., 2010; Quina et al., 2012b).

Recently, genetic analysis revealed that the origin of crop ear from Ireland cattle was due to homozygous mutation in a conserved non-coding element of *HMX1*, reinforcing its regulatory role in ear development (Turner & Cox, 2014; Koch et al., 2013).

1.11. EphA6 / Sema3f / Ptpro

In order to introduce the result chapter of my thesis, I will briefly present 3 genes involved in our research of *HMX1* function and pathway.

A recent study has shown that HMX1 dimer repressed *EPHA6* promoter *in vitro* (Marcelli et al., 2014). As described in section 1.6, ephrins are crucial guidance cues that regulate topography of RGC principally via repulsive interaction. *EphA6* harbours a particular pattern of expression within the retina and visual output during retinotopic mapping. And also because, as discussed in section 1.7, ephrin are involved in CNC patterning and craniofacial morphogenesis.

Ptpro is a negative regulator of Ephrin receptors (Shintani et al., 2006), and is involved in axonal guidance and cerebellar formation in chicken and zebrafish (Stepanek et al., 2001; Liao et al., 2013).

Finally, *Sema3f* is, as described in section 1.7.1, involved in CNC patterning. Knockout mouse model have shown that *Sema3f* is a guidance cue for oligodendroglia and retinocollicular map formation (Spassky et al., 2002; Claudepierre et al., 2008).

Therefore I have mainly focused on ephrin and semaphorin signalling pathway for the dumbo mice analysis.

2. **Result / Publications**

Identification of HMX1 target genes: A predictive promoter model approach

Boulling A, Wicht L, Schorderet DF

Molecular vision

2013

19:1779-1794

- Experiments shown in figure 6 have been made by me.
- Experiments shown in figures 1 to 5 and 7, have been made by A. Boulling.
- The paper has been written by A. Boulling, myself and D. Schorderet.

Identification of *HMX1* target genes: a predictive promoter model approach

Running title: HMX1 targets identification

Arnaud Boulling[1], Linda Wicht[1,2] and Daniel F. Schorderet[1,2,3*]

Affiliations

[1]Institute for Research in Ophthalmology, Sion, Switzerland;

[2]School of Life Sciences, Federal Institute of Technology (EPFL), Lausanne, Switzerland;

[3]Department of Ophthalmology, University of Lausanne, Lausanne, Switzerland

* Address correspondence to Daniel F. Schorderet at daniel.schorderet@irovision.ch

Key words: *Hmx1*, eye development, oculoauricular syndrome, *cis*-regulatory module, homotypic cluster, promoter model

Abstract

A homozygous mutation in *HMX1* is responsible for a new oculoauricular defect leading to eye and auricular developmental abnormalities as well as early retinal degeneration (MIM 612109). *HMX1* is expressed in the developing eye, ear and in some other parts of the nervous system. It recognizes the CAAGTG canonical binding sequence. However, the *HMX1* pathway remains poorly understood. To identify *HMX1* target genes, we developed a predictive promoter model (PPM) approach using a comparative transcriptomic analysis in the retina at P15 between a mouse model lacking functional *Hmx1* (*dmbo* mouse) and its respective wild type. This PPM was based on the hypothesis that HMX1 binding sites (HMX1-BSs) clusters should be more represented in promoters of *HMX1* target genes. The most differentially expressed genes in the microarray experiment that contained HMX1-BSs clusters were used to generate the PPM, which was then statistically validated. Finally, we developed two genome-wide target prediction methods: one that focused on the conservation of PPM features in both human and mouse and the other that was based on the co-occurrence of HMX1-BS pairs fitting the PPM, in human or in mouse, independently. The PPM construction revealed that *Sgcg*, *Tshz2* and *Slc6a9* were *Hmx1* targets in the mouse retina at P15. Moreover, the genome-wide target prediction revealed that mouse genes belonging to the retinal axon guidance pathway were targeted by *Hmx1*, which fits well with our current knowledge of the role of this gene. This hypothesis was then validated by Luciferase assay.

Introduction

The HMX (Homeobox) family of transcription factors is characterized by the presence of a 60-amino acid homeobox domain. Currently, this family contains 4 members: *HMX1*, *HMX2*, *HMX3* (also known as *Nkx5-3*, *Nkx5-2* and *Nkx5-1*, respectively) and *SOHo1* [1]. Expression of *HMX1*, *HMX2* and *HMX3* is highest in the sensory organs, *i. e.* eye and inner ear, and in the peripheral and central nervous systems [2,3]. During mouse development, *Hmx1* is expressed in the trigeminal ganglion and in the second branchial arches early as E9.5, and in the dorsal root ganglia at E10.5. Later on, it is expressed in the lens, in the neural epithelium of the eye, in the sympathic and vagal nerve ganglia and in the mesenchyme near the developing ear [4]. More recently, the discovery of an *HMX1* loss-of-function mutation responsible for a new oculoauricular syndrome (MIM 612109) in a Swiss consanguineous family has prompted us to evaluate the role of this transcription factor [5].

In 2009, the description of two mutant mice called “dmbo” and “misplaced ears” exhibiting microphthalmia, besides ear and cranial malformations, was reported. Mapping and sequencing analyses of these mice revealed a nonsense mutation in the first exon of *Hmx1* in *dmbo* and a frameshift mutation in exon 2 of “misplaced ears” mice [6]. The absence of *Hmx1* protein in *dmbo* was further confirmed in a study showing that *Hmx1* was required for the normal development of somatosensory neurons in the geniculate ganglion [7]. Moreover, a *dmbo* rat strain with a similar phenotype and a deletion in an ancient distal putative enhancer of *Hmx1* was described very recently [8]. All these rodent mutants underline the prominent role of *Hmx1* in eye development and represent good models. Despite these recent advances, the role of *Hmx1* in transcriptional regulation remains widely unknown. A major challenge in deciphering the *Hmx1* pathway involved in eye development is the identification of target genes. However, this represents a difficult task as no HMX1 chromatin immunoprecipitation-grade antibody seems to exist in the mouse. Therefore, we decided to construct a predictive promoter model (PPM). This approach is based on the analysis of differentially co-expressed genes between two different biological states and represents a powerful tool as was recently shown [9]. In our case, we used a comparative transcriptomic analysis between retinas at post-natal day 15 (P15) of wild-type (WT) and *dmbo* mice. Basically, a promoter model is defined as a framework of two or more transcription factor binding sites (TFBSs) with a defined

distance range and strand orientation. In a given promoter, a functional pattern involving multiple TFBSs is called *cis*-regulatory module (CRM). CRMs represent the next level of organization after individual TFBSs and are often involved in tissue specific expression (reviewed in [10] and [11]). The promoter model is called predictive when it is based on a functional hypothesis instead of the analysis of experimentally validated TFBSs. In theory, the promoter model represents a specific and flexible structures shared by the promoter of genes belonging to the same pathways.

Despite the lack of knowledge about *Hmx1*, some critical information was sufficient to identify specific features about its target. In fact, Amendt *et al*. showed that HMX1 binds to the canonical CAAGTG sequence and acts as a transcriptional antagonist of Nkx2-5, a well studied transcription factor that recognizes a consensus sequence TNAAGTG overlapping HMX1-BSs [12]. The mouse and rat *ANF* proximal promoters include two validated Nkx2-5-BSs involved in transcriptional activation. Additional sites are located in distal enhancer regions upstream of the transcription start site (TSS) [13-15]. Similar Nkx2-5-BSs clusters have also been observed in the *H15 mid* locus of the Drosophila and the functionality of one of them has been demonstrated in cardioblasts [16]. This type of CRM involving multiple similar TFBSs is called homotypic CRMs, or homotypic clusters of TFBSs, and is widely represented in proximal promoters and enhancers of mammals and invertebrates [17]. This observation is particularly true for TFBSs of several TFs, including *Nkx2-5*.

To identify targets of *HMX1*, we developed a PPM based on HMX1-BSs clusters, by analogy to *Nkx2-5* and succeeded in constructing and validating a PPM based on the presence of multiple HMX1-BSs. We report the first *Hmx1* targets in the mouse retina at P15. Moreover, applying our PPM to mouse and human genomes allowed us to identify additional potential target genes that are involved in the embryonic eye development.

Materials and Methods

Animals handling and tissue isolation

These studies adhered to the Association for Research in Vision and Ophthalmology (ARVO) statement for the use of animals in ophthalmic and vision research and were

approved by the Veterinary Service of the State of Valais (Switzerland). WT C57BL/6J mice were obtained from Janvier (Janvier, Le Genest St Isle, France) and *dmbo* mice from Jackson Laboratory (Jackson Laboratory, Bar Harbor, ME). *Dmbo* mice were backcrossed with C57BL/6JWT mice for 3 additional generations to obtain a homogeneous genetic background and to remove the *Rd1* mutation they unexpectedly carried. All mice were genotyped by polymerase chain reaction analysis of DNA tails. Animals were maintained in a 12-hours light/12-hours dark cycle with free access to food and water. Mice were killed by cervical dislocation at P15 or P60 and their eyes were enucleated. Retinas were isolated under a microscope to remove extra retinal tissue and snap-frozen at -80°C.

RNA extraction and dosage

Total RNA was individually isolated from each whole retina and purified using the RNeasy minikit as described by the manufacturer. RNA quantities were assessed by NanoDrop®ND-1000 spectrophotometer. Four and three different animals for each condition were used for microarray and RT-PCR respectively.

Microarray procedure

RNA quality was assessed using RNA 6000 NanoChips with the Agilent 2100 Bioanalyzer (Agilent, Palo Alto, CA). For each sample, 100ng of total RNA were amplified using the WT sense strand Target Labelling kit (Affymetrix, Santa Clara, CA); 5.5µg of the resulting sense cDNA was fragmented by UDG (uracil DNA glycosylase) and APE 1 (apurinic/apyrimidic endonuclease 1) and biotin-labelled with TdT (terminal deoxynucleotidyltransferase) using the GeneChip® WT Terminal labelling kit (Affymetrix). Affymetrix Mouse Gene 1.0 ST arrays were hybridized with 2.7µg of biotinylated target for 17 hours at 45°C washed and stained according to the protocol described in Affymetrix GeneChip® Expression Analysis Manual (Fluidics protocol FS450_0007). The arrays were scanned using the GeneChip® Scanner 3000 7G (Affymetrix) and raw data were extracted from the scanned images and analyzed with the Affymetrix Power Tools software package. All statistical analyses were performed using the free high-level interpreted statistical language R and various Bioconductor packages (http://www.Bioconductor.org). Hybridization quality was assessed using the Expression

Console software (Affymetrix). Normalized expression signals were calculated from Affymetrix CEL files using RMA normalization method. Differential hybridized features were identified using Bioconductor package "limma" that implements linear models for microarray data [18]. The *P*-values were adjusted for multiple testing with Benjamini and Hochberg's method to control for false discovery rate (FDR) [19]. Probe sets showing at least 1.2-fold change and a FDR<0.1 were considered significant. Gene expression data have been deposited in GEO (GSE47002).

Functional annotation of microarray data

Differentially expressed genes (FDR<0.1) were annotated in accordance with the Gene Ontology (GO) classification system. GO terms were classified into categories related to molecular function, cell component and biological process in the aim of assessing the statistical enrichment of differentially expressed genes in these categories in comparison with the full mouse genome. Annotation and statistical calculation were realized using the DAVID algorithm (http://david.abcc.ncifcrf.gov/home.jsp) [20,21]. In addition, the MetaCore software from GeneGo Inc. was used to bring to highlight most relevant GeneGO Process Networks. Each process represents a pre-set network of protein interactions characteristic for the process. For both DAVID and MetaCore enrichment analyses, only results with a *P*-Value<0.1 were taken into consideration. MetaCore and DAVID use a hypergeometric model to determine the significance of enrichment.

PPM construction and validation

All sequences were collected *via* the UCSC Main Table Browser of the online Galaxy Platform (https://main.g2.bx.psu.edu/). We used the July 2007 (NCBI37/mm9) and Feb 2009 (GRCh37/hg19) genome assemblies' versions and genes absent in the refGene table were retrieved in Genbank and checked manually. All gene accession numbers related to the genes cited in the article are summarized in Table S1. [-250;+250] region selection and motif combinations analyses in the (+) and (-)-training sets were obtained from Galaxy. The (-)- training set was constituted by random selection of 2000 RefSeq gene promoter sequences. Finally, statistical validation of the model was performed with the Fisher's exact test. PPM specificity and sensitivity were calculated with MedCalc (http://www.medcalc.org/). Cell-specific expression levels of *Hmx1*, *Sgcg*, *Tshz2* and

Slc6a9 were retrieved in the gene expression profile database (http://www.fmi.ch/roska.data/index.php) [22].

PPM-based genome-wide target predictions

All the [-250,+200] sequences fitting the PPM were selected from human and mouse RefSeq databases. PPM-based selection focused on the conserved HMX1-BS pairs was realized by crossing the human and mouse previously obtained selections. Sequences containing more than two HMX1-BSs were analyzed to achieve the target genes selection based on the cooccurrence of HMX1-BS pairs. Axon guidance pathway enrichment analysis was based on the KEGG database (http://www.genome.jp/kegg/kegg2.html) and performed for the mouse predicted targets selection obtained with the PPM co-occurrence based method. The statistical enrichment was assessed against the full mouse genome by taking in consideration the 25,504 unique genes of the ccds table, by means of the Chi-square with Yates' correction test.

Quantitative Reverse Transcription PCR (qPCR)

Reverse transcription was performed with 500 ng RNA, 25 ng/µl OligodT, 1 mM each dNTP, 10 mM dithiothreitol, 2 U/µl RNAseBlock and 1 µl AffinityScript (Agilent) in a final volume of 20 µl at 42°C for 1 hour. Reaction was then kept at 70°C for 15 min and the obtained cDNA was 1:10 diluted. Quantitative PCR was performed in a 25-µL mixture containing 12.5 µL of FastStart Universal SYBR Green Master (ROX) (Roche, Basel, Switzerland), 10 µL of diluted cDNA and 0.3 µM of primer pairs (Table S2). The PCR program had an initial denaturation at 95°C for 10 min, followed by 40 cycles of denaturation at 95°C for 30 s, annealing at 55°C for 1 min, and extension at 72°C for 1 min. All PCRs were realized in triplicate. Transcript levels were normalized using the *Gapdh* housekeeping gene and analyzed by means of the Student’s t-test. All qPCR efficiencies were calculated from the slope of a standard dilution curve to allow relative comparison of gene mRNA levels.

Immunohistochemistry

Enucleated eyes were fixed for 45 min at 4°C in 4% paraformaldehyde. Fixation was blocked with 30 % sucrose, eyes were then embedded in Yazzula and vertically sliced at 10 μm thickness in a cryostat. Sections were washed three times with phosphate-buffered saline (PBS), treated with blocking buffer (2 % native goat serum containing 0.2% Triton X-100) at room temperature for 10 min, and left overnight at 4°C with the anti-SGCG primary antibody (Proteintech) diluted 1:100. Controls were prepared by omitting the primary antibody during the incubation. The following morning, sections were rinsed three times with PBS, blocked 10 min and incubated at room temperature for 1 hour with Alexa Fluor® 594 goat anti-rabbit IgG (Invitrogen, Zug, Switzerland) secondary antibody diluted 1:1500. After three additional washing, sections were stained with DAPI diluted 1:1500 for 10 min at room temperature, washed three times again and mounted with Citifluor AF1 (Citifluor Ltd, Leicester, United Kingdom). Stained slides were imaged on a Zeiss microscope and image analysis was performed using the ZEN lite 2011 software (Zeiss, Zürich, Switzerland).

Construction of reporter and expression plasmids

PCR primer pairs used for molecular cloning were designed to generate an amplicon spanning the TSS of *Sgcg*, *Sema3f* and *Ptpro* and to carry all the HMX1-BS identified in the proximal promoter region. All promoter regions were amplified with the *PfuUltra* High-Fidelity DNA Polymerase (Agilent) according to the manufacturer's instructions. Mouse *Sgcg*, *Sema3f* and *Ptpro* promoter regions were amplified using following primer pairs and annealing temperatures (Ta): 5'-gcgcacgcgtcaaagacacgtcagcctcag-3' and 5'-gcgcctcgaggaaacgctgtacctatctgatttaca-3' (*Sgcg*, Ta = 61°C), 5'-gcgcacgcgtgcaagagtgtatggggaagg-3' and 5'- gcgcctcgagcaggcctctcagcaggtg-3' (*Sema3f*, Ta = 63°C), 5'-gcgcacgcgtcatggaaatcgttgcttgtg-3' and 5'-gcgcctcgagcggcgttgtttaatggctaa-3' (*Ptpro*, Ta = 60°C). Amplified DNA fragments were inserted into the pGL3-basic vector by means of XhoI and MluI restriction enzymes to produce pGL3-*Sgcg*, pGL3-*Sema3f* and pGL3-*Ptpro* reporter constructs. Before the cloning step, the CAAGTG site located just upstream of the multiple cloning site in the pGL3-basic vector was turned into TAATCA by site-directed mutagenesis. The *Hmx1* mouse cDNA was amplified with *PfuUltra* High-Fidelity DNA Polymerase using 5'-atgccggatgagctgaccg-3' and 5'-

tcacactagccccggcatc-3’ primers (Ta = 60°C), then inserted into the pcDNA3.1 vector (pcDNA3.1-Hmx1) by means of the pcDNA3.1/V5-His TOPO TA Expression Kit (Invitrogen).

Cell culture and transfection

Mouse neuroblastoma cells (aka Neuro-2a or N2a) were grown in DMEM supplemented with 10% Fetal Bovin Serum and 100 µg/ml Normocin (Invivogen, Toulouse, France). Twenty-four hours prior transfection, 200 000 cells/well were seeded in 12-wells plates. For one transfection, 900 ng of one pGL3 reporter construct, 900 ng of pcDNA3.1-Hmx1 or empty pcDNA3.1 and 300 ng of pCMV-Beta-Gal control plasmid were mixed together with 4 µl jetPEI (Polyplus, Illkirch, France) and dropped onto the cells.

Luciferase reporter gene assay

Forty-eight hours after transfection, cells were rinsed with PBS and lysed with 100 µl potassium phosphate buffer (100mM K2HPO4 pH7.8, 0.2% triton X-100). After centrifugation, 5 µl supernatant from each sample were added to 20 µl Firefly luciferase reagent. In parallel, 10 µl supernatant from each sample were added to 100 µl β-galactosidase reagent. The relative luciferase activity was determined by dividing the luminescence of Firefly luciferase activity by that of the co-transfected β-galactosidase activity. The experiment was performed 3 times for each reporter construct and transfections were realized in triplicate for each experiment. The significance between the luciferase activity of each reporter construct co-transfected with pcDNA3.1-Hmx1 and with pcDNA3.1 was then assessed for significance by means of the Student’s t-test.

Statistical analysis

Statistical tests used in this study are detailed at the end of “microarray procedure”, “functional annotation of microarray data”, “PPM construction and validation”, “quantitative reverse transcription PCR” and “luciferase reporter gene assay” sections.

Results

Comparative transcriptomic analysis

The comparative transcriptomic analysis of the mouse retina between *dmbo* and WT C57BL/6J mice was realized at P15 to avoid killing pregnant *dmbo* mice and to obtain sufficient amount of tissue. The retina is still developing at this age and it is always expressing *Hmx1*. The analysis showed 146 differentially expressed genes (70 up and 76 down) with a false discovery rate (FDR)<0.1 and at least 1.2-fold change (Figure 1A, Table S3, Table S4). Thirty of these genes were highly confident and had a FDR<0.01 (14 up and 16 down). Analysis of the 146 differentially expressed genes with the MetaCore software from GeneGo Inc. showed 10 enriched GeneGO Process Networks with a *P*-Value<0.1 (Figure 1B). The first three ranked processes are the synaptogenesis (*P*-Value=0.008879), the visual perception (*P*Value= 0.009481) and the synaptic contact (*P*-Value=0.009713). In another approach, the use of the DAVID software allowed us to classify these genes into GO categories, showing that 9 of them were significantly enriched with a *P*-Value<0.1 in molecular function, 3 in cell component and 20 in biological process categories, respectively (Table S5). All of the enriched molecular function categories were related to ion and vitamin binding or transmembrane transport, and all the enriched cell component categories were related to cell projection terms as axoneme and cilium. Enriched biological process categories were more numerous and diversified and concerned, for example, organelle localization or metal ion homeostasis.

Hmx1 target promoter model construction and validation

As explained above, we hypothesized that multiple *Hmx1* sites could form CRMs and act in synergy, as observed for *Nkx2-5* [17]. In this regard, we postulated that the number of motifs could play a role in the transcriptional regulation of *Hmx1* targets. To elaborate our predictive promoter model, we used the promoter sequences of the most confident differentially expressed genes (FDR<0.01 group) and took into consideration the number of CAAGTG motif present. We used a screening window ranging in size from -250 to +200 nucleotides (nt) around the TSS. This window was based on the size of the proximal promoter and the approximate median size of the eukaryote 5'UTR, two regions known to

be enriched in TFBS [23,24]. The CAAGTG motifs located in the [-250,+200] interval were counted. Three of the 30 genes contained 2 motifs, 3 contained 1 motif, and the last 24 did not contain any motif. The 3 genes containing 2 motifs, considered as theoretical *Hmx1* targets, were used to generate a framework (Figure 2A-B) that should correspond to a feature specific for *Hmx1* target promoters. The orientation of the motifs was disregarded but we took into consideration the space between the two motifs and kept a distance range spanning from 90 to 190 nt. Unexpectedly, only one HMX1-BS in *Tshz2* promoter was strictly conserved between human and mouse.

It is important to keep in mind that this theoretical promoter model is predictive and needs to be statistically validated, as it is based on arbitrary criteria. Therefore, we calculated the enrichment of this particular feature between the FDR<0.01 group (used as the positive (+)- training set) and a control group of random promoters (used as the negative (-)-training set). We observed a 22.2-fold significant enrichment (*P*-Value=0.0006) of the PPM specific feature in the (+)-training set compared to the (-)-training set within the [-250,+200] region (Figure 2C). This enrichment was also observed in the FDR<0.1 group but to a lesser extent (*P*-Value<0.0091). There was no significant enrichment when the genes containing at least 1 motif were considered. From these data, we concluded that the high enrichment of this particular feature in the (+)-training set validated our promoter model and supported the idea that *Sgcg, Tshz2* and *Slc6a9* were direct *Hmx1* targets.

To complete our approach, we also tried to build a PPM with lower specificity and higher sensitivity. For this, we replaced the canonical sequence CAAGTG by the minimal core motif CAAG also able to bind HMX1 but with a lower affinity [12]. We generated a low specific PPM (LS-PPM) and a very low specific PPM (VLS-PPM) fitting the same distance and orientation criterias than the initial PPM, but carrying respectively one or two CAAG in place of the canonical HMX1-BS (Table 1). Both of them retrieved a better rate of positive genes but showed very low specificity (1.37 and 1.01-fold enrichment for low and very low PPM respectively). These two PPM with lower specificity were not reused for next analyses.

Characterization of Sgcg, Tshz2 and Slc6a9 expression

To minimize the possibility that *Sgcg*, *Tshz2* and *Slc6a9* were false positive targets of *Hmx1*, we confirmed their level of deregulation between eyes from *dmbo* and WT mice, and checked for colocalization with *Hmx1*. The retina is made of many different cell types with specific expression profiles. We therefore assessed the expression of *Hmx1*, *Sgcg*, *Tshz2* and *Slc6a9* by qPCR (Figure 3A) and looked for their precise cell subtype expression in the mouse retina, according to an online gene expression profile database [22] (Figure 3B). Transcripts quantification confirmed that *Sgcg* and *Tshz2* were over-expressed in *dmbo* at P15, whereas *Slc6a9* was under-expressed. This deregulation tended to disappear at P60 for *Tshz2* and *Slc6a9*, but remained extremely high for *Sgcg*. As expected, the inspection of a retina specific database revealed a strong overlap of *Hmx1*, *Slc6a9* and *Tshz2* expression in the glycinergic amacrine cells. *Sgcg* expression was not detected in the microarray database probably due to the very weak level of mRNA, as shown by qPCR. However, the γ-sarcoglycan protein encoded by *Sgcg* was detected by immunohistochemistry in the ganglion cell (GCL), the inner plexiform (IPL), the inner nuclear (INL) and the outer plexiform layers (OPL) (Figure 3C), as already shown by Fort *et al*. [25]. No difference in mRNA or protein expression of γ-sarcoglycan was observed between WT and *dmbo* samples (data not shown). The immunohistochemistry staining was higher in some cells of the INL exhibiting a disposition pattern characteristic of the amacrine cells, at the delimiting border between the INL and the IPL. This result was in accordance with colocalization of *Sgcg* and *Hmx1* expression.

PPM-based genome-wide screening for HMX1 putative targets

Our model was based on a comparative transcriptomic analysis realized in mouse retina at P15. However, *Hmx1* is highly expressed in the mouse eye as early as E10.5 suggesting an important role in development. Assuming that the PPM we developed was specific for *HMX1* targets (with 0.45% vs. 10% representation in the (-) and (+)-training sets, respectively) we decided to screen the full human and mouse genomes. Such a global approach should provide an exhaustive view of all putative *HMX1* targets, including those expressed during embryonic eye development. As a first step, we used the PPM to screen both mouse and human RefSeq databases *via* the Galaxy platform. These two databases contained a total of 30,490 and 43,695 sequences respectively, which corresponded to all

transcripts of reference, including all isoforms and alternative promoters. We considered for each gene all potential alternative promoters whereas all redundant promoter sequences due to alternative splicing were discarded. The gene accession numbers of all isoforms corresponding to our predicted genes are listed in Table S1.

Screening of the full mouse RefSeq database using the PPM within the [-250,+200] region retrieved 157 sequences corresponding to unique protein-coding genes (Figure 4A, Table S1). Similarly, the screening of the human genome retrieved 100 sequences corresponding to unique protein-coding genes. Such an approach allowed us to generate an exhaustive list of all possible *HMX1* targets, but the high number of positive hits resulted in some difficulties with their interpretation. In fact, some of these genes were probably true *HMX1* targets, but several could also be false-positives, representing targets related to TFs with the same binding sites (for example *HMX3* or *NKX2-5*). To improve the selectivity of the analysis and to focus on the most interesting candidate genes, we decided to add additional filters.

Initially, we developed a PPM approach based on the conservation of the HMX1-BS pairs between human and mouse. In fact, comparative genomics is one of the usual methods that aimed at discriminating functional TFBSs from irrelevant ones (reviewed in [11]). To keep a relative flexibility, our method was only based on the presence of an HMX1-BS pair and did not implicate a strict conservation of the positions or orientations of the HMX1-BSs between both species. As already demonstrated, traditional approaches, like phylogenetic footprinting, give good predictions but are also likely to miss important conserved regulatory elements [26]. Crossing the two datasets showed that only 10 genes contained the PPM features in both species (Figure 4B). These genes were classified according to the localization of their expression.

In a second phase, we used another PPM approach based on the co-occurrence of HMX1-BS pairs, driven by the basic idea that increasing the number of HMX1-BS in the promoter region should increase their interaction with HMX1. Such a phenomenon should result in a more efficient transcription regulation. To assess this hypothesis, we looked at the HMX1- BSs occurrence in all the mouse and human promoter sequences fitting the PPM. We observed that the promoter regions contained a maximum of 4 HMX1-BSs within the [-250,+200] window. Always in accordance with the PPM criteria, we determined that 3 sites might form 3 different homotypic HMX1-BSs pairs (P1-2,P1-

3,P2-3), even if it is unlikely that all 3pairscould be considered at the same time due to the minimum distance range constraint of 90bp (Figure 5A).

Similarly, 4 sites might lead to a maximum of 5 combinations (P1-2, P1-3,P2-3, P2-4, P3-4). It is noticeable that a single given site can be involved in multiple combinations. The screening of the mouse genome with this method retrieved 9 genes with 3 sites allowing 2 different pair combinations, and 1 gene (*Epha6*) with 4 sites allowing 3 different pair combinations (Figure 5B). Interestingly, 3 of these 10 genes (*Epha6*, *Ptpro* and *Sema3f*) are expressed in the retina and are involved in axonal growth repulsion (see Figure 6and discussion). It represents a 56.6- fold enrichment (*P*-Value<0.0001) in the mouse axon guidance KEGG pathway (mmu04360). *Ptpro* was incorporated within the pathway although it was not initially reported in the KEGG database, in spite of its role as a guidance cue in retinal neurons [27,28]. Moreover, a deeper examination of *Epha6* showed an additional HMX1-BS at position [+245,+250] and an additional HMX1-BSs cluster fitting the PPM within the first intron (Figure 5C). Among the mouse HMX1-BSs, two were conserved in the human *EPHA6* proximal promoter. One was unique to the human gene. With a similar approach, we identified 8 genes with 3 sites allowing 2 interactions in the human genome (Figure 5B).

Experimental validation of several predicted targets by luciferase assay

We experimentally validated some of these results by luciferase assays performed in N2A cells. We first assessed the reliability of our system by co-transfecting the pGL3-*Sgcg* positive control reporter construct with the pcDNA3.1-*Hmx1* expression construct. *Hmx1* cotransfection decreased pGL3-*Sgcg* luciferase expression by 63%, which was expected given the *dmbo* qPCR *Sgcg* results (Figure 6). Co-transfection of Hmx1 repressed pGL3-*Ptpro* and pGL3-*Sema3f* luciferase expression by 50 and 66%, respectively.

Discussion

The major goal of this study was to identify target genes of *Hmx1* in the mouse retina.The integration of *in vitro* data from Ament *et al*. and our *in vivo* microarray data allowed us to obtain a clear picture of the typical basic structure of an *HMX1* target promoter [12]. In

addition, experimental controls concerning transcript amounts, expression co-localization and luciferase assay strongly supported these findings.

The microarray data yielded a first set of information about the molecular phenotype of the *dmbo* retina. The MetaCore analysis underlined that a lack of HMX1 protein altered synaptogenesis and visual perception, two biological processes occurring at P15 [29]. At this time, we cannot say whether these observations were directly linked to *Hmx1* loss of activity or if they derived from anterior impairments occurring during eye development.

Then, we used the microarray data to construct a high specific PPM based on HMX1-BS clusters. It revealed that *Sgcg*, *Tshz2* and *Slc6a9* were *Hmx1* targets in the mouse retina at P15. Using degenerated binding motifs for PPM construction, such as the minimal CAAG core motif, led to higher sensitivity but also to very low specificity with no significant enrichment. Such a low specific PPM cannot be used for prediction because it would probably yield an extremelyhigh number of false positives. However, we thought that *Hmx1* probably binds degenerate motifs *in vivo* but no position weight matrix is currently available to perform a better PPM for *Hmx1*. Moreover, it's important to keep in mind that the sensitivity of the original PPM is very likely under-estimated because some of the differential expressions observed for gene belonging to the (+)-training set probably result from secondary events and are not directly linked to Hmx1.

The expression of *Hmx1*, *Tshz2*, *Slc6a9* and probably *Sgcg* were observed in the glycinergic amacrine cells, a cell type which establishes synaptic contacts with rod-driven bipolar cells and play an important role in neurotransmission. *Tshz2* (Tshirt zinc finger family member 2) is involved in axonal growth network in the mouse retina and is also expressed in the zebrafish neural retina at 48 hours post fertilization [30,31]. *Slc6a9* is specifically expressed in the glycinergic amacrine cells where it plays an important role in glycine uptake, and also controls N-methyl-D-aspartic acid receptor coagonist occupancy in the mouse retina [32]. The role of both these genes in the retina needs to be further investigated. However, their expression seemed to be totally or partially compensated at P60, suggesting that *Hmx1* does not solely regulate them. The positive deregulation of *Sgcg* in qPCR was very impressive (about 1000-fold) but it didn't correlate with a higher amount of proteins in *dmbo* retina. It is likely that *Sgcg* was strongly regulated at the level of translation which would explain why this dramatic increase of transcripts had no effect on the protein level, as shown for other genes related to cell adhesion [33]. Besides, the

overexpressed γ-sarcoglycan could form aggregates which could be degraded in the endoplasmic reticulum, as supported by the proteolysis process enrichment in MetaCore analysis (Figure 1B). Its role in the *dmbo* retinal phenotype remains unclear. Another finding resulting from the microarray analysis was that *Hmx1* could act *in vivo* as a transcriptional repressor or activator. The first *in vitro* study done by Ament *et al*. Showed only a repressor effect, but their work was done in HeLa cells indicating that cellular context may play a role in mediating *HMX1* activity [12].

The second part of our study consisted to use our PPM to screen the genome and discover other putative targets of *HMX1*. More precisely, we focused our attention on the identification of *HMX1* targets that could be involved in eye development. This would help in understanding the bases of the human oculoauricular syndrome caused by *Hmx1* mutation [5]. The first method consisted in using the PPM to screen the RefSeq database of mouse and human. It retrieved a large but expected number of genes despite the short screening window that was used. Many of these genes represented interesting candidates (See Table S1 for a complete list). In order to be more selective, we crossed human and mouse selections to keep only genes fitting the PPM in both species. Among the 10 genes that we retrieved, four have been reported to be expressed in the eye, during development (*EPHA6*, *MARCKS* and *UHRF1*), or during adult life (*SEPT4*) [34-37]. In addition, *SH3KBP1* was predicted to be a target of *Hmx1* and is highly expressed in Schwann cells, where it is regulated by *SOX10* [38]. Interestingly, a recent study showed that a balance between *SOX10* and *HMX1* regulates neuronal versusSchwann cell precursor and melanocyte fates [39]. Our second method based on the cooccurrence of HMX1-BS pairs retrieved 10 genes in the mouse genome and 8 in the human genome. *EPHA6*, *UHRF1* and *SH3KBP1* were identified by both methods, increasing the confidence that these 3 targets were true targets. In the mouse, the *Epha6* promoter showed the highest number of HMX1-BS pairs combinations with 4 sites located within [-250,+200]. A wider examination of the region surrounding its TSS showed additional HMX1-BS clusters fitting the PPM in the proximal promoter and in the first intron. With *Ptpro* and *Sema3f*, *Epha6* belongs to the retinal axon guidance pathway and plays an important role in retinotopic mapping [34,40,27,28,41]. In addition, these three predicted targets occupy key places as inputs of the axon repulsion signaling pathway, supporting a specific and effective action of *Hmx1* in this process (see Figure 7 for more details). Finally, the strong and highly significant enrichment of 20 this pathway in the mouse selection obtained with

HMX1-BS pairs co-occurrence based method underlined the likely role of *Hmx1* in the establishment of retinal topography. The luciferase assay results gave some experimental evidences to validate this hypothesis. As a positive control, we first showed that *Hmx1* can act as a repressor and decrease the activity of the *Sgcg* promoter in the N2A cells. This result was expected based on the dramatic increase of *Sgcg* expression in *dmbo* mice. Then, we showed that *Hmx1* represses the activity of *Ptpro* and *Sema3f* promoters. In the future, we will specifically focus our efforts on the functional study of *Epha6*, all the more so as the Ephrin pathway was already considered by Schorderet *et al.* to be a putative target of *Hmx1* [5]. We also noted that the human selection contained a new interesting gene expressed in the eye, *FOXP1* [42], in addition to *UHRF1* and *EPHA6*. Finally, some of the remaining predicted targets unrelated to the eye could be potential *HMX1*, *NKX2-5* or *HMX3* targets in other tissues and will need further investigation.

Several recurrent questions about TFBSs identification arose from our study. The first concerns the conservation of CRMs between human and mouse. In fact, we observed a poor conservation of our PPM between both species, whereas numerous studies showed that evolutionary conserved regions overlap functional regulatory elements (reviewed in [11]). Actually, approaches integrating comparative genomics data succeed to identify CRMs with a high positive predictive value but overlook CRMs specific for a given species. Single-genome bioinformatic approaches are more convenient to solve this problem. In this manner, a study based on empirical potential energy of TFs revealed that CRMs occur in conserved and nonconserved regions, and about 55% of them have a poor conservation score [43]. In particular, this study underlined that the less well-conserved CRMs concern genes related to neural activity. It could be explained by the fact that the nervous system function is specific for species, by contrast with more fundamental processes as transcription for example. Prediction of neural specific TFBSs appears to be harder than others; fortunately it has been showed that homotypic CRMs are a good predictor of regulatory elements, especially for target genes related to TFs involved in neural development [17]. In a general way, homotypic CRMs are strongly associated with the region surrounding the TSS and the developmental enhancers, with no systematic phylogenetic conservation. These observations rationalize the results we obtained with a singlegenome approach and the PPM-based method focused on the co-occurrence of HMX1-BS pairs, in particular with the mouse axon guidance pathway enrichment. Finally, we think that adding a distance range constraint to the PPM gave more accurate

results than simply count the TFBSs in the screening window. Actually, optimal distances for interactions are supposed to be specific for a given TF and including this parameter in the model should give more specific results [26].

In conclusion, our strategy was successful in identifying *HMX1* targets because the PPM we constructed based on the P15 microarray data revealed, *a posteriori*, an important pathway involved in retinal development (*i.e,*. axon repulsion during retinal axon guidance) in addition to the first three targets (*i.e,.Sgcg, Tshz2 and Slc6a9*). These subsequent outcomes brought an additional proof of the robustness of our PPM approach, and open new opportunities to focus experimental investigations on this specific aspect of the *Hmx1* pathway.

Acknowledgement

We thank the Center for Integrative Genomics of the University of Lausanne. This work was supported by grants n°31003A-124990 and 31003A-143474 from the Swiss National Science Foundation. The funders had no role in study design, data collection and analysis, decision to publish, or preparation of the manuscript.

References

1. Stadler HS, Murray JC, Leysens NJ, Goodfellow PJ, Solursh M. Phylogenetic conservation and physical mapping of members of the H6 homeobox gene family. Mamm Genome. 1995; 6:383-8.

2. Wang W, Lo P, Frasch M, Lufkin T. Hmx: an evolutionary conserved homeobox gene family expressed in the developing nervous system in mice and Drosophila. Mech Dev. 2000; 99:123-37.

3. Wang W, Lufkin T. Hmx homeobox gene function in inner ear and nervous system celltype specification and development. Exp Cell Res. 2005; 306:373-9.

4. Yoshiura K, Leysens NJ, Reiter RS, Murray JC. Cloning, characterization, and mapping of the mouse homeobox gene Hmx1. Genomics. 1998; 50:61-8.

5. Schorderet DF, Nichini O, Boisset G, Polok B, Tiab L, Mayeur H, Raji B, De la Houssaye G, Abitbol MM, Munier FL. Mutation in the human homeobox gene NKX5-3 causes an oculo-auricular syndrome. Am J Hum Genet. 2008; 82:1178-84.

6. Munroe RJ, Prabhu V, Acland GM, Johnson KR, Harris BS, O'Brien TP, Welsh IC, Noden DM, Schimenti JC. Mouse H6 Homeobox 1 (Hmx1) mutations cause cranial abnormalities and reduced body mass. BMC Dev Biol. 2009; 9:27.

7. Quina LA, Tempest L, Hsu Y-WA, Cox TC, Turner EE. Hmx1 is required for the normal development of somatosensory neurons in the geniculate ganglion. Dev Biol. 2012; 365:152-63.

8. Quina LA, Kuramoto T, Luquetti DV, Cox TC, Serikawa T, Turner EE. Deletion of a conserved regulatory element required for Hmx1 expression in craniofacial mesenchyme in the dumbo rat: a newly identified cause of congenital ear malformation. Dis Model Mech. 2012; 5:812-22.

9. Shelest E, Wingender E. Construction of predictive promoter models on the example of antibacterial response of human epithelial cells. Theor Biol Med Model. 2005; 2:2.23

10. Werner T, Fessele S, Maier H, Nelson PJ. Computer modeling of promoter organization as a tool to study transcriptional coregulation. FASEB J. 2003; 17:1228-37.

11. Hardison RC, Taylor J. Genomic approaches towards finding cis-regulatory modules in animals. Nat Rev Genet. 2012; 13:469-83.

12. Amendt BA, Sutherland LB, Russo AF. Transcriptional antagonism between Hmx1 and Nkx2.5 for a shared DNA-binding site. J Biol Chem. 1999; 274:11635-42.

13. Warren SA, Terada R, Briggs LE, Cole-Jeffrey CT, Chien W-M, Seki T, Weinberg EO, Yang TP, Chin MT, Bungert J, Kasahara H. Differential role of Nkx2-5 in activation of the atrial natriuretic factor gene in the developing versus failing heart. Mol Cell Biol. 2011; 31:4633-45.

14. Kasahara H, Usheva A, Ueyama T, Aoki H, Horikoshi N, Izumo S. Characterization of homo- and heterodimerization of cardiac Csx/Nkx2.5 homeoprotein. J Biol Chem. 2001; 276:4570-80.

15. Lee Y, Shioi T, Kasahara H, Jobe SM, Wiese RJ, Markham BE, Izumo S. The cardiac tissue-restricted homeobox protein Csx/Nkx2.5 physically associates with the zinc finger protein GATA4 and cooperatively activates atrial natriuretic factor gene expression. Mol Cell Biol. 1998; 18:3120-9.

16. Ryu J-R, Najand N, Brook WJ. Tinman is a direct activator of midline in the Drosophila dorsal vessel. Dev Dyn. 2011; 240:86-95.

17. Gotea V, Visel A, Westlund JM, Nobrega MA, Pennacchio LA, Ovcharenko I. Homotypic clusters of transcription factor binding sites are a key component of human promoters and enhancers. Genome Res. 2010; 20:565-77.

18. Smyth GK. Linear models and empirical bayes methods for assessing differential expression in microarray experiments. Stat Appl Genet Mol Biol. 2004; 3:Article3.

19. Benjamini Y, Hochberg Y. Controlling the false discovery rate: a practical and powerful approach to multiple testing. J R Stat Soc. Series B Stat Methodol. 1995; 57:289-300.

20. Huang DW, Sherman BT, Lempicki RA. Systematic and integrative analysis of large gene lists using DAVID bioinformatics resources. Nat Protoc. 2009; 4:44-57.

21. Huang DW, Sherman BT, Lempicki RA. Bioinformatics enrichment tools: paths toward the comprehensive functional analysis of large gene lists. Nucleic Acids Res. 2009; 37:1-13.

22. Siegert S, Cabuy E, Scherf BG, Kohler H, Panda S, Le Y-Z, Fehling HJ, Gaidatzis D, Stadler MB, Roska B. Transcriptional code and disease map for adult retinal cell types. Nat Neurosci. 2012 Mar; 15:487-495.

23. Vinson C, Chatterjee R, Fitzgerald P. Transcription factor binding sites and other features in human and Drosophila proximal promoters. Subcell Biochem. 2011; 52:205-22.

24. Bernard V, Lecharny A, Brunaud V. Improved detection of motifs with preferential location in promoters. Genome. 2010; 53:739-52.

25. Fort P, Estrada F-J, Bordais A, Mornet D, Sahel J-A, Picaud S, Vargas HR, Coral-Vázquez RM, Rendon A. The sarcoglycan-sarcospan complex localization in mouse retina is independent from dystrophins. Neurosci Res. 2005; 53:25-33.

26. Hu Z, Hu B, Collins JF. Prediction of synergistic transcription factors by function conservation. Genome Biol. 2007; 8:R257.

27. Stepanek L, Sun QL, Wang J, Wang C, Bixby JL. CRYP-2/cPTPRO is a neurite inhibitory repulsive guidance cue for retinal neurons in vitro. J Cell Biol. 2001; 154:867-78.

28. Shintani T, Ihara M, Sakuta H, Takahashi H, Watakabe I, Noda M. Eph receptors are negatively controlled by protein tyrosine phosphatase receptor type O. Nat Neurosci. 2006; 9:761-9.

29. Tian N. Visual experience and maturation of retinal synaptic pathways. Vision Res. 2004; 44:3307-16.

30. Freeman NE, Templeton JP, Orr WE, Lu L, Williams RW, Geisert EE. Genetic networks in the mouse retina: growth associated protein 43 and phosphatase tensin homolog network. Mol Vis. 2011; 17:1355-72.

31. Santos JS, Fonseca NA, Vieira CP, Vieira J, Casares F. Phylogeny of the teashirt-related zinc finger (tshz) gene family and analysis of the developmental expression of tshz2 and tshz3b in the zebrafish. Dev Dyn. 2010; 239:1010-8.

32. Reed BT, Sullivan SJ, Tsai G, Coyle JT, Esguerra M, Miller RF. The glycine transporter GlyT1 controls N-methyl-D-aspartic acid receptor coagonist occupancy in the mouse retina. Eur J Neurosci. 2009; 30:2308-17.

33. Schwanhäusser B, Busse D, Li N, Dittmar G, Schuchhardt J, Wolf J, Chen W, Selbach M. Global quantification of mammalian gene expression control. Nature. 2011; 473:337-42.

34. Carreres MI, Escalante A, Murillo B, Chauvin G, Gaspar P, Vegar C, Herrera E. Transcription factor Foxd1 is required for the specification of the temporal retina in mammals. J Neurosci. 2011; 31:5673-81.

35. Zolessi FR, Arruti C. MARCKS in advanced stages of neural retina histogenesis. Dev Neurosci. 2004; 26:371-9.

36. Tittle RK, Sze R, Ng A, Nuckels RJ, Swartz ME, Anderson RM, Bosch J, Stainier DYR, Eberhart JK, Gross JM. Uhrf1 and Dnmt1 are required for development and maintenance of the zebrafish lens. Dev Biol. 2011; 350:50-63.

37. Pache M, Zieger B, Bläser S, Meyer P. Immunoreactivity of the septins SEPT4, SEPT5, and SEPT8 in the human eye. J Histochem Cytochem. 2005; 53:1139-47.

38. Hodonsky CJ, Kleinbrink EL, Charney KN, Prasad M, Bessling SL, Jones EA, Srinivasan R, Svaren J, McCallion AS, Antonellis A. SOX10 regulates expression of the SH3-domain kinase binding protein 1 (Sh3kbp1) locus in Schwann cells via an alternative promoter. Mol Cell Neurosci. 2012; 49:85-96.

39. Adameyko I, Lallemend F, Aquino JB, Pereira JA, Topilko P, Müller T, Fritz N, Beljajeva A, Mochii M, Liste I, Usoskin D, Suter U, Birchmeier C, Ernfors P. Schwann cell precursors from nerve innervation are a cellular origin of melanocytes in skin. Cell. 2009; 139:366-79.

40. Bevins N, Lemke G, Reber M. Genetic dissection of EphA receptor signaling dynamics during retinotopic mapping. J Neurosci. 2011; 31:10302-10.

41. Claudepierre T, Koncina E, Pfrieger FW, Bagnard D, Aunis D, Reber M. Implication of neuropilin 2/semaphorin 3F in retinocollicular map formation. Dev Dyn. 2008; 237:3394- 403.

42. Cheng L, Chong M, Fan W, Guo X, Zhang W, Yang X, Liu F, Gui Y, Lu D. Molecular cloning, characterization, and developmental expression of foxp1 in zebrafish. Dev Genes Evol. 2007; 217:699-707.

43. Yu X, Lin J, Zack DJ, Qian J. Identification of tissue-specific cis-regulatory modules based on interactions between transcription factors. BMC Bioinformatics. 2007; 8:437.

Legends and figures

Figure 1 Summary of microarray results. A) Up and down regulated genes with a foldchange>1.2 and a FDR<0.1 or <0.01. B) MetaCore GeneGO Process Networks enrichment analysis of the FDR<0.1 group of differentially expressed genes.

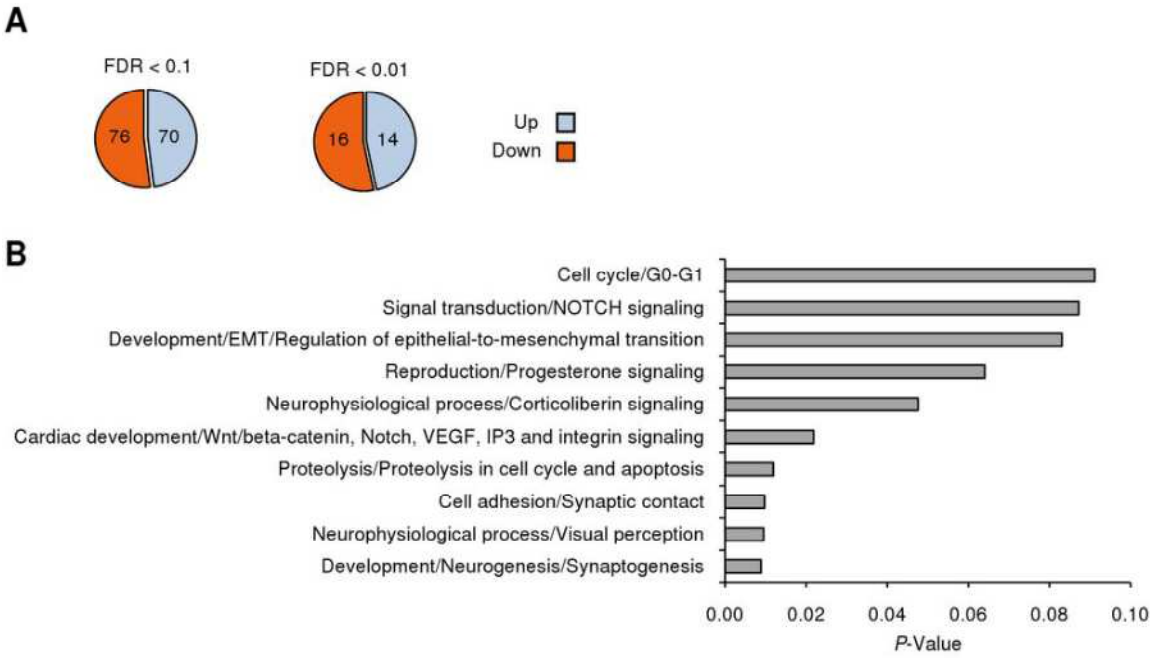

Figure 2 Elaboration and statistical validation of an Hmx1 PPM. A) Flowchart of the PPM construction. #see (B) for details. B) Details of *Sgcg*, *Tshz2* and *Slc6a9* promoter structure. Forward (CAAGTG) and reverse (CACTTG) HMX1-BSs are symbolized by black and white triangles respectively. The H letter indicates an HMX1-BS that is strictly conserved in human. C) Statistical validation of the PPM. Columns represent the percentage of promoters carrying at least 1 HMX1-BS or fitting the PPM in each group. Promoter count details are indicated for the FDR<0.1 group and the (+)-training set (FDR<0.01 group). **P*-Value<0.01, ***P*-Value<0.001.

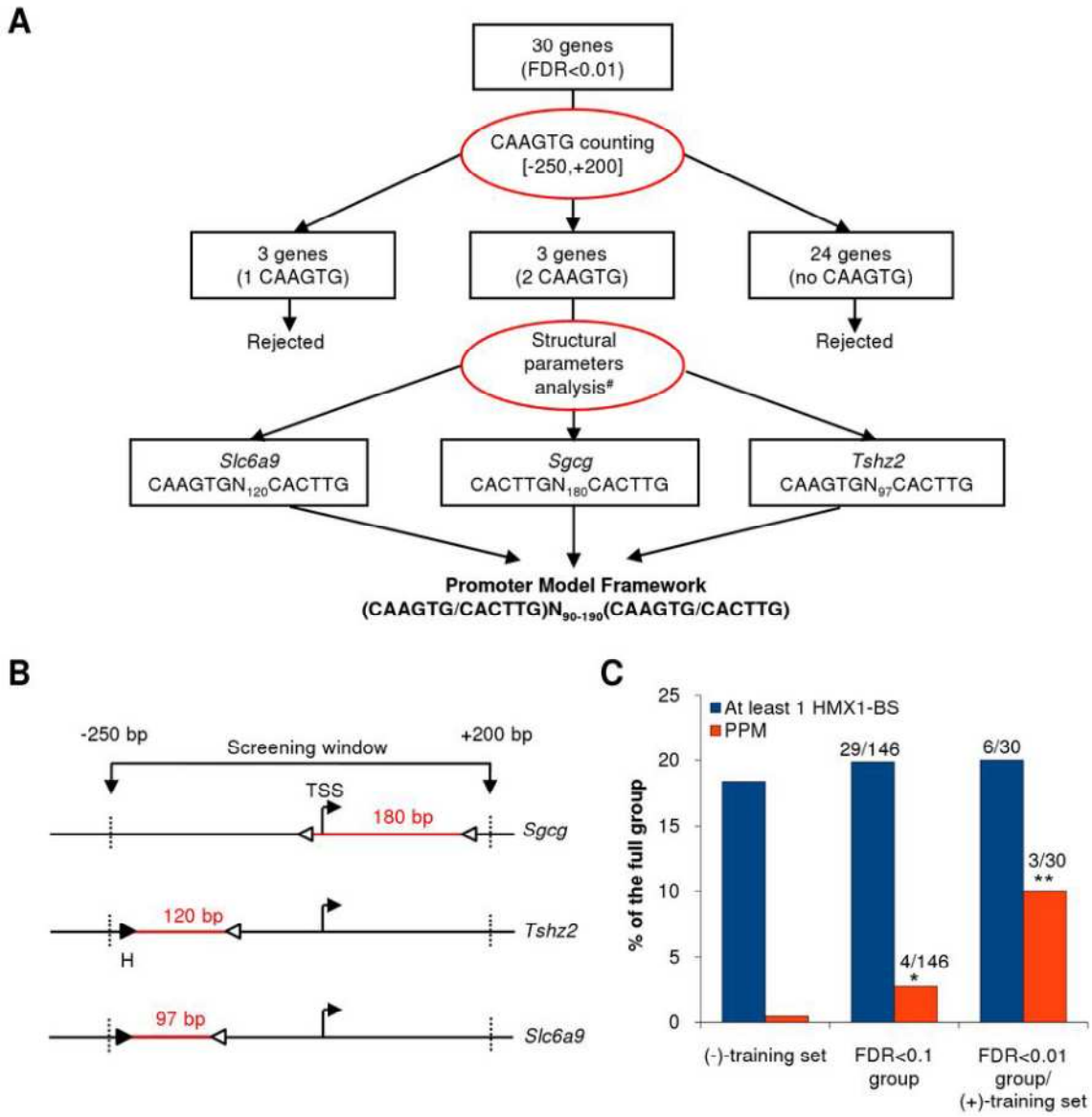

Figure 3 Characterization of *Sgcg*, *Tshz2* and *Slc6a9* expression. A) qPCR analysis of *Sgcg*, *Tshz2* and *Slc6a9* expression in WT, heterozygous (HT) and *dmbo* whole retina at P15 and P60. The significance of the differences between WT and HT or *dmbo* mean mRNA expression levels are determined by three independent experiments done in triplicate. All qPCR efficiencies are above 1.96 with a Pearson's r above 0.99. mRNA levels are expressed as a ratio of the *Hmx1* WT level, in P15 and P60 experiments, independently. Bars, SD; **P*Value<0.01, ***P*-Value<0.05, ****P*-Value<0.001. AU, arbitrary units. B) Heatmap representation of *Hmx1*, *Sgcg*, *Tshz2* and *Slc6a9* expression in the different cell types of the mouse retina according to the gene expression profile database [22]. C) Immunostaining of γ-Sarcoglycan in WT and *dmbo* retina at P15. White arrows indicate an accumulation of γ-Sarcoglycan at the border delimitating the INL and the IPL. DAPI, DAPI staining; Merge, overlap between DAPI and γ-SG immunostaining. ONL, Outer nuclear layer; OPL, Outer plexiformlayer; INL, Inner nuclear layer; IPL, Inner plexiform layer; GCL, Ganglion cell layer.

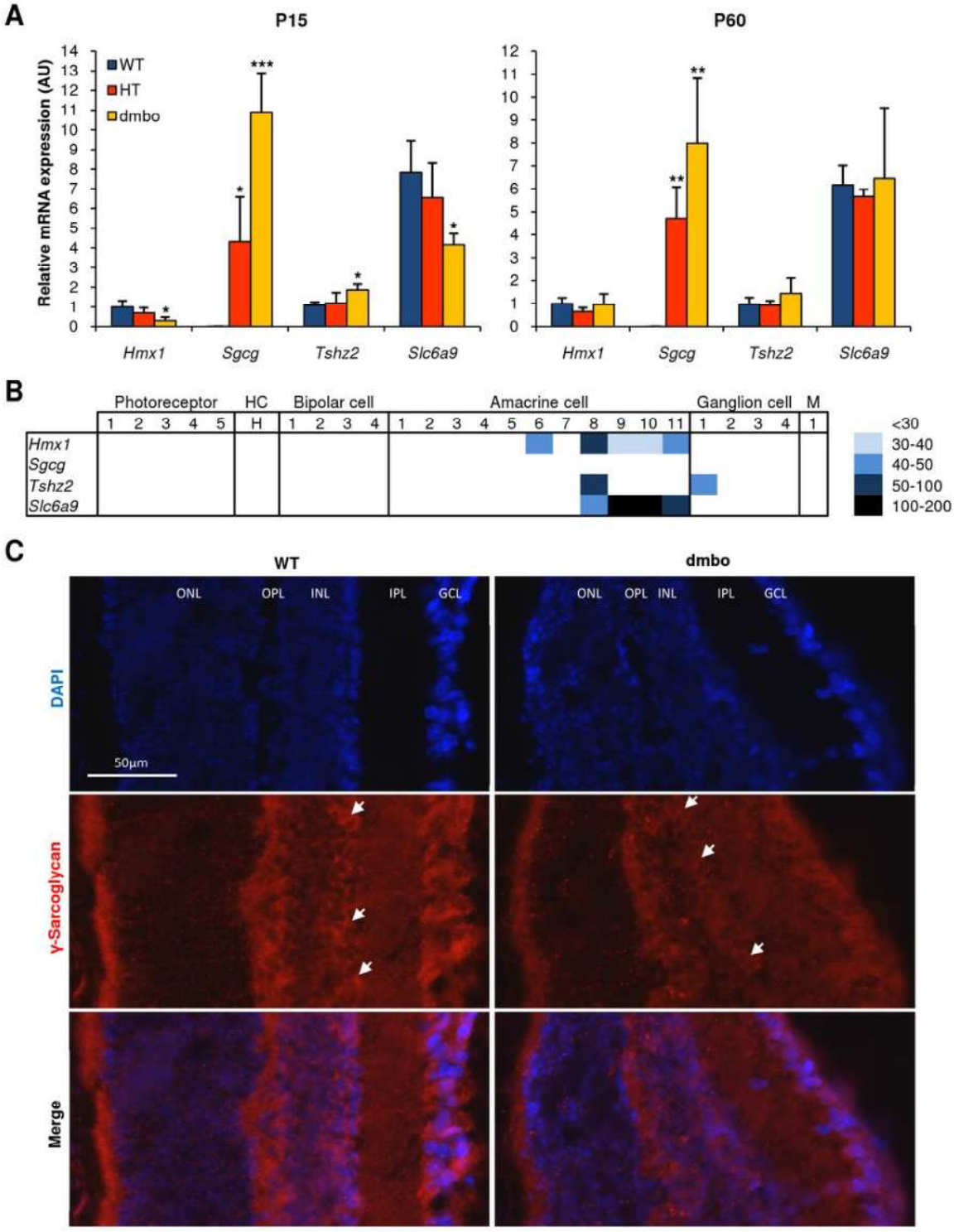
A
P15
P60
Relative mRNA expression (AU)
WT
HT
dmbo
Hmx1
Sgcg
Tshz2
Slc6a9
B
Photoreceptor
HC
Bipolar cell
Amacrine cell
Ganglion cell
M
<30
30-40
40-50
50-100
100-200
C
WT
dmbo
ONL
OPL
INL
IPL
GCL
DAPI
50µm
γ-Sarcoglycan
Merge

Figure 4 PPM-based genome-wide target selection focused on the conserved HMX1-BS pairs. A) Flowchart of the PPM-based genome-wide target selection. B) Venn diagram illustrating the overlap between human and mouse target selections. Expression localization in the eye is indicated for genes carrying an HMX1-BS pair in both species.

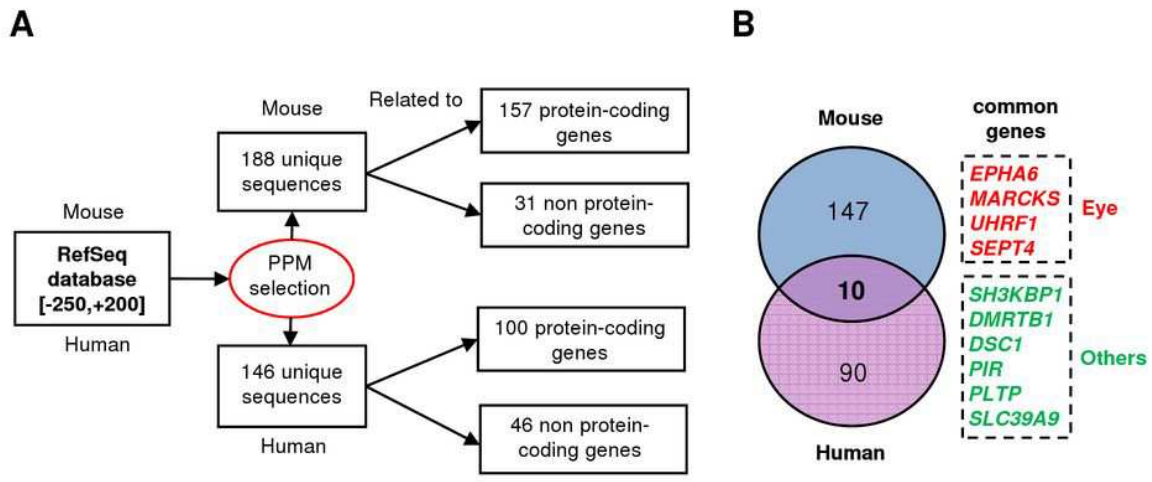

Figure 5 PPM-based genome-wide target selection focused on the co-occurrence of HMX1-BS pairs. A) Simultaneous possible combinations of HMX1-BS pairs allowed by the PPM with 3 or 4 HMX1-BSs. Pairs are identified according to HMX1-BSs numbers. B) Flowchart of the mouse and human PPM-based selections filtering according to HMX1-BS pairs counting. #see Figure 4 for details regarding the PPM-based selection process. Expression localization in the retina is indicated for genes carrying multiple HMX1-BS pairs. Significant enrichment in axon guidance pathway is also indicated (see text). C) Details of human and mouse *EPHA6* structure in the region surrounding the TSS. Forward (CAAGTG) and reverse (CACTTG) HMX1-BSs are symbolized respectively by black and white triangles. Distances (bp) between HMX1-BSs are indicated in red.

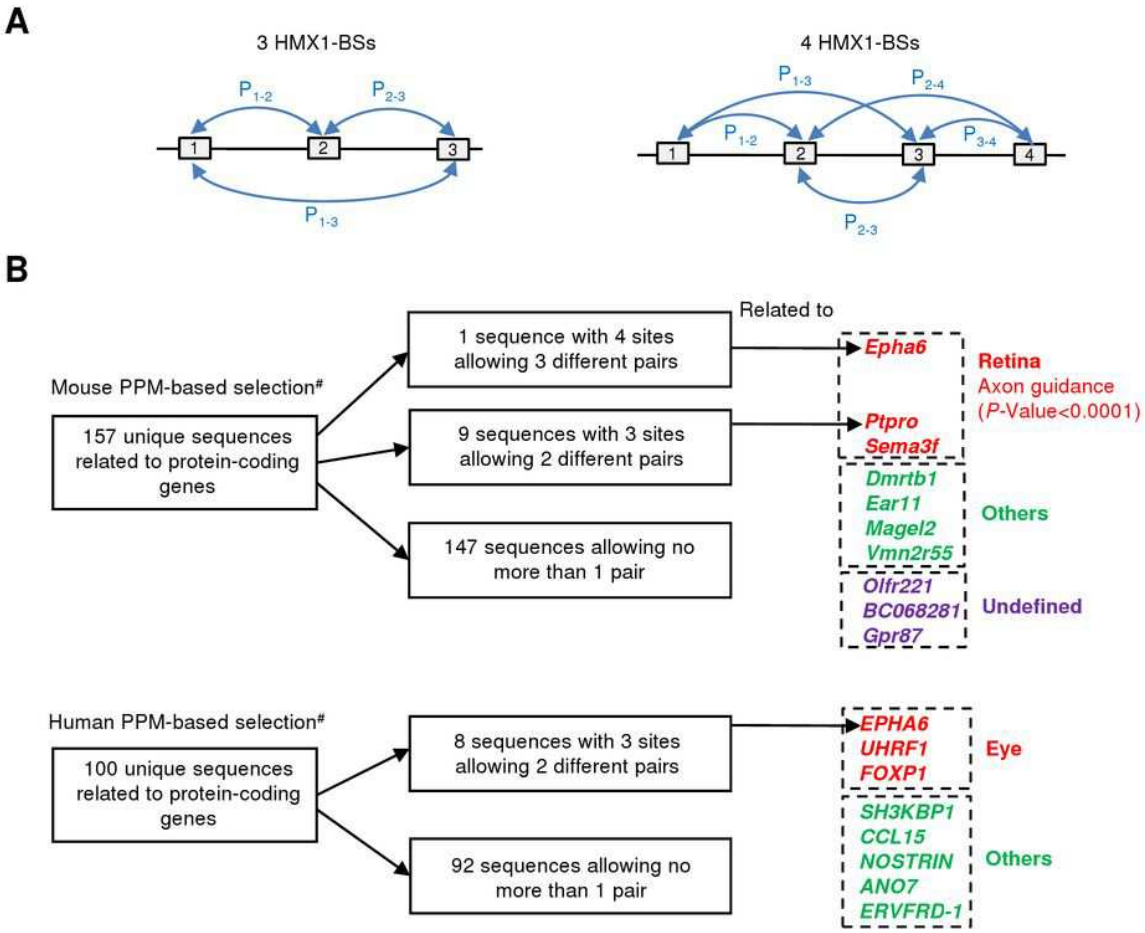
A
3 HMX1-BSs
P1-2
P2-3
P1-3
1
2
3
4 HMX1-BSs
P1-3
P2-4
P1-2
P3-4
P2-3
B
Mouse PPM-based selection#
157 unique sequences related to protein-coding genes
1 sequence with 4 sites allowing 3 different pairs
9 sequences with 3 sites allowing 2 different pairs
147 sequences allowing no more than 1 pair
Related to
Epha6
Ptpro
Sema3f
Retina
Axon guidance
(P-Value<0.0001)
Dmrtb1
Ear11
Magel2
Vmn2r55
Others
Olfr221
BC068281
Gpr87
Undefined
Human PPM-based selection#
100 unique sequences related to protein-coding genes
8 sequences with 3 sites allowing 2 different pairs
92 sequences allowing no more than 1 pair
EPHA6
UHRF1
FOXP1
Eye
SH3KBP1
CCL15
NOSTRIN
ANO7
ERVFRD-1
Others
C
-250 bp
+200 bp
+1000 bp
Exon 1
M. musculus
156
118
11
143
159
190
Exon 1
H. sapiens
2
155

Figure 6 Transcriptional repression of predicted target genes by *Hmx1*. The pGL3-*Sgcg* (positive control), pGL3-*Sema3f* and pGL3-*Ptpro* reporter plasmids were co-transfected with the empty pcDNA3.1 or the pcDNA3.1-Hmx1 expression vectors into the N2A cells. For each gene, the activities are shown relative to the pGL3 constructs co-transfected with the control empty pcDNA3.1. Firefly luciferase activities were normalized against the co-transfected β-galactosidase activity. Bars, SD; **P*-Value<0.01, ****P*-Value<0.001. AU, arbitrary units.

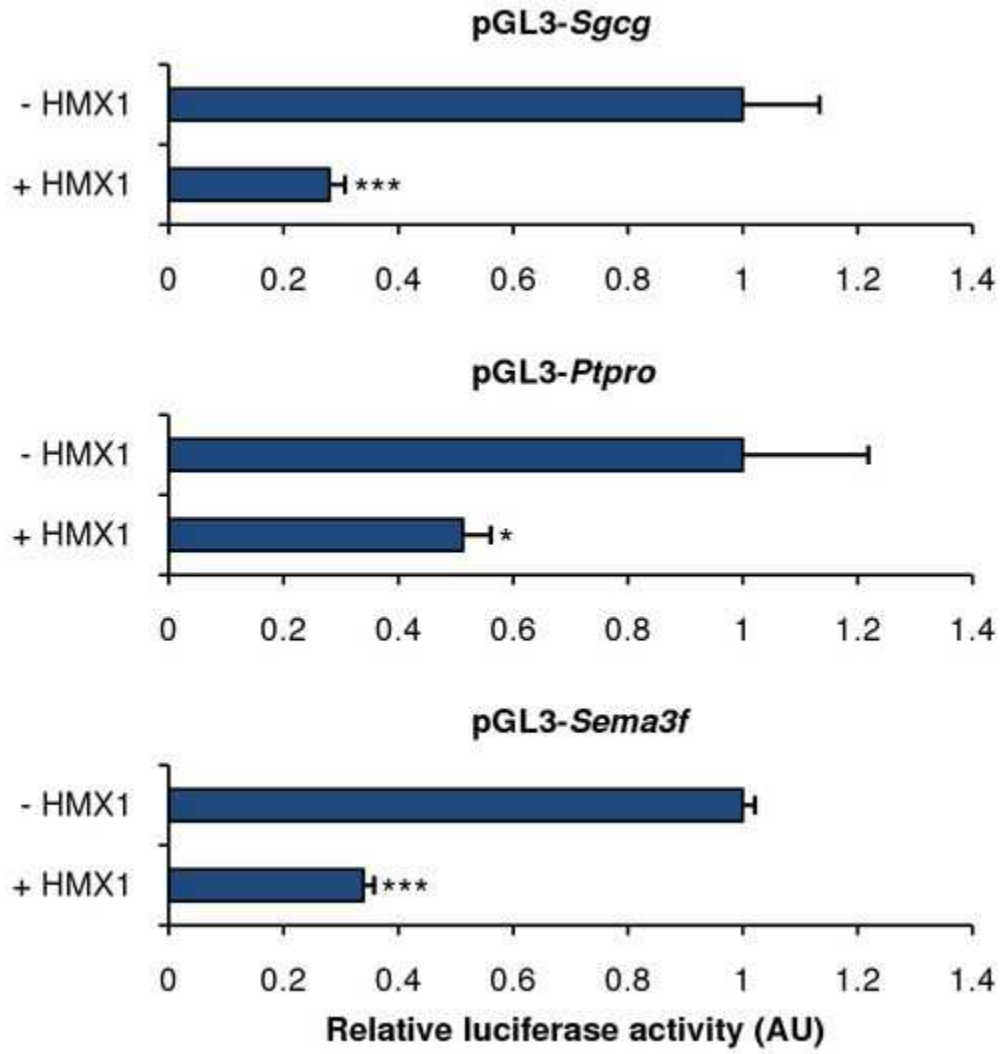

Figure 7 Mouse axon guidance pathway map. Adaptated from the mmu04360 KEGG pathway. EphA6, Sema3F and PTPRO are localized in red in the pathway. Note that PTPRO was originally absent from the map. Outputs of ephrin and semaphorin pathways are underlined with red dotted lines. See KEGG website for legend details (http://www.genome.jp/kegg/document/help_pathway.html).

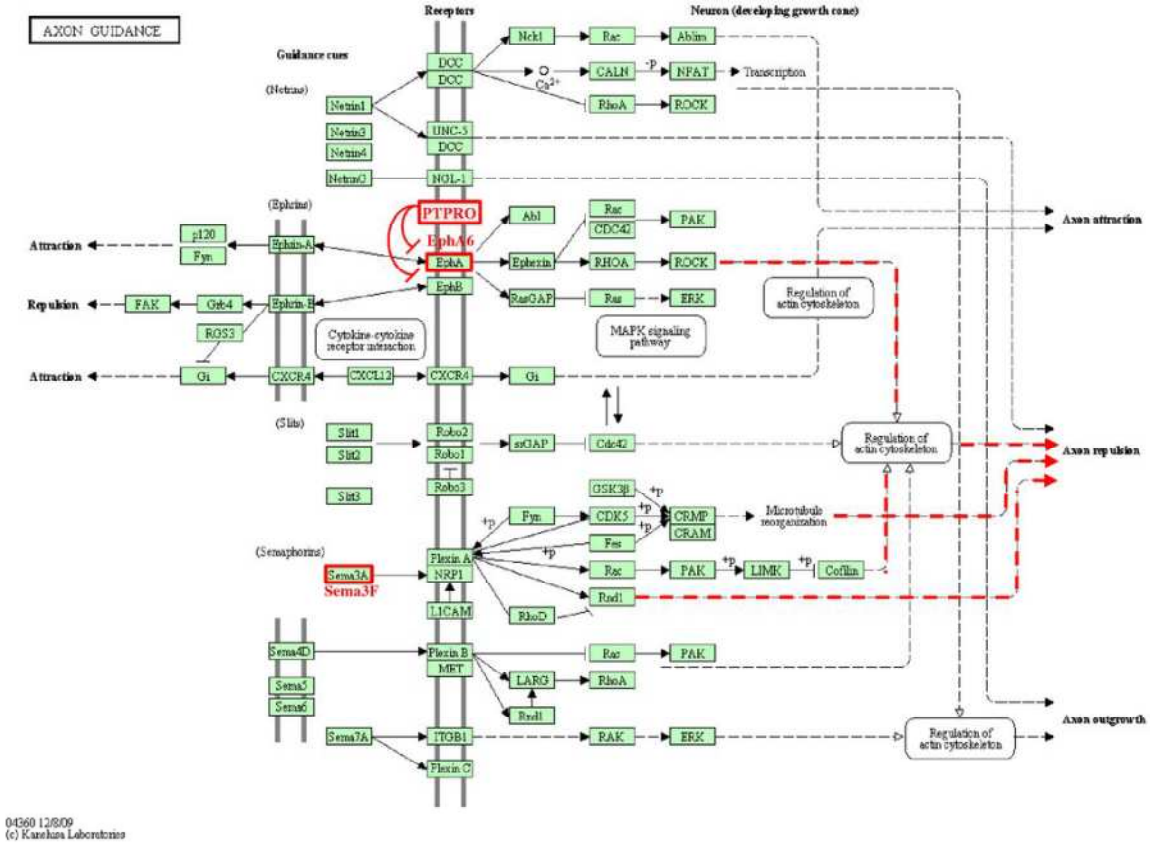

Table 1 Specificity of PPM-based selection methods. LS-PPM, Low specific PPM; VLS-PPM, Very low specific PPM. 95% CI, 95% confidence interval.

	PPM (2 HMX1-BS)	LS-PPM (1 HMX1-BS + 1 CAAG)	VLS-PPM (2 CAAG)
Predicted targets in the (-)-training set (%)	0.45	14.65	59.25
Predicted targets in the (+)-training set (%)	10.00	20.00	63.33
Fold-enrichment; *P*-Value (if <0.05)	22.22; 0.0006	1.37	0.01
Sensitivity	10.00% (95% CI: 2.23% - 26.56%)	20.00% (95% CI: 7.76% - 38.58%)	63.33% (95% CI: 43.86% - 80.05 %)
Specificity	99.55% (95%CI: 99.15% - 99.79%)	85.35% (95% CI: 83.72 % - 86.87 %)	40.75% (95% CI: 38.59 % - 42.94 %)

Table S1 Official gene symbols and gene accession numbers of all predicted targets

Gene accession number	Official symbol
NM_025904	1600012F09RIK
NM_025487	1700011A15RIK
NM_026625	1700067P10RIK
NM_025577	2810428I15Rik
NM_001033799	4930428D18RIK
NM_001204904	4930558K02RIK
NM_177213	ABCA15
NM_001252508	AC152451.1
NM_175324	Acad11
NM_001042542	AKAP4
NM_011921	ALDH1A7
NM_021710	AP4S1
NM_009700	AQP4
NM_001162423	ARHGAP4
NM_001162424	ARHGAP4
NM_138630	ARHGAP4
NM_019824	ARPC3
NM_025338	AURKAIP1
NM_023057	B230120H23RIK
NM_001170858	BC068281
NM_173416	BC068281
NM_013483	BTN1A1
NM_175938	BTN2A2
NM_007576	C4BP
NM_198663	C87499
NM_027062	C8G
NM_145575	CALD1
NM_001008420	CDH12
NM_009881	CDYL
NM_007739	COL8A1
NM_001033851	CPNE8
NM_025815	CPNE8
NM_009910	CXCR3
NM_001048227	DBNDD2
NM_007838	DDOST
NM_007868	DMD
NM_019872	DMRTB1
NM_013504	DSC1
NM_007894	EAR1
NM_053113	EAR11
NM_007895	EAR2
NM_019398	EAR5
NM_001033464	EFCAB4B
NM_207685	ELAVL2
NM_001252666	EPB4.9
NM_007938	EPHA6
NM_029310	FABP12
NM_033146	FAM158A
NM_001164739	Fam47a-ps
NM_010216	FIGF
NM_008035	FOLR2
NM_177863	FREM1
NM_001081454	FURIN
NM_001037716	Gm10439
NM_177571	GM13103
NM_001085531	GM13283
NM_001198988	GM15080
NM_001198987	GM15097
NM_001081648	GM15107
NM_001114400	GM15127
NM_001122735	GM15127
NM_001195672	GM221
NM_001033407	Gm815
NM_001038703	GPR146
NM_032399	GPR87
NM_029095	HHATL
NM_008354	IL12RB2

NM_008372	IL7R
NM_001163637	JAKMIP2
NM_001168354	KCNJ1
NM_153094	KLRB1F
NM_001099301	LCN14
NM_001164885	LPIN2
NM_146245	LRIT1
NM_001113379	LRRC32
NM_001136071	LSP1
NM_001114383	LUZP4
NM_010758	MAG
NM_013779	MAGEL2
NM_022012	MAP3K11
NM_008538	MARCKS
NM_001114179	MCART6
NM_029730	MOSPD2
NM_203492	MRGPRG
NM_010834	MSTN
NM_010888	NDUFS6
NM_008691	NEFM
NM_016743	NELL2
NM_025998	NKAIN1
NM_023409	NPC2
NM_008733	NRAP
NM_198059	NRAP
NM_173748	NUDCD3
NM_026950	OCIAD2
NM_147068	OLFR166
NM_001001808	OLFR221
NM_001011733	OLFR288
NM_146347	OLFR390
NM_146346	OLFR397
NM_146305	OLFR420
NM_146266	OLFR772
NM_207008	OLFR773
NM_146827	OLFR983
NM_024289	OSBPL5
NM_008769	OTC
NM_001122734	OTT
NM_011022	OTT
NM_001081050	PARD3B
NM_020264	PATE4
NM_053131	PCDHB6
NM_008888	PHOX2B
NM_027153	PIR
NM_011125	PLTP
NM_025901	POLR3K
NM_001205188	PPP2R2A
NM_028032	PPP2R2A
NM_001164199	PRKACB
NM_025532	PRL2B1
NM_001164058	PRL7A1
NM_008930	PRL7A1
NM_001195673	PRR22
NM_001164401	PTPRO
NM_011216	PTPRO
NM_030554	RAB27B
NM_207246	RASGRP3
NM_001081013	RLF
NM_019642	RPN2
NM_012052	RPS3
NM_001025364	RTN2
NM_177652	RYR3
NM_023248	SBDS
NM_013657	SEMA3C
NM_011349	SEMA3F
NM_011129	SEPT4
NM_177920	SERPINA7

NM_023134	SFTPA1
NM_011892	SGCG
NM_021389	SH3KBP1
NM_030683	SLC14A2
NM_207651	SLC14A2
NM_026244	SLC39A9
NM_022025	SLC5A7
NM_008135	SLC6A9
NM_011474	SPRR2H
NM_054103	STK33
NM_001252578	SULF2
NM_133670	SULT1A1
NM_022027	SYNE1
NM_001159751	TCEA1
NM_001253862	TCF12
NM_001114140	TCF20
NM_013836	TCF20
NM_009443	TGOLN1
NM_001161355	TIMD2
NM_031880	TNK1
NM_080455	TSHZ2
NM_178897	TYW1
NM_177823	UBASH3A
NM_001111079	UHRF1
NM_010931	UHRF1
NM_001104644	VMN2R53
NM_001081449	VMN2R54
NM_001104645	VMN2R55
NM_001105180	VMN2R65
NM_001102580	VMN2R76
NM_007701	VSX2
NM_177697	VWA3A
NM_001127376	WISP3
NM_001081016	ZC3H7B
NM_019747	ZFP113

Official full name
RIKEN cDNA 1600012F09 gene
RIKEN cDNA 1700011A15 gene
RIKEN cDNA 1700067P10 gene
RIKEN cDNA 2810428I15 gene
RIKEN cDNA 4930428D18 gene
RIKEN cDNA 4930558K02 gene
ATP-binding cassette, sub-family A (ABC1), member 15
uncharacterized protein LOC268595 [Source:RefSeq peptide
acyl-Coenzyme A dehydrogenase family, member 11
A kinase (PRKA) anchor protein 4
aldehyde dehydrogenase family 1, subfamily A7
adaptor-related protein complex AP-4, sigma 1
aquaporin 4
Rho GTPase activating protein 4
Rho GTPase activating protein 4
Rho GTPase activating protein 4
actin related protein 2/3 complex, subunit 3
aurora kinase A interacting protein 1
RIKEN cDNA B230120H23 gene
cDNA sequence BC068281
cDNA sequence BC068281
butyrophilin, subfamily 1, member A1
butyrophilin, subfamily 2, member A2
complement component 4 binding protein
expressed sequence C87499
complement component 8, gamma polypeptide
caldesmon 1
cadherin 12
chromodomain protein, Y chromosome-like
collagen, type VIII, alpha 1
copine VIII
copine VIII
chemokine (C-X-C motif) receptor 3

dysbindin (dystrobrevin binding protein 1) domain containing 2
dolichyl-di-phosphooligosaccharide-protein glycotransferase
dystrophin, muscular dystrophy
DMRT-like family B with proline-rich C-terminal, 1
desmocollin 1
eosinophil-associated, ribonuclease A family, member 1
eosinophil-associated, ribonuclease A family, member 11
eosinophil-associated, ribonuclease A family, member 2
eosinophil-associated, ribonuclease A family, member 5
EF-hand calcium binding domain 4B
ELAV (embryonic lethal, abnormal vision, Drosophila)-like 2 (Hu antigen B)
erythrocyte protein band 4.9
Eph receptor A6
fatty acid binding protein 12
family with sequence similarity 158, member A
family with sequence similarity 47, member A, pseudogene
c-fos induced growth factor
Mus musculus folate receptor 2 (fetal)
Fras1 related extracellular matrix protein 1
furin (paired basic amino acid cleaving enzyme)
predicted gene 10439
predicted gene 13103
predicted gene 13283
predicted gene 15080
predicted gene 15097
predicted gene 15107
predicted gene 15127
predicted gene 15127
predicted gene 221
predicted gene 815
G protein-coupled receptor 146
G protein-coupled receptor 87
hedgehog acyltransferase-like
interleukin 12 receptor, beta 2

interleukin 7 receptor
janus kinase and microtubule interacting protein 2
potassium inwardly-rectifying channel, subfamily J, member 1
killer cell lectin-like receptor subfamily B member 1F
lipocalin 14
lipin 2
leucine-rich repeat, immunoglobulin-like and transmembrane domains 1
leucine rich repeat containing 32
lymphocyte specific 1
leucine zipper protein 4
myelin-associated glycoprotein
melanoma antigen, family L, 2
mitogen-activated protein kinase kinase kinase 11
myristoylated alanine rich protein kinase C substrate
mitochondrial carrier triple repeat 6
motile sperm domain containing 2
MAS-related GPR, member G
myostatin
NADH dehydrogenase (ubiquinone) Fe-S protein 6
neurofilament, medium polypeptide
NEL-like 2 (chicken)
Na+/K+ transporting ATPase interacting 1
Niemann Pick type C2
nebulin-related anchoring protein
nebulin-related anchoring protein
NudC domain containing 3
OCIA domain containing 2
olfactory receptor 166
olfactory receptor 221
olfactory receptor 288
olfactory receptor 390
olfactory receptor 397
olfactory receptor 420
olfactory receptor 772

olfactory receptor 773
olfactory receptor 983
oxysterol binding protein-like 5
ornithine transcarbamylase
predicted gene 15093
predicted gene 15093
par-3 partitioning defective 3 homolog B (C. elegans)
prostate and testis expressed 4
protocadherin beta 6
paired-like homeobox 2b
pirin
phospholipid transfer protein
polymerase (RNA) III (DNA directed) polypeptide K
protein phosphatase 2 (formerly 2A), regulatory subunit B (PR 52), alpha isoform
protein phosphatase 2 (formerly 2A), regulatory subunit B (PR 52), alpha isoform
protein kinase, cAMP dependent, catalytic, beta
prolactin family 2, subfamily b, member 1
prolactin family 7, subfamily a, member 1
prolactin family 7, subfamily a, member 1
proline rich 22
protein tyrosine phosphatase, receptor type, O
protein tyrosine phosphatase, receptor type, O
RAB27b, member RAS oncogene family
RAS, guanyl releasing protein 3
rearranged L-myc fusion sequence
ribophorin II
ribosomal protein S3
reticulon 2 (Z-band associated protein)
ryanodine receptor 3
Shwachman-Bodian-Diamond syndrome homolog (human)
sema domain, immunoglobulin domain (Ig), short basic domain, secreted, (semaphorin) 3C
sema domain, immunoglobulin domain (Ig), short basic domain, secreted, (semaphorin) 3F
septin 4
serine (or cysteine) peptidase inhibitor, clade A (alpha-1 antiproteinase, antitrypsin), member 7

surfactant associated protein A1
sarcoglycan, gamma (dystrophin-associated glycoprotein)
SH3-domain kinase binding protein 1
solute carrier family 14 (urea transporter), member 2
solute carrier family 14 (urea transporter), member 2
solute carrier family 39 (zinc transporter), member 9
solute carrier family 5 (choline transporter), member 7
solute carrier family 6 (neurotransmitter transporter, glycine), member 9
small proline-rich protein 2H
serine/threonine kinase 33
sulfatase 2
sulfotransferase family 1A, phenol-preferring, member 1
Nesprin-1 [Source:UniProtKB/Swiss-Prot
transcription elongation factor A (SII) 1
transcription factor 12
transcription factor 20
transcription factor 20
trans-golgi network protein
T cell immunoglobulin and mucin domain containing 2
tyrosine kinase, non-receptor, 1
teashirt zinc finger family member 2
tRNA-yW synthesizing protein 1 homolog (S. cerevisiae)
ubiquitin associated and SH3 domain containing, A
ubiquitin-like, containing PHD and RING finger domains, 1
ubiquitin-like, containing PHD and RING finger domains, 1
vomeronasal 2, receptor 53
vomeronasal 2, receptor 54
vomeronasal 2, receptor 55
vomeronasal 2, receptor 65
vomeronasal 2, receptor 76
visual system homeobox 2
von Willebrand factor A domain containing 3A
WNT1 inducible signaling pathway protein 3
zinc finger CCCH type containing 7B

zinc finger protein 113

Gene accession number	Official symbol
NM_133446	AGAP4
NM_001077686	AGAP8
NM_001142445	ANK1
NM_020478	ANK1
NM_020480	ANK1
NM_001242814	ANKRD6
NM_001001666	ANO7
NM_001001891	ANO7
NM_014715	ARHGAP32
NM_001113738	ARL17A
NM_001128149	ATXN7
NM_001170719	BCAR1
NM_001001342	BLOC1S2
NM_024688	C10orf68
NM_174896	C1ORF162
NM_182584	C20orf203
NM_001739	CA5A
NM_001014435	CA7
NM_201570	CACNB2
NM_001033952	CALCA
NM_001033953	CALCA
NM_001741	CALCA
NM_153038	CCDC140
NM_032965	CCL15
NM_001025158	CD74
NM_001025159	CD74
NM_004355	CD74
NM_006536	CLCA2
NM_006580	CLDN16
NM_001025233	CLLU1
NM_000634	CXCR1
NM_144970	CXORF38
NM_001010969	CYP4A22
NM_004228	CYTH2
NM_017457	CYTH2
NM_015345	DAAM2
NM_198963	DHX57
NM_033067	DMRTB1
NM_004948	DSC1
NM_024421	DSC1
NM_001256304	DTNB
NM_024007	EBF1
NM_001080448	EPHA6
NM_207582	ERVFRD-1
NM_001122646	FAM178B
NM_015864	FAM65B
NM_031950	FGFBP2
NM_001244816	FOXP1
NM_001018071	FRMPD2
NM_001007122	FSD2
NM_001242628	GFOD1
NM_002075	GNB3
NM_001145639	GPSM1
NM_005319	HIST1H1C
NM_004133	HNF4G
NM_001161772	HTR3A
NM_000596	IGFBP1
NM_002188	IL13
NM_001024660	KALRN
NM_003947	KALRN
NM_002235	KCNA6
NM_023930	KCTD14
NM_015925	LSR
NM_205834	LSR
NM_205835	LSR
NM_024871	MAP6D1
NM_002356	MARCKS
NM_001040179	MCHR2
NM_032503	MCHR2
NM_152513	MEI1
NM_001135863	METTL20
NM_001145450	MORN2
NM_005372	MOS
NM_005953	MT2A
NM_014342	MTCH2
NM_001171631	NOSTRIN
NM_024844	NUP85
NM_001001920	OR4C15
NM_013340	PCDHB1
NM_001197219	PDE4D
NM_001018109	PIR
NM_003662	PIR
NM_001242920	PLTP
NM_006227	PLTP
NM_182676	PLTP
NM_001256569	PPFIBP2
NM_001197098	PRSS3
NM_000316	PTH1R
NM_198964	PTHLH
NM_198966	PTHLH
NM_020336	RALGAPB
NM_182665	RASSF5
NM_001166283	RGMA

NM_002922	RGS1
NM_014139	SCN11A
NM_004574	SEPT4
NM_001024666	SH3KBP1
NM_197965	SLC10A6
NM_152527	SLC16A14
NM_001171170	SLC25A21
NM_030631	SLC25A21
NM_145282	SLC25A48
NM_006516	SLC2A1
NM_001252148	SLC39A9
NM_001252150	SLC39A9
NM_018375	SLC39A9
NM_001080537	SNTN
NM_001012415	SOHLH1
NM_001101677	SOHLH1
NM_001014291	SPRR2G
NM_006415	SPTLC1
NM_178324	SPTLC1
NM_206861	TACC2
NM_206862	TACC2
NM_006134	TMEM50B
NM_001168215	TMEM92
NM_003842	TNFRSF10B
NM_147187	TNFRSF10B
NM_016372	TPRA1
NM_013282	UHRF1
NM_130776	XAGE3
NM_130775	XAGE5
NM_001080412	ZBTB38
NM_014717	ZNF536

Official full name
ArfGAP with GTPase domain, ankyrin repeat and PH domain 4
ArfGAP with GTPase domain, ankyrin repeat and PH domain 8
ankyrin 1, erythrocytic
ankyrin 1, erythrocytic
ankyrin 1, erythrocytic
ankyrin repeat domain 6
anoctamin 7
anoctamin 7
Rho GTPase activating protein 32
ADP-ribosylation factor-like 17A
ataxin 7
breast cancer anti-estrogen resistance 1
biogenesis of lysosomal organelles complex-1, subunit 2
chromosome 10 open reading frame 68
chromosome 1 open reading frame 162
chromosome 20 open reading frame 203
carbonic anhydrase VA, mitochondrial
carbonic anhydrase VII
calcium channel, voltage-dependent, beta 2 subunit
calcitonin-related polypeptide alpha
calcitonin-related polypeptide alpha
calcitonin-related polypeptide alpha
coiled-coil domain containing 140
chemokine (C-C motif) ligand 15
CD74 molecule, major histocompatibility complex, class II invariant chain
CD74 molecule, major histocompatibility complex, class II invariant chain
CD74 molecule, major histocompatibility complex, class II invariant chain
chloride channel accessory 2
claudin 16
chronic lymphocytic leukemia up-regulated 1
chemokine (C-X-C motif) receptor 1
chromosome X open reading frame 38
cytochrome P450, family 4, subfamily A, polypeptide 22
cytohesin 2
cytohesin 2
dishevelled associated activator of morphogenesis 2
DEAH (Asp-Glu-Ala-Asp/His) box polypeptide 57
DMRT-like family B with proline-rich C-terminal, 1
desmocollin 1
desmocollin 1
dystrobrevin, beta
early B-cell factor 1
EPH receptor A6
endogenous retrovirus group FRD, member 1
family with sequence similarity 178, member B
family with sequence similarity 65, member B

fibroblast growth factor binding protein 2
forkhead box P1
FERM and PDZ domain containing 2
fibronectin type III and SPRY domain containing 2
glucose-fructose oxidoreductase domain containing 1
guanine nucleotide binding protein (G protein), beta polypeptide 3
G-protein signaling modulator 1
histone cluster 1, H1c
hepatocyte nuclear factor 4, gamma
5-hydroxytryptamine (serotonin) receptor 3A, ionotropic
insulin-like growth factor binding protein 1
interleukin 13
kalirin, RhoGEF kinase
kalirin, RhoGEF kinase
potassium voltage-gated channel, shaker-related subfamily, member 6
potassium channel tetramerisation domain containing 14
lipolysis stimulated lipoprotein receptor
lipolysis stimulated lipoprotein receptor
lipolysis stimulated lipoprotein receptor
MAP6 domain containing 1
myristoylated alanine-rich protein kinase C substrate
melanin-concentrating hormone receptor 2
melanin-concentrating hormone receptor 2
meiosis inhibitor 1
methyltransferase like 20
MORN repeat containing 2
v-mos Moloney murine sarcoma viral oncogene homolog
metallothionein 2A
mitochondrial carrier 2
nitric oxide synthase trafficker
nucleoporin 85kDa
olfactory receptor, family 4, subfamily C, member 15
protocadherin beta 1
phosphodiesterase 4D, cAMP-specific
iron-binding nuclear protein
pirin (iron-binding nuclear protein)
phospholipid transfer protein
phospholipid transfer protein
phospholipid transfer protein
PTPRF interacting protein, binding protein 2 (liprin beta 2)
protease, serine, 3
parathyroid hormone 1 receptor
parathyroid hormone-like hormone
parathyroid hormone-like hormone
Ral GTPase activating protein, beta subunit (non-catalytic)
Ras association (RalGDS/AF-6) domain family member 5
RGM domain family, member A

regulator of G-protein signaling 1
sodium channel, voltage-gated, type XI, alpha subunit
septin 4
SH3-domain kinase binding protein 1
solute carrier family 10 (sodium/bile acid cotransporter family), member 6
solute carrier family 16, member 14 (monocarboxylic acid transporter 14)
solute carrier family 25 (mitochondrial oxoadipate carrier), member 21
solute carrier family 25 (mitochondrial oxoadipate carrier), member 21
solute carrier family 25, member 48
solute carrier family 2 (facilitated glucose transporter), member 1
solute carrier family 39 (zinc transporter), member 9
solute carrier family 39 (zinc transporter), member 9
solute carrier family 39 (zinc transporter), member 9
sentan, cilia apical structure protein
spermatogenesis and oogenesis specific basic helix-loop-helix 1
spermatogenesis and oogenesis specific basic helix-loop-helix 1
small proline-rich protein 2G
serine palmitoyltransferase, long chain base subunit 1
serine palmitoyltransferase, long chain base subunit 1
transforming, acidic coiled-coil containing protein 2
transforming, acidic coiled-coil containing protein 2
transmembrane protein 50B
transmembrane protein 92
tumor necrosis factor receptor superfamily, member 10b
tumor necrosis factor receptor superfamily, member 10b
transmembrane protein, adipocyte asscociated 1
ubiquitin-like with PHD and ring finger domains 1
X antigen family, member 3
X antigen family, member 5
zinc finger and BTB domain containing 38
zinc finger protein 536

Table S2 Sequences and amplicon sizes of qPCR primer pairs used in this study

Gene	qPCR Primer	Sequence	Exon	Product Size (bp)
Gapdh	Forward	gaggccggtgctgagtatgt	3	288
	Reverse	ggtggcagtgatggcatgga	5	
Hmx1	Forward	ggctacggaggtggtctaag	1	242
	Reverse	gtgcgcgtcttcttcctg	2	
Sgcg	Forward	gccatcctcgttgtgaatct	2	148
	Reverse	ctttggcatacagcggaaat	3	
Tshz2	Forward	atgccaaggaggaaacagc	1	146
	Reverse	gtgtcattgctgctctggtg	2	
Slc6a9	Forward	aaggcactgaacgcaagagt	2	146
	Reverse	cgtgtgaggttctggtcctt	3	

Table S3 Up-regulated genes with a FDR<0.1 and a fold-change>1.2. #Orientation of HMX1-BSs are indicated; F, forward strand (CAAGTG); R, reverse strand (CACTTG).

Fold change	FDR	Gene symbol	Gene accession number	HMX1-BSs within [-250,+200]#
5.69	0.0000213	Sgcg	NM_011892	R[-23,-18],F[+165,+170]
1.91	0.0000933	Cmbm6	NM_026066	
2.01	0.0006455	3632451O06Rik	BC023359	
1.89	0.0012053	Foih1	NM_016770	
1.66	0.0012438	4930485B16Rik	BC046659	
1.45	0.0012786	Mt2	NM_008630	
1.61	0.0022895	Pigz	NM_172822	
1.43	0.0027723	Gpct	NM_027455	
1.51	0.0058628	Hist2h2bb	NM_175666	F[+194,+199]
1.47	0.0060470	Igsf9	NM_033608	
1.48	0.0068103	Tshz2	NM_080455	F[-238,-233],R[-112,-107]
1.58	0.0077030	Lmo51	NM_001162974	
1.27	0.0099155	Rpl15	NM_025586	
1.98	0.0099155	Snord53	NR_028551	
1.48	0.0100244	A930018M24Rik	BC144873	R[+125,+130]
1.31	0.0100401	4930485B16Rik	BC115566	
1.26	0.0104377	Car14	NM_011797	
1.42	0.0118919	Krt18	NM_010664	
1.31	0.0126647	B430203G13Rik	AK046603	
1.48	0.0151762	Pdzd8	NM_001033222	
1.26	0.0164274	1700003M02Rik	NM_027041	
1.44	0.0180454	Bcar3	NM_013867	R[+21,+26]
1.34	0.0180454	Tctex1d2	NM_026329	F[-109,-104]
1.66	0.0186336	Agl	NM_001081326	
1.33	0.0238892	Bche	NM_009738	R[-213,-208]
1.46	0.0243864	Gm5631	NM_001013820	
1.35	0.0254713	Gm4983	BC030401	
1.30	0.0256207	B230354O11Rik	AK046228	
1.26	0.0269053	Mt1	NM_013602	
1.31	0.0297905	Adamts16	NM_172053	
1.43	0.0394752	Gprc5b	NM_022420	
1.22	0.0447511	Zcchc34	NM_001101433	
1.51	0.0476012	Rras2	NM_025846	
1.34	0.0478588	Cadps2	NM_153163	
1.20	0.0478588	Uhmk1	NM_010633	
1.43	0.0480480	C730048C13Rik	NM_177002	
1.41	0.0480480	Guca1a	NM_008189	
1.43	0.0480480	P4ha3	NM_177161	
1.20	0.0487413	Tulp3	NM_011657	
1.29	0.0489888	4930465K10Rik	NR_027978	
1.21	0.0509040	Slc14a1	NM_001171010	
1.22	0.0510000	Kcnj10	NM_001039484	
1.55	0.0523636	Mir204	NR_029591	
1.24	0.0526240	Map3k5	NM_008580	
1.27	0.0555035	Tmm36	NM_178872	
1.57	0.0576586	Cyp2j13	NM_146548	F[+46,+60],F[+61,+66]
1.35	0.0598401	Rps3a	BC084675	
2.02	0.0615193	Ritin2	NM_001081346	
1.21	0.0636835	3630406C13Rik	NM_146061	
1.84	0.0636835	Atp1a2	NM_178405	
1.23	0.0683989	Fat3	NM_021458	
1.22	0.0683989	Pappa	NM_021362	
1.29	0.0726221	Mogat1	NM_026713	
1.23	0.0726601	Aqp4	NM_009700	F[-169,-164],F[-23,-18]
1.26	0.0737333	Ptpro16	NM_015796	
1.25	0.0737333	Jam3	NM_023277	
1.61	0.0750994	Agpt2l1	NM_027907	
1.38	0.0857396	Aktap6	NM_198111	
1.25	0.0857396	Zfp365	NM_178675	R[-84,-79]
1.29	0.0866818	1810011O10Rik	NM_026931	
1.23	0.0866818	Ctsc	NM_009982	
1.39	0.0866818	Spata1	NM_027617	
1.27	0.0881148	Orf1489	NM_146636	
1.32	0.0900386	E230001N04Rik	BC096647	
1.23	0.0929631	Nign1	NM_139666	
1.27	0.0965127	Gm8292	AK132630	
1.23	0.0965127	Lypd6	NR_033304	
1.24	0.0965127	Selenbp2	NM_019414	F[-180,-175],R[-131,-126]
1.26	0.0965127	Slc44a5	NM_001081263	
1.30	0.0971102	Picz1	NM_054066	

Table S4 Down-regulated genes with a FDR<0.1 and a fold-change>1.2. #Orientation of HMX1-BSs are indicated; F, forward strand (CAAGTG); R, reverse strand (CACTTG).

Fold change	Adj. P-Value	Gene symbol	Gene accession number	HMX1-BSs within [-250,+200]#
-3.19	5.67E-07	Duoxl	NM_153389	
-2.03	1.71E-06	D14Ertd449e	NM_026311	
-1.49	0.0003666	Pelt2	NM_033602	
-1.46	0.0005821	6720456H20Rik	NM_172600	
-1.54	0.0005821	Gm6498	NR_003630	
-1.70	0.0005821	Mkl2	NM_153588	
-1.63	0.0006206	Plac9	NM_207229	
-1.61	0.0013202	4930503L19Rik	BC057927	
-1.42	0.0016333	Pcsk6	NM_011048	
-1.47	0.0018071	Katna2	NM_027721	
-1.30	0.0034387	Slc6a9	NM_008136	F[-238,-230],R[-131,-124]
-1.59	0.0041139	5330426P16Rik	NR_028300	
-1.74	0.0046260	Zfp125	ENSMUST00000079237	
-1.53	0.0063212	Stard6	NM_029019	F[+65,+70]
-1.41	0.0066867	Rec8	NM_020002	
-1.30	0.0073895	Cacna2d3	NM_009785	F[-38,-33]
-1.34	0.0117462	Pdxdc1	NM_053181	
-1.45	0.0126647	Slc39a2	NM_001039676	
-1.26	0.0143769	3222401L13Rik	ENSMUST00000097608	
-1.25	0.0154891	Rpgrip1	NM_023879	
-1.36	0.0184944	1810030N24Rik	BC027608	R[-163,-158]
-1.47	0.0184944	Gm4792	NR_033209	R[+109,+114]
-1.30	0.0196269	Osgep	NM_133676	
-1.34	0.0198850	5430419D17Rik	NM_175166	
-1.31	0.0213000	6530401N04Rik	NM_029545	F[+63,+68]
-1.26	0.0219338	Ncoa2	NM_008678	F[-41,-36]
-1.48	0.0221016	Flip1l	NM_001040397	
-1.47	0.0231733	Cyp2r1	NM_177382	
-1.23	0.0231733	Rundc3a	NM_001163498	
-1.22	0.0231733	Slc4a3	NM_009208	
-1.34	0.0231733	Thrsp	NM_009381	F[+11,+16]
-1.29	0.0243854	Ppox	NM_008911	
-1.42	0.0246307	Rpn2	NR_004439	
-1.29	0.0246307	Trib1	NM_144549	
-1.47	0.0246394	Tnfrsf8	NM_009401	
-1.28	0.0252309	Snord15a	NR_002172	F[-284,-279]
-1.38	0.0256207	Adra2a	NM_007417	
-1.24	0.0260646	Scamp1?	NR_028660	F[+143,+148]
-1.27	0.0267674	Arhgap31	NM_030260	
-1.36	0.0267674	Dnanc9	NM_001099633	
-1.27	0.0267674	Tpm3	NM_022314	
-1.80	0.0313997	Hjurp	NM_199002	
-1.32	0.0313997	Pot1b	NM_028370	
-1.30	0.0384742	P2ry14	NM_133200	F[-79,-66]
-1.24	0.0388900	Trpc3	NM_019510	R[-195,-190]
-1.21	0.0390602	Olfr472	NM_146774	F[-214,-209]
-1.28	0.0420486	Thr	NM_022312	
-1.22	0.0480480	Thrb	NM_009380	
-1.23	0.0480480	Wtbc10	NM_001039501	
-1.21	0.0505848	Apoa2	NM_013474	
-1.40	0.0514604	Fmn2	NM_019445	
-1.31	0.0526340	Kctd13	NM_172747	
-1.32	0.0526340	Ndufb2	NM_153064	F[-146,-141]
-1.36	0.0534332	Slit1	NM_019748	
-1.27	0.0546000	1110001A16Rik	NM_001177403	
-1.33	0.0633489	Calb1	NM_009788	
-1.79	0.0636835	Car3	NM_007606	
-1.25	0.0660967	Tac2	NM_009312	
-1.81	0.0665375	Myo7a	NM_008663	
-1.25	0.0683989	Shisa2	NM_145463	R[-141,-136]
-1.22	0.0726221	Pla2r1	NM_008867	F[+19,+24]
-1.46	0.0737333	Adh6b	ENSMUST00000090166	
-1.71	0.0737333	Egr1	NM_007913	
-1.43	0.0737333	Ptch-ps1	NR_003517	
-1.30	0.0786461	Bai1	NM_174891	R[-216,-211]
-1.25	0.0786461	Cetn4	NM_145825	
-1.33	0.0805296	Calcrl	NM_018782	
-1.22	0.0844679	Hdhd2	ENSMUST00000097522	
-1.26	0.0844679	Nipa1	NM_153578	
-1.21	0.0847722	Btrc	NM_001037758	
-1.26	0.0866818	1110038F14Rik	BC038324	F[-147,-142]
-1.25	0.0866818	Dgkg1	NM_177639	
-1.33	0.0866818	Rnu1b1	NR_004412	
-1.22	0.0909977	Col12a1	NM_007730	
-1.26	0.0966127	6330527O06Rik	NM_029630	
-1.20	0.0971102	9430419L09Rik	NM_029982	

Table S5 Gene functional classification of FDR<0.1 differentially expressed genes according to DAVID software

Cell component

Category	Term	Count	%	PValue
GOTERM_CC_ALL	GO:0005930~axoneme	3	0.24979184	0.02488712
GOTERM_CC_ALL	GO:0005929~cilium	4	0.333055787	0.060501552
GOTERM_CC_ALL	GO:0042995~cell projection	8	0.666111574	0.087134173

Molecular function

Category	Term	Count	%	PValue
GOTERM_MF_ALL	GO:0022892~substrate-specific transp	11	0.915903414	0.040841631
GOTERM_MF_ALL	GO:0019842~vitamin binding	4	0.333055787	0.041974993
GOTERM_MF_ALL	GO:0022891~substrate-specific transr	10	0.832639467	0.043879413
GOTERM_MF_ALL	GO:0043167~ion binding	34	2.830974168	0.044126502
GOTERM_MF_ALL	GO:0046872~metal ion binding	33	2.747710241	0.053438211
GOTERM_MF_ALL	GO:0043169~cation binding	33	2.747710241	0.059530551
GOTERM_MF_ALL	GO:0005372~water transporter activity	2	0.166527893	0.073753738
GOTERM_MF_ALL	GO:0022857~transmembrane transpo	10	0.832639467	0.076449386
GOTERM_MF_ALL	GO:0008324~cation transmembrane t	7	0.582847627	0.090200532

Biological process

Category	Term	Count	%	PValue
GOTERM_BP_ALL	GO:0051656~establishment of organe	4	0.333055787	0.001443265
GOTERM_BP_ALL	GO:0051640~organelle localization	4	0.333055787	0.00543927
GOTERM_BP_ALL	GO:0007263~nitric oxide mediated sig	2	0.166527893	0.013178504
GOTERM_BP_ALL	GO:0010273~detoxification of copper	2	0.166527893	0.019703173
GOTERM_BP_ALL	GO:0030001~metal ion transport	8	0.666111574	0.027040781
GOTERM_BP_ALL	GO:0006882~cellular zinc ion homeos	2	0.166527893	0.045377764
GOTERM_BP_ALL	GO:0046688~response to copper ion	2	0.166527893	0.045377764
GOTERM_BP_ALL	GO:0055069~zinc ion homeostasis	2	0.166527893	0.051691759
GOTERM_BP_ALL	GO:0006812~cation transport	8	0.666111574	0.054146939
GOTERM_BP_ALL	GO:0051234~establishment of localiza	23	1.915070774	0.054561691
GOTERM_BP_ALL	GO:0007059~chromosome segregatic	3	0.24979184	0.066951758
GOTERM_BP_ALL	GO:0002087~regulation of respiratory	2	0.166527893	0.076537201
GOTERM_BP_ALL	GO:0044065~regulation of respiratory	2	0.166527893	0.076537201
GOTERM_BP_ALL	GO:0042044~fluid transport	2	0.166527893	0.076537201
GOTERM_BP_ALL	GO:0006833~water transport	2	0.166527893	0.076537201
GOTERM_BP_ALL	GO:0051650~establishment of vesicle	2	0.166527893	0.076537201
GOTERM_BP_ALL	GO:0015674~di-, tri-valent inorganic c	4	0.333055787	0.090851462
GOTERM_BP_ALL	GO:0051648~vesicle localization	2	0.166527893	0.094747616
GOTERM_BP_ALL	GO:0006836~neurotransmitter transpo	3	0.24979184	0.098170576
GOTERM_BP_ALL	GO:0006811~ion transport	9	0.74937552	0.098468846

Genes	List Total	Pop Hits	Pop Total	Fold Enrich	Bonferroni	Benjamini	FDR
TULP3, DNAHC9, RPGRIP1	106	37	15855	12.12774	0.99266	0.99266	26.98984
TULP3, MYO7A, DNAHC9, RPGRIP1	106	135	15855	4.431866	0.999995	0.997723	54.11307
ARHGAP31, TULP3, MYO7A, DNAHC9, CETN	106	575	15855	2.08105	1	0.99733	67.95207

Genes	List Total	Pop Hits	Pop Total	Fold Enrich	Bonferroni	Benjamini	FDR
SLC6A9, TRPC3, STARD6, AQP4, KCNJ10, A	99	840	15404	2.037566	0.999996	0.999996	42.67146
AGXT2L1, P4HA3, CALB1, PDXDC1	99	121	15404	5.143668	0.999997	0.998284	43.56873
SLC6A9, TRPC3, AQP4, KCNJ10, ATP1A2, C/	99	734	15404	2.119836	0.999998	0.988231	45.04724
PLCZ1, TSHZ2, ZCCHC24, THRB, ADAMTS1(	99	3934	15404	1.344754	0.999998	0.964947	45.23642
PLCZ1, TSHZ2, ZCCHC24, THRB, ADAMTS1(	99	3850	15404	1.33368	1	0.961696	51.94189
PLCZ1, TSHZ2, ZCCHC24, THRB, ADAMTS1(	99	3885	15404	1.321665	1	0.952075	55.90895
AQP4, SLC14A1	99	12	15404	25.93266	1	0.961252	64.02121
SLC6A9, TRPC3, AQP4, KCNJ10, ATP1A2, C/	99	819	15404	1.899829	1	0.947793	65.39347
SLC6A9, TRPC3, KCNJ10, ATP1A2, CACNA2I	99	487	15404	2.236492	1	0.955822	71.67101

Genes	List Total	Pop Hits	Pop Total	Fold Enrich	Bonferroni	Benjamini	FDR
FMN2, MYO7A, NLGN1, SLIT1	95	34	14219	17.60867	0.67865	0.67865	2.187592
FMN2, MYO7A, NLGN1, SLIT1	95	54	14219	11.08694	0.986253	0.882752	8.013347
MT2, MT1	95	2	14219	149.6737	0.99997	0.96906	18.38547
MT2, MT1	95	3	14219	99.78246	1	0.979966	26.26961
PLCZ1, TRPC3, NIPA1, KCNJ10, ATP1A2, CA	95	442	14219	2.709026	1	0.986558	34.28324
MT2, MT1	95	7	14219	42.76391	1	0.99772	50.89433
MT2, MT1	95	7	14219	42.76391	1	0.99772	50.89433
MT2, MT1	95	8	14219	37.41842	1	0.997419	55.63963
PLCZ1, TRPC3, NIPA1, KCNJ10, ATP1A2, CA	95	515	14219	2.325028	1	0.995786	57.36627
PLCZ1, TRPC3, MYO7A, NLGN1, AQP4, NIPA	95	2358	14219	1.459921	1	0.992553	57.65167
FMN2, REC8, HJURP	95	64	14219	7.015954	1	0.99569	65.39822
NLGN1, ATP1A2	95	12	14219	24.94561	1	0.996619	70.4595
NLGN1, ATP1A2	95	12	14219	24.94561	1	0.996619	70.4595
AQP4, SLC14A1	95	12	14219	24.94561	1	0.996619	70.4595

AQP4, SLC14A1	95	12	14219	24.94561	1	0.996619	70.4595
MYO7A, NLGN1	95	12	14219	24.94561	1	0.996619	70.4595
PLCZ1, TRPC3, NIPA1, CACNA2D3	95	161	14219	3.718601	1	0.998048	76.74501
MYO7A, NLGN1	95	15	14219	19.95649	1	0.997567	78.2253
SLC6A9, NLGN1, ATP1A2	95	80	14219	5.612763	1	0.996976	79.45265
PLCZ1, TRPC3, NIPA1, KCNJ10, ATP1A2, CA	95	712	14219	1.891943	1	0.995625	79.55648

Mutation in *Hmx1* causes craniofacial and chest deformities in mice

Linda Bapst-Wicht, Fabienne Marcelli, Victor Steininger, Mélissa Pochon, Valérie Malfroy Camine, Ulrike Kettenberger, Daniel F. Schorderet

Submitted

2015

- Experiments shown in figures 1 to 5 and 7 have been made by myself
- Experiments shown in figure 6 have been made by myself, V. Steininger, V. Malfroy Camine and U. Kettenberger
- Experiments shown in figure 8 have been made by F. Marcelli
- Experiments shown in sup. Figure 1 have been made by myself and M. Pochon
- The paper has been written by myself and D. Schorderet for abstract, introduction, result and discussion
- The materials and methods section has been written by myself, F. Marcelli, V. Malfroy Camine, U. Kettenberger and D. Schorderet

Mutation in *Hmx1* causes craniofacial and chest deformities in mice

Running title:

Craniofacial deformities in Dumbo mice

Linda Bapst-Wicht[1,2], Fabienne Marcelli[1], Victor Steininger[2], Mélissa Pochon[2], Valérie Malfroy Camine[2], Ulrike Kettenberger[2], Daniel F. Schorderet[1,2,3,*]

[1]IRO-Institute for Research in Ophthalmology, Sion, Switzerland; [2]EPFL- Faculty of Life Science, Swiss Federal Institute of Technology, Lausanne, Switzerland; [3]UNIL-Dept. of Ophthalmology, University of Lausanne, Lausanne

* Corresponding author

Address correspondence to:

Daniel F. Schorderet, Institute for Research in Ophthalmology, Av. du Grand-Champsec 64, 1950 Sion, Switzerland.

E-mail: daniel.schorderet@irovision.ch

Keywords

Hmx1, craniofacial malformation, cleft palate, chest deformity, cranial neural crest.

ABSTRACT

The H6 homeobox 1 (*HMX1*) gene encodes a transcription factor from the *HMX/NKX5* family. Hmx1 is expressed in the developing sensory nervous system, retina and craniofacial mesenchyme. Mutations at the *HMX1* locus lead to mild craniofacial defects restricted to the ear and neighbouring structures in humans, rats, cows and mice. In humans, mutations in *HMX1* are responsible for the oculo-auricular syndrome of Schorderet-Munier-Franceschetti (OAS-SMF), a developmental defect causing multiple ophthalmic anomalies, microphthalmia, retinal degeneration and external ear malformations. The mouse model for *Hmx1* loss-of-function mutation, called dumbo ($Hmx1^{dmbo}$), also exposes ear deformities and exhibits 50% perinatal lethality. In the dumbo mouse embryo, Hmx1 is expressed in the craniofacial mesenchyme in specific regions of the 2nd branchial arch, the developing eye, otic vesicle and in the posterior mesenchyme. Dumbo mice show general growth retardation, and persistence of microphthalmia in adulthood, but without the OAS eye phenotype. Here we introduce a new perspective through detailed analysis of the craniofacial defects present in stillborn dumbo pups. The death ratio of newborn homozygous individuals confirms the perinatal lethality of the mutation. Unlike their surviving littermates, dumbo stillborns present critical craniofacial and chest deformities, such as cleft palate and bone hypoplasia of premaxilla, maxilla, palate, zygomatic process, frontal and mandible. In some cases, thoracic cage malformations were also observed. These lethal deformities provide a new explanation for the lethality of the mutated mice. They also highlight a new HMX1 pathway in craniofacial morphogenesis.

INTRODUCTION

Transcription factors from the homeobox gene family were first described in the *Drosophila melanogaster*, and later identified in most mammals and birds [1]. In human, a 60-amino acid homeobox domain defines the HMX homeobox family of transcription factors, previously known as NKX5 family. Homeobox genes are known to play critical roles in organ development, and deregulation of the process has morphological consequences [1-2]. Within this family, the H6 family homeobox 1 (*HMX1*) gene (MIM 142992), located on human chromosome 4, is expressed in the retina in 5 week-old human embryos, in the developing auricular mesenchymal cells and in the perichondrium of the intrinsic cartilages of the pinna in 20 week-old fetuses [3]. In the developing mouse, Hmx1 is expressed in the peripheral nervous system, the otic vesicle and in cranial neural crest derived cells: the developing eye, the trigeminal ganglion, and the 2nd branchial arch [4,5]. To date, mutations at the *HMX1* locus have been linked to mild craniofacial defects restricted to the ear and its neighbouring structures in cows, rats and mice [4,6,7,8]. In human, homozygous mutations in *HMX1* are responsible for the oculo-auricular syndrome of Schorderet-Munier-Franceschetti (OAS-SMF) (MIM : 612109) [3,9,10]. This syndrome is characterized by several features including ophthalmic anomalies (microcornea, microphthalmia, cataract, anterior-segment dysgenesis, coloboma, rod-cone dystrophy, and retinal pigment epithelial modifications) and an unusual cleft earlobe. In this study, we focused on the dumbo mouse originating from a random ENU mutagenesis of proximal mouse chromosome 5 [11]. The *Hmx1* dmbo allele involves a nonsense mutation that lies in the amino-terminal side of the homeodomain, resulting in an undetectable truncated mutant protein. The *Hmx1* dmbo allele is thus considered a functionally null mutation [5]. Dumbo mice exhibited enlarged ear pinnae with apparent ventrolateral shift. Skull malformations were mild, with only hyperplasia of the gonial bone and irregularities along the caudal border of the squamous temporal bone. Only moderate degrees of microphthalmia were reported, and no retinal degeneration was detected, whether in young or adult mice [4]. Despite recent studies, the *HMX1* pathway remains incompletely understood and the dumbo mouse should represent a good model for further investigation.

In the study of craniofacial birth defects, mouse models have enabled progress in the understanding of evolution and regulation of both craniofacial development and syndromes [12]. The molecular mechanisms underlying fate determination of cranial

neural crest (CNC) cells, which eventually form craniofacial structures such as bone, cartilage, teeth, nerves and muscle, are complex and numerous. Several pathways, including Endothelin, Ephrin and other members belonging to the transforming growth factors family (such as *Bmp4* or *Fgf8*) have already been shown to be critical [12,13,14,15].

Like humans [10], dumbo mice exhibit some craniofacial malformations. Since cells expressing Hmx1 are found in the CNC-derived progenitor site from which most of the craniofacial skeleton and cartilage originates [16,17] (Fig. 1), we decided to investigate the potential implications of *Hmx1* in craniofacial development. This study also aims at providing a new explanation for the semi-lethality in dumbo mice and suggesting new potential roles for *HMX1*.

RESULTS

Perinatal lethal mutation of Hmx1

For this study we obtained dumbo mice bearing the *Hmx1 dmbo* allele (*Hmx1*^{dmbo}) strain C57BL/6;C3HeB/FeJ-Hmx1$^{dmbo/Rw/JcsJKjn}$, from Jackson Laboratories (Stock #008677). Mice were then backcrossed to C57BL/6J for 5 generations to eliminate the rd1 phenotype due to a mutation in *Pde6b*, also located on chromosome 5 (see *Materials and methods*).

To decipher unrevealed impact of Hmx1 mutation we monitored 4 mixed crossings of *Hmx1*$^{dmbo/dmbo}$ with *Hmx1*$^{dmbo/+}$ mice, and 6 crossings of heterozygous *Hmx1*$^{dmbo/+}$ parental mice. Pregnancy of females was recorded by daily weight measurements in the morning, which allowed detection of premature loss of litters (S1 Figure), and precise counting of litters at birth, including the number of stillborn (Table 1). We observed an increased level of perinatal death compared to control C57BL/6J mice, generating 30 stillborn over 77 births in dumbo breeding (39% of total birth) (Table 1). Z-Test of proportion (lower tailed test, $p = 0.05$) confirmed that the occurrence of the *Hmx1*$^{dmbo/dmbo}$ genotype in heterozygous crossings as well as in mixed crossings was lower than the expected Mendelian proportion. In heterozygous crossings, a Chi-Square Test of Independence ($p = 0.05$), confirmed that *Hmx1*$^{dmbo/dmbo}$ had reduced chances of survival compared to *Hmx1*$^{dmbo/+}$ and *Hmx1*$^{+/+}$ newborns. It is important to mention that the overall high perinatal mortality also observed in non-homozygous pups could be due to the stress of the dams induced by the daily weighting during pregnancy. Nevertheless this bias was the same for all members of the breeding experiment. The stillborns were genotyped and further analyzed.

Table 1: Breeding statistics in Dumbo strain.

Genotype	Mendelian proportion	# Individuals total	# Individuals alive	# Individuals dead	Observed proportion
Hmx1$^{dmbo/+}$ cross *Hmx1*$^{dmbo/+}$					
Hmx1$^{+/+}$	0.25	14	7	7	0.33
Hmx1$^{dmbo/+}$	0.5	23	17	6	0.53
Hmx1$^{dmbo/dmbo}$	0.25	6	1	5	0.14
Hmx1$^{dmbo/+}$ cross *Hmx1*$^{dmbo/dmbo}$					
Hmx1$^{dmbo/+}$	0.5	24	21	3	0.71
Hmx1$^{dmbo/dmbo}$	0.5	10	1	9	0.29

Finally, as with the data found for the dumbo mice backcrossed with C57BL/6N [5], we did not detect exencephaly in the collected stillborn pups, this being only observed in the *Dmbo Rw* mice. Our results confirm the previous hypothesis that this phenotype arises from interactions with other alleles associated with *Rw* or 6N genetic backgrounds [4,11].

Craniofacial and chest deformities in dumbo stillborn

As many dumbo mice were stillborn, or died within the first few days of life, we investigated their craniofacial and chest phenotypes in detail and compared them to surviving dumbo mice. Because of its particular specific expression in the otic vesicle and developing eye, *Hmx1* has mainly been studied for its role in the development of these organs [4]. However, Hmx1 is also present in CNC-derived cells and in the 2nd branchial arch, these giving rise to most of the cartilage and bones of the skull, facial and branchial skeletons [18] (Fig. 1). To characterize bone morphology, control C57BL/6J newborns from P1 to P3 were euthanized by decapitation. Stillborns from dumbo breeding, being either from control genotypes (*Hmx1*$^{+/+}$ and *Hmx1*$^{dmbo/+}$) or homozygous genotype

(*Hmx1*$^{dmbo/dmbo}$), were collected after birth. Genotypes were assessed by *Hmx1* sequencing. Among the dumbo crosses, craniofacial or chest malformations were observed in 8 out of 11 *Hmx1*$^{dmbo/dmbo}$, 1 out of 10 *Hmx1*$^{dmbo/+}$ and 0 out of 3 *Hmx1*$^{+/+}$ mice. There is a significant predominance of craniofacial malformation in homozygote dumbo stillborn compared to heterozygote stillborn (T-test: $p = 0.05$). Two out of 8 C57BL/6J control mice also showed some craniofacial deformity, i.e., hyperplasia of the tympanic bullae that was never observed in the dumbo mice.

Fixed skeletal whole mounts were stained with alizarin red and alcian blue to directly visualize bone and cartilage (Fig. 2-5). In addition, microCT scans of several specimens were taken (Fig. 6). Both types of analysis confirmed craniofacial and chest deformities in dumbo homozygous stillborn mice. As previously reported [4,11], surviving dumbo homozygotes present phenotypic variations of a skeletal nature: laterally-protruding ears, hyperplasia of the gonial bone, deformation of the border of the squamous temporal bone and enlargement of its retrotympanic process. In addition, we showed that stillborn homozygotes presented critical craniofacial and chest deformities, such as cleft palate, bone hypoplasia of premaxilla, maxilla, palate, zygomatic process, orbital region and mandible (Fig. 2-6). At birth, the maxillary and palatine processes converged toward the midline in wild-type mice (Fig. 2A). In *Hmx1*$^{dmbo/dmbo}$ stillborn mice, palatal deformity was observed. The maxillary and palatine processes were absent (Fig. 2B,C and 6B,F), thus forming a cleft palate and exposing the vomer and the presphenoid. The maxilla was the most impacted bone of the craniofacial structure. In 6/11 of the affected specimens, we observed maxilla hypoplasia (Supporting table 1). The ocular globe develops between the supportive orbitosphenoid bone and the zygomatic process; in dumbo mice both structures were altered. *Hmx1*$^{dmbo/dmbo}$ stillborn mice presented hypoplasia of the orbitosphenoid and an incomplete closure of the anterior ethmoid foramen rising from the frontal bone in 2/11 of the cases (Fig. 3B,C and 6D). Moreover, the zygomatic process failed to form (Fig. 6D,H), with hypoplasia of the jugal and the zygomatic process of the squamosal and maxilla in 3/11 of the cases (Supporting table 1). Mandibles were afflicted to a lesser extent. In general, only the dental structure failed to form and the lower incisors were missing (Fig. 4C,D). One exception was observed in an animal presenting massive malformations with a large part of both mandibles missing (Fig. 4B), with no possible doubt of damaged inflicted by maternal eating as the skin was not affected.

Although not derived from cranial neural crest cell progenitors, bones of the chest presented deformities in 5/11 of the cases (S2 Table). Two types of malformations were observed: either an asymmetric fusion of the ribs causing an asymmetric deformity of the stenebrae (Fig. 5B and 6I), or an axial segmentation of the 4^{th} stenebra and the xiphisternum (Fig. 5C,D,E).

The remainder of the skeleton and the limbs appeared normal (data not shown) despite their smaller size according to the growth curve of homozygous mice (see below). We conclude that a lack of Hmx1 specifically affects the growth of craniofacial and sternal bones. A summary of the affected cranial bones in dumbo mice is detailed in Fig. 7.

Eye phenotype in dumbo mice

As suggested by the name of the mutation, dumbo mice exhibit a marked displacement of the pinna, visible both in adults [4,19] and in newborns [6]. Additionally to the ear, microphthalmia has been quantitatively associated in newborn dumbo homozygotes with a reduction of 9% of the eye diameter [6]. In the present study, measurements of the enucleated eye diameter in homozygotes compared to heterozygotes revealed that microphthalmia was conserved until adulthood with an ocular diameter at 2 months of 3.02 ± 0.15 mm compared to 3.32 ± 0.09 mm for the heterozygotes ($p < 0.0001$). We also observed in several dumbo homozygote mice an association of blepharophimosis with microphthalmia (data not shown).

Decreased body mass in dumbo mice

Dumbo homozygote mice were reported to have a reduced body mass between P3 and P10 [4]. To further investigate whether a catch-up phenomenon was taking place during growth, mice from both intercrosses of homozygotes together or homozygotes and heterozygotes were weighed once a week from week 4 to week 26. Both males and females weighed around 15% less than heterozygotes up to 6 months (Fig. 8).

DISCUSSION

The dumbo mouse is an interesting model to study *Hmx1*. The fact that stillborn exhibit unexpected craniofacial and chest deformities compared to all previously published

phenotypes [4,6,11] brings a new perspective to its role. The skeletal structure deformities in dumbo mice observed in our study were not restricted to the pinna, but were also observed in the following bones at various degrees: maxilla, squamous, palate, jugal, frontal, orbitosphenoid, mandible and stenebrae.

Expression patterns of *Hmx1* and craniofacial development

It has previously been shown that *Hmx1* was expressed in craniofacial mesenchyme originating from both neural crest and mesoderm derived progenitors [5]. It is therefore interesting to focus on the connection between those cells and craniofacial development. The head structure, from the hyoid to the tip of the parietal, emerges from the extension of branchial arches (BA) 1 to 4. BAs expand during embryonic development by proliferation of neural crest cells from the neural plate: forebrain, midbrain and hindbrain [20]. This migration of CNC cells occurs between the rostral cranial axis and the posterior-anterior cranial axis and is concomitant with the activation of several homeodomain transcription factors, including *Hox*, *Dlx*, *Otx* and *Emx* genes [18,21].

We previously showed that *Ptpro,* a negative regulator of Ephrin receptors [22], *Epha6*, and *Sema3f* expressions were regulated by Hmx1 [23,24]. Both mutations reported so far in the OAS-SMF syndrome abolished HMX1 ability to regulate EPHA6, *Sema3f* and *Ptpro* [10,24]. In mice, Neuropilin 2 receptor is expressed in migrating CNC cells targeting BA1 and BA2 and its ligand Sema3f is secreted in the caudal midbrain. They synergistically prevent intermingling of the CNC cells stream between BA1 and BA2, and are essential for CNC cells migration and trigeminal ganglion condensation [25].

Later in development, craniofacial skeletal elements formation is driven by two structures: BA mesoderm and mesenchyme on one hand and neural crest progenitors on the other hand [18,20,26,27]. As *Hmx1* is not expressed in the bone precursor cells located at the sites of malformation between E10.5 and E13.5 [4,5], it would be interesting to analyze expression patterns at later embryonic stages, for example when the palatal process development occurs between E11.5 and E16.5 [12]. Taken together, this indicates that Hmx1 may play a regulatory role during the segregation of the migrating CNC cells. Therefore, absence of Hmx1 in dumbo mice might either affect the fate determination of CNC cells, and/or influence Ephrin and Semaphorin signaling, resulting in the observed craniofacial malformations. Thus, even if *Hmx1* is not expressed in the

maxillary process of BA1, its location along the midbrain could potentially interact with the maxillary and frontal development. In this study we essentially focused on the skeletal derivatives, and it remains to be determined if cranial nerve and muscle derivatives are also affected by the absence of Hmx1 in the dumbo mouse model.

Cleft palate, frontal and maxilla hypoplasia & chest deformities

The fate of CNC cells does not solely rely on an intrinsic program, but also depends on several growth factor signaling pathways that are expressed by the ectoderm and endoderm. The mandible originates from the mandibular process of BA1 and relies on two major signaling pathways: Fgf at the proximal part and Bmp at the distal part. Specifically, loss of Bmp signaling can lead to defects of the distal region or a completely missing mandible [28]. Bmp4 is also responsible for the development of incisors from the mandibular ectoderm. In this study we only observed modification impacting the lower incisor, while molar development could not be assessed, as these teeth are not observable at birth.

Palate development is a multistep process including palatal shelf growth and elevation, fusion of the shelves and disappearance of the midline epithelium. This process starts at E11.5 and terminates around E16.5. In most models of cleft palate, gene mutations result in the failure of cell proliferation that occurs on various areas of palate growth, depending on the gene mutated [12]. Interestingly, in our study the palatine cleft and the failure of bone closure from each shelf are concordant with multiplication failure of the embryonic craniofacial mesenchymal cells, as observed in Basonuclin 2 (*Bnc2*) null mice [29,30]. In this model, all palatogenesis processes occur normally up to elevation at E15.5, but growth insufficiency of the palatal processes leads to a cleft at birth. We observed the same feature in the dumbo mice, where palatal processes of palate and maxilla are present but very reduced (Fig. 2). However, unlike with *Bnc2*$^{-/-}$, we did not observe calvarial defects. This suggests that Hmx1 might act on the multiplication of mesenchymal cells and be restricted to specific bones. Another mouse model that exhibits several of the features observed in dumbo is the Ephrin-B1 null mouse. During development, Ephrin-B1 binds to EphB2 and EphB3 receptors, and its complete loss of function results in variable degrees of cleft palate, malformation of the tympanic ring and rib pairing defects [31]. The rib defects resemble those of dumbo mice (Fig. 5). Compound heterozygous

mutations in *EphB2* and *EphB3* also lead to a cleft palate phenotype [32]. The implication of EphB1 and EphB2 in the development of the calvarial bone [33], a structure not deficient in dmbo mice, would suggest that they are not targets of Hmx1. The potential interaction of Hmx1 on EphB3 remains open.

In our study, the maxilla was one of the most frequently impacted bones (Fig. 6B,D,H). Suture of the frontal and the maxillary bone occurs between E19 and P0 and is crucial for the support of the eye. Malformation of the palatal process is a common pattern in cleft palate and elucidates part of the observed phenotype in dumbo mice. However, concerning the hypoplasia of the rostral part of the maxilla including the suture with the frontal and the zygomatic processes (Fig. 6D,H), we failed to find a similar mouse phenotype in the literature. A potential explanation could be that *EphA6*, a direct target of Hmx1 [24] and a gene expressed in the maxillary process at E12.5 [32], is dysregulated during this process. However, this remains to be shown.

Concerning the optic area, an interesting mouse model with selective modulation of *Fgf8* expression presented comparable malformations of the optic capsule with maxilla, ala orbitalis, alisphenoid and orbitosphenoid defects [34]. However, the *Fgf8* mutant also exhibits complete midline cleft, which was not the case in dumbo mice.

The dumbo mouse is a model for craniofacial morphogenesis defect

Until now, it was suggested that, with the exception of humans, Hmx1 was restricted to the developmental pathway of pinna morphogenesis [6]. However, our current data indicate that craniofacial malformations are a prominent feature of dumbo stillborn mice and that Hmx1 contributes to the development of skeletal structures such as maxilla, squamous, palate, jugal frontal, orbitosphenoid, mandible and stenebrae. Interestingly, the phenotype observed in humans with OAS-SMF seems to be more restricted to the eye [3,10]. This difference might be explained by the absence of data concerning neonatal cases of lethality in this syndrome. In the future, it will be interesting to study the eye phenotype of stillborn dumbo mice. Moreover, our observations did not allow us to exclude intrauterine death or embryonic developmental retardation, as the overall Mendelian ratio was lower than expected even when counting dead animals (Table 1). It is possible that some pups may have been unaccounted for because the dams ate them before the first inspection. It may be interesting to evaluate this further.

To conclude, our data suggest an important implication of Hmx1 in the branchial arch patterning and craniofacial morphogenesis. Several pathways mimicking the dumbo phenotype are key targets for further studies. An emphasis on Semaphorin and Ephrin pathways should be given in regard to the latest in vitro studies performed on Hmx1 [10,23,24].

MATERIALS AND METHODS

Mice and genotyping

Hmx1 mice bearing the *dmbo* allele (*Hmx1*^{dmbo}) strain C57BL/6;C3HeB/FeJ-Hmx1$^{dmbo/Rw/JcsJKjn}$ were obtained from Jackson Laboratories (Stock #008677). The *Hmx1*^{dmbo} allele was induced by ENU mutagenesis of C57BL/6 inbred mice. By routine genetic control of the strain we detected a mutation in the *Pde6b* gene, also located on the chromosome 5, leading to the rd1 phenotype, characterized by early retinal degeneration. To eliminate the latter mutation we backcrossed the mice to C57BL/6J for 2-5 generations prior to the aforementioned experiments. Mice were housed at our animal facility in 1284L Eurostandard type II L cages from Techniplast (Indulab AG, Gams, Switzerland) fitted with Lignocel select (J. Rettenmaier & Söhne, Rosenberg, Germany) under a 12/12 hr light/dark cycle. All animals had unrestricted access to tap water and food (pellet standard diet, Provimi-Kliba SA, Kaiseraugst, Switzerland). Couples were put together until pregnancy was obvious, then males were separated. Analyzing all the pups, including stillborn, helped comply with the 3Rs. The studies adhered to the Association for Research in Vision and Ophthalmology (ARVO) Statement for the Use of Animals in Ophthalmic and Vision Research and were approved by the Veterinary Service of the State of Valais (Switzerland). C57BL/6J mice were obtained from Janvier (Le Genest St Isle, France).

Genotypes were determined by PCR of ear punch genomic DNA in the case of living individuals and of tail genomic DNA in the case of stillborn and sacrificed individuals. Genotyping of the *Hmx1*^{dmbo} and wild-type *Hmx1* (*Hmx1*$^{+}$) alleles were performed by PCR using oligonucleotide primers surrounding the *dmbo* mutation (forward primer: 5'-GCGCTCAACCCAGGGCGATG -3', reverse primer: 5'-ACCACCTCCGTAGCCGCCGTGCAC-3'). The amplicon obtained was then sequenced and analyzed by Sanger methods using the forward primer to decipher wild-type, homozygous and heterozygous dumbo mice.

Skeletal analysis

Newborns, from P1 to P3, from control group (C57BL/6J) were sacrificed by decapitation. Stillborn from dumbo breeding, either controls (*Hmx1*$^{+/+}$ and *Hmx1*$^{dmbo/+}$) or homozygote (*Hmx1*$^{dmbo/dmbo}$) mice were collected after birth. Alcian blue and alizarin red staining was performed on pups' skeleton according to prior published methods [35].

Images were acquired on a dissecting microscope equipped with a digital camera (Leica DFC 310 FX).

MicroCT imaging, data processing and analysis

CT scans were performed with a small rodent microCT (Skyscan 1076, Bruker microCT, Kontich, Belgium) to assess the bone structure of the head and chest skeletal part of newborn mice from the control (C57BL/6J) and homozygote (*Hmx1*$^{dmbo/dmbo}$) groups. Scanning of the homozygotes was done after alcian blue and alizarin red staining. The skeletal parts were initially stored in 1:1 glycerol:ethanol solution and transferred to 1.5 ml Eppendorf tubes filled with pure ethanol for scanning. All skeletal parts were separated with paraffin films to avoid contact between the different samples. The scanning parameters were the following: no filter, voltage 40 kV, current 250 µA, exposure time 750 ms and rotation step 0.5°. The spatial resolution was set to 9.2 µm. A reconstruction of the projection images was done with NRecon Server (Bruker microCT, Kontich, Belgium) using a ring artefact correction of 15 and a dynamic range for image conversion extending from 0.005 to 0.07. Stacks of cross-sections in 8-bit bitmap format were received as reconstruction output. The datasets were segmented and visualized manually with the Amira software (FEI Visualization Sciences Group, Mérignac, France).

Survey of lethality in dumbo mice

4 mixed crossings of *Hmx1*$^{dmbo/dmbo}$ with *Hmx1*$^{dmbo/+}$ mice and 6 crossings of heterozygous *Hmx1*$^{dmbo/+}$ parental mice were observed daily for mating and survey of pregnancy. Females were weighed each day during 83 days to assess the progression of the pregnancy and detect premature loss of litter. At birth, newborn and stillborn were counted, and the later ones removed for further analysis. All individuals were genotyped (see *Mice and genotyping*), and statistical analysis was performed on the proportion of each genotype among the litter and on the death ratio (Table 1).

Measurement of microphthalmia

Hmx1$^{dmbo/dmbo}$ and *Hmx1*$^{dmbo/+}$ mice were sacrificed at 2 months-of-age by cervical dislocation, eyes were extracted and the measurement of eye diameter was performed perpendicularly to the optic nerve axis under a stereomicroscope with a graduated objective.

Weighing of mice

10 *Hmx1*$^{dmbo/+}$ and 10 *Hmx1*$^{dmbo/dmbo}$ mice were weighed once a week from 4 weeks to 6 months-of-age.

ACKNOWLEDGMENTS

We would like to thank Pr. Pioletti from the Laboratory of Biomechanical Orthopedics at EPFL, Lausanne, Switzerland for allowing us to use the microCT scan and for the help with data processing. Ms Susan E. Houghton for editing the manuscript.

REFERENCES

1. Wang W, Lo P, Frasch M, & Lufkin T. Hmx: an evolutionary conserved homeobox gene family expressed in the developing nervous system in mice and Drosophila. *Mech Dev.* 2000; 99: 123–37.
2. Stanfel MN, Moses KA, Schwartz RJ, Zimmer WE.. Regulation of organ development by the NKX-homeodomain factors: an NKX code. *Cell Mol Biol.* 2005; 51: 785-799.
3. Schorderet DF, Nichini O, Boisset G, Bozena P, Tiab L, Mayeur H, Munier FL. Mutation in the Human Homeobox Gene NKX5-3 Causes an Oculo-Auricular Syndrome. *Am J Hum Genet.* 2008; 82: 1178–1184.
4. Munroe RJ, Prabhu V, Acland GM, Johnson KR, Harris BS, O'Brien TP, Schimenti, JC. Mouse H6 Homeobox 1 (Hmx1) mutations cause cranial abnormalities and reduced body mass. *BMC Developmental Biology.* 2009; 9: 27.
5. Quina LA, Tempest L, Hsu Y-WA, Cox TC, & Turner EE. Hmx1 is required for the normal development of somatosensory neurons in the geniculate ganglion. *Dev Biol.* 2012; 365: 152–163.
6. Quina LA, Kuramoto T, Luquetti DV, Cox TC, Serikawa T, & Turner EE. Deletion of a conserved regulatory element required for Hmx1 expression in craniofacial mesenchyme in the dumbo rat: a newly identified cause of congenital ear malformation. *Dis Model Mech.* 2012; 5: 812–22.
7. Koch CT, Bruggmann R, Tetens J, & Drögemüller C. A Non-Coding Genomic Duplication at the HMX1 Locus Is Associated with Crop Ears in Highland Cattle. *PLoS ONE.* 2013; 8: e77841.
8. Turner EE, & Cox TC. Genetic evidence for conserved non-coding element function across species-the ears have it. *Frontiers in Physiology.* 2014; 5: 7.
9. Vaclavik V, Schorderet DF, Borruat F-X, & Munier FL. Retinal dystrophy in the oculo-auricular syndrome due to HMX1 mutation. *Ophthalmic Genet.* 2011; 32: 114–7.
10. Gillespie RL, Urquhart J, Lovell SC, Biswas S, Parry NR, Schorderet DF, Lloyd IC, Clayton-Smith J, Black GC. Abrogation of HMX1 Function Causes Rare Oculoauricular Syndrome Associated With Congenital Cataract, Anterior Segment Dysgenesis, and Retinal Dystrophy. *Invest Ophthalmol Vis Sci.* 2015; 56: 883-891.

11. Wilson L, Ching Y, Farias M, Hartford SA, Howell G, Shao H, Schimenti JC. Random mutagenesis of proximal mouse chromosome 5 uncovers predominantly embryonic lethal mutations. *Genome Res.* 2005; 15: 1095–1105.
12. Chai Y, & Maxson RE. Recent advances in craniofacial morphogenesis. *Dev Dyn.* 2006; 235: 2353–75.
13. Clouthier DE, Garcia E, Schilling TF. Regulation of facial morphogenesis by Endothelin signaling: Insight from Mice and Fish. *Am J Med Genet.* 2011; 152: 2962–2973.
14. Hajihosseini MK, Lalioti MD, Arthaud S, Burgar HR, Brown JM, Twigg SRF, Heath JK. Skeletal development is regulated by fibroblast growth factor receptor 1 signalling dynamics. *Development.* 2004; 131: 325–35.
15. Ivkovic S, Yoon BS, Popoff SN, Safadi FF, Libuda DE, Stephenson RC, Daluiski A, Lyons KM. Connective tissue growth factor coordinates chondrogenesis and angiogenesis during skeletal development. *Development.* 2003; 130: 2779–2791.
16. Yoshiura K, Leysens NJ, Reiter RS, & Murray JC. Cloning, characterization, and mapping of the mouse homeobox gene Hmx1. *Genomics.* 1998; 50: 61–8.
17. Yoshida T, Vivatbutsiri P, Morriss-Kay G, Saga Y, & Iseki S. Cell lineage in mammalian craniofacial mesenchyme. *Mech Dev.* 2008. 125, 797–808.
18. Minoux M, & Rijli FM. Molecular mechanisms of cranial neural crest cell migration and patterning in craniofacial development. *Development.* 2010; 137: 2605–21.
19. Kuramoto T, Yokoe M, Yagasaki K, Kawaguchi T, Kumafuji K, & Serikawa T. Genetic Analyses of Fancy Rat-Derived Mutations. *Exp Anim.* 2010; 59: 147–155.
20. Noden D. M., & Trainor, P. A. Relations and interactions between cranial mesoderm and neural crest populations. *J Anat.* 2005; 207: 575–601.
21. Matsuo I, Kuratani S, Kimura C, Takeda N, & Aizawa S. Mouse Otx2 functions in the formation and patterning of rostral head. *Genes & Dev.* 1995; 9: 2646–2658.
22. Shintani T, Ihara M, Sakuta H, Takahashi H, Watakabe I, & Noda M. Eph receptors are negatively controlled by protein tyrosine phosphatase receptor type O. *Nature Neurosci.* 2006; 9: 761–9.
23. Boulling A, Wicht L, & Schorderet DF. Identification of HMX1 target genes: a predictive promoter model approach. *Mol Vis.* 2013; 19: 1779–94.
24. Marcelli F, Boisset G, & Schorderet DF. A dimerized HMX1 inhibits EPHA6/epha4b in mouse and zebrafish retinas. *PloS One.* 2014 ; 9: e100096.

25. Gammill LS, Gonzalez C, & Bronner-Fraser M. Neuropilin 2 / Semaphorin 3F Signaling is Essential for Cranial Neural Crest Migration and Trigeminal Ganglion Condensation. *J Neurobiol.* 2006; 67: 47–56.
26. Trainor PA, & Krumlauf R. Hox genes, neural crest cells and branchial arch patterning. *Curr Opin Cell Biol.* 2001; 13: 698–705.
27. Helms JA, & Schneider RA. Cranial skeletal biology. *Nature.* 2003; 423: 326-331.
28. Liu W, Selever J, Murali D, Sun X, Brugger SM, Ma L, Martin JF. Threshold-specific requirements for Bmp4 in mandibular development. *Dev Biol.* 2005; 283: 282–93.
29. Vanhoutteghem A, Maciejewski-Duval A, Bouche C, Delhomme B, Hervé F, Daubigney F, Djian P. Basonuclin 2 has a function in the multiplication of embryonic craniofacial mesenchymal cells and is orthologous to disco proteins. *Proc Natl Acad Sci USA.* 2009; 106: 14432–7.
30. Opperman LA. Cranial Sutures as Intramembranous Bone Growth Sites. *Dev Dyn.* 2000; 219: 472–485.
31. Bush JO, & Soriano P. Ephrin-B1 regulates axon guidance by reverse signaling through a PDZ-dependent mechanism. *Genes & Dev.* 2009; 23: 1586–1599.
32. Agrawal P, Wang M, Kim S, Lewis AE, & Bush JO. Embryonic Expression of EphA Receptor Genes in Mice Supports Their Candidacy for Involvement in Cleft Lip and Palate. *Dev Dyn.* 2014; 243: 1470–1476.
33. Benson MD, Opperman LA, Westerlund J, Fernandez CR, San Miguel S, Henkemeyer M, & Chenaux G. Ephrin-B stimulation of calvarial bone formation. *Dev Dyn.* 2012; 241: 1901–10.
34. Griffin JN, Compagnucci C, Hu D, Fish J, Klein O, Marcucio R, Depew MJ. Fgf8 Dosage deterimines midfacial integration and polarity within the nasal and optic capsules. *Dev Biol.* 2013; 374: 185–197.
35. Ovchinnikov D, Alcian Blue/Alizarin Red Staining of Cartilage and Bone in Mouse, *Cold Spring Harb Protoc.* 2009; doi:10.1101/pdb.prot5170.
36. Depew MJ, Simpson CA, Morasso M, & Rubenstein JLR. Reassessing the Dlx code : the genetic regulation of branchial arch skeletal pattern and development. *J Anat.* 2005; 207: 501–561.
37. McBratney-Owen B, Iseki S, Bamforth SD, Oslen BR, Morris-Kay GM. Development and tissue origins of the mammalian cranial base. *Dev Biol.* 2008; 322: 121–132.

38. Hallgrímsson B, Lieberman DE, Liu W, Ford-hutchinson AF, & Jirik FR. Epigenetic interactions and the structure of phenotypic variation in the cranium. *Evol Dev.* 2007; 91: 76–91.
39. Lapinski PE, Meyer MF, Feng G-S, Kamiya N, & King PD. Deletion of SHP-2 in mesenchymal stem cells causes growth retardation, limb and chest deformity, and calvarial defects in mice. *Dis Model Mech.* 2013; 6: 1448–58.
40. Wang W, & Lufkin T. Hmx homeobox gene function in inner ear and nervous system cell-type specification and development. *Exp Cell Res* 2005; 306: 373–9.

FIGURE LEGENDS

Fig. 1. Schematic drawing of the CNC and paraxial mesoderm fate. Purple represent mesoderm-derived cells, pink represent CNC-derived cells (modified from [12,17,20,36,37,38]). A) Side view of an E10.5 mouse embryo. Red represents Hmx1 expression pattern [4,5]. Hmx1 expression is localized in the caudal dorsal and ventral part of BA1 encompassing the mnTG, in the caudal part of BA2, in the posterior mesenchyme including part of the spinal cord and further in the caudal drg. The pink areas represent the repartition of the CNC-derived cells after migration from the rostral brain region source. In BA1 and BA2, dotted purple draw means that the mesoderm-derived cells are present in the centre of the arch and are overall surrounded by CNC-derived cells. B) Schematic drawing of a newborn mouse skull. C) Schematic drawing of an adult mouse skull (adapted from [20,36]). BA1: branchial arch 1, BA2: branchial arch 2, drg: dorsal root ganglia, FSAG: faciostatoacoustic ganglion complex, mn: mandibular process, mnTG: mandibular lobe of the trigeminal ganglion, mx: maxillary process, mxTG: maxillary lobe of the trigeminal ganglion, op: optic vesicle, ov: otic vesicle, as: alisphenoid, bo: basisoccipital, bs: basisphenoid, eo: exooccipital, ft: frontal, g: gonal, i: incus, ip: interparietal, jg: jugal, la: lacrymal, m: malleus, md: mandible, mx: maxilla, na: nasal, nc: nasal capsule (ethmoid), ob: otic bulla, os: orbitosphenoid, pa: parietal, pmx: premaxilla, pl: palate, ps: presphenoid, pt: pterygoid, s: stape, sq: squamosal, so: supraoccipital, ty: tympanic ring, vo: vomer, *: anterior ethmoid foramen, **: optic foramen.

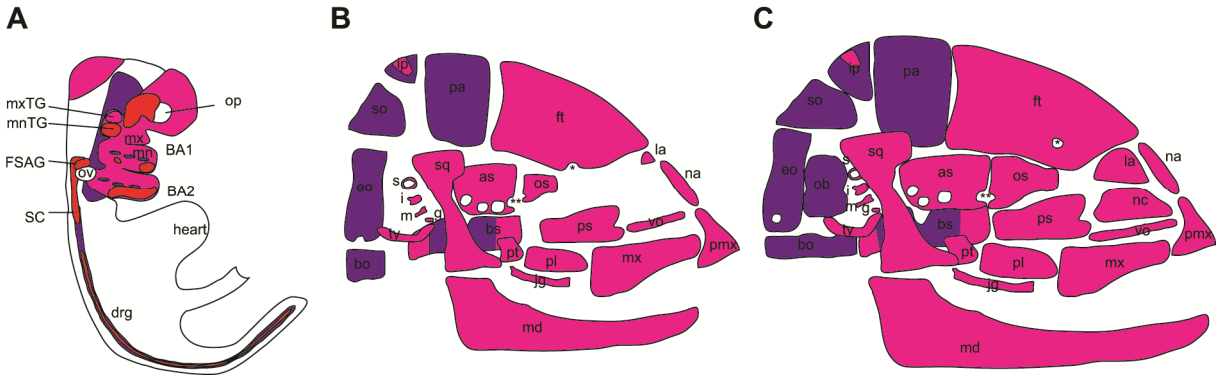

Fig. 2. Palatal deformities in stillborn Dumbo mice. Newborn mice from the control group and stillborn from the dumbo group were stained with alcian blue/alizarin red and cleared with KOH. Inferior view of the palatal structure after removal of the mandible. (A) Control P1 C57BL/6J mouse. Note the correct contouring of the bone highlighted by the red dotted line. The maxillary and palatine processes have converged toward the midline. (B-C) *Hmx1*$^{dmbo/dmbo}$ stillborn mouse. Numbers refer to mouse case number of table S1. Note that the maxillary and palatine processes are absent (red arrow) thus forming a cleft palate (red star) and exposing the vomer and the presphenoid. As: alisphenoid, bs: basisphenoid, cl pl*: cleft palate, mx: maxilla, pl: palate, pmx: premaxilla, ps: presphenoid, pt: pterygoid, vo: vomer.

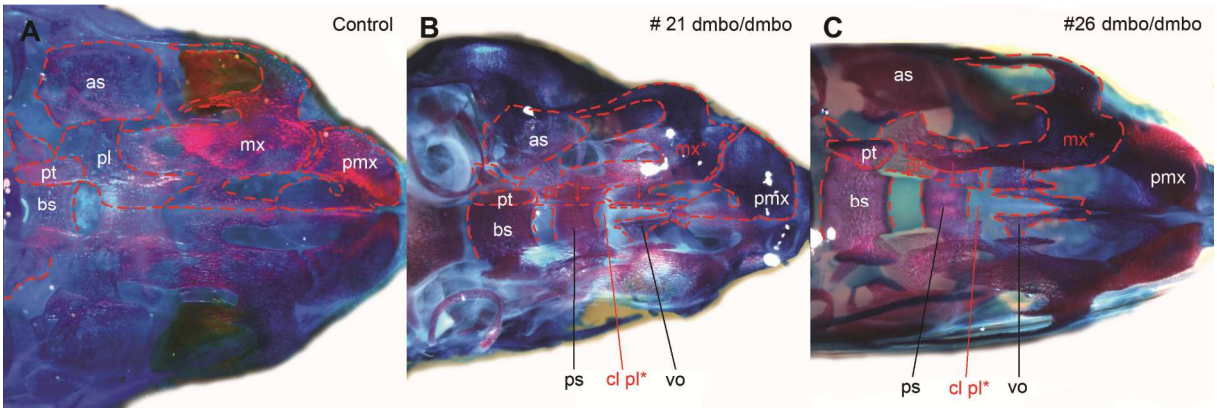

Fig. 3. Orbital deformities in stillborn dumbo mice. Newborn mice from the control group and stillborn from the dumbo group were stained with alcian blue/alizarin red and cleared with KOH. Lateral view of the skull. (A) Control P1 C57BL/6J mouse. Note the correct place of the suture line between orbital and maxilla bone (red dotted line), the starting ossification of the orbitosphenoid and the complete closure of the anterior ethmoid foramen. (B-C) *Hmx1*$^{dmbo/dmbo}$ stillborn mouse. Numbers refer to mouse case number of table S1. Note the hypoplasia of the frontal and orbitosphenoid and the incomplete closure of the anterior ethmoid foramen. As: alisphenoid, aef: anterior ethmoid foramen, ft: frontal, mx: maxilla, os: orbitosphenoid.

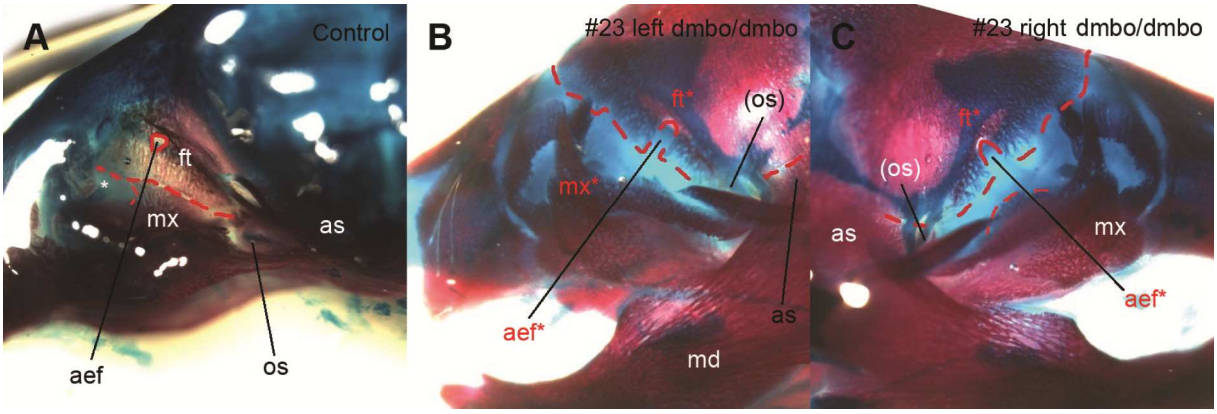

Fig. 4. Mandible deformities in stillborn dumbo mice. Left and right mandibles from newborn mice from the control group and stillborn from the dumbo group were stained with alcian blue/alizarin red and cleared with KOH. (A) Control P1 C57BL/6J mouse. Wild-type mandible structure. (B) *Hmx1*$^{dmbo/dmbo}$ stillborn mouse. Large hypoplasia of the mandible up to the dentary, cartilaginous structures were surrounding the edge of the malformed mandible (red arrow). (C-D) *Hmx1*$^{dmbo/dmbo}$ stillborn mouse. Numbers refer to mouse case number of table S1. The lower incisor failed to develop (dotted circle) and a local hypoplasia of the dentary (red star) occurred. Agp: angular process, cdp: condylar process, crp: coronoid process, dnt: dentary, li: lower incisor, t*: tooth missing.

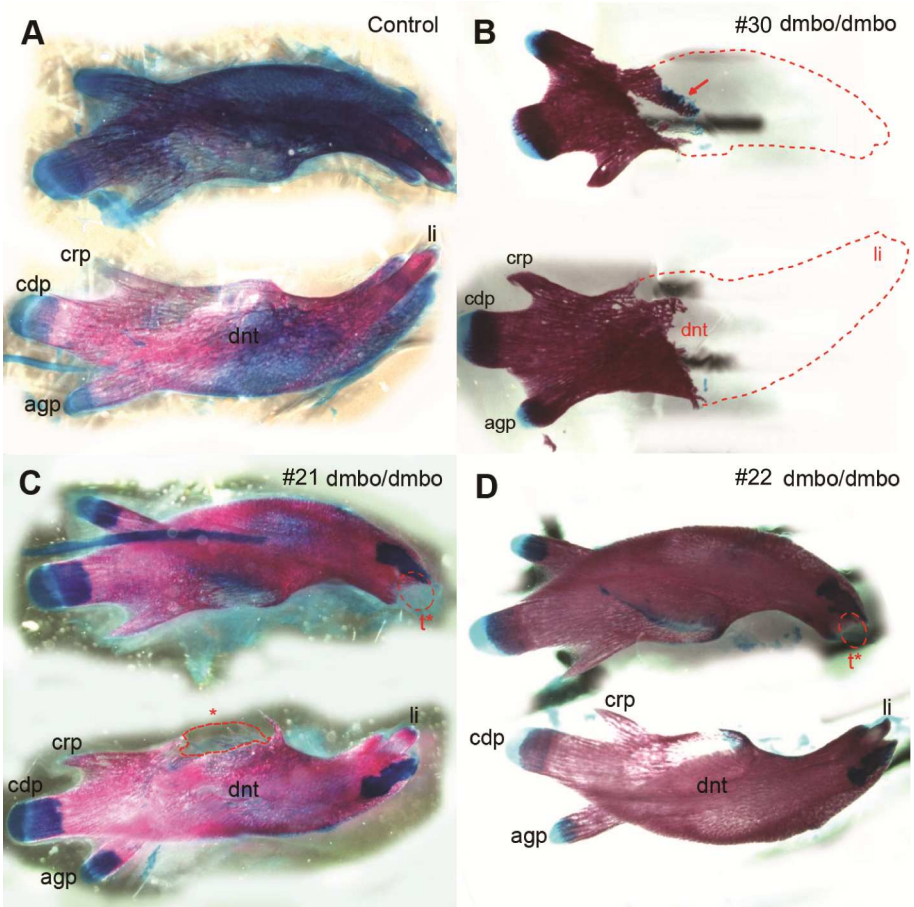

Fig. 5. Chest deformities in stillborn dumbo mice. Newborn mice from the control group and stillborn from the dumbo group were stained with alcian blue/alizarin red and cleared with KOH. Front view of the chest. (A) Control P1 C57BL/6J mouse. Morphology of wild-type mouse chest. (B-D) *Hmx1*$^{dmbo/dmbo}$ stillborn mouse. Numbers refer to the case number in table S1. (B) Asymmetric fusion of the rib and asymmetric deformity of the stenebrae 1 to 4. (C) Axial segmentation of the sternum between stenebra 4 and xiphisternum (yellow dotted line). (D) Axial segmentation of the xiphisternum and absence of xiphoid cartilage (yellow dotted line). (E) Axial segmentation of the xiphisternum and hypoplasia of the 4th stenebra. Ma: manubrium, st: stenebra, xi: xiphisternum, xi c: xiphoid cartilage.

Fig. 6. Skeletal abnormalities in stillborn dumbo mice. MicroCT 3D reconstruction of the skull from a control mouse and of the skull and chest from a dumbo mouse. Notice that the bone porosity of the homozygote appears stronger due to the alizarin and alcian staining procedure. The bone of interest is highlighted by a red dotted line. (A, C, E, G) Control P1 C57BL/6J mouse exhibiting a normal bone structure. (B, D, F, H, I) *Hmx1*$^{dmbo/dmbo}$ stillborn mouse. Numbers refer to mouse case number of table S1. (B) Note that the maxillary and palatine processes are absent, thus forming a cleft palate (red star) and exposing the vomer and the presphenoid bones. (D, H) The zygomatic process is underdeveloped due to hypoplasia of the jugal and zygomatic processes of the squamosal and maxilla (red stars). (D) The frontal bone failed to form completely (red star) and the anterior ethmoid foramen is absent. (F) The maxillary and palatine processes have failed to converge toward the midline, leading to a cleft palate (red star). (H) Absence of the lower incisor (red dotted circle). (I) Asymmetric fusion of the rib and asymmetric deformity of the stenebrae 1 to 4. As: alisphenoid, bo: basal occipital, bs: basisphenoid, cl pl*: cleft palate, ft: frontal, hy: hyoid, jg: jugal, lo: lamina obturans, ma: manubrium, mx: maxilla, na: nasal, os: orbitosphenoid, pl: palate, pmx: premaxilla, ps: presphenoid, pt: pterygoid, sq: squamosal, st: stenebra, t*: tooth missing, vo: vomer, xi: xiphisternum, xi c: xiphoid cartilage, zpmx: zygomatic process of the maxilla, zps: zygoamtic process of the squamosal.

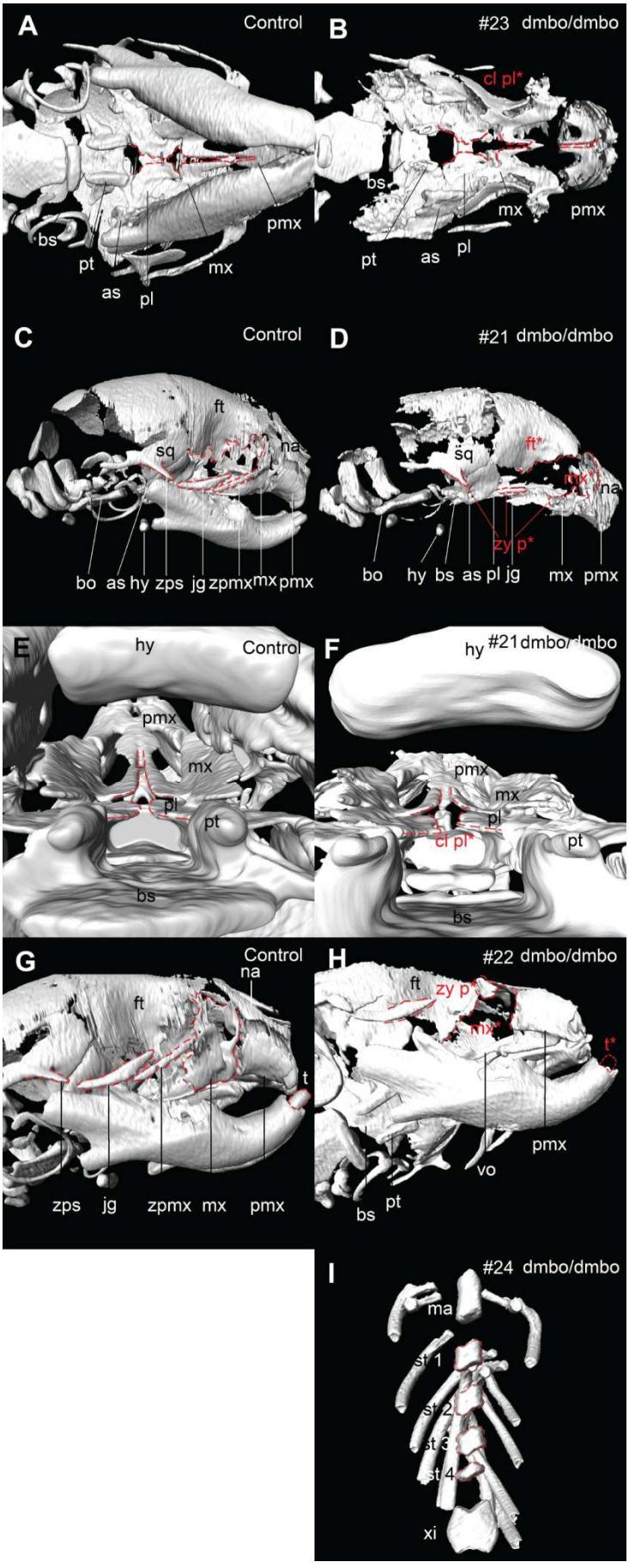
A
Control
bs
pt
as
pl
mx
pmx
B
#23 dmbo/dmbo
cl pl*
bs
pt
as
pl
mx
pmx
C
Control
ft
sq
na
bo
as
hy
zps
jg
zpmx
mx
pmx
D
#21 dmbo/dmbo
sq
ft*
mx*
na
zy
p*
bo
hy
bs
as
pl
jg
mx
pmx
E
hy
Control
pmx
mx
pl
pt
bs
F
hy
#21 dmbo/dmbo
pmx
mx
pl
cl pl*
pt
bs
G
Control
na
ft
t
zps
jg
zpmx
mx
pmx
H
#22 dmbo/dmbo
ft
zy p*
mx
t*
pmx
vo
pt
bs
I
#24 dmbo/dmbo
ma
st 1
st 2
st 3
st 4
xi

Fig. 7. Schematic representation of the craniofacial defect in stillborn dumbo mice. Schematic drawing of a newborn mouse skull. A) Red areas represent BA1 and BA2 skeletal derivatives at birth [36,37] concomitant with Hmx1 expression pattern at E10.5 [4,5]. B) Summary of all skeletal elements affected in stillborn Dumbo mice. As: alisphenoid, bo: basisoccipital, bs: basisphenoid, eo: exooccipital, ft: frontal, g: gonal, i: incus, ip: interparietal, jg: jugal, la: lacrymal, m: malleus, md: mandible, mx: maxilla, na: nasal, os: orbitosphenoid, pa: parietal, pmx: premaxilla, pl: palate, ps: presphenoid, pt: pterygoid, s: stape, sq: squamosal, so: supraoccipital, ty: tympanic ring, vo: vomer, *: anterior ethmoid foramen, **: optic foramen.

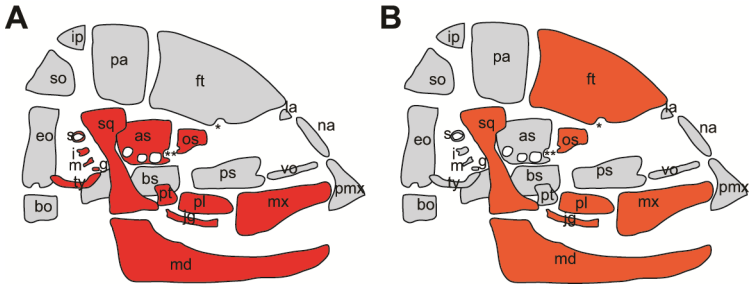

Fig. 8. Body mass of dumbo mice from weaning to adulthood. Weight of *Hmx1*$^{dmbo/+}$ and *Hmx1*$^{dmbo/dmbo}$, for both male and female subjects, was assessed for 26 weeks, (n=10 mice for each group). The homozygous mice were significantly lighter. (ANOVA: $p<0.0001$, errors bars show S.D).

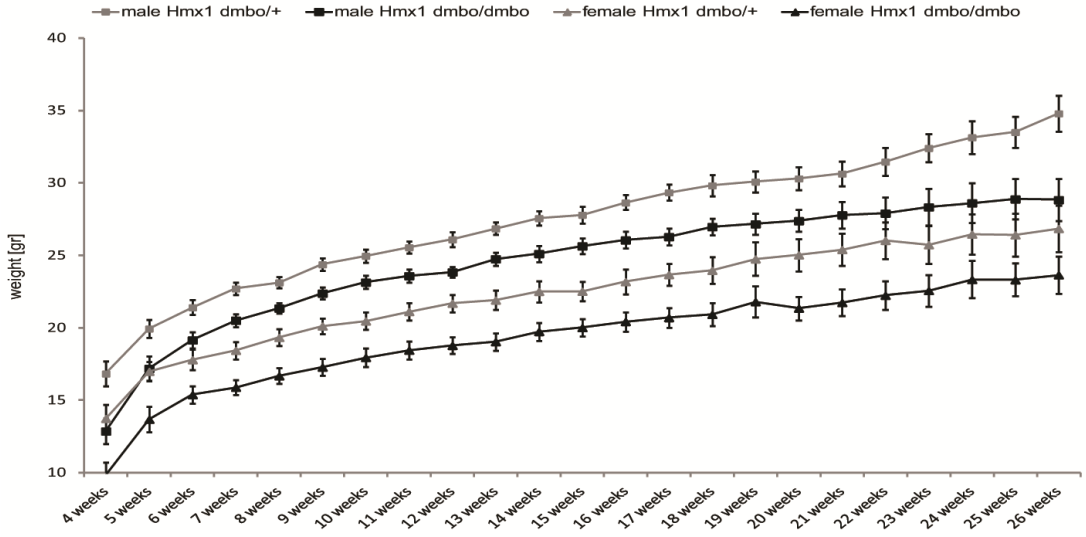

Supporting fig. 1. Survey of body mass of dumbo females during breeding.

Body mass measurements of females from the 10 crossings. Weight was taken each day during 83 days, allowing detection of premature loss of litter which corresponds to a drop of weight back to normal before the 21 days of gestation (symbolized by red arrows). Genotypes of both female and male of each cross are described in the legend pannel, pink arrows represent birth event.

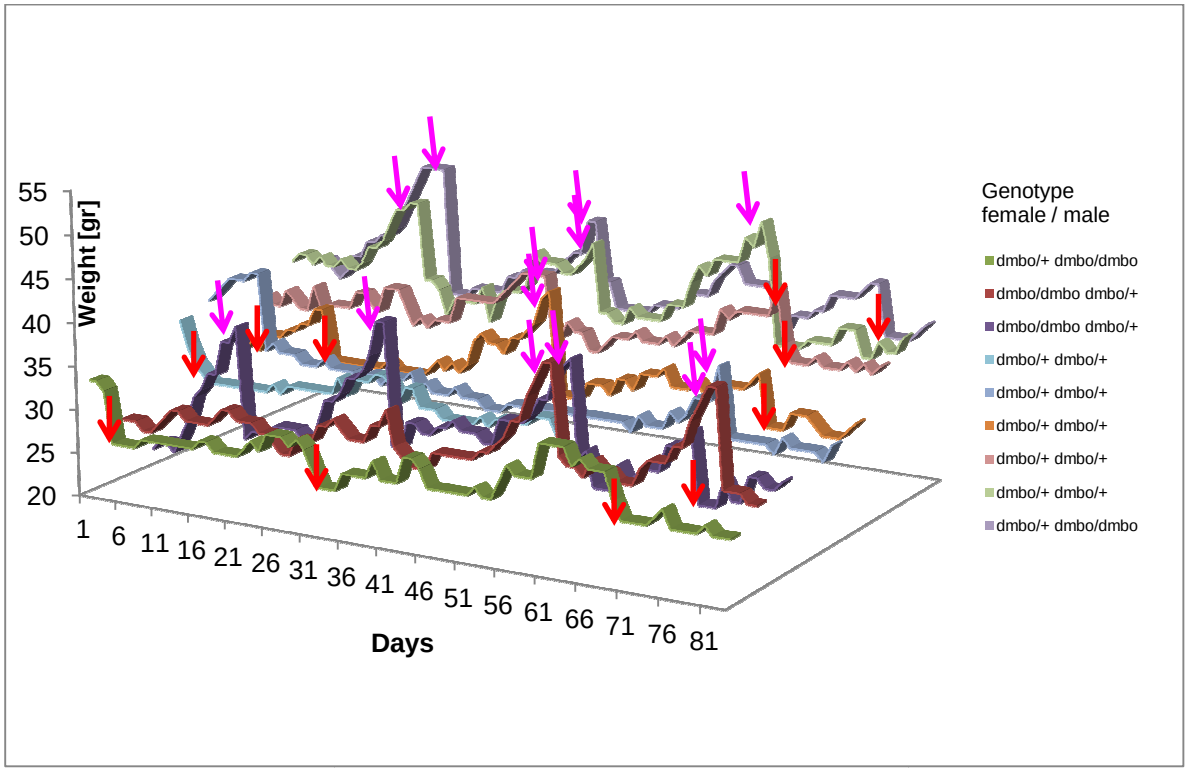

Supporting table 1: Assignment of the craniofacial and chest malformations.

	Case n°	Hmx1 allele	maxilla	Zygomatic process	orbitosphenoid	cleft palate	mandible	teeth	xiphisternum	stenebrae	xiphoid cartilage	tympanic bulla
C57BL/6J	1	+/+										
	2	+/+										
	3	+/+										yes
	4	+/+										
	5	+/+										
	6	+/+										yes
	7	+/+										
	8	+/+										
Dumbo	9	+/+										
	10	+/+										
	11	+/+										
	12	dmbo/+										
	13	dmbo/+										
	14	dmbo/+										
	15	dmbo/+										
	16	dmbo/+										
	17	dmbo/+										
	18	dmbo/+	yes			yes						
	19	dmbo/+										
	20	dmbo/+										
	21	dmbo/dmbo	yes	yes	yes	yes	yes	yes	yes	yes		
	22	dmbo/dmbo	yes					yes				
	23	dmbo/dmbo			yes	yes			yes	yes		
	24	dmbo/dmbo								yes		
	25	dmbo/dmbo	yes	yes		yes						
	26	dmbo/dmbo	yes			yes						
	27	dmbo/dmbo										
	28	dmbo/dmbo										
	29	dmbo/dmbo	yes			yes			yes	yes		
	30	dmbo/dmbo	yes	yes			yes	yes	yes		yes	
	31	dmbo/dmbo										

Listing of newborns of the indicated genotypes from crosses of C57BL/6J mice and from crosses of *Hmx1*$^{dmbo/+}$ parental mice or mixed crossings of *Hmx1*$^{dmbo/dmbo}$ with *Hmx1*$^{dmbo/+}$ (n = 32 mice), note that not all the dead pups from table 1 were analyzed either due to partial eating by the dams or because they were used for others studies. All analyzed P0 to P1 newborns were either stillborn or died naturally after 1 day, except for 5 out of 8 P0 newborn C57BL/6J mice that were sacrificed. All listed animals bare a case number to identify them within skeletal analysis figures. The two wild-type mice from the control group harbour a tympanic bulla hyperplasia that was never observed in the stillborn dumbo mice: (data not shown).

Visual deficit in *Hmx1-/-*mice is due to optic nerve hypoplasia and abnormal retinotectal projection

Linda Bapst-Wicht, Fabienne Marcelli, Marine Coral Gadea, Marie Abbet, Daniel F. Schorderet

Submitted

2015

- Experiments shown in figures 3, 5, 6B to F and 7B to D have been made by myself
- Experiments shown in figures 1A, 2, 4 and 6A have been made by F. Marcelli
- Experiments shown in figures 1B have been made by myself and F. Marcelli
- Experiments shown in figures 7A have been made by myself and M. Abbet
- Experiments shown in figures 8 have been made by myself and M. Coral Gadea
- The paper has been written by me, F. Marcelli and D. Schorderet for result and materials and methods sections, by myself and D. Schorderet for abstract, introduction and discussion sections.

Visual deficit in *Hmx1-/-*mice is due to optic nerve hypoplasia and abnormal retinotectal projection

Short title: Hmx1 in retinotopic mapping

Linda Bapst-Wicht[1,2], Fabienne Marcelli[1], Marine Coral Gadea[2], Marie Abbet[2], Daniel F. Schorderet[1,2,3,*]

[1]IRO-Institute for Research in Ophthalmology, Sion, Switzerland; [2]EPFL- Faculty of Life Science, Swiss Federal Institute of Technology, Lausanne, Switzerland; [3]UNIL-Dept. of Ophthalmology, University of Lausanne, Lausanne

Corresponding author

Daniel F. Schorderet, Institute for Research in Ophthalmology, Av. Du Grand-Champsec 64, 1950 Sion, Switzerland.

Phone: 4127 205 7900, e-mail: daniel.schorderet@irovision.ch

Keywords

Dumbo, retinotopic mapping, axon guidance, optic nerve, retina.

Key findings:

- *Hmx1*$^{dmbo/dmbo}$ mice have impaired visual acuity not related to retinal phenotype.
- *Hmx1*$^{dmbo/dmbo}$ mice share microphthalmia and optic nerve hypoplasia phenotype of the oculo-auricular syndrome of Schorderet-Munier-Franceschetti.
- *Hmx1* mutation causes retinotopic mapping defect responsible of the vision disorder in mice.

ABSTRACT

Background: During mouse development, the homeodomain transcription factor, H6 family homeobox 1 (*Hmx1*) is expressed in the peripheral nervous system, the otic vesicle, the developing eye, the trigeminal ganglion, and the 2nd branchial arch. In human, homozygous *HMX1* mutations lead to the oculo-auricular syndrome of Schorderet-Munier-Franceschetti (OAS-SMF). Results: We analyzed the dumbo mouse, a mouse model of OAS-SMF, bearing null mutation on *Hmx1* allele. Homozygous dumbo mice showed that the development of the retina and its electrophysiological response were normal. The eye phenotype was characterized by microphthalmia and cataract. Although, all the retinal cell types were present, visual acuity, as measured by a virtual-reality optomotor system, was reduced to near blindness. HMX1 deletion also leads to severe optic nerve atrophy with reduction in diameter up to the optic chiasm. Retinal axons failed to reach the lateral geniculate nucleus and the superior colliculus, resulting in marked defect of retinotopic mapping. Conclusions: Considering the known target of *HMX1* we propose that *HMX1* lies upstream of Ephrin and Semaphorin signalling pathway and coordinates retinotopic mapping.

INTRODUCTION

The pattern of synaptic connections in the visual system is established via complex guidance mechanisms. Retinal ganglion cells (RGC), generated in mice between E11 and E19, extend their axons to the optic nerve head located on the central retina. Then, controlled by the Sonic hedgehog (Shh), they exit the globe via the lamina cribrosa to form the optic nerve in parallel with its gliogenesis. RGC axons project to their targets after reaching the optic chiasm by E14. The major outputs of RGC in the mouse are the contralateral superior colliculus (SC) and the contralateral dorsal lateral geniculate nucleus (dLGN). RGC axons outgrowth is present in the SC by E15 and in the dLGN by E16. During this first phase, axons extend beyond their termination zones. The refinement of the retinotopic topography during embryogenesis and after birth occurs via complex sets and gradients of regulators such as Semaphorins, Ephrins and Teneurins. On activation of these molecular cues, axons undergo fasciculation, segregation, correct targeting, and pruning in order to achieve their correct topography. In mice, the final retinocolicular map is achieved within the second postnatal week prior to eye opening, first in the SC, then in the dLGN (Wilks et al., 2013; Harada et al., 2007). Among these regulating signalling pathways, Eph receptors and ephrins are gradually expressed during development of the nervous system. Eph/ephrins will alternatively attract or repulse the growth cones of the developing axons, whether they are of type A or B. However, experiments in knockout mouse models have shown that they are not the only masters of retinotopic mapping (Triplett et al., 2012).

HMX homeobox family members are transcription factors regulating crucial developmental processes of sensory organs (Stanfel et al., 2005). Study of homeobox genes first started in *Drosophila melanogaster*, and then homologues were identified in mammals and birds (Wang et al., 2000). Human H6 family homeobox 1 (*HMX1*) gene, located on chromosome 4, was identified as being responsible for the oculo-auricular syndrome of Schorderet-Munier-Franceschetti (OAS-SMF), and two homozygous mutations have been reported so far (Schorderet et al. 2008; Gillespie et al., 2015). The OAS-SMF phenotype (MIM: 142992) is characterized by ophthalmic anomalies (microcornea, microphthalmia, cataract, anterior-segment dysgenesis, optic nerve dysplasia, coloboma, rod-cone dystrophy, and aberration of the retinal pigment epithelium) resulting in a decreased visual acuity of patients and an unusual cleft or aplastic ear lobule. The time window and pattern of expression of HMX1 is clearly

related to its developmental role in sensory organs. In 5-week-old human embryos, *HMX1* is expressed in the retina, and later in the 20-week-old foetus, in the developing auricular mesenchymal cells and in the perichondrium of the intrinsic cartilages of the pinna (Schorderet et al., 2008).

Genetically engineered mice have provided beneficial insights into the pathways involved in many syndromes including ophthalmic, and more widely into the molecular mechanisms that regulate retinal axon guidance. To date, mutations at the *Hmx1* locus have been linked to defects of the ear with mild or no eye phenotype in cows, rats and mice (Koch et al., 2013, Munroe et al., 2009; Quina et al. 2012b). The dumbo mouse model harbours an ENU generated nonsense mutation in *Hmx1* (Wilson et al. 2005). The *Hmx1* dmbo allele presents a functionally null mutation that lies in the amino-terminal side of the homeodomain, resulting in an undetectable truncated mutant protein (Quina et al., 2012a). In mouse embryos, HMX1 is detected in the peripheral nervous system, the otic vesicle and in cranial neural crest derived cells: the developing eye, the trigeminal ganglion and the 2nd branchial arch (Munroe et al., 2009, Quina et al., 2012a). As mentioned, dumbo mice principally exhibit enlarged ear pinnae with apparent ventrolateral shift, hence their name. We have recently refined the phenotype of these mice and have shown that branchial arch 1 and 2-derived cranial bones as well as thoracic bones are malformed in a subset of nonviable newborns (Bapst-Wicht L, Marcelli F, Steininger V, Pochon M, Malfroy Camine V, Kettenberger U, . Schorderet DF, submitted, 2015).

The initial mouse eye phenotype description reported moderate degrees of microphthalmia, and no retinal degeneration (Munroe et al., 2009; Quina et al., 2012b). To study and better understand the role of *HMX1* in the ophthalmic defects of OAS-SMF, we decided to extensively investigate the ophthalmic anomalies in dumbo mice, and now report a new pattern of vision-linked defects due to *Hmx1* mutations.

Results

Hmx1$^{dmbo/dmbo}$ mice have cataract and microphthalmia

OAS-SMF leads to several eye disorders, including congenital nystagmus, bilateral microcornea, posterior synechiae, cataract, iris coloboma, microphthalmia, stromal iris

cyst, irido-corneal adherences and rod-cone dystrophy (Schorderet et al., 2008; Vaclavik et al., 2011; Gillespie et al., 2015). In comparison, most *Hmx1*$^{dmbo/dmbo}$ mice are microphthalmic, with low grade keratoconjunctivitis sicca and entropion, but the eyes show no evidence of microcornea, anterior segment dysgenesis, cataract, coloboma, retinal detachment or retinal degeneration (Munroe et al., 2009). For our study, mice were backcrossed into a C57Bl/6J background in order to remove the *Rd1* mutation present in the C3H strains. Two phenotypes were observed: microphthalmia and cataract. Both phenotypes were very variable, ranging from normal eye size and absence of cataract to severe microphthalmia and total cataract. Microphthalmia was always associated with cataract, whereas cataract could occur without microphthalmia. These phenotypes were already present on the day of eye opening (P13-14, data not shown). To quantify the proportions of each phenotype, 68 *Hmx1*$^{dmbo/dmbo}$ mice were classified into three categories after visual assessment of the eye size and the ocular globe opacity: normal eye, cataract, and cataract plus microphthalmia. 28% (n=19) of *Hmx1*$^{dmbo/dmbo}$ mice presented normal eyes, 23.5% (n=16) cataract, and 48.5% (n=33) cataract plus microphthalmia. All *Hmx1*$^{dmbo/+}$mice presented a normal eye phenotype (N=86) (Fig. 1A).

Hmx1$^{dmbo/dmbo}$ *mice have visual acuity impairment*

OAS-SMF patients suffer from markedly decreased vision, with rods being more severely affected than cones (Schorderet et al., 2008; Vaclavik et al., 2011; Gillespie et al., 2015). To assess whether *Hmx1*$^{dmbo/dmbo}$ mice suffered from vision impairment, a virtual-reality optomotor system was used on C57Bl/6J, *Hmx1*$^{dmbo/+}$and *Hmx1*$^{dmbo/dmbo}$ mice between one and six months of age. This system has been widely used for visual acuity assessment of animal models including mice (Cuenca et al., 2014, Douglas et al., 2005). Only *Hmx1*$^{dmbo/dmbo}$ mice with normal external eye phenotype were used for this experiment, as all mice with cataract and microphthalmia were completely blind (no results for optometry measurements and unrecordable ERG, data not shown). Even with this experimental bias, *Hmx1*$^{dmbo/dmbo}$ mice showed very low vision (visual acuity of 0.0-0.1 cycles per degree (c/d)), whereas *Hmx1*$^{dmbo/+}$ mice had a vision comparable to C57Bl/6J mice (0.3-0.4 c/d) (Lehmann et al., 2012) (Fig. 1B).

Electroretinograms of dumbo mice

In order to complement the phenotype, electroretinograms (ERG) were performed on two- (Fig. 2, pannel 1) and six- (Fig. 2, pannel 2) month-old animals of the three genotypes, in both scotopic (Fig. 2A, C and E) and photopic (Fig. 2B, D and F) conditions. As for the virtual-reality optomotor analysis, only *Hmx1*$^{dmbo/dmbo}$ mice without cataract were used. No qualitative differences were observed in the retinal cell responses between C57Bl/6J, *Hmx1*$^{dmbo/+}$ and *Hmx1*$^{dmbo/dmbo}$ mice (Fig. 2, pannel 1). At six months of age, the ERG recordings were still normal for *Hmx1*$^{dmbo/dmbo}$ mice (Fig. 2, pannel 2). A-wave and b-wave average of both scotopic and photopic ERG of *Hmx1*$^{dmbo/+}$ and *Hmx1*$^{dmbo/dmbo}$ mice (Fig. 3) show no significant differences (*: p=0.1, no stars: 0.9>p>0.1). These experiments indicate that the retina seems to function normally in *Hmx1*$^{dmbo/dmbo}$ mice. This contrasts with OAS-SMF patients who suffer from early onset and rapidly degenerating retinal dystrophy affecting rods before cones (Schorderet et al., 2008; Vaclavik et al., 2011; Gillespie et al., 2015).

Hmx1$^{dmbo/dmbo}$ *mice present a normal retinal phenotype*

To confirm our findings, histological analysis was performed on mice between one and twelve months of age. Hematoxylin-eosin staining revealed that all retinal layers were present, and no degeneration was observed up to twelve months of age (Fig. 4A, B). Retinal thickness was slightly reduced in *Hmx1*$^{dmbo/dmbo}$ mice compared to heterozygous individuals, but this might be due to the general reduction in eye size observed in these mice (L. Bapst-Wicht, F. Marcelli, V. Steininger, M. Pochon, V. Malfroy Camine, U. Kettenberger, D.F. Schorderet, submitted; Munroe et al., 2009). We also analyzed retinal integrity using a non-invasive method. Optical coherence tomography (OCT) was performed on *Hmx1*$^{dmbo/dmbo}$ mice between 6 to 8 months of age and compared to their littermate controls (*Hmx1*$^{dmbo/+}$) (Fig. 5). Despite the decreased quality of the OCT due to cataract in homozygous mice (Fig. 5C,D), we were able to decipher all retina layers and observed no alternation (N=3).

Hmx1 is not required for neuronal differentiation in the retina

Hematoxylin-eosin staining reveals the general retinal structure, but does not provide information on the presence or absence of the different cell types. Therefore,

immunohistochemistry was performed with antibodies against several retinal cell types (Fig. 4 pannel 1 and 2). Rods were stained with recoverin (Fig. 4C, D), cones with S- and M-opsin (Fig. 4E, F and G, H, respectively), bipolar cells with Pkcα (Fig. 4I, J), horizontal cells with calbindin (Fig. 4K, L), amacrine cells with glycine (staining only glycinergicamacrine cells) (Fig. 4M, N), Müller cells with Gfap (Fig. 4O, P), and ganglion cells with Brn-3 (Fig. 4Q, R). Ganglion cell axons were stained with Thy-1 (Fig. 4S, T). All antibodies presented an identical staining between controls and *Hmx1*$^{dmbo/dmbo}$ mice, indicating that all retinal cell types were present, and confirming the retinal functionality observed with the ERG.

Defects in axon guidance and atrophy in the Hmx1$^{dmbo/dmbo}$ *optic nerve*

Processing of vision from the retina to visual cortex areas requires proper propagation of information along the optic nerve and across the optic chiasm to the lateral geniculate nucleus (LGN) and superior colliculus (SC). There is no clinical data about optic nerve defect at the optic chiasm in OAS-SMF, but examination of the posterior segment revealed optic nerve dysplasia in several patients (Schorderet et al., 2008; Gillespie et al., 2015). As *Hmx1*$^{dmbo/dmbo}$ mice experience visual impairment but display normal retinas, we postulated that the problem occurred in the central visual pathways: optic nerve, LGN or SC, contributing to deficits in visual processing. This hypothesis was supported by the fact that HMX1 represses *EPHA6* expression, a gene implicated in retinal axon guidance (Marcelli et al., 2014). To determine whether a normal number of axons leaves the retina, optic nerve thickness was measured at the level of the lamina cribrosa in young (1-2 months) and adult (6-12 months) animals. No significant difference was observed between *Hmx1*$^{dmbo/dmbo}$ mice and controls (N=5, p=0.4, Fig. 6A,B), suggesting an implication of the central visual pathways rather than the number of RGC axons exiting the retina. We analyzed optic nerve thickness and structures around the optic chiasm and performed whole brain explants from adult heterozygote and homozygote mice from 13 to 26 months of age. Five *Hmx1*$^{dmbo/+}$ mice were used as controls. They all presented normal morphology of the optic chiasm (Fig. 6D). However, 3 out of the 4 *Hmx1*$^{dmbo/dmbo}$ mice analyzed presented obvious changes in optic nerve and chiasm morphology (Fig. 6E,F). Measurements of the relative size of optic nerve thickness and optic chiasm width from both genotypes confirmed optic nerve hypoplasia with a significant reduction of

diameter (p = 0.002) and significant shrinking of the optic chiasm (p = 0.007) in homozygote dumbo mice (Fig. 6A,C).

Normal optic nerves are composed of axon fibers of RGC, astrocytes and oligodentrocytes (Watson et al., 2012, Howell et al., 2007). To further study the modifications of optic nerves and analyze axonal morphology, cross sections of optic nerve were imaged. Nissl staining is an effective method to look for nerve modifications and to identify cells types (Fruttiger et al., 1999, Mescher, 2010, Scudamore, 2014, Gresle et al., 2012, Weimer et al., 2006). On light microscopy the general morphology of cresyl stained optic nerve appeared well preserved with numerous glial cells surrounding axon bundles (Fig. 7A). However, the overall number of Nissl positive bodies detected around axons appeared to be lower in dumbo mice compared to control animals (Fig. 7B). Moreover, the decrease of astrocytes around nerve cells was proportional to the severity of hypoplasia, concordant with mouse models of optic nerve deterioration (data not shown, Mao et al., 2008).

Retinotopic mapping is abnormal in Hmx1$^{dmbo/dmbo}$ mice

To determine whether the visual defect was due to disrupted axonal guidance during brain development in dumbo mouse model, we performed anterograde labelling of RGC axons using fluorescent lipophilic dye (dioctadecyloxacarbocyanine perchlorate, DiO and dioctadecyltetramethylindocarbocyanine, DiI). After incubation, the fluorescent dye allows for whole tracing of the projections along the optic tract towards the visual input (Chan et al., 1998, Chung et al., 2000, Conway et al., 2011, Herrera et al., 2004, Godement et al., 1994). To assess whether the hypoplasia of the optic nerve and optic chiasm observed in adult dumbo mice was due to a decrease in axon numbers in dumbo mice, we evaluated the average size of axon bundles composing the optic nerve as it reached the optic chiasm. Because axon bundle size presented a certain heterogeneity (Pearson's Chi-square test, $p<0.01$) within heterozygote and homozygote dumbo mice, the analysis of axon bundle led to no significant difference in axon bundle area between the two genotypes (Fig. 7C, D). These results suggest that the optic nerve hypoplasia (ONH) observed in Dumbo mice is not a consequence of thinning of axon bundles, but rather a decrease in the number of them. This is consistent with the general decrease of cell density observed in cross sections.

To further address the possibility of abnormal retinotopic mapping, we examined the path of optic nerve projections along the brain on coronal cryosections. Positions of the labelled axons were annotated and reported on a retinofugal path scheme (Fig. 8A,A',I). The combined observations obtained for the control group (C57BL/6J and *Hmx1*$^{dmbo/+}$) and dumbo group (*Hmx1*$^{dmbo/dmbo}$) allowed us to recapitulate the output of RGC axons. Whereas optic projections followed a precise path along the retinofugal path (Fig. 8A,I), we observed that *Hmx1*$^{dmbo/dmbo}$ RGC axons did not correctly follow retinotopic mapping (Fig. 8A',I). Various abnormal outputs of labelled RGC axons were detected throughout the brain of dumbo mice, contrary to the control group. Heterozygote dumbo mice presented normal retinotopic mapping with projections of the RGC axons along the optic tract (Fig. 8D-F), and output in the LGN (Fig. 8F-H). Mapping of RGC axons between LGN and SC is somewhat controversial as some models propose an internal axon path ventrally towards LGN (Wilks et al., 2013, Paxinos& Franklin, 2013) while others propose an external path temporal and posterior to the LGN (Assali et al., 2014). Some of the projections in heterozygote mice were co-localized with the thalamic nucleus below the fibrium of the hippocampus (Fig. 8D-E). This location was more likely to be the projection of the optic nerve layer of the superior colliculus, which lies tangential to the hippocampus, and axial variation of our coronal section explained the position switch. Our data reinforce the ventral path hypothesis, suggesting that our observations were the projections going towards the SC. Homozygote dumbo mice axons targeted the optic chiasm and, to a lesser extent, followed the optic tract (Fig. 8F',G'), but surprisingly some outputs were found in the third ventricle (Fig. 8D'-F'), others in the lateral ventricle (Fig. 8C') and the dorsal 3rd ventricle (Fig. 8D'). Failure in the targeting of the optic axons was not consistent among the mutant mice (Fig. 8I). While some exhibited mistargeting, others showed a normal axon tract path up to the middle of the optic tract and no observable prolongation to the LGN. This latest observation is consistent with the fact that dumbo mice showed a tendency to have fewer axons forming the optic nerve and projecting to the brain visual cortex.

Discussion

Hmx1 depletion causes blindness and ONH, a bridge towards OAS-SMF

The first description of the dumbo mouse supported the view that there was no clear link between mouse and human ophthalmic phenotype, apart from a prevalence of microphthalmia (Fig. 1) (Munroe et al., 2009, Quina et al., 2012b). Our study presents a complete analysis of the ophthalmic characteristics of the dumbo mice and reveals decreased visual acuity and ONH comparable to OAS-SMF (Schorderet et al., 2008, Gillespie et al., 2015). Both species share a common variability of ONH (Fig. 6), which was observed during posterior segment examination in 3 out of 5 patients (Gillespie et al., 2015). In human, ONH is a common cause of blindness or visual impairment (Garcia-Filion & Borchert, 2013). In mice, genetic mutations causing ONH are often linked to axon guidance molecules involved in retinal axon exit at the optic disc, such as netrin-1, L1 and several EphBs (Harada et al., 2007). In some cases, such as *ALDH1A3* loss-of-function mutation (Yahyavi et al., 2013), microphthalmia is associated with ONH (Kaur et al., 2013). In the mouse, it is not clear why ONH was not observable posterior to the eye until twelve months of age (Fig. 6A). It could be explained by a temporary inflammation status, an adult onset degeneration phase or temporary glial compensation, but this needs to be further evaluated. It is also important to mention that clinical assessments of children with ONH often reveal hypoplasia or agenesis of the corpus callosum (Garcia-Filion & Borchert, 2013, Kaur et al., 2013), suggesting that deeper histological analysis of dumbo mice brain could reveal other defects.

Hmx1 is crucial for axon guidance in the developing mouse brain

Loss of visual acuity in OAS-SMF is likely due to retinal disorder and cataract, whereas *Hmx1*$^{dmbo/dmbo}$ mice have retinas and ERG comparable to the control group, reinforcing an integrative cause of the visual defect in this model. Our observation of the retinal projections in dumbo mice (Fig. 8) is consistent with the embryogenic theory suggesting a retrograde degeneration of RGC consecutive to abnormal optic chiasm and brain development (Kaur et al., 2013). Regulator genes of retinal neurogenesis could be excluded from the potential targets of *Hmx1*, as we observed no alterations of the neural retina. However, genes implicated in optic nerve maturation and in retinotopic mapping

are more likely to be involved. Taken sequentially, the sonic hedgehog (Shh) signalling pathway plays an important role in establishing retinotopic mapping and gliogenesis when RGC axons start to extend from the optic nerve head. After birth, neurotrophins and their receptors are involved in the second period of retinal programmed cell death that regulates the final number of RGC (Assali et al., 2014, Harada et al., 2007). It will be interesting to investigate whether these genes act on Hmx1 during development.

Retinotopic mapping presents some limitations. Indeed, even if anterograde tracing is a well-proven technique for embryo and newborn visual system analysis (Conway et al., 2011, Herrera et al., 2004, Godement et al., 1994, Chung et al., 2000, Chan e al., 1998), to our knowledge no studies have been performed in adult mice. We were able to label parts of the RGC projections using lipophilic tracer but, contrary to embryos, adults presented a much longer path for the fluorophore to travel, explaining the low power of our tracer and the lower percentage of axons efficiently labelled. Alternative methods for visual system analysis, such as MRI (Sun et al., 2011), do exist but were not available for this study.

Hmx1 target genes and their role in axon guidance

Several classes of regulators including Slit/Robo, Ephrins and Semaphorins govern retinocollicular topographic mapping. RGC axon guidance is triggered by attractive and repulsive interactions between expressed signalling molecules and their receptors, either expressed by RGC or target outputs from the diencephalon (Harada et al., 2007). Whereas Semaphorins and B class Ephrins are responsible for the crossing choice at the optic chiasm (Petros et al., 2008), both A and B Ephrins control for the axial mapping of retina, SC and LGN (Erskine et al., 2007). Knockout mouse models have largely been used to show that perturbation of Ephrin signaling leads to axon guidance errors (Huberman et al., 2008).

We previously demonstrated that expression of *Ptpro*, a negative regulator of Ephrin receptors (Shintani et al., 2006), *Epha6*, and *Sema3f* was regulated by HMX1 (Boulling et al., 2013, Marcelli et al., 2014) and that both mutations reported so far in OAS-SMF remove the ability of HMX1 to regulate them (Marcelli et al., 2014, Gillespie et al., 2015). The HMX1 dimer complex inhibits the expression of *Epha6* (Marcelli et al., 2014). This receptor is normally expressed in high temporal to low nasal gradient in the retina guiding the axons towards the SC region where their Ephrin A binding partners are

less expressed (Triplett & Feldheim, 2012). Based on the *in vitro* studies, similar comments could be made about the potential interaction between HMX1, PTPRO and the Ephrin receptor expression. On the basis of our data, we suggest that an upregulation and missexpression of EPHA6 caused by the absence of HMX1 in dumbo mouse and in OAS-SMF could explain the mistargeting and the decreased overall number of RGC axons projecting to the LGN and SC.

Interestingly, the predicted promoter model approach developed by Boulling et al. (2013) also proposed that *Sema3f* was a target gene regulated by HMX1. SEMA3F is a cue molecule, involved in central nervous system axon guidance and retinocollicular mapping. This repulsive ligand, found in the SC, binds to the neuropilin 2 receptor (Nrp), which is expressed in a nasal-temporal gradient in RGC (Sahay et al., 2003, Claudepierre et al., 2008). SEMA3F/Nrp signalling also controls cranial gangliogenesis and axon guidance through neural crest cells (Schwarz et al., 2008, Gammil et al., 2006). Previous studies of dumbo mice demonstrated that lack of HMX1 resulted in marked defects in the geniculate (VII) ganglion (Quina et al., 2012a). Taken together, these results suggest that HMX1 is required for axon guidance in the developing retinotectal projection mapping of the mouse.

Materials and methods

Animals

Dumbo mice bearing the *dmbo* allele (*Hmx1*^{dmbo}) strain C57BL/6; C3HeB/FeJ-Hmx1$^{dmbo/Rw/JcsJKjn}$ were purchased from Jackson Laboratories (Stock #008677). The *Hmx1*^{dmbo} allele was obtained by ENU mutagenesis of C57BL/6 inbred mice. By routine genetic control of the strain we detected a mutation in the *Pde6b* gene, also located on chromosome 5, leading to the Rd1 phenotype, characterized by early retinal degeneration. The mice were therefore backcrossed in C57BL/6J wild-type animals for 2-5 generations in order to eliminate the Rd1 mutation. The studies adhered to the Association for Research in Vision and Ophthalmology (ARVO) Statement for the Use of Animals in Ophthalmic and Vision Research and were approved by the Veterinary Service of the State of Valais (Switzerland). C57BL/6J mice were obtained from Janvier (Le Genest St Isle, France).

Mouse genotyping was performed by PCR on ear punch genomic DNA in the case of living individuals, and on tail genomic DNA in the case of stillborn and euthanized individuals. Amplifications of the *Hmx1*^{dmbo} and wild-type *Hmx1* (*Hmx1*$^{+}$) alleles were done by PCR using oligonucleotide primers surrounding the *dmbo* mutation (forward primer: 5'- GCG CTC AAC CCA GGG CGA TG -3', reverse primer: 5'- ACC ACC TCC GTA GCC GCC GTG CAC-3'). The amplicon obtained was then sequenced using the forward primer to determine wild-type, homozygous and heterozygous dumbo mice.

Eye phenotype analysis

86 *Hmx1*$^{dmbo/+}$ and 68 *Hmx1*$^{dmbo/dmbo}$ mice between 1 and 12 months of age were examined. Eyes were illuminated and visually classified into three categories: normal, cataract, or cataract and microphthalmia.

Hematoxylin and eosin staining

Hematoxylin and eosin staining was performed according to standard protocols on 10-µm cryosections fixed with 4% paraformaldehyde (PFA) and embedded in Yazzulla (30% albumin, 3% gelatine in dH_2O) from retina of mice between 1 and 12 months of age. Slides were analyzed with an Olympus BX61 microscope with the Cell^{M} software (Olympus).

Immunohistochemistry and antibodies

Immunohistochemistry staining was performed according to standard protocols on 10-µm cryosections fixed with 4% PFA and embedded in Yazzulla from retina of mice between 1 and 12 months of age. The following antibodies and dilutions were used: Rho 1D4, 1/100, (courtesy of Prof. R.S. Molday (UBC)), Rabbit Anti-Opsin, blue, 1/500, AB5407 (Chemicon International), Rabbit Anti-Opsin, red/green, 1/1000, AB5405 (Chemicon International), PKC α (H-7), 1/500, sc-8393 (Santa Cruz Biotechnology), Rabbit anti-Calbindin D- 28K, 1/1500, AB1778 (Chemicon International), Rabbit Antibody to Glycine, 1/10000, IG1001 (ImmunoSolution), Anti-Glial Fibrillary Acidic Protein, 1/400, Z 0334 (DakoCytomation), Brn-3 (C-13), 1/100, sc-6026 (Santa Cruz Biotechnology) and Thy-1 (H-110), 1/100, sc-9163 (Santa Cruz Biotechnology). The slides were analyzed with an Olympus BX61 microscope with the Cell^{M} software (Olympus).

Virtual-reality optomotor system

The virtual-reality optomotor system was used as described in Marcelli et al, 2012. Briefly, mice of each genotype were analyzed between 1 and 6 months of age, each eye counted individually (number of eyes per genotype written for each measurement). Mouse were taken out of the cage and gently deposed on the platform of the optomoter system. Virtual projection of a rotating cylinder covered with a vertical sine wave was started and "testing" mode chosen on the software OptoMotry version 1.7.7 (CerebralMechanics). This mode avoids a bias in the analysis by the experimentator as the spatial frequency (how often the gratings repeat per unit of distance in cycles/degree) used for the test is not known to him. The system proposed random spatial frequencies and experimentator assesses the optokinetic reflex (by clicking "yes" or "no") of the mouse by visualizing it on a screen. The software calculates the number of repetitions of each frequency needed to set a significant result of visual acuity. Thus the experiment duration can vary between animals.

Electroretinogram

The day before the ERG, mice of the desired age and genotype were placed into total darkness. Until the end of the scotopic ERG, only red light was used. Mice were anesthetized with 10 µl/g of mouse of anaesthesia "ON" solution (600 µl 50 mg/ml ketamine solution (12%), 500 µl 1 mg/ml medetomidine solution (10%), 3.9 ml 0.9% NaCl), by intraperitoneal injection. Pupils were dilated using 0.5% tropicamide and 10%

phenylephrin hydrochloride. Scotopic and photopic ERGs were recorded with an Ocuscience^{TM}HMsERG on 4 *Hmx1*$^{dmbo/dmbo}$ and 4 *Hmx1*$^{dmbo/+}$ heterozygous mice. Scotopic ERGs were recorded at 100, 300, 1000, 3000, 10'000 and 25'000 mcd*sec/m^2, four flashes each 10 sec (0.10 Hz). Photopic ERGs were taken after 10 minutes of bright light illumination and recorded at 10, 30, 100, 300, 1000, 3000, 10'000 and 25'000 mcd*sec/m^2, 32 flashes each 0.5 sec (2.00 Hz). After measurements, 10-15 µl/g of mouse of anaesthesia "OFF" solution (125 µl atipamezole 5 mg/ml solution, 6 ml 0.9% NaCl) was given by intraperitoneal injection and the mice placed on a heating pad until waking. Data were analyzed with the ERGView 4.350 software (Ocuscience^{TM}).

Optic nerve morphology analysis

Five heterozygote and 4 homozygote dumbo mice from 13 to 26 months of age were euthanized by cervical dislocation. Mice were then decapitated and the heads transferred into an ice-cold DMEM/F12 serum free (Gibco®) filled Petri dish for dissection. Using fine surgical tools under a binocular microscope, all the flesh, muscles and bones surrounding brain, optic nerve, ocular globe and olfactory bulb were dissected out to leave these structures completely free with both eyes floating and connected to the brain only by the optic nerve (Fig.5 D-F). Presence of ONH was visually assessed under a dissecting microscope.

Optic nerve thickness measurement

Two types of optic nerve thickness measurements were performed. Firstly, thickness was measured on histological sections where the optic nerve exits the retina at choroidal level (Fig. 6, #1). Measurements were made with a graduated objective on an Olympus BX61 microscope. Five optic nerves of 1 to 2-month-old *Hmx1*$^{dmbo/+}$ and *Hmx1*$^{dmbo/dmbo}$ mice, and 5 optic nerves of 6 to 12-month-old *Hmx1*$^{dmbo/+}$ and *Hmx1*$^{dmbo/dmbo}$ mice were measured. Thickness of 1 to 2-month-old *Hmx1*$^{dmbo/+}$ animals was arbitrarily set to 100, and other measurements represent percentages relative to this value. Secondly, we measured size of the optic nerve (Fig. 6, #2) and optic chiasm (Fig. 6, #3) in ratio to the hypothalamus and assessed occurrence of ONH in adult mice from 13 to 26 month-old. Images of each brain were acquired on a dissecting microscope equipped with a digital camera (Leica DFC 310 FX). Relative sizes (i.e., pixel size) of the hypothalamus, optic chiasm and optic nerve were measured using imageJ software (Fig. 6A,C).

Anterograde labelling of RGC axons

RGC axons of both genotypes were labelled after the morphological analysis in newborn and adult mice from a control group (4 C57BL/6J and 6 *Hmx1*$^{dmbo/+}$) and a dumbo group (5 *Hmx1*$^{dmbo/dmbo}$), detailed list on panel I from figure 8. Brain explants were transferred into DMEM/F12, 10% foetal bovine serum and penicillin-streptomycin medium. With the adult specimens, 2 mm anterior to the optic chiasm, 0.1µl of DiO solution (2mg/ml of dioctadecyloxacarbocyanine perchlorate in ethanol, Sigma-Aldrich, #D4292) was injected into the optic nerve with a Hamilton syringe under a dissecting microscope. With newborns, and in the contralateral eye of adult mice, 0.1 µl of DiI solution (2mg/ml of dioctadecyltetra methylindocarbocyanine perchlorate in ethanol (Sigma-Aldrich, #42364) was injected with a Hamilton syringe under a dissecting microscope directly into the vitreous body of the eye. After 72 hours of incubation at 37°C in the dark, brains were fixed in 4% PFA for 1 week to allow complete migration of lipophilic tracer. Finally, still protected from light with aluminium foils, brains were infused in a 30% sucrose solution for 2 days and embedded in Yazzulla for cryosection.

Retinofugal pathway analysis and optic nerve axon bundle analysis

Sequential 20-µm thick coronal cryosections of labelled brains were obtained from the olfactory lobes to the tip of the cerebellum. DiO and DiI tracing of the RGC axon projections was analyzed under a binocular microscope (Leica MZ16F) with illumination, and the path recorded slice by slice with a camera (Leica DFC310FX), from the optic chiasm towards the optic tract, the lateral geniculate nucleus and the superior colliculus. Schematic representation of the retinofugal path of control mice (C57BL/6J and *Hmx1*$^{dmbo/+}$) and *Hmx1*$^{dmbo/dmbo}$ mice was obtained to summarize the observations (Fig.8). Images were then processed with Adobe Photoshop CS5, using adjustment replace colour option. Lightness of the black colour of each image was increased by an index of 25 to 35 in order to allow a better view of the fluorescent signal (either in green or red). No modifications were applied on the fluorescent values.

Cryosections were selected at the level of the DiO injection into the optic nerve for further morphometric analysis. Images were taken under a microscope (Olympus DP71) at 40x magnification to allow visualization of individual axon bundles provided by the fluorescent labelling. Optic nerve cross sections of 3 *Hmx1*$^{dmbo/+}$ and 3 *Hmx1*$^{dmbo/dmbo}$

mice were analyzed with ImageJ software and single areas of eight axons bundles per slice were measured.

Nissl bodies labelling and counting

20-µm thick coronal cryosections of adult mouse brain were selected at the end point of the optic nerve anterior to the optic chiasm. Sections were fixed in 4% PFA for 1 hour, rehydrated and stained with a solution of cresyl violet acetate (0.53 mg/ml in 0.6% acetic acid, 6 mM sodium acetate, pH 3.5 solution) at 60°C for 30 min. Finally, sections were dehydrated and mounted with Eukitt. Cresyl stained cross sections of both optic nerves from 4 *Hmx1*$^{dmbo/+}$ (N=8) and 3 *Hmx1*$^{dmbo/dmbo}$ animals (except for one dumbo mouse where hypoplasia was too severe to obtain a qualitative section of the nerve, N=5), were imaged under a light microscope (Olympus DP71). Images were analyzed with ImageJ software and Nissl positive bodies counted using counter cell plugins.

Optical coherence tomography (OCT)

Mice were anesthetized with 10 µl/g of anaesthesia "ON" solution (600 µl 50 mg/ml ketamine solution (12%), 500 µl 1 mg/ml medetomidine solution (10%), 3.9 ml 0.9% NaCl), injected intraperitoneally. Pupils were dilated using 0.5% tropicamide and 10% phenylephrin hydrochloride. Fundus photography and OCT analysis were performed with a Micron III system (Phoenix Research Labs, CA, USA) on 3 *Hmx1*$^{dmbo/dmbo}$ and 3 *Hmx1*$^{dmbo/+}$ heterozygous mice. After measurements, 10 µl/g of anaesthesia "OFF" solution (125 µl atipamezole 5 mg/ml solution, 6 ml 0.9% NaCl) were injected intraperitoneally and the mice placed on a heating pad until waking. Data were analyzed with Stream Pix 6 and Micron OCT V7_2_4_2 (Phoenix Research Labs, CA, USA).*Statistical analysis*

P-values are based on Student t-tests or Pearson's Chi-square test as mentioned in the text.

Acknowledgments

Prof. R.S. Molday (University of British Columbia, Vancouver, Canada) for the Rho 1D4 antibody and Ms Susan E. Houghton for editing the manuscript. This work was supported by a grant from the Swiss National Science Foundation (31003A_143474). The funders had no role in study design, data collection and analysis, decision to publish, or preparation of the manuscript.

References

Assali A, Gaspar P, Rebsam A. 2014. Activity Dependent Mechanisms of Visual Map Formation - From Retinal Waves to Molecular Regulators. Semin Cell Dev Biol 35:136–46.

Boulling A, Wicht L, & Schorderet DF. 2013. Identification of HMX1 target genes: a predictive promoter model approach. Mol Vis 19: 1779–94.

Bush JO, Soriano P. 2009. Ephrin-B1 Regulates Axon Guidance by Reverse Signaling through a PDZ-Dependent Mechanism. Gene Dev 23:1586–99.

Chan SO, Wong KF, Chung KY, Yung WH. 1998. Changes in Morphology and Behaviour of Retinal Growth Cones before and after Crossing the Midline of the Mouse Chiasm - a Confocal Microscopy Study. Eur J Neurosci 10:2511–22.

Chung KY, Taylor JS, Shum DK, Chan SO. 2000. Axon Routing at the Optic Chiasm after Enzymatic Removal of Chondroitin Sulfate in Mouse Embryos. Development 127:2673–83.

Claudepierre T, Koncina E, Pfrieger FW, Bagnard D, Aunis D, Reber M. 2008. Implication of Neuropilin 2 / Semaphorin 3F in Retinocollicular Map Formation. Dev Dyn 237:3394–3403.

Conway CD, Price DJ, Pratt T, Mason JO. 2011. Analysis of Axon Guidance Defects at the Optic Chiasm in Heparan Sulphate Sulphotransferase Compound Mutant Mice. J Anat 219:734–42.

Cuenca N, Fernández-Sánchez L, Sauvé Y, Segura FJ, Martínez-Navarrete G, Tamarit JM, Fuentes-Broto L, Sanchez-Cano A, Pinilla I. 2014. Correlation between SD-OCT,

immunocytochemistry and functional findings in an animal model of retinal degeneration. Front Neuroanat 8: doi:10.3389/fnana.2014.00151.

Douglas RM, Alam NM, Silver BD, McGill TJ, Tschetter WW, Prusky GT. 2005. Independent visual threshold measurements in the two eyes of freely moving rats and mice using a virtual-reality optokinetic system. Vis Neurosci 22: 677-684.

Erskine L, Herrera E. 2007. The Retinal Ganglion Cell Axon's Journey: Insights into Molecular Mechanisms of Axon Guidance. Dev Biol 308:1–14.

Fruttiger M, Karlsson L, Hall AC, Abramsson A, Calver AR, Boström H, Willets K, Bertold C-H, Heath JK, Betsholtz C, Richardson WD. 1999. Defective Oligodendrocyte Development and Severe Hypomyelination in PDGF-A Knockout Mice. Development 126:457–67.

Gammill LS, Gonzalez C, Bronner-Fraser M. 2006. Neuropilin 2 / Semaphorin 3F Signaling Is Essential for Cranial Neural Crest Migration and Trigeminal Ganglion Condensation. J Neurobiol 67:47–56.

Garcia-Filion P & Borchert M. 2013. Optic Nerve Hypoplasia Syndrome : A Review of the Epidemiology and Clinical Associations. Curr Treat Options Neurol. 15:78–89.

Gillespie RL, Urquhart J, Lovell SC, Biswas S, Parry NR, Schorderet DF, Lloyd IC, Clayton-Smith J, Black GC. 2015. Abrogation of HMX1 Function Causes Rare Oculoauricular Syndrome Associated With Congenital Cataract, Anterior Segment Dysgenesis, and Retinal Dystrophy. Invest Ophthalmol Vis Sci 56, 883-891.

Godement P, Wang L-C, Mason CA. 1994. Retinal Axon Divergence in the Optic Chiasm: Dynamics of Growth Cone Behavior at the Midline. J Neurosci 14:7024–39.

Gresle M, Alexandrou A, Wu Q, Egan G, Jokubaitis V, Ayers M, Jonas A, Doherty W, Friedhuber A, Shaw G, Sendtner M, Emery B, Kilpatrick T, Butzkueven H. 2012. Leukemia Inhibitory Factor Protects Axons in Experimental Autoimmune Encephalomyelitis via an Oligodendrocyte-Independent Mechanism. PloS One. 7:e47379.

Harada T, Harada C, and Luis F. Parada LF. 2007. Molecular Regulation of Visual System Development : More than Meets the Eye. Genes Dev 21: 367–78.

Herrera E, Marcus R, Li S, Williams SE, Erskine L, Lai E, Mason C. 2004. Foxd1 Is Required for Proper Formation of the Optic Chiasm. Development 131:5727–39.

Howell GR, Libby RT, Jakobs TC, Smith RS, Phalan FC, Barter JW, Barbay JM, Marchant JK, Mahesh N, Porciatti V, Whitmore AV, Masland RH, John SWM. 2007. Axons of Retinal Ganglion Cells Are Insulted in the Optic Nerve Early in DBA/2J Glaucoma. J Cell Biol 179:1523–37.

Huberman AD, Feller MB, Chapman B. 2009. Mechanisms Underlying Development of Visual Maps and Receptive Fields. Annu Rev Neurosci 31: 479–509.

Kaur S, Jain S, Sodhi HBS, Rastogi A, Kamlesh. 2013. Optic Nerve Hypoplasia. Oman J Ophthalmol 6:77–82.

Koch CT, Bruggmann R, Tetens J, & Drögemüller C. 2013. A Non-Coding Genomic Duplication at the HMX1 Locus Is Associated with Crop Ears in Highland Cattle. PLoS One 8, e77841.

Lehmann K, Schmidt K-F, Löwel S. 2012. Vision and visual plasticity in ageing mice. Restor Neurol Neurosci 30: 161-178.

Mao C-A, Wang SW, Pan P, Klein WH. 2008. Rewiring the Retinal Ganglion Cell Gene Regulatory Network: Neurod1 Promotes Retinal Ganglion Cell Fate in the Absence of Math5. Development 135:3379–88.

Marcelli F, Escher P, Schorderet DF. 2012. Exploration of the Visual System: Part2: In Vivo Analysis Methods: Virtual-Reality Optomotor System, Fundus Examination, and Fluorescent Angiography. Curr Protoc Mouse Biol 2:207-218.

Marcelli F, Boisset G, & Schorderet DF. 2014. A dimerized HMX1 inhibits EPHA6/epha4b in mouse and zebrafish retinas. PloS One 9, e100096.

Mescher AL. 2010. Lange Junqueira Basic Histology: text and atlas. McGraw-Hill Professional, New-York, NY.

Munroe RJ, Prabhu V, Acland GM, Johnson KR, Harris BS, O'Brien TP, Schimenti JC. 2009. Mouse H6 Homeobox 1 (Hmx1) mutations cause cranial abnormalities and reduced body mass. BMC Dev Biol. 9, 27.

Paxinos G & Franklin KBJ. 2013. The Mouse Brain In Stereotaxic Coordinates. Elsevier, Oxford, UK.

Petros TJ, Rebsam A, Mason CA. 2008. Retinal Axon Growth at the Optic Chiasm: To Cross or Not to Cross. Annu Rev Neurosci 31:295–315.

Quina LA, Tempest L, Hsu Y-WA, Cox TC, & Turner EE. 2012a. Hmx1 is required for the normal development of somatosensory neurons in the geniculate ganglion. Dev Biol 365, 152–163.

Quina LA, Kuramoto T, Luquetti DV, Cox TC, Serikawa T, & Turner EE. 2012b. Deletion of a conserved regulatory element required for Hmx1 expression in craniofacial mesenchyme in the dumbo rat: a newly identified cause of congenital ear malformation. Dis Model Mech 5, 812–22.

Sahay A, Molliver ME, Ginty DD, Kolodkin AL. 2003. Semaphorin 3F Is Critical for Development of Limbic System Circuitry and Is Required in Neurons for Selective CNS Axon Guidance Events. J Neurosci 23:6671–80.

Schorderet DF, Nichini O, Boisset G, Bozena P, Tiab L, Mayeur H, Munier FL. 2008. Mutation in the Human Homeobox Gene NKX5-3 Causes an Oculo-Auricular Syndrome. Am J Hum Genet 82, 1178–1184.

Schwarz Q, Vieira JM, Howard B, Eickholt BJ, Ruhrberg C. 2008. Neuropilin 1 and 2 Control Cranial Gangliogenesis and Axon Guidance through Neural Crest Cells. Development 136:347–347.

Scudamore CL. 2014. A practical guide to te histology of the mouse. Wiley, Hoboken, NJ.

Shintani T, Ihara M, Sakuta H, Takahashi H, Watakabe I, & Noda M. 2006. Eph receptors are negatively controlled by protein tyrosine phosphatase receptor type O. Nat Neurosci 9: 761–9.

Stanfel MN, Moses KA, Schwartz RJ, Zimmer WE. 2005. Regulation of organ development by the NKX-homeodomain factors: an NKX code. Cell Mol Biol 51: 785-799.

Sun S-W, Campbell B, Lunderville C, Won E, Liang H-F. 2011. Noninvasive Topical Loading for Manganese-Enhanced MRI of the Mouse Visual System. Invest Ophthalmol Vis Sci 52:3914–20.

Triplett JW, Feldheim DA. 2012. Eph and Ephrin Signaling in the Formation of Topographic Maps. Semin Cell Dev Biol 23:7–15.

Vaclavik V, Schorderet DF, Borruat F-X, & Munier FL. 2011. Retinal dystrophy in the oculo-auricular syndrome due to HMX1 mutation. Ophthalmic Genet 32, 114–7.

Wang W, Lo P, Frasch M, & Lufkin T. 2000. Hmx: an evolutionary conserved homeobox gene family expressed in the developing nervous system in mice and Drosophila. Mech Dev 99: 123–37.

Watson C, Paxinos G, Puelles L. 2012. The mouse nervous system. Elsevier, Oxford, UK.

Weimer JM, Custer AW, Benedict JW, Alexander NA, Kingsley E, Federoff HJ, Cooper JD, Pearce DA. 2006. Visual Deficit. Neurobiol Dis 22:284–93.

Wilks TA, Harvey AR, Rodger J. 2013. Seeing with Two Eyes: Integration of Binocular Retinal Projections in the Brain, Functional Brain Mapping and the Endeavor to Understand the Working Brain, Dr. Francesco Signorelli (Ed.), ISBN: 978-953-51-1160-3, InTech, DOI: 10.5772/56491.

Wilson L, Ching Y, Farias M, Hartford SA, Howell G, Shao H, Schimenti JC. 2005. Random mutagenesis of proximal mouse chromosome 5 uncovers predominantly embryonic lethal mutations. Genome Res 15, 1095–1105.

Yahyavi M, Abouzeid H, Gawdat G, de Preux A-S, Xiao T, Bardakjian T, Schneider A, Choi A, Jorgensen E, Baier H, El Sada M, Schorderet DF, Slavotinek AM. 2013. ALDH1A3 Loss of Function Causes Bilateral Anophthalmia/microphthalmia and Hypoplasia of the Optic Nerve and Optic Chiasm. Hum Mol Genet 22:3250–58.

Figures and legends

Figure 1. *Hmx1*$^{dmbo/dmbo}$ eyes and vision. (*A*) Quantification of external eye phenotypes. 68 *Hmx1*$^{dmbo/dmbo}$ and 86 *Hmx1*$^{dmbo/+}$ eyes were classified into three categories: normal, cataract, and cataract plus microphthalmia. (*B*) Measurement of visual acuity. *Hmx1*$^{dmbo/dmbo}$ mice with normal eye phenotype presented reduced visual acuity compared to wild-type or heterozygous mice. ** = P<0.01, *** = P<0.0001 (Student's T-test).

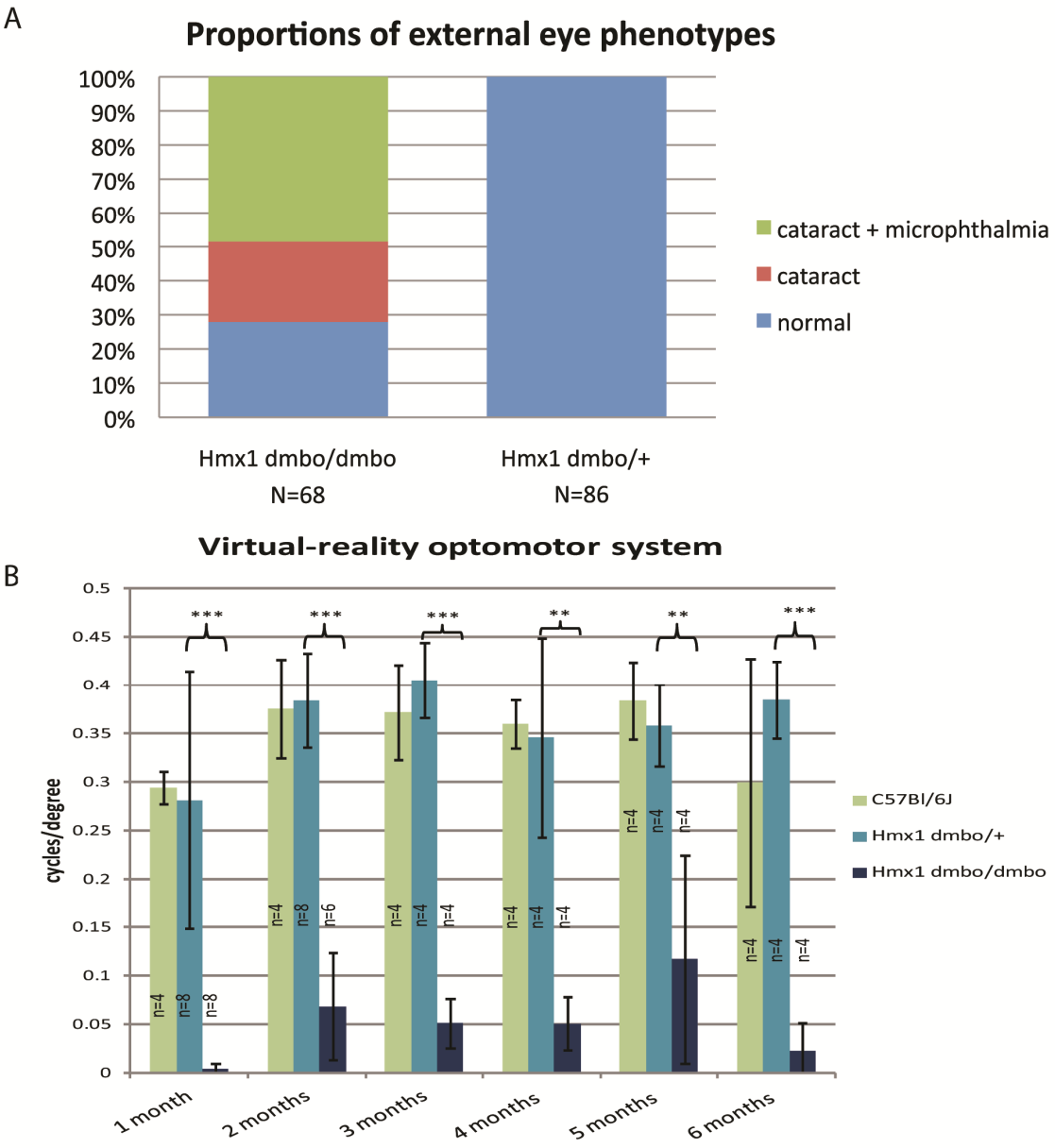

Figure 2. Pannel 1. Representative electroretinograms on 2-month-old animals. **Pannel 2.** Representative electroretinograms on 6-month-old animals. (*A*) C57Bl/6J traces in scotopic conditions and (*B*) in photopic conditions. (*C*) *Hmx1*$^{dmbo/+}$ traces in scotopic conditions (*D*) and in photopic conditions. (*E*) *Hmx1*$^{dmbo/dmbo}$ traces in scotopic conditions and (F) in photopic conditions.

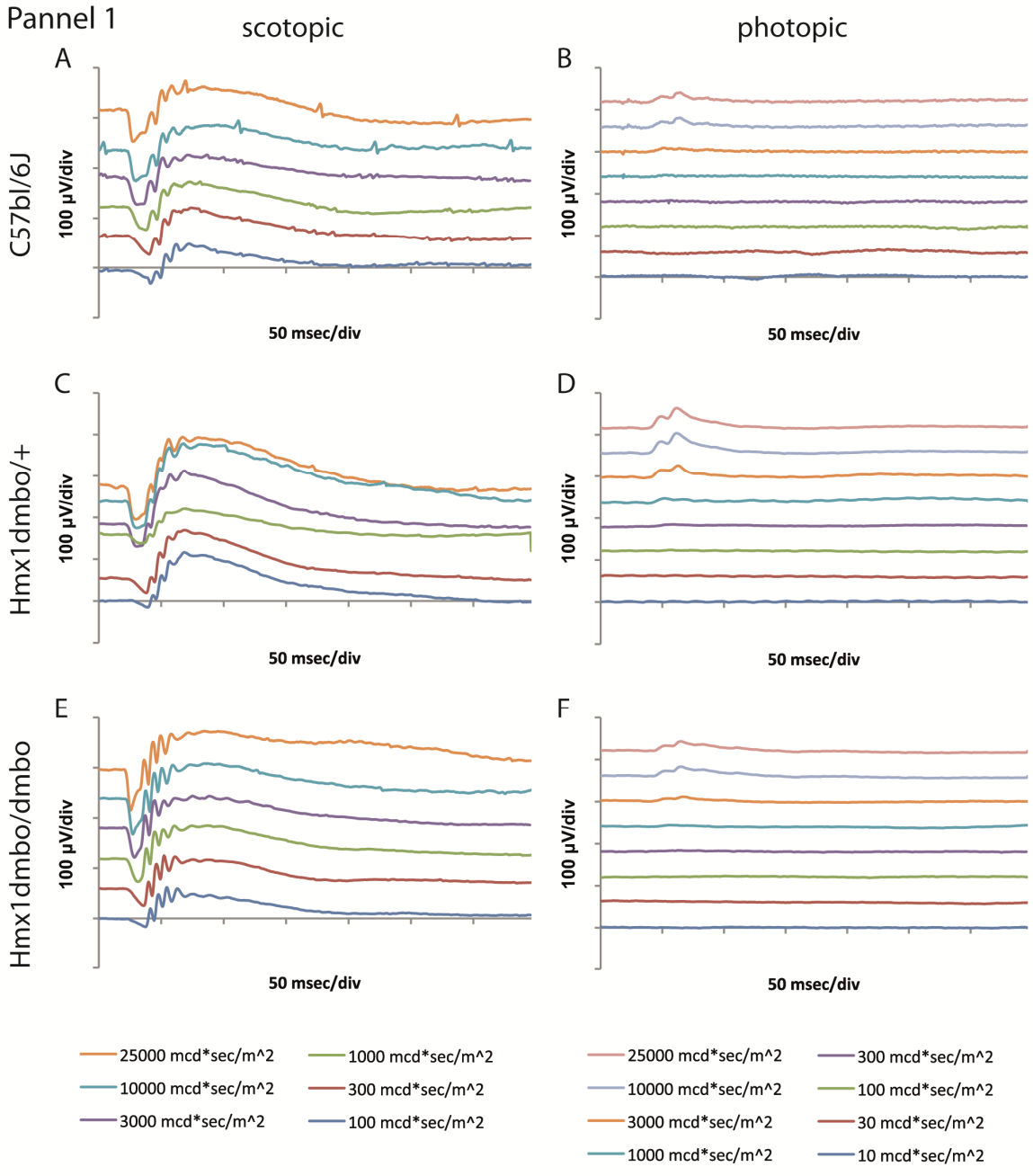

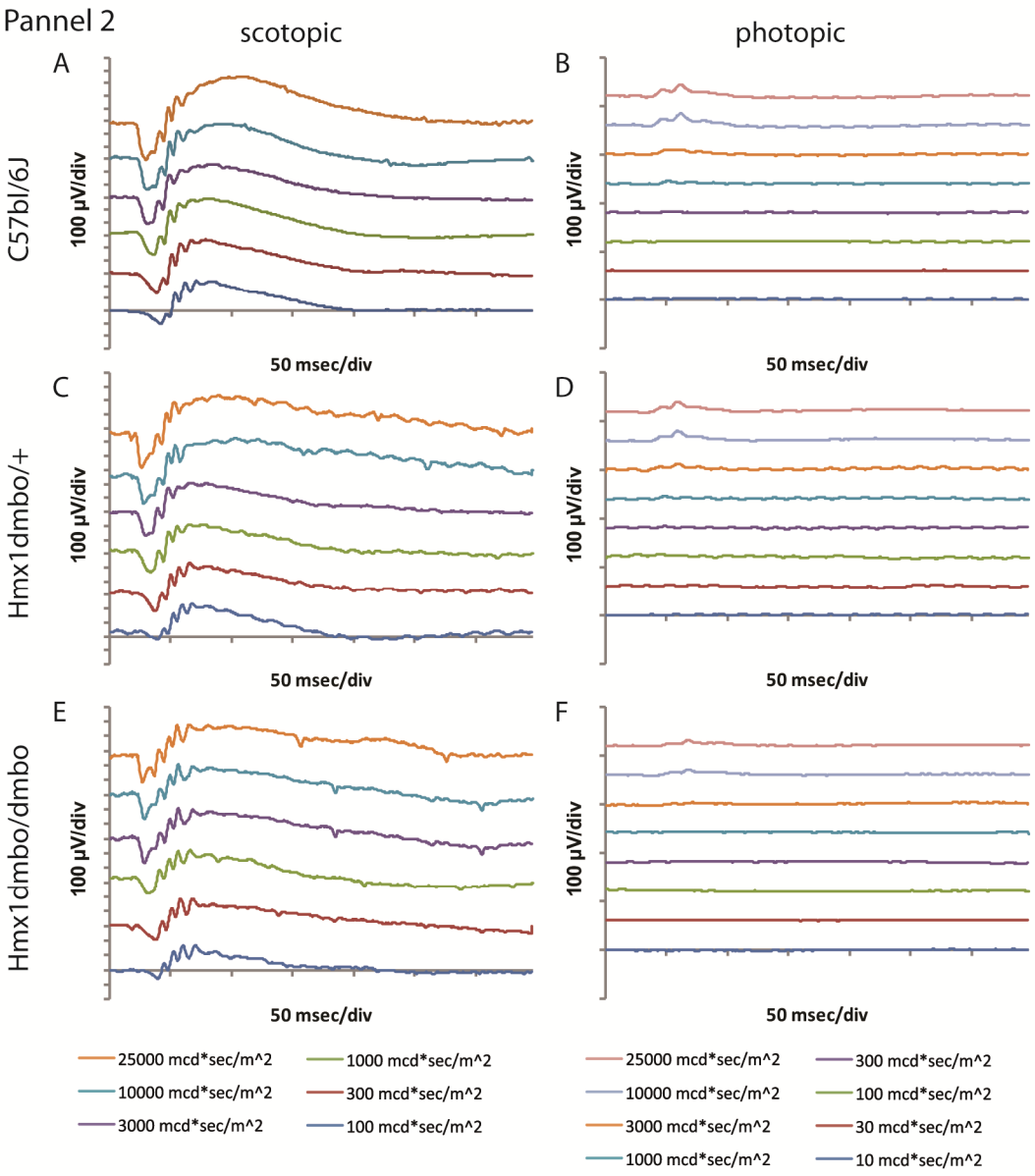
Pannel 2
scotopic
photopic
A
B
C
D
E
F
C57bl/6J
Hmx1dmbo/+
Hmx1dmbo/dmbo
100 µV/div
50 msec/div
25000 mcd*sec/m^2
10000 mcd*sec/m^2
3000 mcd*sec/m^2
1000 mcd*sec/m^2
300 mcd*sec/m^2
100 mcd*sec/m^2
30 mcd*sec/m^2
10 mcd*sec/m^2

Figure 3. Electroretinograms (ERG) statistics of 2 month-old *Hmx1*$^{dmbo/+}$ and *Hmx1*$^{dmbo/dmbo}$ **mice.** A-wave and b-wave amplitude of scotopic and photopic ERG, number of eyes tested per genotype written on each graph. Difference of amplitude response between genotypes are not significant (* = p < 0.1, no star: 0.1<p<0.9, Student's T-test).

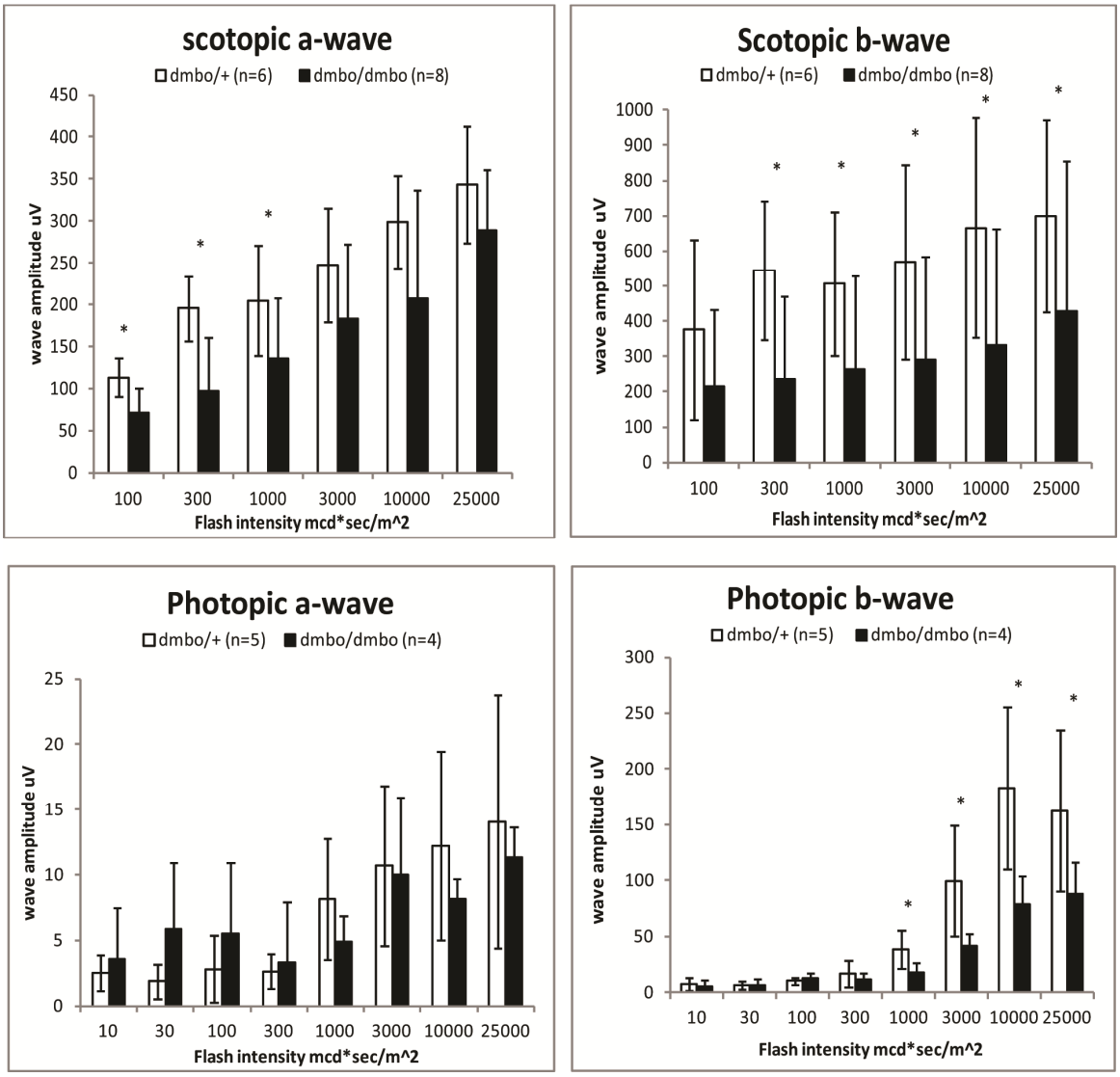

Figure 4. Pannel 1. Histological analyses of *Hmx1*$^{dmbo/dmbo}$ retinas. Negative controls are shown in figure S1. (*A,B*) Hematoxylin-eosin staining. (*C,D*) Recoverin, staining rod photoreceptors. (*E,F*) Opn1sw, staining S-cone photoreceptors. (*G,H*) Opn1mw, staining M-cone photoreceptors. (*I,J*) Pkcα, staining bipolar cells. (*K,L*) Calbindin, staining horizontal cells. (*M,N*) Glycine, staining glycinergicamacrine cells. (*O,P*) Gfap, staining Müller cells. (*Q,R*) Brn-3, staining ganglion cells. (*S,T*) Thy-1, staining axons. Scale bar in D represents 100µm and is valid for all pannels. **Pannel 2.** Negative controls of histological analyses of *HMX1*$^{dmbo/dmbo}$ retinas. (A,B) Hematoxylin-eosin staining. (C,D) Recoverin, staining rod photoreceptors. (E,F) Opn1sw, staining S-cone photoreceptors. (G,H) Opn1mw, staining M-cone photoreceptors. (I,J) Pkcα, staining bipolar cells. (K,L) Calbindin, staining horizontal cells. (M,N) Glycine, staining glycinergicamacrine cells. (O,P) Gfap, staining Müller cells. (Q,R) Brn-3, staining ganglion cells. (S,T) Thy-1, staining axons. Scale bar in D represents 100µm and is valid for all pannels.

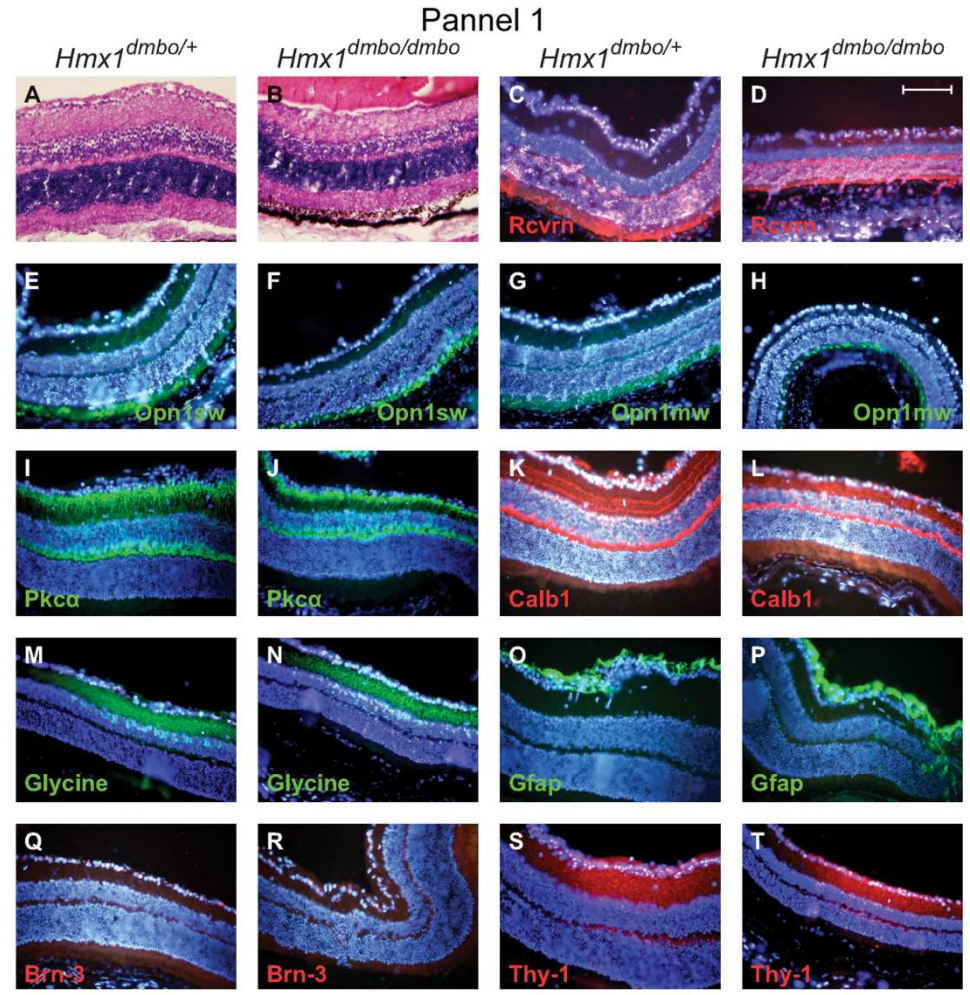
Pannel 1
Hmx1dmbo/+
Hmx1dmbo/dmbo
Hmx1dmbo/+
Hmx1dmbo/dmbo
A
B
C
D
Rcvrn
Rcvrn
E
F
G
H
Opn1sw
Opn1sw
Opn1mw
Opn1mw
I
J
K
L
Pkcα
Pkcα
Calb1
Calb1
M
N
O
P
Glycine
Glycine
Gfap
Gfap
Q
R
S
T
Brn-3
Brn-3
Thy-1
Thy-1

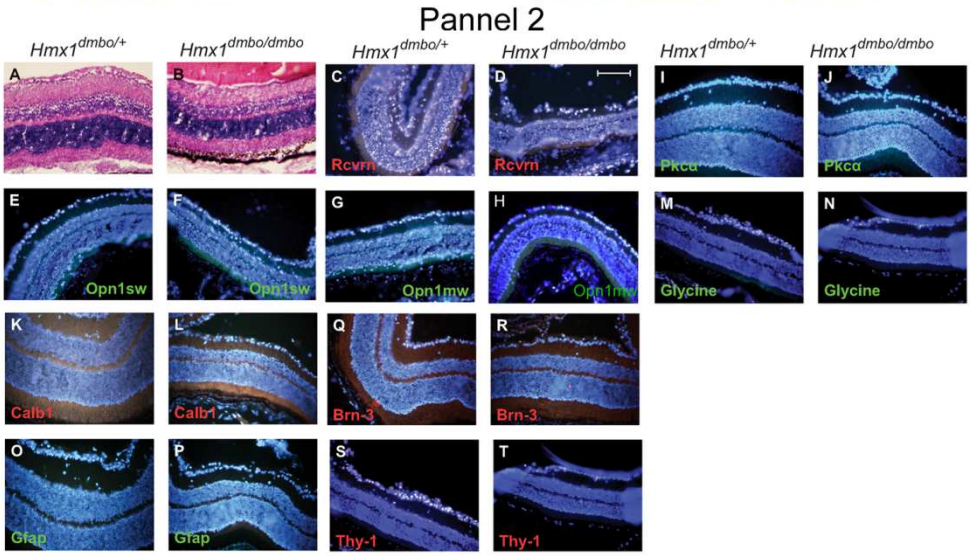
Pannel 2
Hmx1dmbo/+
Hmx1dmbo/dmbo
Hmx1dmbo/+
Hmx1dmbo/dmbo
Hmx1dmbo/+
Hmx1dmbo/dmbo
A
B
C
D
I
J
Rcvrn
Rcvrn
Pkcα
Pkcα
E
F
G
H
M
N
Opn1sw
Opn1sw
Opn1mw
Opn1mw
Glycine
Glycine
K
L
Q
R
Calb1
Calb1
Brn-3
Brn-3
O
P
S
T
Gfap
Gfap
Thy-1
Thy-1

Figure 5. Retinal scanning and optical coherence tomography (OCT). (A, C) Fundus picture with indicated orientation of cross-sectional SD-OCT scans. (B,D) Corresponding OCT B-scans at the optic nerve head, scale bar represent 100 µm. (A,B) *Hmx1*$^{dmbo/+}$ mouse. (C,D) *Hmx1*$^{dmbo/dmbo}$ mouse, notice that the presence of cataract is reducing the OCT signal response and downscaling B-scan resolution (red arrow). GC/IPL: Ganglion cell / Inner plexiform layer, INL: Inner nuclear layer, OPL: Outer plexiform layer, ONL: Outer nuclear layer, OLM: Outer limiting membrane, I/OS: Inner-/outer segment border, RPE/CC: RPE/Choriocapillary complex.

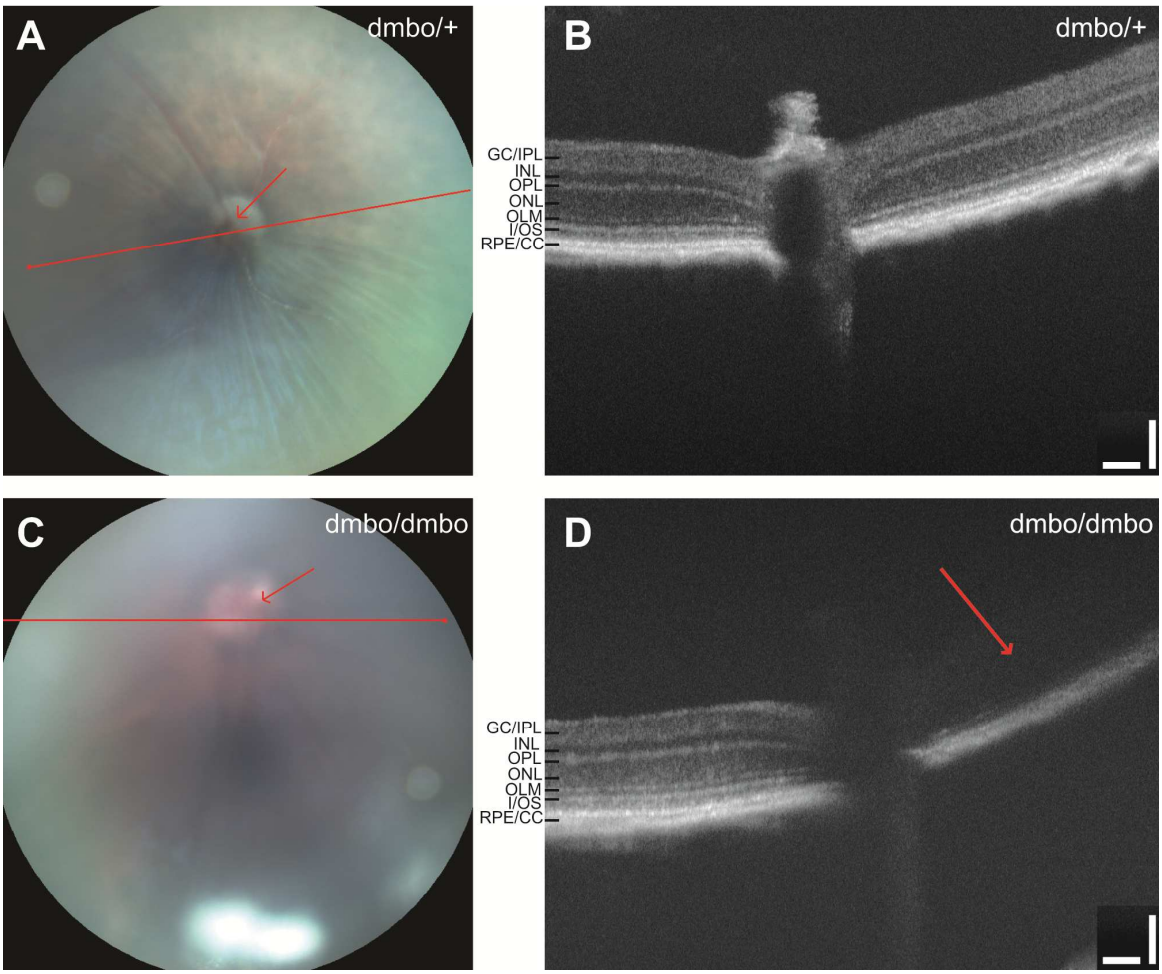

Figure 6. Dumbo mice present ONH. (A) Scheme representing the localization of optic nerve # 1 and #2 thickness, the optic chiasm #3 thickness and the hypothalamus length measurement (*B*) Optic nerve thickness at the level of the choroid in young (1-2 months) and older (6-12 months) animals. Thickness of *HMX1*$^{dmbo/+}$ animals was arbitrarily set to 100. Heterozygous and homozygous dumbo mice showed no difference in optic nerve thickness from 1 to 12 months. (*C*) Optic nerve hypoplasia measurement on dumbo mice (N=4) compared to control mice (N=5). Relative size of the optic chiasm (oc) thickness and optic nerve (on) thickness was normalized over the hypothalamus length to balance the age and size variation of the brain. ONH in dumbo mice resulted in a significantly decreased optic chiasm ($p<0.007$) and optic nerve ($p<0.002$) size compared to heterozygotes. (*D*) Representative retinofugal pathway including eye, optic nerve, optic chiasm and hypothalamus (hyp) of a heterozygous dumbo mouse. (*E*,*F*) Representative retinofugal pathway of dumbo mice presenting either bilateral (*E*) or unilateral *(F*) ONH, and a thinning of the dense core of the optic chiasm. Vertical bars delimit hyp, oc, and on size. Hd: harderian gland.

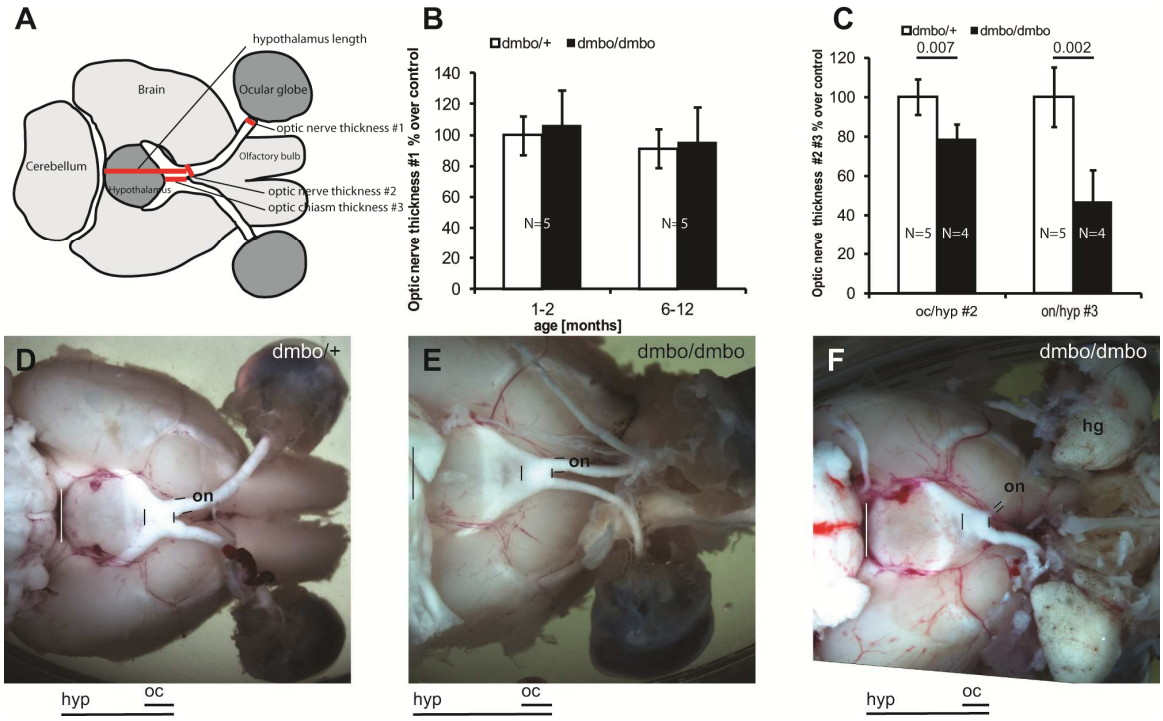

Figure 7. Optic nerve analysis of heterozygote and homozygote dumbo mice. (*A*) Optic nerve cross sections were stained with cresyl to label Nissl bodies. Homozygote mice present morphological changes due to optic nerve hypoplasia (i.e., smaller diameter) (scale bar = 0.02 cm). (*B*) Despite the apparent decrease of Nissl bodies, the variance between both *Hmx1*$^{dmbo/+}$ and *Hmx1*$^{dmbo/dmbo}$ were large and the absolute difference is not significant ($p<0.1$). (*C*) Optic nerves were filled with DiI or DiO to label the axons of RGC neurons and optic nerve bundle areas (green circles) were measured on optic nerve cross sections (scale bar = 0.02 cm). (*D*) Histogram displays average area of optic axon bundles in both genotypes. No difference was observed.

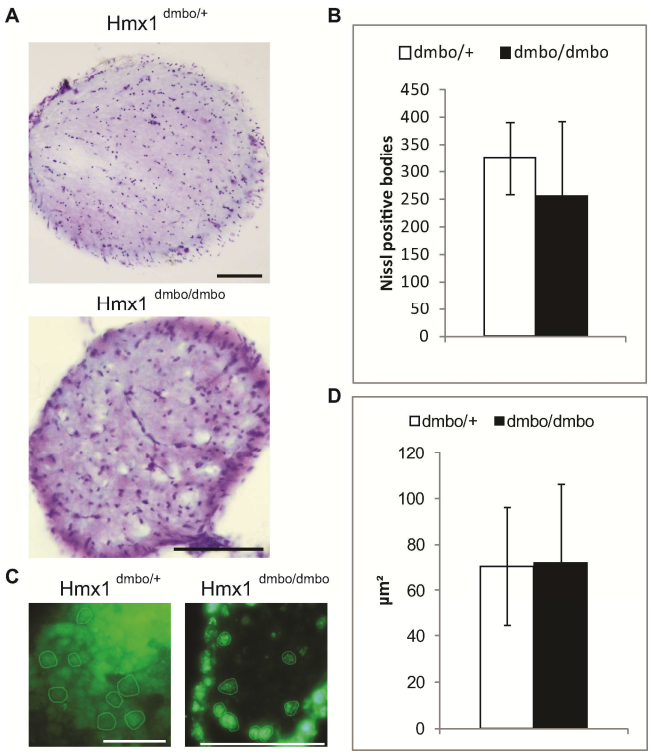

Figure 8: Retinotopic topography is abnormal in dumbo mice. (*A*) Schematic representation of the retinotopic map of *Hmx1*$^{dmbo/+}$ and (*A'*) Hmx1$^{dmbo/dmbo}$ mice as observed after DiI or DiO injection. The straight segment depicts the site of injection of the fluorescent dye, alternatively injected. Red (DiI) and green (DiO) paths depict the observed traces of anterograde labelling along the optic tract. The alphabetic grid represents the position chosen for representative photographs of brain cross sections from *Hmx1*$^{dmbo/+}$ and *Hmx1*$^{dmbo/dmbo}$ mice. (*B-H and B'-F'*) Pannels are schematic illustration representing brain areas as observed and coloured elements depict retinotopic area labelled after fluorophore injection. Area localization was based on the mouse stereotaxis atlas of Paxinos and Franklin (2013). Fluorescent images are representative selections of brain coronal cross sections of *Hmx1*$^{dmbo/+}$ *(B-H)* mice and *Hmx1*$^{dmbo/dmbo}$ mice (*B'-H').* Fluorescent signal is emphasized by black arrows. *(I)* Summary of results obtained by retrograde labelling of optic nerve projections. The table lists all specimens with genotype and age, and indicates the observation of fluorescence in the visual outputs (e.g.: optic nerve, optic chiasm, lateral geniculate, superior colliculus) and in aberrant target (ventricles). Aca: anterior part of anterior commissure, av: anteroventral thalamic nucleus, cc: corpus callosum, dg: dentate gyrus, dlg: dorsal lateral geniculate nucleus, d3v: dorsal 3rd ventricle, ec: external capsule, fi: fimbria of the hippocampus, hip: hippocampus, ld: laterodorsal thalamic nucleus, lv: lateral ventricle, on: optic nerve, op: optic nerve layer of superior colliculus, opt: optic tract, ot: nucleus of the optic tract, vhc: ventral hippocampal commissure, 3v: 3rd ventricle.

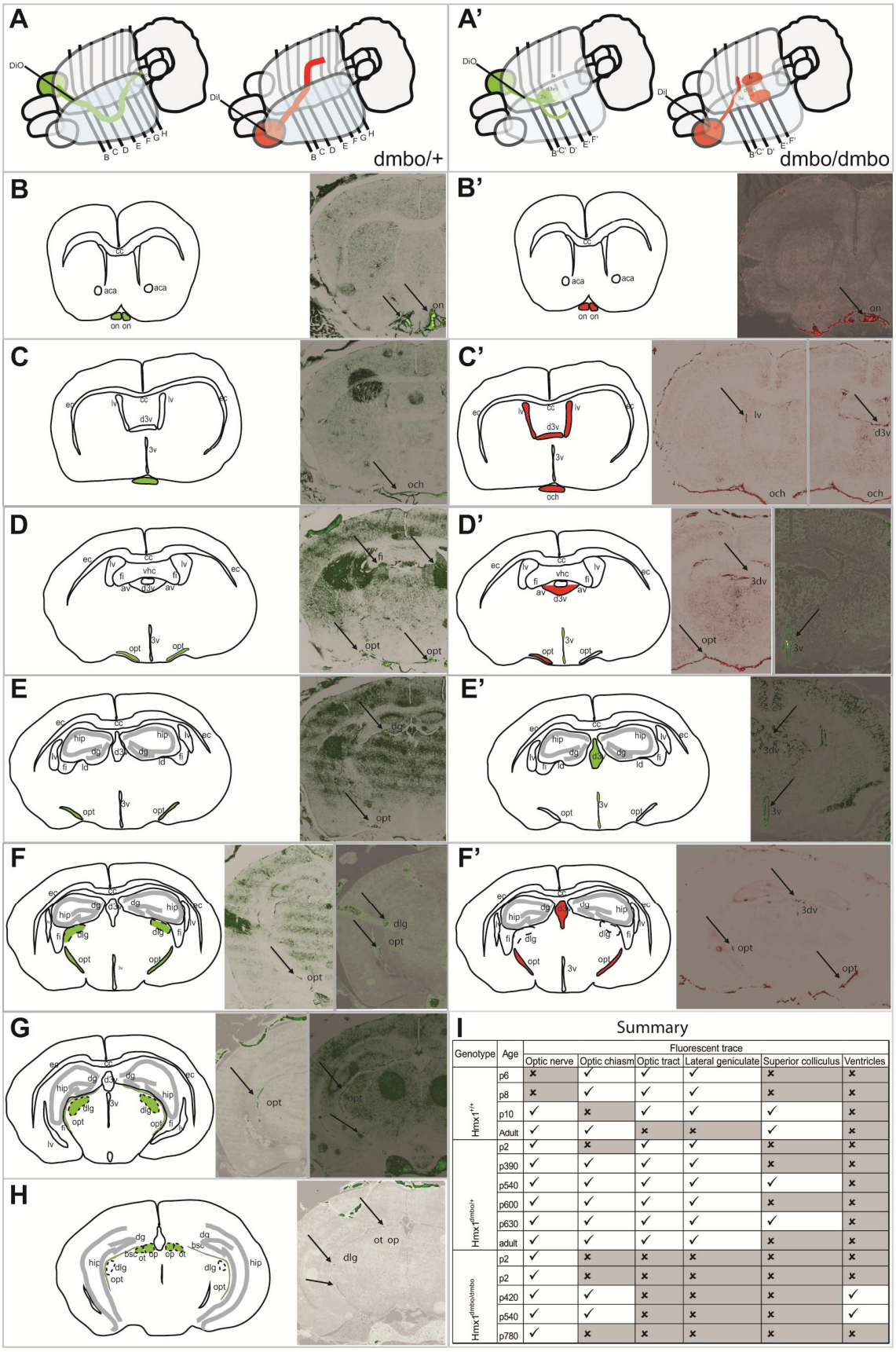

I Summary

Genotype	Age	Fluorescent trace					
		Optic nerve	Optic chiasm	Optic tract	Lateral geniculate	Superior colliculus	Ventricles
$Hmx1^{+/+}$	p6	×	✓	✓	✓	×	×
	p8	×	✓	✓	✓	×	×
	p10	✓	×	✓	✓	✓	×
	Adult	✓	✓	×	×	✓	×
$Hmx1^{dmbo/+}$	p2	✓	×	✓	✓	×	×
	p390	✓	✓	✓	✓	×	×
	p540	✓	✓	✓	✓	✓	×
	p600	✓	✓	✓	✓	×	×
	p630	✓	✓	✓	✓	✓	×
	adult	✓	✓	✓	✓	×	×
$Hmx1^{dmbo/dmbo}$	p2	✓	×	×	×	×	×
	p2	✓	×	×	×	×	×
	p420	✓	✓	×	×	×	✓
	p540	✓	✓	×	×	×	✓
	p780	✓	×	×	×	×	×

3. Discussion

When I joined the *HMX1* project at the Institute for research in Ophthalmology, the study on the predictive promoter model (PPM) approach had already started. The goal of the project was to find target genes of *Hmx1* in the mouse retina. And more largely to discover genes involved in the mouse eye development. These last findings were then involved in my research.

Potential targets of *Hmx1* were identified through a detailed transcriptome analysis. This analysis was based on the repetition of the transcription factor binding site within promoter regions. What was missing were the *in vitro* studies validating these *in silico* results. My work was then to design and perform the luciferase assay to test the transcriptional activity of *Hmx1* over promoter region of the target genes: *Sgcg*, *Ptpro* and *Sema3f*. *Sgcg* was taken as a positive control as its expression was dramatically increased in dumbo mice. *Ptpro* and *Sema3f* belong to the retinal axon guidance pathway and play an important role in retinotopic mapping (Shintani et al., 2006, Stepanek et al., 2001). As related in the previous section, we were able to show the repressor activity of HMX1 protein over those three promoters. These results focused our consideration concerning the implication of the ephrin pathway as it was already recognized to be a putative in vivo target of *Hmx1* by Shorderet et al. and Marcelli et al..

The other part of my study concentrated on a detailed analysis of the dumbo mouse model. Because at first sight this mouse model seems to not hold all the promises that lie in a transgenic animal model, I decided to go over a wide range of structural analysis of this animal. I look after various parameters and performed multiple analyses ranging from metabolite analysis of the circadian system, embryogenesis or breeding ability of homozygous individuals. The crucial discovery has been achieved after I performed a survey on dumbo breeding. This work allowed me to uncover the potential of information that were hiding behind all the perinatal death of pups. Thus the phenotypic analysis led to the promising finding on morphogenesis impairment observed in homozygous dumbo stillborn.

The craniofacial deformity patterns observed in the stillborn dumbo mice suggested that *Hmx1* target are not only involved in the eye development but also in the craniofacial development. Based on the previous PPM approach results we suggested that there is a potential interaction of *Hmx1* in the cranial neural crest cell migration process toward the regulation of *Sema3f*. Then concerning new targets of *Hmx1*, we proposed that potentially other member of the ephrin pathway should be tested. Indeed, we already know that *EphA6* expression is regulated by *Hmx1*, but considering the cleft palate phenotype observed in most of the homozygous stillborn, *EphB3* appears as a very interesting candidate.

Previous analysis of the visual perception of *Hmx1*$^{dmbo/dmbo}$ mice performed by one of the co-authors of the paper from section 2, demonstrated that these mice were blind and that this blindness was not related to retinal defect. The rational was then to analyze central visual pathway of dumbo in order to understand the cause of this visual impairment. This led us to the discovery of retinotopic mapping defects.

Unlike human afflicted by a homozygous *HMX1* mutation, dumbo mice were not presenting a retinal degeneration that would explain the vision defect observed. With the qualitative analysis of the retinotopic mapping in these mice, we brought here a valid cause of this blindness. We also brought to light the presence of optic nerve hypoplasia (ONH) at adult stage that corroborates what is observed in OAS-SMF. More generally ONH is often linked to axon guidance molecules defects and mutation in genes involved in optic nerve development (Garcia-Filion & Brochert, 2013 and Kaur et al., 2013). An important point to discuss here is the evolution of the optic nerve status and its projection during dumbo mouse's life. Our findings didn't allow at this point to assess whether the abnormal retinotoppic mapping observed early in the dumbo mouse is caused by a degenerative process or a failure in axon growth and guidance during embryogenesis. What we can say is that the optic nerve hypoplasia of the dumbo mouse, which is only observed in adult and not before 12-month-old, is most likely due to a retrograde degeneration due to the abnormal mapping of axons. The issue here remains open concerning the varied aspect of the ONH. We would suggest pursuing here the molecular study of *EphA6*, *Ptpro*, and *Sema3f* to establish their link with *Hmx1* in vivo and their expression variation due to HMX1 protein depletion.

The results presented in this thesis and throughout the three publications bring a new lighting on the HMX1 pathway. Homeobox genes are complicated to study because they involve developmental pathways that crossact with a multitude of partners. But the information we discovered allowed us to focus on precise potential target genes, partners and pathways where *HMX1* could be involved.

Much remains to be performed concerning *HMX1*. The main goal of following studies would be to analyze the presented interaction at a molecular level. Because even if we have established a new phenotypic trait linked to *Hmx1* mutation involving craniofacial malformation, molecular proof remains to be presented. We still do not know the target genes that mediate those defects. And we also do not know the pathway involved in bone patterning or growth, affected in the absence of the HMX1 transcription factor.

Concerning the visual defect, I would highly recommend pursuing the research on ephrin and semaphorin pathway. It would be very interesting to analyze expression patterns of those guidance cues in homozygote either adult or stillborn, and find the molecular link between the lack of HMX1 and the mistargeting of RGC axons. Concerning the eye structure, we didn't go through a histological analysis of the stillborn dumbo pups. A control of the layering and

expression level of major guidance cue would allow orientating the debate in a more precise direction.

Finally as most of the semaphorin or neuropilin knockout mouse model exhibit a cerebral patterning defect, it would be interesting to perform histological analysis of adult and stillborn brain explants.

4. Bibliography

Articles

Ackman JB, Crair MC. (2014). Role of emergent neural activity in visual map development. *Curr Opin Neurobiol.* 24: 166-175.

Adameyko I, Lallemend F, Aquino JB, Pereira JA, Topilko P, Müller T, Fritz N, Beljajeva A, Mochii M, Liste I, Usoskin D, Suter U, Birchmeier C, Ernfors P. (2009). Schwann cell precursors from nerve innervation are a cellular origin of melanocytes in skin. *Cell*. 139: 366-379.

Arshavsky VY, Wensel TG. (2013). Timing is everything: GTPase regulation in phototransduction. *Invest Ophthalmol Vis Sci.* 54 : 7725-7733.

Assali A, Gaspar P, Rebsam A. (2014). Activity dependent mechanisms of visual map formation – From retinal waves to molecular regulators. *Semin Cell Dev Biol.* 35: 136-146.

Boisset G, Schorderet DF. (2012). Zebrafish hmx1 promotes retinogenesis. *Exp Eye Res.* 105: 34-42.

Chai Y, Maxson REJ. (2006). Recent advances in craniofacial morphogenesis. *Dev Dyn.* 235: 2353-2375.

Cheng H, Khan NW, Roger JE, Swaroop A. (2011). Excess cones in the retinal degeneration *rd7* mouse, caused by the loss of function of orphan receptor *Nr2e3*, originate from early-born photoreceptor precursors. *Hum Mol Genet*. 20: 4102-4115.

Claudepierre T, Koncina E, Pfrieger FW, Bagnard D, Aunis D, Reber M. (2008). Implication of Neuropilin 2 / Semaphorin 3F in Retinocollicular Map Formation. *Dev Dyn.* 237:3394–3403.

Clouthier DE, Garcia E, Schiling TF. (2010). Regualtion of facial morphogenesis by endothelin signalling: Insight from mice and fish. *Am J Med Genet A.* 152: 2962-2973.

Depew MJ, Simpson CA, Morasso M, Rubenstein JLR. (2005). Reassessing the *Dlx* code: the genetic regulation of branchial arch skeletal pattern and development. *J Anat.* 207: 501-561.

Erskine L, Herrera E. (2007). The retinal ganglion cell axon's journey: Insights into molecular mechanisms of axon guidance. *Dev Biol.* 308: 1-14.

Fitzpatrick DR, van Heyningen V. (2005). Developmental eye disorders. *Curr opin genet dev.* 15: 348-353.

Forrester JV, Xu H, Kuffová L, Dick AD, McMenamin PG. (2010). Dendritic cell physiology and function in the eye. *Immunological Reviews.* 234:282-304.

Forrester D & Swaroop A. (2012). Minireview: The role of nuclear receptors in photoreceptor differentiation and disease. *Mol Endocrinol.* 26: 905-915.

Furimsky M, Wallace VA. (2006). Complementary Gli activity mediates early patterning of the mouse visual system. *Dev Dyn*. 235: 594-605.

Furlan A, Lübke M, Adameyko I, Lallemend F, Ernfors P. (2013). The transcription factor Hmx1 and growth factor receptor activities control sympathetic neurons diversification. *EMBO J.* 32: 1613-1625.

Gillespie RL, Urquhart J, Lovell SC, Biswas S, Parry NRA, Schorderet DF, Lloyd IC, Clayton-Smith J, Black GC. (2015). Abrogation of HMX1 Function Causes Rare Oculoauricular Syndrome Associated With Congenital Cataract, Anterior Segment Dysgenesis, and Retinal Dystrophy. *Invest Ophth Vis Sci.* 56, 883-891.

Graw J. (2003). The genetic and molecular basis of congenital eye defects. *Nature.* 4: 876-888.

Harada T, Harada C, Parada LF. (2007). Molecular regulation of visual system development : more than meets the eye. *Genes & Dev*. 21: 367-378.

Heavner W, Pevny L. (2012). Eye development and retinogenesis. *Cold Spring Harb Perspect Biol.* 4: a008391.

Hennig AK, Peng G-H, Chen S. (2008). Regulation of photoreceptor gene expression by Crx-associated transcription factor network. *Brain Res.* 1192: 114-133.

Huberman AD, Feller MB, Chapman B. (2008). Mechanisms underlying development of visual maps and receptive fields. *Annu Rev Neurosci.* 31: 479-509.

Johnson JM, Moonis G, Green GE, Carmody R, Burnank HN. (2011). Syndromes of the first and second branchial arches, part 1: Embryology and characteristic defects. *Am J Neuroradiol.* 32: 14-19.

Kevany BM, Palczewski K. (2010). Phagocytosis of retinal rod and cone photoreceptors. *Physiology*. 25: 8-15.

Kiser PD, Golczak M, Maeda A, Palczewski K. (2012). Key enzymes of the retinoid (visual) cycle in vertebrate retina. *Biochim Biophys Acta.* 1821: 137-151.

Koch CT, Bruggmann R, Tetens J, Drögemüller C. (2013) A Non-Coding Genomic Duplication at the *HMX1* Locus Is Associated with Crop Ears in Highland Cattle. *PLoS ONE.* 8: e77841.

Kuwajima T, Yoshida Y, Takegahara N, Petros TJ,Kumanogoh A, Jessell TM, Sakurai T, Mason C. (2012). Optic chiasm presentation of semaphorin6D in the context of plexin-A1 and Nr-CAM promotes retinal axon midline crossing. *Neuron*. 74: 676-690.

Kuramoto T, Yokoe M, Yagasaki K, Kawaguchi T, Kumafuji K, Serikawa T. (2010) Genetic Analyses of Fancy Rat-Derived Mutations. *Exp Anim.* 59: 147–155.

Marcelli F, Boisset G, Schorderet DF. (2014). A dimerized HMX1 inhibits *EPHA6/epha4b* in mouse and zebrafish retinas. *PloS ONE.* 9: e100096.

Matsuo I, Kuratani S, Kimura C, Takeda N, Aizawa S. (1995). Mouse *Otx2* functions in the formation and patterning of rostral head. *Genes & Dev.* 9: 2646–2658.

McBratney-Owen B, Iseki S, Bamforth SD, Olsen BR, Morriss-Kay GM. (2008). Development and tissue origins of the mammalian cranial base. *Dev Biol.* 322: 121-132.

McLaughlin T, Hindges R, O'Leary DDM. (2003). Regulation of axial patterning of the retina and its topographic mapping in the brain. *Curr opin Neurobiol.* 13: 57-69.

Minoux M, Rijli FM. (2010). Molecular mechanisms of cranial neural crest cell migration and patterning in craniofacial development. *Development*. 137: 2605-2621.

Munroe RJ, Prabhu V, Acland GM, Johnson KR, Harris BS, O'Brien TP, Welsh IC, Noden DM, Schimenti JC. (2009). Mouse H6 Homeobox 1 (Hmx1) mutations cause cranial abnormalities and reduced body mass. *BMC Dev Biol.* 9: 27.

Noden DM., Trainor PA. (2005). Relations and interactions between cranial mesoderm and neural crest populations. *J Anat.* 207, 575–601.

Oster SF, Bodeker MO, He F, Sretavan DW. (2002). Invariant Sema5A inhibition serves an ensheating function during optic nerve development. *Development.* 130: 775-784.

Petros TJ, Rebsam A, Mason CA. (2008). Retinal axon growth at the optic chiasm: to cross or not to cross. *Annu Rev Neurosci.* 31: 295-315.

Quina LA, Tempest L, Hsu Y-WA, Cox TC, & Turner EE. (2012a). Hmx1 is required for the normal development of somatosensory neurons in the geniculate ganglion. *Dev Biol* 365, 152–163.

Quina LA, Kuramoto T, Luquetti DV, Cox TC, Serikawa T, & Turner EE**.** (2012b). Deletion of a conserved regulatory element required for Hmx1 expression in craniofacial mesenchyme in the dumbo rat: a newly identified cause of congenital ear malformation. *Dis Model Mech.* 5, 812–822.

Ramkumar HL, Zhang J, Chan C-C. (2010). Retinal ultrastructure of murine models of dry age-related macular degeneration (AMD). *Prog Retin Eye Res.* 29: 169-190.

Rasband K, Hardy M, Chien C-B. (2003). Generating X: Formation of the optic chiasm. *Neuron.* 39: 885-888.

Reis LM, Semina EV. (2015). Conserved genetic pathways associated with microphthalmia, anophthalmia, and coloboma. *Birth Defects Res C Embryo Today.* Doi: 10.1002/bdrc.21097

Schorderet DF, Nichini O, Boisset G, Polok B, Tiab L, Mayeur H, Raji B, de la Houssaye G, Abitbol MM, Munier FL. (2008). Mutation in the Human Homeobox Gene *NKX5-3* Causes an Oculo-Auricular Syndrome. *Am J Hum Genet.* 82, 1178–1184.

Shintani T, Ihara M, Sakuta H, Takahashi H, Watakabe I, Noda M. (2006). Eph receptors are negatively controlled by protein tyrosine phosphatase receptor type O. *Nat Neurosci.* 9: 761–769.

Spassky N, de Castro F, Le Bras B, Heydon K, Quéraud-LeSaux F, Bloch-Gallego E, Chédotal A, Zalc B, Thomas J-L. (2002). Directional guidance of oligodendroglial migration by class 3 semaphorins and Netrin-1. *J Neurosci.* 22: 5992-6004.

Stepanek L, Sun QL, Wang J, Wang C, Bixby JL. (2001) CRYP-2/cPTPRO is a neurite inhibitory repulsive guidance cue for retinal neurons in vitro. *J Cell Biol.* 154: 867-878.

Strauss O. (2005). The retinal pigment epithelium in visual function. *Physiol Rev.* 85: 845-881.

Swaroop A, Chew EY, Bowes Rickman C, Abecasis GR. (2009). Unraveling a multifactiorial late-onset disease: from genetic susceptibility to disease mechanisms for age-related macular degeneration. *Annu Rev Genomics Hum Genet.* 10:19-43.

Swaroop A, Kim D, Forrest D. (2010). Transcriptional regulation of photoreceptor development and homestasis in the mammalian retina. *Nat Neurosci.* 11: 563-576.

Triplett JW, Feldheim DA. (2012). Eph and ephrin signalling in the formation of topographics maps. *Semin Cell Dev Biol.* 23: 7-15.

Turner EE, Cox TC. (2014). Genetic evidence for conserved non-coding element function across species-the ears have it. *Front physiol. 5:7.* Doi: 10.3389/fphys.2014.00007.

Wang W, Lo P, Frasch M, & Lufkin T. (2000). *Hmx*: an evolutionary conserved homeobox gene family expressed in the developing nervous system in mice and *Drosophila*. *Mech Develop.* 99: 123–37.

Wilks TA, Harvey AR, Rodger J. 2013. Seeing with Two Eyes: Integration of Binocular Retinal Projections in the Brain, Functional Brain Mapping and the Endeavor to Understand the Working Brain, Dr. Francesco Signorelli (Ed.), ISBN: 978-953-51-1160-3, InTech, DOI: 10.5772/56491.

Yoshiura K-I, Leysens NJ, Reiter RS, Murray JC. (1998). Cloning, characterization, and mapping of the mouse Homeobox gene *Hmx1. Genomics.* 50: 61-68.

Textbooks

Purves D, Augustine G, Fitzpatrick D, Hall WC, LaMantia A-S, McNamara JO, White LE. (2008). Neuroscience. Fourth edition. *Sinauer. USA.*

Watson C, Paxinos G, Puelles L. (2012). The mouse nervous system. First edition. *Academic Press, Elsevier.*

Kaufman MH. (1998). The atlas of mouse development. Revised edition. *Academic Press, London.*

Forrester JV, Dick AD, McMenamin PG, Lee WR. (2002). The eye. Basic science in practice. 2nd edition. Saunders. Elsevier.

CURICULUM VITAE

Linda Bapst-Wicht

Ch. De Pierreval 4,
1007 Lausanne, Switzerland
++41-79-704-65-48
bapst.linda@gmail.com

Swiss and Chilean
5 may 1985
married
Biochemist

Education and Qualifications

2010-present	Swiss Federal Institute of Technology (EPFL), Lausanne, Switzerland, Doctoral School of Neuroscience, Life Science. **PhD** in Neuroscience, to be achieved in April 2015. Specialization: Genetics, Immunology, Fluorescence Microscopy, Ophthalmic and Degenerative Disease, Mice Handling and Neurosurgery, Analytical Chemistry
10.2013	Diploma of **Leadership** level 1, Swiss manager association.
07.2012-02.2013	Military Officer School, Birmensdorf. Promotion to **Lieutenant**
2003-2009	Swiss Federal Institute of Technology (EPFL), Lausanne, Switzerland, School of Chemistry and Chemical engineering. **Master** in Molecular and Biological Chemistry, EPFL, 2009. Master thesis: Guanine nucleotide binding proteins expression and purification for biophysical studies, Laboratory of Physical Chemistry of Polymers and Membranes, EPFL. Modules (short list): Cellular Signalling, Chemical Biology, Neurophysiology, Nanobiotechnology and Biophysics, Mass spectrometry, Advanced NMR, Target Synthesis, Food chemistry, Glycobiology and advanced glycochemistry. **Bachelor** in Chemistry and Chemical engineering, EPFL, 2008. Modules (short list): Molecular and cellular biophysics I-II, Biological chemistry I-III, Bioinorganic chemistry, Molecular Biology I, Genetics, Immunology and Microbiology, Cellular and Molecular Biotechnology, Asymmetric synthesis and Medicinal chemistry.
2000-2003	High school, Nyon, Switzerland High school diploma and Certificate, 2003 **Prize** of Chemistry (at high school final exam), 2003.

Publications

Identification of Hmx1 target genes : A predictive promoter model approach, Boulling A., Wicht L., Schorderet D.F., Molecular Vision, Volume 19, Pages : 1779-1794, Published : Aug-6-2013.

Mutation in *Hmx1* causes craniofacial and chest deformity in mice, Bapst-Wicht L., Marcelli F., Steininger V., Pochon M., Schorderet D.F., Disease Models and Mechanisms, submitted.

Visual deficit in *Hmx1-/-* mice is due to optic nerve hypoplasia and abnormal retinotectal projection. Bapst-Wicht L, Marcelli F, Coral Gadea M, Abbet M, Schorderet DF, submitted.

Deciphering the effects of the bisretinoid A2E on mitogen-activated protein kinase in the retinal pigmented epithelium, Balmer D., Bapst-Wicht L., Emery M., Schorderet F. D., and Roduit R.; in preparation.

Professional experience

10.2009-present	**PhD student** at the Institute for Research in Ophthalmology, Sion, Switzerland.
02.2012-04.2013	Military service, infantry troop, exploration unit, Swiss Army.
03.2009-05.2009	**Assistant** for the course of introduction to chemical engineering, EPFL.
August 2008	Summer **internship** in the laboratory of physical chemistry of polymers and membranes (LCPPM, EPFL), familiar with confocal microscopy, cell culture and molecular biology.
05.2007-12.2008	Shop assistant in a croissant shop at Nyon station, at Fairexpress SA.
August 2006	Summer job for the post of QA Documentation at the laboratory of microbiology, department quality control, at Novartis Consumer Health SA in Nyon.
12.2003-06.2004	Officer for OVB (Suisse) SA society for patrimony advice, in Nyon.
10.2002-02.2004	Shop assistant in a croissant shop at Nyon station, at JPC SHOPS SA.

Voluntary experience

02.10.2013-present	Committee member of Military officer association UNIL-EPFL “OfcampusLausanne”.
03.2009-06.2010	Committee member of community association “ACCA”.
10.2007-present	Committee member of “Féerie d’une nuit” association.
09.2004-2013	Committee member of astronomy association “Callista” at EPFL.
03.2007-01.2008	Vice-chairwoman of student association Baramine at EPFL.
04.2005 and 08.2005	Voluntary work for “Marche Blanche” association.
09.2004-03.2005	Voluntary work for “association de la musique actuelle” association (AMA).

Skills

Language: French (mother thongue), English (spoken and written fluently), German (spoken and written), Spanish (spoken and written).

Computing: Good knowledge of Matlab 7.0 and Mathematica software, of data treatment and statistic software (G*power, R, data explorer, CTAn, FlowJow, Ape), of Office, OpenOffice and ChemOffice environment. Use of Internet, research programs (Copernic, Google, pubmed, expasy, SwissProt), and picture treatment (Adobe Photoshop, Adobe Illustrator).

Hobbies: Triathlon, running, skydiving, shooting, astronomy and reading.